

# **The *In-Silico* Neocortical Microcircuit: From Structure to Dynamics**

THÈSE N° 6168 (2014)

PRÉSENTÉE LE 28 MAI 2014  
À LA FACULTÉ DES SCIENCES DE LA VIE  
PROJET BLUEBRAIN  
PROGRAMME DOCTORAL EN NEUROSCIENCES

ÉCOLE POLYTECHNIQUE FÉDÉRALE DE LAUSANNE

POUR L'OBTENTION DU GRADE DE DOCTEUR ÈS SCIENCES

PAR

**Michael REIMANN**

acceptée sur proposition du jury:

Prof. C. Petersen, président du jury  
Prof. H. Markram, Prof. S. L. Hill, directeurs de thèse  
Prof. G. Einevoll, rapporteur  
Prof. W. Gerstner, rapporteur  
Dr A. Holtmaat, rapporteur



ÉCOLE POLYTECHNIQUE  
FÉDÉRALE DE LAUSANNE

Suisse  
2014





[...]All I ask is a tall ship and a star to steer her by,  
And the wheel's kick and the wind's song and the white sail's shaking,  
And a grey mist on the sea's face, and a grey dawn breaking.  
— John Masefield,  
*Salt-Water Ballads* (1902)

To my parents...



# Acknowledgements

After exactly five years since I started my endeavours at the Blue Brain and in the time I have met some of the most amazing people. I would like to thank all of them for being a great influence in my life. This is especially true for the first and second generation of Blue Brainers, they made me know that I had found the right place for my PhD work.

First thanks go to the people that first got it started :

Thanks to Felix Schürmann for giving the presentation that made me apply at Blue Brain, to Henry Markram for accepting me and to Sean Hill for getting me up to speed.

If you come to the conclusion that this work has actually any scientific value, know that it was only possible with the help of the following great scientists :

Here is thanks to Costas Anastassiou, a brilliant person with a frequent-flier account that must soon be overflowing and great to work with. Thanks also to Srikanth Ramaswamy for always, *always*, **always** knowing where the precise information that I needed could be found. Finally thanks to Eilif Muller for preserving the vision of Blue Brain and my belief in its mission.

I enjoyed great support in the times when my sanity levels dropped low :

Thanks to Catherine Hanriot and Michelle Bonnard for inexhaustible patience and helping me navigate the bureaucratic nightmares. Thanks to Srikanth Ramaswamy, Eilif Muller, the *Whisky Connoisseurs Association* and the *11.30 Breakfast Club* for adding the fun to 'structural to *functional* synaptic conversion'.

In addition, there is a number of great people whose help and support made this work — the very document you are reading — possible in the first place. Without them it would not even be worth the paper it is printed on :

Here is thanks to Eilif Muller, Srikanth Ramaswamy and Julian Shillcock for helpful writing suggestions and proofreading : 'Me fail English ? That is impossible !'.

*Lausanne, 5 March 2014*

M.W. R.



# Abstract

The neocortex is one of the most important brain regions, occupying more than 80% of the brain volume in mammals and contributing massively to its capability of perceiving and interpreting then environment. While it has been extensively studied, it is still largely unclear how it accomplishes the enormous computational tasks it is faced with. A number of structural features are conserved across the cortex, such as its vertical organization in six individual layers with a large number of morphologically unique neuron types. The exceptional horizontal uniformity, lead to the hypothesis of horizontally repeated *unitary microcircuits*, the idea that the cortex consists of a number of relatively uniform horizontally repeated modules, each with their own function in the concert of neural activity. While a rough mapping of function to cortical region is virtually identical between individuals and very similar between species, the extraordinary plasticity of the cortex allows functions of damaged parts to be taken over by neighboring regions. This indicates that flexible, "reprogrammable" modules implement the functions of the cortex.

The Blue Brain Project (BBP) aims to build a facility for the collection and integration of available data on the fundamental structure and operating principles of the cortex to build and continuously refine a detailed, bottom-up model of the unitary microcircuit. It can then be used as a building block for the construction and simulation of larger cortical regions.

A bottom-up model such as the one of the BBP aims to match the object being represented primarily on an underlying physical level. As such it is guaranteed to be anchored in real world physical constraints, this however comes with the disadvantage that on a higher level the behavior of the model is undetermined. The goal of this thesis is to study and characterize the model to learn more about its function and what determines it. In order to ensure the biological relevance, this endeavour was to be tightly linked with comparisons to and validations against relevant experimental data. I concluded that the simulation of extracellular electrical signals are the right tool to link characterization and validation, due to their great importance in *in-vitro* work.

I authored several improvements to the model to ensure the biological accuracy of the computed extracellular signals, the most important being the derivation of the local connectome inside the modeled microcircuit. Next, I implemented software for the calculation of extracellular signals during the course of a simulation on a BlueGene/P supercomputer. The method for the calculation is flexible and can discern between the contributions of individual cells. In

## Acknowledgements

---

addition to validating the signal against *in-vitro* data, this allowed us to analyze the composition of the signals in a way that is impossible outside of a simulation. The method revealed the crucial role of active currents in the *local field potential*, i.e. the relatively slow deflections in extracellular signals. We also extensively analyzed and quantified the varying contributions of individual cell types and membrane mechanisms to extracellular signals at different frequencies.

## Keywords

Neocortical Microcircuit, *in-silico*, connectome, synaptic pathways, plasticity, cable-theory, extracellular potential, local field potential, frequency scaling, synaptic currents, action potential

# Zusammenfassung

Der Neocortex, eine der wichtigsten Gehirnregionen, nimmt in Säugetieren mehr als 80% des Hirnvolumens ein und leistet einen enormen Beitrag zu seiner Fähigkeit, die Umwelt wahrzunehmen und zu interpretieren. Die Region war das Ziel zahlreicher wissenschaftlicher Studien, dennoch bleibt unklar, wie sie ihre enorm komplizierten Aufgaben wahrnimmt. Strukturell ist der Cortex über seine gesamte Oberfläche erstaunlich gleichförmig; beispielsweise besteht er überall aus sechs unterschiedlichen, vertikal angeordneten Schichten mit einer großen Anzahl morphologisch unterschiedlicher Neuronen. Die außerordentliche horizontale Gleichförmigkeit führte zur Hypothese eines *einheitlichen Mikroschaltkreises*, der Idee, dass der Cortex aus zahlreichen, relativ einheitlichen Modulen besteht, die — ein jedes mit einer eigenen Aufgabe — die gesamte Fläche des Cortex ausmachen. Grob gesehen hat die gleiche cortikale Region stets auch eine gleiche Funktion, sowohl zwischen Individuen als auch zu einem gewissen Grad zwischen verschiedenen Spezies. Gleichzeitig erlaubt die enorme Plastizität des Cortex, dass die Funktion einer beschädigten Region von einer benachbarten übernommen werden kann. Dies ist ein weiteres Indiz dafür, dass flexible, "reprogrammierbare" Module diese Funktionen ausmachen.

Ziel des Blue Brain Projects (BBP) ist es, eine Stätte einzurichten für das Sammeln und Integrieren der verfügbaren Daten über die fundamentale Struktur und Arbeitsweise des Cortex und ein von Grund aufbauendes Modell des einheitlichen Schaltkreises zu konstruieren und stetig zu verfeinern. Das Modell kann dann quasi als ein Baustein benutzt werden, um größere cortikale Regionen zu bauen und zu simulieren.

Ein *bottom-up* Ansatz beim Modellieren, wie er im BBP verfolgt wird, versucht das repräsentierte Objekt in erster Linie auf der zugrunde liegenden physikalischen Ebene zu erfassen. Dies garantiert, dass das Modell tief in der physischen Realität verankert ist, hat jedoch den Nachteil, dass das übergeordnete Verhalten zunächst einmal unklar ist. Das Ziel dieser Arbeit ist es, das Modell des einheitlichen, cortikalen Mikroschaltkreises des BBP zu studieren und zu charakterisieren und zu erforschen, welche Bestandteile seine Funktion bestimmen. Um biologisch relevant zu bleiben, gehören dazu Vergleiche und Validierungen gegen relevante experimentelle Daten. Ich kam zu dem Schluss, dass extrazelluläre elektrische Signale ein wichtiges Mittel für die Charakterisierung und Validierung sind auf Grund ihrer herausragenden Bedeutung in experimentellen *in-vitro* Studien.

Ich führte mehrere Verbesserungen des Modells ein, um die biologische Genauigkeit der



## Acknowledgements

---

simulierten extrazelluläre Signale sicherzustellen; die wichtigste war die Herleitung des "lokalen Connectoms", das heißt der synaptischen Verbindungen zwischen den Neuronen des Modells. Danach implementierte ich ein Programm für die Berechnung der extrazellulären Signale einer Simulation auf einem BlueGene/P Supercomputer. Die Methode zur Berechnung ist sehr flexibel und kann zwischen den Beiträgen individueller Zellen unterscheiden. Zusätzlich zur Validierung erlaubte dies uns die Zusammensetzung der Signale zu erforschen auf eine Weise, die außerhalb einer Simulation unmöglich wäre. Diese Methode offenbarte die entscheidende Rolle aktiver Ionenkanäle im "local field potential", das heißt in den relativ langsamen Deflektionen des extrazellulären Signals. Weiterhin analysierten und quantifizierten wir die veränderlichen Beiträge individueller Zelltypen und Membranmechanismen zum extrazellulären Signal in verschiedenen Frequenzen.

## Stichworte

Neocortikaler Mikroschaltkreis, *in-silico*, Konnektom, Synaptische Verbindungen, Plastizität, Kabeltheorie, Extrazelluläres Potentials, Lokales Feld Potential, Frequenzskalierung, Synaptische Ströme, Aktionspotential

# Contents

<b>Acknowledgements</b>	<b>v</b>
<b>Abstract (English/Deutsch)</b>	<b>vii</b>
<b>List of figures</b>	<b>xiii</b>
<b>List of tables</b>	<b>xvii</b>
<b>I Introduction</b>	<b>1</b>
<b>1 Motivation</b>	<b>3</b>
1.1 The Significance of Modeling Work . . . . .	3
1.2 Reconstruction and Modeling of a Neocortical Microcircuit by the BBP . . . . .	3
1.3 Validating, Predicting and Understanding Microcircuit Activity . . . . .	4
1.4 Extraction of Extracellular Potentials from a Neocortical Microcircuit Simulation	5
1.5 Prerequisites for a biologically accurate extracellular potential <i>in-silico</i> . . . . .	5
1.5.1 The Relevance of a Local Connectome Derivation . . . . .	5
1.5.2 The Relevance of Unitary Synaptic Conductances . . . . .	6
1.5.3 The Relevance of Cell Placement . . . . .	7
1.5.4 The Relevance of Generating Microcircuit Input . . . . .	8
<b>2 An overview of the Blue Brain microcircuit model building process</b>	<b>9</b>
<b>3 Summary of Results</b>	<b>13</b>
<b>II Microcircuit Modeling Methods</b>	<b>15</b>
<b>4 An Algorithm to Predict the Connectome of Neural Microcircuits</b>	<b>17</b>
4.1 Abstract . . . . .	18
4.2 Introduction . . . . .	18
4.3 Results . . . . .	19
4.4 Discussion . . . . .	27
4.5 Methods . . . . .	30
4.6 Figures, tables and legends . . . . .	32

## Contents

---

A	Supplementary Material . . . . .	42
<b>5</b>	<b>Further Methods</b>	<b>53</b>
5.1	Derivation of Synaptic Quantal Conductances . . . . .	53
5.1.1	The approach to conductance prediction . . . . .	54
5.1.2	The prediction method . . . . .	54
5.1.3	Validating predictions . . . . .	55
5.2	Cell Placement . . . . .	57
5.2.1	Relevance . . . . .	57
5.2.2	Method . . . . .	57
5.2.3	Results . . . . .	59
5.3	Input Generation . . . . .	60
5.3.1	Thalamocortical Input . . . . .	60
5.3.2	Simulated Extracellular Stimulation . . . . .	65
<b>III</b>	<b>Microcircuit Modeling Results</b>	<b>69</b>
<b>6</b>	<b>An Analysis of the Predicted Connectome of Neural Microcircuits</b>	<b>71</b>
6.1	Abstract . . . . .	72
6.2	Introduction . . . . .	72
6.3	Results . . . . .	73
6.4	Discussion . . . . .	79
6.5	Methods . . . . .	81
6.6	Figures, tables and legends . . . . .	83
A	Supplementary Material . . . . .	91
<b>7</b>	<b>In-silico measurements of extracellular potentials</b>	<b>95</b>
7.0.1	Overview . . . . .	95
7.0.2	Implementing a volume conductor based calculation of extracellular potentials . . . . .	95
<b>8</b>	<b>A Biophysically Detailed Model of Neocortical Local Field Potentials Predicts the Critical Role of Active Membrane Currents</b>	<b>99</b>
8.1	Summary . . . . .	101
8.2	Introduction . . . . .	102
8.3	Results . . . . .	103
8.4	Discussion . . . . .	109
8.5	Methods . . . . .	113
8.6	Figures . . . . .	117
A	Supplementary Material . . . . .	130

<b>9 Further Results</b>	<b>141</b>
9.1 The limits of spike detection in extracellular signals . . . . .	141
9.1.1 Introduction . . . . .	141
9.1.2 Spike detection and mapping methods . . . . .	141
9.1.3 Results . . . . .	143
9.1.4 Conclusions . . . . .	146
9.2 Comparing Structural and Functional Inhibition under In-Vitro and In-Vivo Conditions . . . . .	146
9.2.1 Introduction . . . . .	146
9.2.2 Methods . . . . .	148
9.2.3 Results . . . . .	148
9.2.4 Conclusions . . . . .	150
 <b>IV Concluding Remarks</b>	 <b>151</b>
<b>10 Context and Relevance of This Work</b>	<b>153</b>
<b>11 Ongoing and Future Work</b>	<b>155</b>
<b>A Supplementary Material</b>	<b>157</b>
A.1 Example of a thalamocortical projection specification . . . . .	157
<b>B A Brief Introduction into the Underlying Neuroscientific Concepts</b>	<b>161</b>
B.1 From Brain to Neocortex to Microcircuits . . . . .	161
B.2 About Extracellular Measurements in Neural Tissue . . . . .	162
<b>C Reconstruction of the Neocortical Microcircuit</b>	<b>163</b>
C.1 Introduction . . . . .	165
C.2 Biological Reconstruction Process . . . . .	166
C.3 Morphological diversity . . . . .	167
C.4 Morpho-electrical diversity . . . . .	170
C.5 The Connectome . . . . .	170
C.6 Neuronal Physiology . . . . .	173
C.7 Synaptic Physiology . . . . .	174
C.8 Network dynamics - spontaneous activity . . . . .	176
C.9 Network dynamics - evoked activity . . . . .	178
C.10 Discussion . . . . .	179
C.11 Figures and Legends . . . . .	184
A Supplementary Figures . . . . .	208
 <b>Bibliography</b>	 <b>240</b>
<b>Curriculum Vitae</b>	<b>241</b>



# List of Figures

2.1	Overview over the steps of the reconstruction workflow . . . . .	9
4.1	Incidental axonal appositions contain information about connectivity . . . .	32
4.2	Naive approaches to apposition filtering do not reproduce biological connectivity . . . . .	33
4.3	Schematic of the three pruning steps . . . . .	34
4.4	Resulting synapse numbers and parameters . . . . .	35
4.5	Biological data and their inter-dependencies constrain synaptic pruning . .	36
4.6	Generalized and emerging results . . . . .	37
4.7	Connectome derivation results in the near absence of biological data . . . .	38
4.8	Robustness of emerging connectivity . . . . .	39
S1	Dendritic and axonal volume filling fractions . . . . .	42
S2	Volumetric density and specificity of inhibitory synapses . . . . .	43
S3	Mean Bouton densities emerging from the extreme generalization approach	44
5.1	Mean PSP amplitudes for different conductances / reversal potentials . . . .	55
5.2	Comparing predicted to actual PSP amplitude scaling . . . . .	56
5.3	Super-linear PSP amplitude scaling in an excitatory connection . . . . .	56
5.4	Biological cell density depth profile . . . . .	57
5.5	Overview of selecting appropriate morphologies . . . . .	58
5.6	Overview of scoring of L5_TTPC2 and L5_MC cells . . . . .	60
5.7	Predicted synapse densities compared to biological data . . . . .	61
5.8	Biological density profile of thalamocortical synapses . . . . .	61
5.9	Overview of thalamocortical projection generation . . . . .	62
5.10	Structure and physiology of in-silico thalamocortical projections . . . . .	64
5.11	Population response to in-silico thalamic stimulation . . . . .	65
5.12	Extracellular stimuli in cable theory . . . . .	66
5.13	In-silico effect of extracellular stimulation on a single cell . . . . .	66
5.14	Comparing in-vitro and in-silico effect of extracellular stimulation . . . . .	67
6.1	Multi-synapse connections in the predicted connectome . . . . .	83
6.2	An example of pathway specific connectivity metrics . . . . .	84
6.3	Predicting external input . . . . .	85
6.4	Emerging connection probabilities . . . . .	86

## List of Figures

---

6.5	Predicting the common neighbor rule for most pathways . . . . .	87
6.6	Intra- and inter-laminar connection specificity . . . . .	88
6.7	Specificity of structural innervation patterns of inhibitory synapse types . .	89
6.8	The relative structural strength of pathways follows a power law . . . . .	90
S1	Predicted connection probabilities at different distances . . . . .	91
S2	Distribution of m-types of synaptic contacts to / from L5_TTPC2 cells . . . .	92
S3	Distribution of the predicted number of efferent synapses per bouton . . . .	93
S4	Emerging distance-dependent connection probabilities . . . . .	94
7.1	Extracellular as a matrix multiplication . . . . .	97
8.1	Intracellular and extracellular biophysics of individual neurons . . . . .	117
8.2	Extracellular potentials under simulated network activity . . . . .	118
8.3	LFP- and CSD-contribution of individual cell populations . . . . .	120
8.4	Comparison of the LFP depth profiles between active and passive membranes	121
8.5	Two cases with altered synaptic input correlation . . . . .	123
8.6	Horizontal reach of extracellular population signals . . . . .	124
8.7	Ionic Contributions to the LFP . . . . .	126
8.8	Frequency- and distance-scaling of LFP . . . . .	128
S1	Exemplary morphologies . . . . .	133
S2	Comparing membrane conductance on active and passive morphologies . .	135
S3	LFP- and CSD-contribution of individual cell populations for the passive mem- brane simulation . . . . .	137
S4	Input correlation statistics for the three network cases . . . . .	139
9.1	Shape and amplitude of extracellular spikes of pyramidal cells . . . . .	142
9.2	Mapping of detected extracellular events to intracellular spikes . . . . .	143
9.3	Extracellular detection of isolated spikes in the presence of electrode noise .	144
9.4	Extracellular spike detection during ongoing full population activity . . . .	145
9.5	Structural and functional inhibition of an L5_TTPC . . . . .	147
9.6	Domain specificity of structural and function inhibition . . . . .	149
10.1	Types of work required for continuous usage of the microcircuit model . . . .	154
C.1	Collage of neocortical neurons. . . . .	184
C.2	Reconstructing morphological diversity. . . . .	185
C.3	Reconstructing morphological composition. . . . .	186
C.4	Reconstructing cell densities and positions. . . . .	187
C.5	Morphologically reconstructed microcircuit. . . . .	188
C.6	Validating morphological composition. . . . .	189
C.7	Reconstructing morpho-electrical neuron types. . . . .	190
C.8	Morpho-electrically reconstructed microcircuit. . . . .	191
C.9	Reconstructing the connectome. . . . .	192
C.10	Insights obtained from the predicted map of connectivity. . . . .	194

C.11	<b>Workflow for reconstructing morpho-electrical behaviors.</b>	195
C.12	<b>Validating and predicting passive and active properties.</b>	196
C.13	<b>Reconstructing quantal synaptic conductances.</b>	197
C.14	<b>Reconstructing synaptic dynamics.</b>	199
C.15	<b>Extrapolated map of synaptic dynamics.</b>	200
C.16	<b>Predicting the synaptome.</b>	201
C.17	<b>Validating and predicting spontaneous activity.</b>	202
C.18	<b>Predicting evoked emergent network states.</b>	203
C.19	<b>Predicting the functions of neurons.</b>	204
C.20	<b>Reconstructing thalamocortical input.</b>	205
C.21	<b>Validating and predicting thalamocortical input.</b>	206
C.22	<b>Predicting network requirements for functional maps.</b>	207
S1	<b>Reconstructing morphologies: Repairing.</b>	208
S2	<b>Reconstructing morphologies: Cloning.</b>	209
S3	<b>Reconstructing inter-laminar architecture.</b>	210
S4	<b>Predicting anatomical properties of a synaptic pathway.</b>	212
S5	<b>Modelling ionic mechanisms.</b>	213
S6	<b>Reconstructed e-types.</b>	214
S7	<b>Ion channel densities reproducing e-types.</b>	215
S8	<b>Reconstructing dynamic synaptic properties for all connections.</b>	216
S9	<b>Predicting physiological properties of the L5_TTPC to L5_MC synaptic pathway.</b>	217
S10	<b>Infrastructural and computing requirements.</b>	218
S11	<b>Ca<sup>2+</sup>-sensitivity of synaptic dynamics.</b>	219
S12	<b>Synchrony of synaptically clustered assemblies of neurons.</b>	220





## List of Tables

4.1	Overview of the failures to recreate biological connectivity measures for different maximal apposition distances . . . . .	40
4.2	Shorthands for synaptic pathways used in Figs 1, 4, 5, S4 . . . . .	41
S1	Emerging synapse numbers and connection probabilities compared to biology for pathways using biological parametrization . . . . .	48
S2	Emerging synapse numbers and connection probabilities compared to biology for pathways using derived parametrization . . . . .	49
S3	Structural functional and biological spine and bouton densities . . . . .	50
7.1	Overview of the steps in <i>in-silico</i> extracellular experiments . . . . .	96
S1	Parameters of the LFP-depth profile in Figs. 7.2, 7.3, 7.4, 7.5 . . . . .	131
S2	Quality-of-fit parameters associated with Fig. 7.8 . . . . .	131
S3	Power-scaling exponent $\alpha$ as calculated for Fig. 7.8 . . . . .	132
S4	Power-scaling exponent $\beta$ for the location closest to the soma as calculated for Fig. 7.8 . . . . .	132



# Introduction **Part I**



# 1 Motivation

## 1.1 The Significance of Modeling Work

The famous quotation of William Thomson, 1st Baron Kelvin: "I am never content until I have constructed a mechanical model of the subject I am studying. If I succeed in making one, I understand; otherwise I do not." pictures a model of a system as the last step in its study. It depicts it as a sign and proof of full understanding, of having conquered the system.

However, even before understanding is complete, a model can serve multiple important purposes. It can serve as a place to integrate existing data and theories, pointing out where data is inconsistent or sparse. It will show you which observed phenomena emerge simply from the known theory and data and where further study is necessary to excavate the underlying causes. Finally, it can generate predictions that have the potential to improve our understanding both if they can be validated experimentally or not.

This type of a model is engaged in a perpetual loop with experimentation, integrating results and contradicting others. To enable such a process we have to ensure that data generated by the model is compatible with experimental data, i.e. the model has to be able to predict analogues of the physical quantities observed in experiments. That way we can start the cycle of integrating, validating and predicting; and ultimately *understanding* – where we can probe the model to find the underlying causes of a phenomenon.

## 1.2 Reconstruction and Modeling of a Neocortical Microcircuit by the BBP

Since its launch in July 2005, it has been the mission of the *Blue Brain Project* (BBP), to build and simulate a model of a unitary microcircuit in the somatosensory cortex of a rat. The model has been continuously updated, even after the first milestone – a model microcircuit containing 10,000 neurons and the ability to simulate its activity [Markram, 2006] – was achieved

in 2007. A significant portion of the individual refinements have been authored by me and describing them will make up part of this thesis.

The continuous cycle of biological data gathering – both from raw measurements and the literature – and model refinement has become an explicit part of the mission statement of the *Human Brain Project* (HBP) initiated by the BBP since October 2013. The focus on constructing a *facility* for ongoing integration and consolidation sets the project apart from similar initiatives at building large-scale brain models [Jones et al., 2009, Kandel et al., 2013]. In this age, where new experimental techniques lead to an exponential growth of generated data, such a facility will prove to be indispensable. It provides a space where the individual data points get an explicit context that highlights their dependencies and consequences, facilitating their interpretation.

From the start, the BBP was described as a "bottom-up" approach to neural modelling, meaning that a primacy of low-level physical measurements over high-level phenomena has to be observed when constraining the model. At the same time, we often find that the more fundamental a data point is, the less complete is our knowledge about it, due to variability within and across cells or brain regions. And mapping out its full variability may not be feasible, even with modern, high-throughput methods. This leads to an intricate interaction between low-level and high-level data, where first – where available – the low-level data is fed into the model, then used to study the relation between it and higher-level phenomena. Finally, the established relation is used to generalize the available data. Examples of this will make up part of this thesis.

An extensive overview of the reconstruction and simulation algorithms that make up the current state of the BBP is available in appendix C, where you can find a draft of the manuscript of the *magnum opus* of the BBP: "Reconstruction of the Neocortical Microcircuit".

### 1.3 Validating, Predicting and Understanding Microcircuit Activity

In line with the theory of permanently integrating modeling work outlined above, it is the purpose of this thesis to contribute to this perpetual cycle. Therefore, among the goals are the following points:

- Find relevant published biological data and develop ways to integrate the data into the circuit, refining it
- Validate the microcircuit model against biological data and develop the tools to do so
- Characterize the emergent activity of the microcircuit model and the underlying parts of the model determining it.

A valuable tool for to this end will be the the *calculation of extracellular potentials* from simulated activity in the model. Extracellular signals are compounded of the contributions of all neurons in a microcircuit, making them a functional characterization of the model.

#### 1.4. Extraction of Extracellular Potentials from a Neocortical Microcircuit Simulation

---

The great availability of extracellular recordings *in-vitro* and literature on that topic can be compared to modeled results, serving as a validation. And finally, as outlined below, the objective of biologically relevant extracellular signals leads to a number of model refinements.

#### 1.4 Extraction of Extracellular Potentials from a Neocortical Microcircuit Simulation

The activity of a cortical microcircuit is first and foremost electrical activity. As such, the microcircuit model of the BBP focuses on the electrical activity of cells and other phenomena – such as the chemical transmission at synapses – are modelled only with respect to their effect on electrical activity. It does this however, with one glaring omission: While the membrane voltage gradient measured in intracellular recordings [Adrian, 1928, Renshaw et al., 1940] is intrinsic to the model [Hines and Carnevale, 1997] the equally or more important technique of extracellular measurements is left out.

The importance of extracellular recordings can hardly be overstated: First attempts go back to the beginning of neuroscience [Caton, 1875, Berger, 1933] and improvements such as the detection of individual spikes [Mountcastle et al., 1969] led to understanding of neural codes in the motor cortex [Georgopoulos et al., 1982, 1986]. It is still used extensively, sometimes indirectly through voltage sensitive dyes [Cohen et al., 1974, Gupta et al., 1981, Roland, 2002, Grinvald and Hildesheim, 2004, Georgopoulos et al., 2007]. The continued importance of extracellular measurements will make them an important tool for the characterization of microcircuit models as well.

#### 1.5 Prerequisites for a biologically accurate extracellular potential *in-silico*

Calculating extracellular potentials will be an important technique to refine our efforts of modelling a cortical microcircuit. In order for the results to be meaningful however, the underlying variables determining the result have to be biologically correct, leading to the following prerequisites:

##### 1.5.1 The Relevance of a Local Connectome Derivation

"Local connectome" refers to the set of connections between neurons in a single microcircuit or brain region. It is one of the most important building blocks of the microcircuit model and especially crucial for the calculation of meaningful extracellular potentials:

First of all, local connections make up a large fraction of the structural input to cortical cells [Stepanyants et al., 2009], as such they will be a main determinant of their activity. In the case of extracellular measurements, an additional aspect plays a role: It is traditionally assumed



that the low-frequency part of an extracellular signal is mainly shaped by synaptic currents [Mitzdorf, 1985, Lindén et al., 2011]. As such, the number and location of synapses — both determined by the local connectome — will impact the amplitude and shape of the generated extracellular signal. So far in the literature on simulations of extracellular signals, synapses have been randomly distributed over the modeled morphologies and activated by random mechanisms with pre-determined statistics [Pettersen et al., 2006, Lindén et al., 2011]. The addition of a biologically accurate Connectome would improve on this by generating the bulk of the synaptic input according to the same rules observed in biological microcircuits, increasing the biological relevance of the results.

However, the biological rules determining the local connectome have not been fully deciphered yet. It is thought to be shaped on a cellular level by interactions of plasticity and homeostatic mechanisms, turning experience into changes in cell-to-cell connectivity [Chklovskii et al., 2004, Hofer et al., 2009, Wilbrecht et al., 2010, Pozo and Goda, 2010]. Yet, on a cell population level certain connectivity trends – such as overall strong connectivity between cells of one certain type and another – are found to be conserved between individuals [Markram et al., 1997, Feldmeyer et al., 1999, 2006a, Le Bé et al., 2007] and many more.

Ideally, a local connectome would be derived by modeling the ontogenesis of the microcircuit, taking into account plasticity and homeostatic rules, cell morphology growth and differentiation as well as realistic input from other regions – an endeavour that is not feasible at this stage. Still, as a first step, the higher level connectivity trends should be enforced in the model. The lack of experience (or input) shaping connectivity on the cellular level means that the microcircuit will implement no useful computation. This can be compared to a freshly manufactured sector of a hard disk, initialized with random bits containing no accessible information, but ready to be written to.

Even this goal is far from trivial: Population level connectivity patterns are reported on a per-pathway basis, where a pathway is defined by a pre- and a postsynaptic cell type. That makes the number of potential pathways equal to the square of the number of defined cell types,  $3025 (= 55^2)$  in the case of the BBP microcircuit model. Only a small fraction of them has been studied experimentally and the extensive amount of work needed to characterize a single pathway means that most of them will not be studied in the near or intermediate future. Therefore, the derivation of the local connectome is a problem characterized by low data availability and tackling it will require the extraction of generalizable rules from the data that is available.

### 1.5.2 The Relevance of Unitary Synaptic Conductances

A derived local connectome as described above will give us biologically relevant synapse numbers and positions, yet one parameter remains to be determined: Synapse strength as described by the unitary synaptic conductance. As with the local connectome, the relevance

## 1.5. Prerequisites for a biologically accurate extracellular potential *in-silico*

---

lies in the effect on the population activity as much as in directly affecting the simulated extracellular measurements.

While attempts to measure the unitary synaptic conductance have been made in the literature [Thomson et al., 1996, Yoshimura et al., 1999], they are highly problematic for use in a model:

The conductance is estimated from measurements using Ohm's Law:

$$G = \frac{I}{V}, \quad (1.1)$$

where  $G$  is the conductance,  $I$  the actually measured quantity: current and  $V$  the voltage. In order to eliminate  $V$  as an unknown quantity, experimenters *hold* the cell at a certain voltage, i.e. they impose via a second electrode a certain voltage on the soma, hoping that the rest of the cell will follow. Proximal dendrites indeed follow the soma voltage, but there will be a gradient along the dendrite towards the natural resting voltage of the cell moving further away from the value held at the soma. If conductances are measured for very distal synapses and/or at holding voltages far from resting, this *space-clamp* error can be significant and has to be taken into account in the conductance calculation.

Unfortunately, if and how it is taken into account varies between publications, there does not seem to be an accepted standard method. Nor are the methods of correction typically extensively described. While the published results are useful qualitatively and have value for comparative studies, they cannot be used in a model without correction. Therefore an alternative method to estimate the unitary conductances is needed .

### 1.5.3 The Relevance of Cell Placement

In a microcircuit model – such as the one of the BBP – that is based on reconstructed neuron morphologies and cable theory, activity can be simulated without spatial information of any kind. Cable theory considers neurons as trees in the graph-theoretical sense synaptic contacts placed on certain edges of the tree ("electrical compartments"), not at spatial locations. Things change however, when the calculation of extracellular potentials is added to the picture. The extracellular potential can be calculated as a weighted sum of the membrane currents emerging from cable theory, where the weight is inverse proportional to the distance from the sampled location [Malmivuo and Plonsey, 1995, Plonsey, 1969, Stevens, 1966, Holt and Koch, 1999]. The distance calculation requires spatial information, making the correct cell placement an important requirement for correct results.

Further, current approaches to the local connectome problem use morphological overlap as a necessary requirement for a cell-to-cell connection [Peters and Feldman, 1976, Braitenberg and Schüz, 1998, Stepanyants and Chklovskii, 2005b, Stepanyants et al., 2008]. Overlap depends on the shape of the morphologies but also on their locations, leading to the prediction

that correct cell placement is a prerequisite of local connectome derivation.

Since neuronal morphologies are typically reconstructed from brain slices [Mize, 1985, Young et al., 1997], their microcircuit context, i.e. their location relative to layer boundaries and other cells, could be determined along with them. Such a morphology would then be used in the model only at locations with an equivalent context. In reality however, most reconstructions lack the circuit context, leading to the need to infer it from morphological features alone.

### 1.5.4 The Relevance of Generating Microcircuit Input

Once all those prerequisites are cleared we can be (more) confident that the simulated neural activity and calculated extracellular potential going along with it are biologically relevant. For a proper analysis however, one more thing is lacking: a way to probe the microcircuit model in a systematic manner. An isolated microcircuit without any stimulus – just as a cortical slice *in-vitro* [Waters, 2006] – will be largely inert with the exception of some spontaneous release occurring with low frequency.

Such a systematic way of inducing activity in simulated neural populations should follow the dictate of biological relevance as well, i.e. it should simulate either (1) an biological process or (2) an *in-vitro* technique. We have done both:

We developed (1) a way to simulate synaptic input from other brain regions as in the biological brain and (2) experimented with a way to simulate the stimulation caused by extracellular electrodes.

## 2 An overview of the Blue Brain micro-circuit model building process

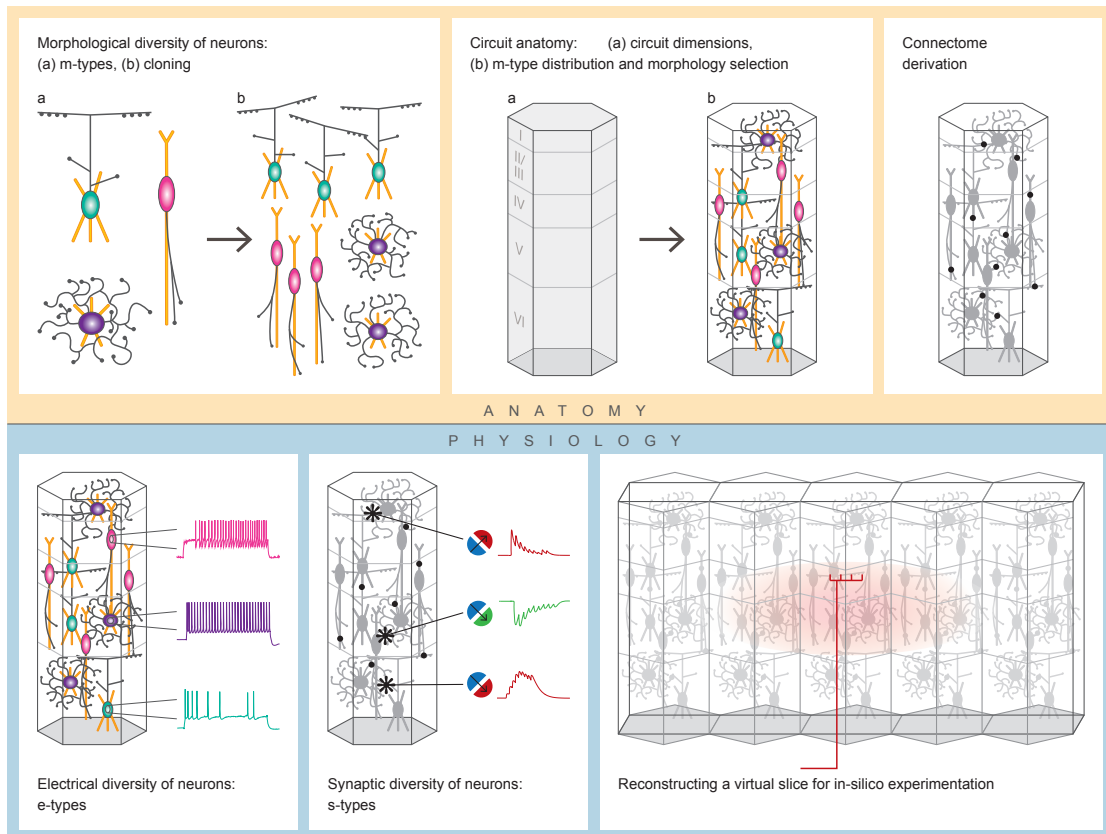


Figure 2.1 – Overview over the steps of the reconstruction workflow

As the work in this thesis is part of the ongoing modelling effort of the Blue Brain Project (BBP), it is best understood in that context. While a brief introduction into the biological principles underlying the significance of this work can be found in Appendix B, and an exhaustive description of the reconstruction of a neocortical microcircuit of the BBP in Appendix C, this chapter will provide a short overview over the steps that go into the construction of an *in-silico* microcircuit to give that context.

The six steps are depicted in Figure 2.1:

- In the first step, the morphological diversity of neurons is captured by generating a pool of reconstructed neuronal morphologies of all morphological types (or **m-types**). Morphologies are reconstructed *in-vitro* by staining them and then tracing their arbors with software assistance under a light microscope. At this stage, 55 distinct m-types (13 excitatory, 42 inhibitory) – all of which had been previously reported in the literature – are defined. M-type names are a combination of their layer of origin (L1, L2/3, L4, L5, L6) and a morphological class identified from axon and dendrite shapes. A full overview can be found in Figure C.2. The diversity with an m-type is enhanced through a process of *cloning* them with slight variations. This step is crucial, as Ramaswamy et al. [2012] showed that morphological diversity is the key for robust *in-silico* synaptic properties.
- In the second step, a hexagonal volume is created and filled with neuron reconstructions, yielding the basic circuit anatomy. The vertical extents of the circuit are defined by layer boundaries measured *in-vitro*; the horizontal extents are defined such that dendritic density in the center has converged to its maximum. The volume is then filled with reconstructed neurons of all m-types according to their individual, experimentally measured densities.
- In the third step, the anatomical locations of synaptic contacts between cells are derived, yielding a predicted connectome. A necessary prerequisite for a synaptic connection is an axonal **apposition**, i.e. an instance of an axon getting close enough to a postsynaptic cell to form a synapse. A small (around 5%) subset of appositions is chosen for synapse placement on a per **pathway** basis, where a pathway – or m-types specific pathway – is defined as the set of connections between cells of a given presynaptic m-type and a given postsynaptic m-type. Thus, the name of a pathway is abbreviated as a combination of m-types, listing the presynaptic one first (e.g. L5\_MC to L5\_UTPC).
- In the fourth step, the electrical diversity of neurons is captured. 13 types of active conductances modelling ion channels are distributed over the surface of the neurons such that they fire action potentials in response to sufficient depolarization. Experimentally, a number of electrical types (**e-types**) were identified, based on the response of a cell to step depolarization *in-vitro* (Figure S6). An evolutionary optimization algorithm finds maximal conductances (modelling ion channel densities) for each channel type, such that certain features of the response are accurately recreated.
- In the fifth step, the anatomical location identified in the third step are turned into actual synaptic contacts. The synapses use the Tsodyks-Markram model [Tsodyks et al., 1998] and are parametrized according to a number of identified synaptic types (**s-types** (Figure C.15)). Thus, the synapses in the microcircuit accurately recreate the experimentally observed dynamics of synaptic transmission (Figure C.14). This step, together with the third step,

---

shape the physiology of synaptic transmission in the reconstructed microcircuit and thus its ability to process information.

- In the final step, the described reconstruction method is used as a building block to construct larger microcircuits, such as virtual slices, to run *in-silico* experiments on.



### 3 Summary of Results

This thesis focuses on improving the characterizing the structure and dynamics of a modeled microcircuit of the rat neocortex as expressed by its connectome (i.e. structure) and by simulated intracellular and extracellular measurements (i.e. dynamics). The work builds on the reconstructed microcircuit, developed in the Blue Brain Project (BBP) from 2005 onwards, but improves it in several ways to ensure greater biological relevance of the results.

The following improvements will be outlined in Part II:

1. The development of a method to connect neurons in the model that can re-create existing and future pathway specific connectivity metrics as they become available and generalizes where such data is unavailable. The work is in process of being submitted to Nature Neuroscience under the title "An Algorithm to Predict the Connectome of Neural Microcircuits" and also constitutes a chapter of the *magnum opus* of the Blue Brain Project, titled "A Reconstruction of the Neocortical Microcircuit" for submission to Nature.
2. A method that scores a pool of reconstructed morphologies for their appropriateness for placement at a given point of the model and selects from the most appropriate to ensure that identified features of the morphology land in the correct layers. That work constitutes a further part of "A Reconstruction of the Neocortical Microcircuit".
3. A method that places additional, external synapses on the dendrites of the model, recreating specifiable density profiles and targeting specifiable cell types. The location of said synapses is used to assign presynaptic cell identities to them, allowing to feed actual spike train instantiations into the model. The method is used to model thalamocortical input in yet another chapter of "A Reconstruction of the Neocortical Microcircuit".
4. A method to simulate the stimulation of neurons in the model via extracellular electrodes.
5. A method to predict unitary synaptic conductances necessary to re-create a given mean amplitude of the post-synaptic potential (PSP).



### Chapter 3. Summary of Results

---

While Part II is restricted to my contributions to improving the quality of the model, they are also available in a wider context in Appendix C. There, an early draft of the *magnum opus* of the Blue Brain modeling effort, "A Reconstruction of the Neocortical Microcircuit" for submission to Nature, can be found.

Part III begins with an analysis of the structure of the reconstructed connectome and its emerging principles. That work is in preparation for submission to Nature Neuroscience under the title "An analysis of the Predicted Connectome of Neural Microcircuits".

Next, the implementation of an established algorithm for the calculation of extracellular potentials in cable theory models is described. This implementation had to take into account the unique BBP infrastructure as well as the exceptional model size.

Building upon this, results of microcircuit characterization using intra- and extracellular measurements as well as purely morphological metrics will be presented. The results describe and validate the complex microcircuit model, but also have relevance beyond it: The crucial role of active currents in measurements of Local Field Potentials predicted may have an effect on the interpretation of extracellular measurements in experiments in the future. This prediction is based on characterizing the constituents of extracellular measurements in a reduced complexity version of the microcircuit model; the work was published under the title "A Biophysically Detailed Model of Neocortical Local Field Potentials Predicts the Critical Role of Active Membrane Currents" in 2013 in NEURON.

This is followed by a number of further results using the derived connectome and extracellular calculation methods:

The extracellular method is used to briefly assess the theoretical limits of spike detection from extracellular traces in the presence of different sources of noise.

The derived connectome was used to predict functional inhibition – as characterized by a local decrease in input resistance – and compare it to the purely structural distribution of inhibitory synapses. This work has been presented as a poster during the annual meeting of the Society for Neuroscience in 2012.

# **Microcircuit Modeling Methods** **Part II**



## **4 An Algorithm to Predict the Connectome of Neural Microcircuits**

*Contributions of the thesis author:*

Development and testing of the algorithm, analysis of results, figure generation and writing of the manuscript.

# An Algorithm to Predict the Connectome of Neural Microcircuits

Michael W. Reimann<sup>1</sup>, Eilif Muller<sup>1</sup>, Srikanth Ramaswamy<sup>1</sup> & Henry Markram<sup>1,†</sup>

<sup>1</sup> Blue Brain Project, Brain Mind Institute, Ecole Polytechnique Fédérale de Lausanne (EPFL),  
1015 Lausanne, Switzerland

<sup>†</sup> Corresponding author

Henry Markram

Blue Brain Project, Brain Mind Institute  
Ecole Polytechnique Fédérale de Lausanne (EPFL),  
1015 Lausanne, Switzerland  
Email: henry.markram@epfl.ch

Submitted to Journal

## 4.1 Abstract

The connectome refers to the map of synaptic connections between the neurons of the brain. With 55 main morphological types of neurons arranged across 6 layers in the neocortex, the local microcircuit of neurons contains theoretically 3025 unique types of morphology-specific synaptic pathways. Only a handful of these pathways have been experimentally characterized in terms of their connection probabilities, numbers of synapses per connection and locations of synapses. We developed a data-driven algorithmic strategy to predictively reconstruct the connectivity of all biologically plausible pathways in the microcircuit. The algorithm is a local and global multi-constraint process simultaneously connecting all possible pairs of neurons by satisfying a set of general principles of synaptic connectivity and a set of connectivity properties specific to each morphology-specific pathway. The result is a complete connectome of the microcircuit with 2258 viable synaptic pathways forming 35 million synapses.

## 4.2 Introduction

The connectome is a key determinant of the computational capability and capacity of the brain [Chklovskii et al., 2004, Hofer et al., 2009]. At the local microcircuit level (a spatial region where all types of neurons can potentially interact locally), the response of each individual neuron is shaped by the spatio-temporal pattern of activation of its input synapses and the impact of a neuron is determined by the output synapses onto its many targets. Mapping all input and output synapses for each neuron is therefore fundamental to understanding the function of a neuron in a microcircuit and ultimately the role played by each type of neuron in the brain.

The complete map of all synapses formed on each of the approximately 30,000 neurons in the smallest

local network of neocortical neurons (a microcircuit), is not known. The neurons of the neocortical microcircuitry have been extensively studied for over a century and these studies collectively report at least **55** main types of morphologically distinct neurons arranged across the 6 layers of the neocortex. This implies that there are theoretically at least 3025 morphology-specific synaptic pathways in the local neocortical microcircuitry. Only 25 of these pathways have been well characterized after 2 decades of experimental study. What is not known is how many of the 3025 theoretically possible pathways are biologically feasible because their neuronal arbors overlap and they have sufficient synapses in the correct locations to form connections, how many synapses are involved in each connection, which portions of the axons are used to form the connections on other types of neurons, which portion of the postsynaptic neuron receives the synapses, and what the connection probabilities between each of these morphological types of neuron are. Even if it were experimentally possible to obtain such a map experimentally, it is most unlikely that this can be obtained for all species, strains, ages and genders, for all brain regions or for the whole brain. A generic strategy to predict the complete connectome using partial data is therefore essential.

We have developed a first principles-based and data-driven algorithmic strategy to predictively reconstruct the connectome of a microcircuit of neurons. We gathered relevant data on synaptic connections between neurons from the literature from which we isolated a set of general principles of synaptic connectivity and pathway specific properties, and developed an algorithm that constrains the properties of pathway-specific connections, adheres to the general principles and constrains the solution for each pathway with each other pathway. This algorithm is now possible because a first draft of the neocortical microcircuit has been reconstructed in the accompanying paper [Markram, 2014]. The reconstruction contains a “periodic table” of all major morphological cell types, their individual densities in each layer and their optimal placement in each layer to respect data on their interlaminar projections. This study describes the derivation and validation of the algorithm, while the following paper provides the fully predicted connectome of the neocortical microcircuit [Reimann et al., b].

## 4.3 Results

A minimal set of principles is required to perform a generic reconstruction of the connectivity of neocortical microcircuits. At the most fundamental level, the local arborization (excluding projecting axons) of virtually all neurons spatially overlap and “touch” each other with a separation that can not be distinguished with a light microscope [Thomson, 1997, Markram et al., 1997, Feldmeyer et al., 1999, Lübke, 2003]. We call these “touches”, *appositions* and refer to this virtually all-to-all structural connectivity as the *structural tabula rasa rule* [Kalisman, 2005]. To identify appositions between 3D model neurons we consider touches with a maximal separation of  $2.5\mu\text{m}$  for excitatory synapses and  $0.5\mu\text{m}$  for inhibitory synapses. For a majority of excitatory synapses, this gap can be bridged by the growth of a spine on the postsynaptic neuron, the swelling of a bouton on the axon, and minor bending of the axon; no directed growth of the axon is required ([Silver, 2003, Karube et al., 2004, Kawaguchi, 2006], for reviews see [Somogyi et al., 1998, Nimchinsky et al., 2002, Stepanyants and Chklovskii, 2005a, Sala and Segal, 2014]).

These appositions contain the set of all possible locations at which synapses can potentially form (see also [Kalisman, 2005]) since the gap can be bridged by the growth of a spine on the postsynaptic neuron, swelling of boutons on the axon, and minor bending of the axon; axons therefore do not need to grow towards a postsynaptic arbor. Indeed, Peters’ rule [Peters and Feldman, 1976] states that synapses are formed at locations where arbors of neurons touch, which has given rise to a number of proposals

for how the location of synapses arise statistically [Braitenberg and Schüz, 1998, Stepanyants and Chklovskii, 2005a, Stepanyants et al., 2008]. An open question was whether neurons are precisely or randomly positioned relative to each other as a requirement for statistical connectivity. A recent study in the neocortex demonstrated that the location of incidental touches that arise when neurons are randomly placed relative to each other (but respecting their vertical orientations and layer locations) matches the biological locations of synapses between neurons [Hill et al., 2012]. The distribution of locations is not only robust to the precise location of the neurons and to variations in the morphologies of neurons, but is also highly invariant across microcircuits reconstructed with different instances of each morphology. In fact, it is the intrinsic morphological diversity within each class that ensures the invariance of the distribution of synapses, in the same way that the joint probability of two distributions is invariant to the actual value of individual entries in the distributions [Ramaswamy et al., 2012]. We call this morphology-determined incidental touch rule, the *synapse location rule*.

A few exceptions to the synapse location rule have been identified in previous studies: 1) excitatory axons do not form synapses on excitatory somata even if the axon touches their somata, predicting a lack of molecular triggers for excitatory synapse formation on excitatory somata; 2) the ascending axon of pyramidal cells forms more synapses than suggested by this statistical connectivity predicting a biased ascending axonal growth, probably along radial glial tracts; 3) even though the axon of most neurons would statistically touch the axons of all other neurons, apparently only chandelier axons form synapses at such touches predicting specific molecular triggers for inhibitory synapse formation between Chandelier axons and those of pyramidal neurons, and; 4) the train of Chandelier synapses can not be recreated by random placement of Chandelier cells, predicting that the axon is molecularly guided down the axon initial segment once it collides with a pyramidal soma to form its distinctive axonal branching pattern and this consequent train of synapses along the axon initial segment. By applying these *exceptions to the synaptic location rule* we obtain the set of all biologically viable and possible *locations* for synapses between all neurons in the neocortical microcircuitry.

Naturally not all appositions in the set can be converted into synapses since this would result in a nearly all-to-all functional connectivity, and unrealistic densities of synapses and boutons on the axons. Indeed, earlier studies observed that a potential connectome based on axo-dendritic touches alone would be massively over-connected and that synapses can only form at a fraction of these appositions - the 'filling fraction' [Stepanyants et al., 2002, Stepanyants and Chklovskii, 2005a]. A seminal study [Shepherd et al., 2005] showed that the *number* of synapses formed between any two neurons is proportional to the density of the overlap in the arbors, which is also consistent with Peters' rule. However, this principle alone however is insufficient to explain the connectivity because it would result in a unimodal distribution of the numbers of synapses formed between most neurons (i.e. most connections would only have 1 synapse), which has not been observed experimentally [Feldmeyer et al., 2006a, 2002, Le Bé et al., 2007, Silberberg and Markram, 2007]. On the contrary, all neocortical synaptic connections exhibit a bimodal distribution of the number of synapses per connection with most (around 90%) neurons being unconnected (0 synapses) and a small fraction of neurons connected (low probability of connectivity) with many synapses and very few or no connections with intermediate numbers of synapses [Feldmeyer et al., 2006a, 2002, Le Bé et al., 2007, Silberberg and Markram, 2007] — the *bi-modal connectivity rule* (see also [Bienenstock et al., 1982]). A critical number of structural appositions are therefore required to form and/or maintain a connection between two neurons and when a connection forms, many, if not all appositions are converted into synapses (Fig. 4.1 b). We call this the *multi-synapse rule*.

A stochastic algorithm [Fares and Stepanyants, 2009] has been described that filters potential synapses in two steps: one to randomly reduce the total number of appositions, the other to remove all those connections with too few appositions. Obtaining a subset of all appositions in this way does reproduce multi-synapse connections observed experimentally, but does not leave any room for neurons to disconnect and reconnect to different neurons with experience (rewiring plasticity). There does exist a reservoir of viable multi-synapse connections because rewiring plasticity has been observed experimentally between the pyramidal cells of the neocortical microcircuitry [Markram and Perin, 2011, Lamprecht and LeDoux, 2004, Neves et al., 2008, Chklovskii et al., 2004, Holtmaat and Svoboda, 2009, Wilbrecht et al., 2010]. In fact, the connection probability nearly doubles after the microcircuit is stimulated, indicating that only around half of the viable multi-synaptic connections are functionally activated [Le Be et al., 2006]. We refer to the principle of leaving multi-synapse connections in reserve for potential rewiring as the *plasticity potential rule*. Because of the *synapse location rule*, microcircuit re-wiring has no effect on the distribution of locations of synapses, nor does it affect the number of synapses/connection between any two types of neuron.

### Fundamental properties of connectivity

The structural connectivity in a microcircuit of neurons is fundamentally determined by five main interdependent anatomical properties of a circuit (Fig 4.1 c). The first is the cell density in each layer and for each morphology ( $C_d$ ). If the density of a certain type of neuron increases for example, this will not only change the connectivity between that cell type and others, it will also change how all those source and target neurons connect with other neurons, because it will occupy more locations where other synapses could have formed, assuming that there is a defined total number of synapses in the microcircuit. We therefore assign the density of different cell-types as the 1st fundamental property of connectivity.

The 2nd fundamental property is the total amount of axon generated by each cell-type ( $A_l$ ) for similar reasons as cell density, but also because it sets the spatial ranges for appositions for each cell type. The positioning of cells in the microcircuit may also be important especially in structured or layered microcircuits, but this property is constrained to some extent by the density and general distribution of the cell-type. Purposefully orienting one cell type relative to another may be another important property, if the average dendritic and axonal densities of all morphologies in a class are asymmetric, which is generally not the case [Markram, 2014].

The 3rd fundamental property is the density of boutons ( $B_d$ ) on the axons of each type of neuron after synapses are assigned for obvious reasons, but also because it creates a strong interdependency between all neurons in a microcircuit. Any change in bouton density has knock-on consequences for the entire microcircuit because it means synapse locations will be freed or dominated by that axon, leading to more or less locations left for other inputs on its target cells. The number of synapses/connection for each pathway ( $S_m$ ) is a 4th fundamental property because it scales the number of target neurons that the axon of a presynaptic neuron can contact with a given number of boutons. The 5th property is the connection probabilities for each pathway ( $C_p$ ). Naturally, if  $C_p$  increases without a change in the other properties, then  $S_m$  must decrease, to illustrate but one of a myriad forms of interdependencies.

Since the  $C_d$  and  $A_l$  are given [Markram, 2014] and fixed, the multi-constraint problem is to reproduce the remaining three microcircuit properties ( $B_d$ ,  $S_m$ ,  $C_p$ ) for each pathway in accordance with the fundamental synaptic rules. Since the solution for any one pathway depends also on the solution for all other pathways, the algorithm must solve a global multi-constraint problem. For example, the  $B_d$  on the axon of any one neuron arises from connections formed onto potentially hundreds of target



neurons occupying synaptic locations that other connections could utilize. Rather than making the problem intractable, these interdependencies make it theoretically possible to use partial data on a few pathways to constrain the solution for all pathways, including those that have not been characterized. In what follows, we describe the logical development of the two-level (local and global) multi-constraint algorithm and the means by which each step is validated.

### Structural appositions contain information on functional connections

We developed the connectome algorithm of the first draft model reconstruction of the neocortical microcircuit described in the accompanying paper [Markram, 2014]. The microcircuit occupies a hexagonal volume 2mm in height and with a diameter of  $462\mu m$  for the circumscribing circle. The volume was filled with a total of 31'000 3D model neurons from 55 morphology types (m-types), each in their estimated biological densities in each layer. Each m-type was further represented by individual morphological variants. Additionally, we ensured that the somata of neurons with axonal and dendritic arbors that cross and target different layers were positioned within the layer to respect the interlaminar architecture. We also reconstructed six such microcircuits surrounding the central microcircuit to eliminate boundary effects. Placing all these neurons within this volume yields a very high density of fibers inside the volume (Fig 4.1 a) with 40% of the volume filled with fibers (6.5% axon, 33.5% dendrites, see Fig S1) and the remaining space with somata (20%) and extracellular space.

Not surprisingly, one finds a very high number of incidental collisions between the arbors of each of the neurons. These collisions are referred to as *appositions*. We algorithmically detected all appositions that occurred within a touch distance ( $2.5\mu m$  for excitatory synapses;  $0.5\mu m$  for inhibitory synapses) [Kozloski et al., 2008] and analyzed the connectome that would emerge if a synapse were to form at each apposition. Considerably more boutons would be formed than biologically reported. In fact, there are more than 4 appositions per  $\mu m$  of axons on most m-types (Table S3), far higher than the biologically reported values ( $\approx 0.2/\mu m$ ) [Wang, 2002, Romand et al., 2011]. This would give rise to some multi-synapse connections (Fig 4.1 b), but pathways will be overly interconnected.

We compared  $C_p$  based on appositions to  $C_p$  found experimentally to determine whether there existed any information in the apposition-based  $C_p$  about the synaptic  $C_p$ . Not surprisingly, the  $C_p$  based on appositions was much higher (approximately 5 times) than the synaptic  $C_p$ , but we did find a strong correlation ( $p < 0.01$ ) between the two measures (Fig. 4.2 a1). We also compared the mean number of appositions per connection with the mean number of synapses per connection ( $S_m$ ) and found that while numbers of appositions/connection were consistently lower (approximately 50%) than the synapses/connection, they were also highly correlated (Fig 4.2 a2). The correlations found in  $C_p$  and  $S_m$  indicate that statistical connectivity holds information about synaptic connectivity. The question then remains as to how to remove excess appositions to match biological synapse locations.

### Naive pruning cannot account for synapse numbers

One way to remove appositions would be to enforce stricter rules with respect to what constitutes a valid apposition, i.e. to reduce the touch distance. As expected, varying the touch distance as a criteria for appositions, significantly changes the number of appositions/connection (Fig 4.2 b2). The problem is that this hardly reduces  $C_p$  (Fig 4.2 b1), because we need to *reduce* the  $C_p$  while *increasing* the number of appositions/connection in order to preserve the *bimodal connectivity rule*. Reducing the touch distance criteria therefore does not provide a solution to eliminating excess appositions.

We explored another possible way to eliminate excess appositions. An extensively used method to predict connectivity from morphology, called Peters Rule [Peters and Feldman, 1976, Braitenberg and Schüz, 1998], proposes that the actual number of synapses along a dendrite is a constant fraction of the number of appositions (but see, [Mishchenko et al., 2010]). The simplest algorithm implementing Peters Rule - its naive implementation - would be to select a fraction of appositions randomly by admitting each touch with a constant, independent probability. By setting the probability to the quotient of an estimated overall bouton density of ( $0.2\mu m^{-1}$ ) and the mean density of axonal apposition ( $4.7\mu m^{-1}$ ) we could reduce the density of synapses to biological levels, but this approach also reduces synapses/connection far more than  $C_p$  (Fig 4.2 c2). To reach biological  $C_p$  values,  $S_m$  values would need to be far lower than reported (Fig. 4.2 c1) [Feldmeyer et al., 2006a, 2002, Le Bé et al., 2007, Silberberg and Markram, 2007]. Peters Rule therefore does not provide a viable solution to eliminating excess appositions in order to match biological connectivity.

### General, multi-synaptic and plasticity pruning

An algorithm has been proposed to ensure the presence of multi-synapse connections in a two step process [Fares and Stepanyants, 2009]. The 1st step is similar to what has been described above as the naive implementation of Peters Rule. The 2nd step selectively removes all those connections with a low number of synapses thus satisfying the *multi-synapse rule*. However, these 2 steps are not constrained by  $B_d$  or  $C_p$  values and therefore cannot generalize easily to the entire microcircuit (the interdependencies within and across pathways can theoretically ensure generalization). In order to develop a modified version of this algorithm, we first ran it on the entire microcircuit and used the best characterized pathway (L5\_TTPC to L5\_TTPC, Fig 4.3) as a benchmark against which we modified the algorithm.

Before the algorithm was executed, we already noticed that there exists a much wider distribution of the number of appositions/connection (i.e. a larger  $S_{sd}$ ) than the distribution of the number of synapses/connection found experimentally (Fig. 4.3 a), indicating too many connections with too few appositions (left side of the distribution) and too many connections with too many appositions (right side). For the 1st step above, we therefore randomly and independently eliminated a fraction of appositions until the right side of the distributions matched the biological data (Fig. 4.3 b). The first parameter of the algorithm,  $f_1$ , is therefore an independent probability of retaining a fraction of appositions for *general pruning*. For the 2nd step above, we pruned all appositions belonging to connections with few appositions to match the left side of the biological distribution (Fig. 4.3 c). The second parameter of the algorithm,  $\mu_2$ , is therefore a cutoff value for *multi-synaptic pruning*. Finding the correct value of  $f_1$  and  $\mu_2$  ensures that both  $S_m$  and  $S_{sd}$  of the appositions/connection match the biological data.

We found however that after these two steps, the emergent  $B_d$  (all boutons on the pyramidal axon onto target cells) were approximately twice as high as the biological values. Guided, by this finding, we added a 3rd pruning step where we randomly removed a fraction of the multi-synapse connections found after the 2nd step (for this pathway, the fraction is **0.51**). The removal is independent of the number of synapses forming the connection, and thus does not change the shape of the distribution of synapses/connection (Fig. 4.3 d). The third parameter,  $a_3$  is therefore the fraction of multi-synapse connections retained in *plasticity pruning*. Not surprisingly, we then matched the biologically reported  $B_d$ , but we also matched the biologically reported distance-dependent connection probabilities for these pyramidal cells (on average at 85% of the biologically reported level) (Fig. 4.3 d; lowermost graph) [Perin et al., 2011].

The connections removed in the 3rd step are all viable multi-synaptic connections and are available

for rewiring the circuit without changing the distribution of synapses/connection, thus satisfying the *rewiring plasticity rule*. In fact, if all viable multi-synapse connections were functional, there would be no potential for circuits to rewire. The finding that around 50% of multi-synapse connections are held in reserve, is substantiated by experiments reporting a doubling of the usual  $C_p$  reported for this pathway following stimulation of the microcircuit [Le Be et al., 2006].

### Validation and Robustness of the Algorithm

By satisfying the *multi-synapse rule* in this way in a microcircuit of all types of neurons, we also satisfy the *bimodal connectivity rule* and by further satisfying the *rewiring plasticity rule* we end up matching the biological  $S_m$ ,  $S_{sd}$  and the  $B_d$ , and a prediction for  $C_p$ . This process obviously works on this exemplar pathway because we could empirically find the parameters ( $f_1$ ,  $\mu_2$  and  $a_3$ ) for each pruning step guided by a complete experimental dataset. The question remains a) does the three step process work for other pathways where there is biological data and b) how can the parameters be found for pathways that have not been characterized?

We next tested whether the three step process also works for other pathways given biological data to constrain the algorithm parameters. We found only 24 further m-type specific pathways for which there are estimates for  $B_d$ ,  $S_m$ ,  $S_{sd}$  and 13 m-type specific pathways with estimates of  $C_p$  in the modeled organism (rat, P14, [Markram, 2014]). When we ran the algorithm on the whole microcircuit, we found a near perfect match with the biological data for the 25 m-type specific pathways (Fig. 4.4 a; purple diamonds). The algorithm can therefore technically be applied to any pathway if the biological data is available. This is not at first very surprising because we could fully constrain the three algorithmic parameters with biological data, but it was interesting to find that a solution for all 25 pathways simultaneously possible even though these solutions are all interdependent.

Before continuing the validation and development of the algorithm to operate on uncharacterized connections, we wanted to test again how sensitive the results are to the touch distance. When we explored the effects of varying the touch distances between  $0.75\mu m$  and  $3.75\mu m$  (Fig 4.4 a). Unlike before, the synapses/connection are now not as sensitive to the touch distance. This is because the algorithm can maintain the number of synapses/connection at the cost of adjusting other parameters; less general pruning (lower  $f_1$ ) and more multi-synapse pruning (higher  $\mu_2$ ), and may not be forced to satisfy the rewiring plasticity rule (free  $a_3$ ) given that  $B_d$  are strictly enforced (see below).

However the algorithm partially fails in layers 2/3 and 4 at touch distances of  $1.25\mu m$  and completely fails in all layers at  $0.75\mu m$ . It fails in these cases, because there are not sufficient appositions to solve the multi-constraint problem. The manner in which the algorithm fails depends on the order of precedence of the biological constraints (i.e. which constraints must be fulfilled even at the cost of the others). For the data in Fig 4.4 a we gave the highest priority to the  $B_d$ , then  $S_m$ , with the  $S_{sd}$  of connections last. In this case, the constraints were broken in the inverse order of their priority (Table 4.1). The first symptom of a failure was that a wider  $S_{sd}$  had to be allowed in order to reach the correct  $S_m$  (for example L23\_PC to L23\_PC at  $1.25\mu m$ ). In most of the failing cases, neither  $S_m$  nor the  $S_{sd}$  could be reached with the specified  $B_d$ . The worst case is one where  $B_d$  can not be reached. This occurred at  $0.75\mu m$ , but even then, it only occurred for two cases (L23\_MC to L23\_PC and L4\_SS to L23\_PC). The results generated by the algorithm are therefore reasonably robust for touch distances greater than  $1.25\mu m$  and highly robust around  $2.5\mu m$ .

By studying how the algorithm struggles to fulfil the multiple constraints with low touch distances for

the major classes of pathways (E-E, E-I, I-E) we learned how to further modify the algorithm in order to generalize it to pathways that have not been biologically characterized. We examined the values of the algorithm parameters (Fig 4.4 b) and found that for touch distances  $\leq 1.25\mu m$  both  $f_1$  (general pruning parameter) and  $a_3$  (plasticity pruning parameter) reach their maximal values of 1.0 for the majority of pathways, indicating that not a single apposition can be spared in order to get close to any of the biological constraints and no multi-synapse pathways can be held in reserve.

For higher touch distances, we observe a very wide distribution of  $f_1$  parameters spanning 80% of the theoretically maximal parameter space. This tells us that a generalization strategy using one set of parameters for all pathways 3025 pathways is not feasible and that each pathway likely requires a unique set of parameters. In the case of  $\mu_2$  (multi-synapse pruning parameter) we observed a clear dependence for the major classes of pathways (Fig. 4.4 b; middle column,  $2.5\mu m$ ). For I-E pathways, we found values between 8 and 10; for E-E below 4, and for E-I values in between. This is substantiated by similar trends found in experiments (for example compare [Markram et al., 2004, Silberberg and Markram, 2007, Markram et al., 1997], and may suggest that inhibitory connections need more synapses to survive. For the parameter  $a_3$  we found even smaller variability within the major classes (0.2 for E-I, 0.3 for I-E and, 0.5 for E-E) and therefore chose to use these values to generalize the pruning step for the remaining 3000 potential pathways.

### Generalizing the multi-constraint solution

In order to generalize to all pathways it is necessary to find the general pruning ( $f_1$ ), the multi-synapse pruning ( $\mu_2$ ) and the plasticity pruning ( $a_3$ ) parameters for each pathway that reproduce  $S_m$ ,  $B_d$  and  $C_p$  of each pathway. As outlined above, if there are insufficient appositions, then some of the parameters reach their maximum and not all these biological constraints can be met. The biological properties are strongly dependent on each other and the dependence is described by the corresponding algorithm parameters (Fig. 4.5 a). These are inevitable interdependencies, independent of the mechanism used to connect neurons.

Since  $C_d$  and  $A_l$  were given,  $B_d$ ,  $S_m$  and  $C_p$  remain constraints to be met. We considered the width of the distribution of synapses per connection (the  $S_{sd}$  or  $S_{cv}$ ) as additional biological constraints. While it is not part of constraints that are inevitably linked, they are related to the main parameters of the algorithm because the width of the distribution of appositions/connection is much higher than the biological distribution [Markram et al., 1997, Feldmeyer et al., 2002, 2006a, Le Be et al., 2006], see also Tables S1, S2). It is possible to predict the effect of the parameters on the biological values because the appositions/ connection always follows a geometric distribution ( $P(n = k) = (1 - p)^{k-1} \cdot p$ ), leading to the option of using the mathematical description of the distribution to find an analytical solution (see supplementary methods). A previous study [van Ooyen et al., 2014] found the same type of distribution (but see [Fares and Stepanyants, 2009]). It is counter intuitive that a higher value for  $\mu_2$  increases  $S_m$  while simultaneously decreasing the  $B_d$  since it seems to violate the dependency between the two measures established (Fig 4.1 c). It is however not a contradiction, because  $C_p$  decreases by an even higher amount at the same time.

We used the interdependencies of biological properties to constrain the parameter space until we found solutions for all connections. Since data is only available for a minute fraction of possible pathways and unlikely to be obtained for more pathways in the near future, it is necessary to establish a generalization strategy. We began simply by using a derived property as a biological constraint where data was missing. Fig 4.5 b,c provides an overview of how each derived property is obtained and used by the algorithm

(see supplementary methods for details). Since  $f_1$  is the only parameter affecting the  $S_{sd}$  it can already be constrained after the first step. The parameter  $\mu_2$  affects only  $S_m$ , and is therefore set after step 2. Finally,  $a_3$  was derived as the fraction of the biological  $B_d$  and the  $B_d$  resulting after step 2 leaving the  $C_p$  as a prediction.

The realization that  $a_3$  can be generalized in this way, opened up the possibility to generalize the algorithm for pathways where reliable experimental data was unavailable. In addition to  $a_3$ , we utilized the finding of a very narrow shape of the distribution of synapses per connection ( $S_{sd}$ ), to constrain other pathways with a  $S_{cv}$  of 0.32 (mean of the biologically constrained pathways). The final constraint was a generalized bouton density, leading to the procedure described in Fig 4.5 c. After  $a_3$  is taken out of the equations, only  $\mu_2$  changes the  $S_{cv}$  and thus  $S_{cv}$  can be used to constrain  $\mu_2$ . Finally,  $f_1$  is adjusted to match the generalized  $B_d$ .

The dependency diagram reveals that other sets of biological data can be used to constrain a pathway, in particular  $C_p$ . We chose not to use  $C_p$  as it is the most unreliably reported value because very few studies normalize for distance which has a profound effect on  $C_p$  [Markram et al., 1997, Holmgren et al., 2003] and fewer still provide a distance-dependent profile of  $C_p$  [Perin et al., 2011].

### Derived parameters as constraints

We tested the derived parametrization on a number of other pathways with reported  $S_m$  values (Fig 4.6 a). While not reaching the quality of fit of the biological parametrization, we still find a significant match to reported values. Overall, the  $S_m$  values predicted and those reported were highly correlated ( $p < 0.01$ ) indicating the the general trend for  $S_m$  in different pathways can be accurately captured. Even individual distributions of synapse numbers matched perfectly ( $p < 0.05$ ) for 14 of the 26 cases (Fig. 4.6 a).

Even though  $C_p$  was not used as a constraint, the strong correlations with biological values remained even after completing the all three pruning steps ( $p < 0.01$ ; Fig 4.6 b). Only for connections from Martinotti Cells (MCs) in layer 5, did the algorithm not predict the high values of over 0.3 that have been reported [Silberberg and Markram, 2007] and some reports even suggest a  $C_p$  near 1 for MC to PC connections in layer 2/3 [Fino and Yuste, 2011]. To better understand the basis for this specific deviation of the biological data, we consider the relations between the biological properties established in Fig 4.1 a (see discussion).

The algorithm reproduces the *densities* (Fig 4.6 c) and *distributions* (Fig 4.6 d) of boutons on the axons of different m-types even though only the mean density is used by the algorithm.

### Extreme generalization in the absence of data

So far we have described a strategy of using biological data as a constraint where available and using mean circuit values to generalize across uncharacterized pathways. We explored the feasibility of an extreme generalization strategy using only the absolute minimum of biological data; the bouton densities. Boutons are involved in forming synapses onto all types of neurons and therefore represent a focal point for the multi-constraint solution for all neurons. We therefore explored a variant of the algorithm where only bouton densities are used as a constraint given any set of neurons.

We have shown that both  $C_p$  and  $S_m$  in m-type specific pathways are correlated with results found in apposition based connectivity (Fig 4.2 a1, a2). Under the assumption that this is a universal principle, we could use the number of appositions per connection to constrain algorithm parameters. We there-

fore calculated the optimal linear fit of the data in Fig 4.2 a2 minimizing the sum of absolute errors as  $S_m = 2.5 \cdot S_m^{struc} - 1$ . We then simply reconstructed a microcircuit constraining all 3025 potential pathways with the predicted  $S_m$  and an average  $S_{cv}$  of 0.32 for all 25 pathways. We applied the average  $B_d$  of 0.2 experimentally obtained for all cells, regardless of m-types (Table S3) (i.e. no m-type classification is required).

The first step in the algorithm is to calculate the  $S_m$  based on the appositions between pairs of neurons and according to the fit above. The general and multi-synapse pruning is then applied as before to match  $S_m$  and  $S_{cv}$ . Next, we calculate the overall bouton density in the circuit after these steps and compare it to the target value of  $0.2\mu m^{-1}$ . This yields a single value of  $a_3$  which is applied to perform the plasticity pruning. Naturally this yields the same rewiring potential for all neurons since no pathway-specific data is used. While, the results were not as significant as when pathway specific biological data was used, both the predicted  $S_m$  (Fig 4.7 a,b;  $p < 0.01$ ) and  $C_p$  (Fig. 4.7 c;  $p < 0.01$ ) values were still highly significantly correlated with biological data. As before, the very high reported  $C_p$  values for MC — PC connections cannot be reproduced (see discussion). Even though a single average  $B_d$  was applied as a global constraint for all cells we found local variations in bouton densities (i.e. some could show a higher density and others a lower, as long as the overall mean  $B_d$  was satisfied). For example, we observed an above average  $B_d$  for L23\_MCs ( $0.24\mu m^{-1}$ ) and below average for L6\_TPC\_L4s ( $0.145\mu m^{-1}$ ), a trend that is mirrored by biology with means of  $0.27\mu m^{-1}$  [Karube et al., 2004] and  $0.21\mu m^{-1}$  (Wang unpublished data) for L23\_MC and  $0.15\mu m^{-1}$  [Anderson et al., 2002] and  $0.19\mu m^{-1}$  (Wang, unpublished). When we plotted all reported pathway-specific  $B_d$  values (see Table S3) against emerged  $B_d$  values we found a marginally significant correlation ( $p < 0.05$ , Fig. S3).

### Low variability and high robustness across microcircuits

We have shown that the connectome algorithm accurately recreates most of the biological connectivity when constrained with biological properties, and to a slightly lesser degree when constrained with derived properties. For the vast majority of uncharacterized pathways the derived connectome allowed us to make verifiable predictions. In order to assess the precision of the predictions we evaluated the internal variability of the algorithm. We generated seven microcircuits from the same pool of reconstructed morphologies, but different random positions and derived a connectome for each of them. As a measure of variability, we calculated the standard deviation of the mean number of synapses per connection and of the mean connection probability at  $100\mu m$  between the microcircuits (Fig 4.8 a,b). We found that on average the 95% confidence interval was smaller than 2% of the mean value for synapse numbers and around 5% of the mean value for connection probabilities. The predictions are therefore made with a precision of roughly  $\pm 2\%$  of the mean when biological properties are known and roughly  $\pm 5\%$  when they are not.

## 4.4 Discussion

We have isolated fundamental synaptic connectivity principles and properties that govern the local connectome and used these in an algorithm to synaptically connect all neurons in a microcircuit simultaneously. Incidental appositions between neuron morphologies placed randomly within their layer and inter-layer constraints, provide the first set of potential synapses. By removing appositions that inevitably occur, but are functionally prevented from forming synapses, we arrive at a subset of potential synapses. This subset is still far greater than the number of synapses formed. We show that naive statistical pruning of the excess appositions is an insufficient subsampling method to

reproduce the biological connectivity in a manner that is consistent with the fundamental principles of connectivity. We show that a three step pruning process; general, multi-synapse and plasticity pruning yields biologically accurate synaptic connections. We further show that the minimal biological data that is required to reconstruct the local connectome formed by a given set of neurons, is the average bouton densities and the relation between the mean number of appositions/connection and the mean number of synapses/connection. We show that the predicted connectome will vary by less than  $\pm 5\%$  across different microcircuit instances.

### Implications for the formation of synaptic connections

The location of synapses is statistically determined with only a few exceptions, indicating that experimental data on exceptions to this statistical rule is one of the most important types of data required to further refine the accuracy of the predicted connectome. The requirement of several synapses to form viable synaptic connections alludes to a fundamental biological mechanism, whereby synapses act synergistically to ensure the survival of a connection between any two neurons — a synapse co-dependency mechanism. The finding in this study that a variable fraction of appositions are converted into synapses for each m-type specific pathway, further points to a variable level of synapse co-dependency operating in different pathways. The algorithm also predicts that if  $S_m$  is decreased,  $C_p$  will increase proportionally (if the other fundamental parameters remain constant). The level of synapse co-dependency therefore determines the number of neurons that any one neuron can exert an influence over. Interestingly,  $S_m$  has been reported to be lower while  $C_p$  is higher between layer 5 pyramidal neurons in an animal model of autism [Rinaldi et al., 2007b]. These experimental data not only further substantiates the algorithm, but together with the insights from the algorithm, suggests that the level of synapse co-dependency is reduced in the animal model of autism.

### Bridging the gap to form a synapse

The algorithm prunes appositions as potential synapses to predict actual synapses. When the appositions were detected within a maximum touch distance criterion of  $1.25\mu m$  for excitatory synapses, the biological connectivity could be reproduced for some pathways, and at  $2.5\mu m$  or above for all known pathways with a significant level of accuracy. These touch distances are reasonable when considering the experimental data on the spine lengths, which is the main structure that bridges the gap between the axon and dendrites of two neurons.

Indeed, one study reported that more than 10% of spine necks are longer than  $1.25\mu m$  [Arellano, 2007]. Including the spine head, around 50% of spines extend beyond  $1.25\mu m$ , with a mean length of  $1.3\mu m$  and a maximum of  $5.1\mu m$  (although 95% remain under  $2.6\mu m$ ; Benavides, DeFelipe, unpublished observations). A bouton bridges an additional  $0.25\mu m$  indicating that a touch criterion of a maximum of  $2.5\mu m$  is biologically plausible. The probability that the signal to form a synapse, succeeds to close this gap and successfully forms a synapse, may determine the fraction of appositions that become synapses in each pathway.

### Deviations from experimental connectivity

The predicted  $C_p$  values matched reasonably well experimental data, especially considering that  $C_p$  is the most unreliable circuit property measured. However the L5\_MC to L5\_TTPC pathways were

underestimated (Fig 4.6 b). Considering the inter-dependencies of circuit properties outlined in Fig. 4.1 c, we see that increasing  $C_p$  beyond the predicted values will require extreme changes to the other parameters. For example, it would require halving  $C_d$  or  $S_m$ , or doubling  $B_d$  or  $A_l$  (or a combination thereof).  $C_d$  for PCs is supported extensively by experimental data and validated in various ways (see Fig S1a; [Markram, 2014]) and is therefore unlikely the source of the deviation.

We tested the possibility that axons were insufficiently reconstructed ( $A_l$  is too low) by comparing the density of inhibitory synapses in the reconstruction against biological estimates. Inhibitory synapses arise from local interneurons and are therefore expected to reach full density in a microcircuit entirely surrounded by six additional microcircuits on all sides (Fig S2a). Indeed, the predicted density of inhibitory synapses was highly correlated with data from electron microscopy, especially for layer 5 where the underestimation of  $C_p$  is apparently the greatest. Increasing  $A_l$  for Martinotti cell axons sufficiently to reproduce the reported  $C_p$  (double  $A_l$ ) would therefore push the predicted inhibitory synapse density well above reported values (also because high density of MCs).

We considered another possible explanation where Martinotti cells are entirely selective, using all their boutons to form synapses only onto pyramidal cells. However, we found that already more than 90% of L5\_MC synapses are formed on pyramidal cells (Fig S2 b), meaning that even a 100% specificity for pyramidal cells would hardly increase  $C_p$ . It is also possible that MC connections to PCs are highly oriented. This possibility is not supported for horizontal orientation, but could be explained by MCs consistently being positioned just below or above PCs [Kozloski, 2001].

A final possibility is that  $S_m$  is overestimated. Indeed, experimental values for  $S_m$  are based on light microscopic analysis and have only been validated using EM for PC to PC connections. We found an even stronger deviation in the  $C_p$  for L5\_MCs to L5\_PCs when using only mean bouton density as a constraint (Fig 4.7 c). We also noticed that  $C_p$  for L5\_PC to L5\_PC using this extreme generalization was underestimated and that  $S_m$  values calculated from a linear fit of synapses/connection to appositions/-connection were overestimated for all pathways in layer 5. Since the extreme generalization relies on the slope of the synapses/connection vs appositions/connection, we re-examined this relationship (see Fig. 4.7a). It appears as if the biologically characterized pathways in layer 5 lie on a steeper slope than other characterized pathways, suggesting that the conversion rate of appositions to synapses may be lower in layer 5 than in other layers (i.e. 2 slopes would reproduce the data).

This analysis illustrates how deviations between the predictions of the algorithm and biological data can be used to challenge the interpretation and feasibility of biological data.

### A large potential for information storage

After multi-synapse pruning, we found that there were still an excess number of appositions ( $B_d$  values higher than reported). This excess number of appositions after step 2 guided step 3 to remove multi-synapse connections and thereby predicted the potential for each pathway to undergo rewiring – the plasticity potential. Rewiring where multi-synapse connections are formed and eliminated has been experimentally demonstrated [Le Be et al., 2006]. The values of the 3rd parameter of the algorithm  $a_3$  was  $\approx 0.5$  for excitatory to excitatory pathways,  $\approx 0.2$  for excitatory to inhibitory pathways, and  $\approx 0.3$  for all inhibitory. This 3rd parameter represents the potential for rewiring in individual pathways. The values  $\ll 1$  and for the most part  $\gg 0$  indicate an enormous plasticity potential, in particular in the excitatory to excitatory pathways, as the number of unique wiring diagrams that can be reached is maximal for a value of 0.5. This predicts that a potential for information storage is maximal in E — E pathways and lower but still substantial in other pathways.



## 4.5 Methods

### Volume generation and detection of potential synapses

A set of potential synaptic contacts was generated by detecting axo-dendritic and axo-somatic (and in the case of Chandelier Cells: axo-axonic) appositions between randomly positioned, reconstructed neurons as described in [Hill et al., 2012]. The maximal distance of a potential contact, i.e. the distance between the surfaces of the axonal and dendritic side, was  $2.5\mu m$  for pathways that are known to place synapses on spines and  $0.5\mu m$  for all others (see for example [Feldmeyer et al., 2002, Kawaguchi, 2005, Kubota et al., 2007, Somogyi et al., 1998]). Only appositions on that part of the morphology that is known to be targeted in a particular pathway are admitted [Silberberg and Markram, 2007, Somogyi et al., 1998], especially efferences from chandelier cells are only admitted on the axon initial segment [Somogyi, 1977, Somogyi et al., 1982, Howard et al., 2005]. Cell composition, density and limits on the placement of cells are described in [Markram, 2014].

### Selecting a subset of potential synaptic contacts

The modeled volume of neural tissue containing cells of different morphology types will contain a large number of axo-dendritic, axo-somatic and axo-axonic appositions (Fig 4.1b). A preparatory filtering step will keep only those appositions that are on biologically plausible parts of the postsynaptic cell, for example on dendrites for pyramidal to pyramidal connections [Feldmeyer et al., 2002, Kawaguchi, 2005, Kubota et al., 2007, Somogyi et al., 1998] or exclusively on the axon initial segment for connections from chandelier cells (ChCs) [Somogyi, 1977, Somogyi et al., 1982, Howard et al., 2005]. The remaining potential synapses give rise to what we call the *apposition-based connectome*, which is characterized by a connection probability close to 1 (Fig 4.1b) and an overly high density of efferent synapses (see Fig4.1c).

In order to derive a biologically plausible connectome we employ a three step pruning algorithm, a modified version of the one proposed in [Fares and Stepanyants, 2009]:

In the first step – *general pruning* – we draw an independent random number  $R$  in the interval  $[0, 1[$  and compare it against a parameter  $f_1$ .

If  $R < f_1$  the synapse is admitted to the second step or else kept inactive in a pool accessible to structural plasticity mechanisms.

In the second step – *multi-synapse pruning* – we draw random numbers  $R \in [0, 1[$  for every connection, which is the set of all synapses between a pre- and a postsynaptic cell. The connection admitted to the next step only if

$$R < \frac{1}{1 + \exp\left[-\frac{16}{\mu_2}(N_s - \mu_2)\right]} \quad (4.5.1)$$

where  $N_s$  is the number of synapses forming said connection and  $\mu_2$  a parameter to this second step.

In the third step – *plasticity pruning* – once again whole connections are randomly and independently removed, but this time we compare  $R < a_3$  ( $a_3$  being the parameter of the third step) to turn the potential connection into an active connection. Connections removed in plasticity pruning are kept in a pool of *viable multi-synaptic connections* for future use in structural plasticity mechanisms.

### Finding parameters for the pruning algorithm

The pruning algorithm as described above takes — in addition to the set of axonal appositions — three parameters as input. We select one set of parameters for each individual pathway, i.e. for each combination of pre- and postsynaptic m-type. The parameters determine the outcome of certain connectivity metrics, such as the mean number of synapses per connection. As such, we used experimentally (*in-vitro*) determined target values for the metrics to constrain the parameter space.

Depending on the pathway, we employed one of two algorithms to find a suitable combination of parameters. For 25 pathways that have been reliably characterized experimentally (Table 4.2), we tried to match the mean and standard deviation of the distribution of synapses per connection (*biological parametrization*). For all other (N=3000) pathways we matched a generalized coefficient of variation of the distribution of synapses per connection and a generalized value for parameter  $a_3$  (*derived parametrization*). In both cases, the total number of efferent synapses on the presynaptic morphology type, derived from biological mean bouton densities multiplied with axon lengths, further constrained the parameter space by providing a target *filling fraction*, i.e. the fraction of structural touches admitted as a functional synapse. Specifically, we used the same target filling fraction for each pathway of the same presynaptic morphology type, i.e. we did not assume a connection specificity except for the one already present in the structural touches.

Both strategies – biological and derived parametrization – fully constrained the parameters. The way biological or generalized constraints lead to algorithm parameters is described in detail in the supplementary methods and outlined briefly in Figs 4.1 c and 4.5. Briefly, we quantified the impact the parameters will have on the connectivity metrics in the derived connectome analytically, based on the finding that the number of synapses per connection follows a geometric distribution. Qualitatively, the following relations emerge: Increasing the value of  $f_1$ , the first parameter increases connection probability, bouton density and the mean and std of synapse numbers; increasing  $\mu_2$  increases the mean number of synapses per connection but decreases connection probability and bouton density; increasing  $a_3$  increases bouton density and connection probability.

Mathematically, the problem turns into equation system with the three parameters as unknowns, meaning that three constraints are needed to find a unique solution. Out of the metrics and parameters introduced in Fig 4.3b any combination of three leads to a unique solution except  $S_{sd}$ ,  $S_{cv}$  and  $S_m$  as the coefficient of variation is fully determined by the combination of mean and standard deviation and therefore redundant.

The two combinations of three constraints we used for connectome derivation were  $\{S_m, S_s d, B_d\}$  or  $\{S_{cv}, a_3, B_d\}$ . The way they lead easily to unique solutions is outlined in Fig 4.3c and Fig 4.3d respectively: In both cases constraints that depend on only one remaining parameter can be identified in each step, leading to a stepwise unraveling of the equation system. In particular, the following equations determine parameter values in the case of biological parametrization:

$$f_1 = \frac{p}{1-p} \cdot \frac{1-p'}{p'}, \quad (4.5.2)$$

where  $p = \frac{1}{\bar{n}_s}$  is the inverse of the initial number of synapses per connection in the apposition-based input-connectome and  $p' = \frac{1}{S_s d + 0.5}$  is the inverse of the mean number of synapses per connection after the first step.

$$mu_2 = 0.5 + S_m - S_s d \quad (4.5.3)$$

$$a_3 = \frac{B_d}{B^{1,2}}, \quad (4.5.4)$$

where  $B^{1,2}$  is the bouton density after the first two pruning steps.

Equation for derived parametrizations are more complicated and can be found in the supplementary material.

## 4.6 Figures, tables and legends

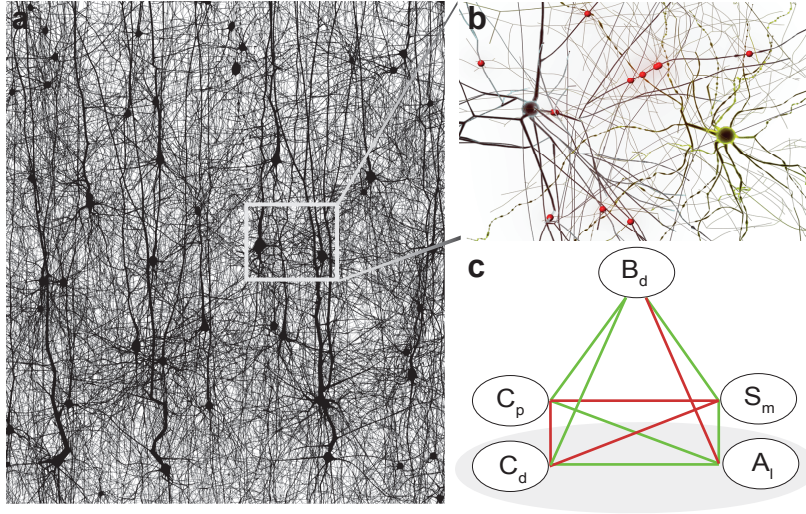
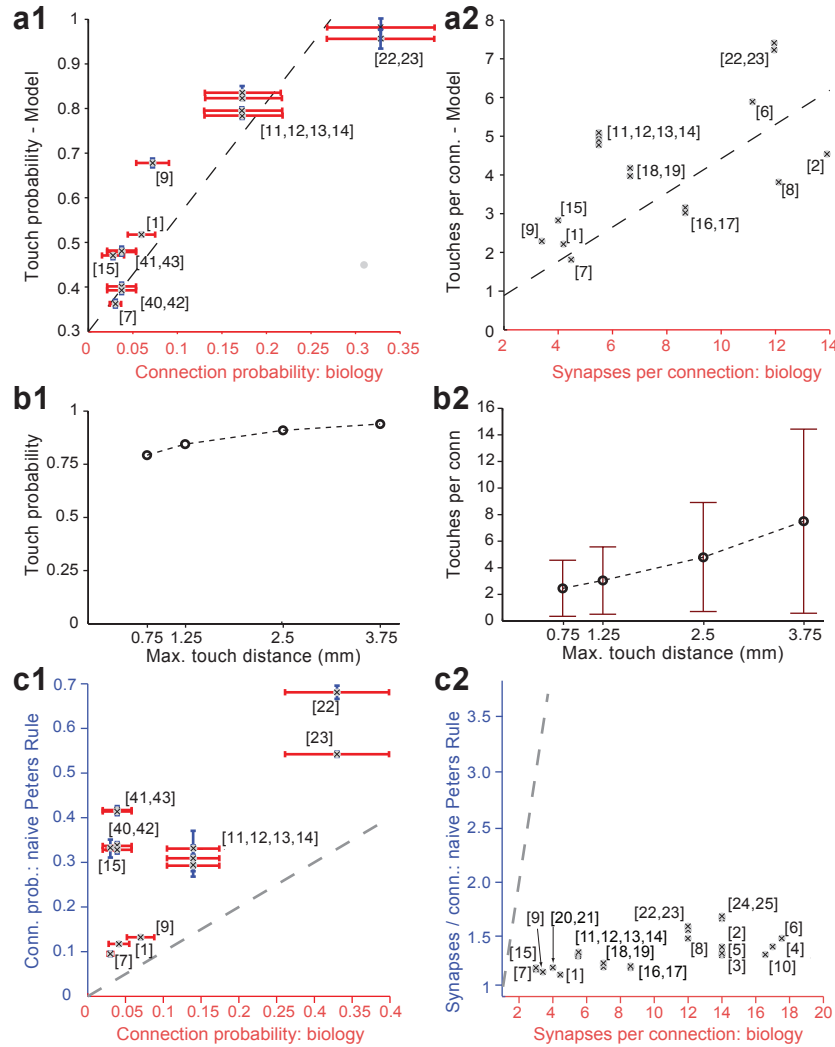


Figure 4.1 – **Incidental axonal appositions contain information about connectivity**

(a) The unitary microcircuit after all morphologies are placed (5% cell density shown). The resulting high density of fibers leads to a myriad of pairwise morphological appositions. (b) Example of a pair of morphologies with all 12 axonal appositions between them highlighted. (c) Logical dependencies between connectivity metrics in a pathway. Green edges indicate that when one metric increases the other increases as well, provided the rest remains unchanged, vice versa for red. Metrics are: Bouton density ( $B_d$ ), connection probability ( $C_p$ ), mean number of synapses per connection ( $S_m$ ), cell density ( $C_d$ ) and axonal length ( $A_l$ ).



**Figure 4.2 – Naive approaches to apposition filtering do not reproduce biological connectivity**

(a) Comparing connectivity based on all appositions to biological data: A synapse is placed at every single apposition. (a1) Connection probabilities, (a2) mean number of synapses per connection. Numbers refer to pathways listed in Table 4.2. (b) Connection probability (b1) and synapse numbers (b2) in a network of L5\_TTPC2 neurons (maximal distance  $100\mu m$ ) based on all appositions when the maximal distance of an apposition is changed. Bars indicate means, error bars standard deviations. (c) Comparing a naive implementation of Peters' rule to biological data: Every single apposition is removed with a uniform, independent probability, otherwise a synapse is allowed to form. (c1) Connection probabilities, (c2) mean number of synapses per connection.

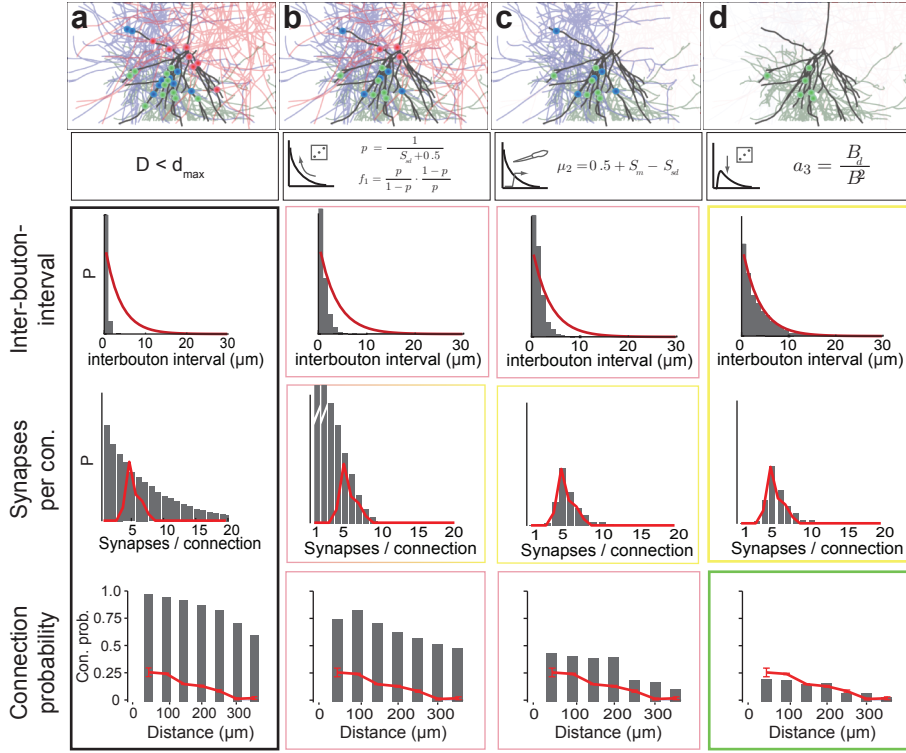


Figure 4.3 – Schematic of the three pruning steps

For an exemplary pathway (L5\_TTPC2 to L5\_TTPC2) we show how the distributions of inter-bouton intervals (ibi, inverse of bouton density), synapses per connection and connection probability are matched after three pruning steps. (a) Connectivity based on all touches is characterized by short **ibis**, an extremely wide distribution of synapses per connection and almost 100% connection probability. Top: An exemplary L4\_PC surrounded by 3 LBCs with all axonal appositions highlighted. (b) Choosing  $f_1 = \frac{1}{\sigma(n)^* + 0.5}$  removes the right hand side of the distribution of synapses per connection. Top: This removes step removes a fraction of appositions in all connections. (c) Choosing  $\mu_2 = 0.5 + \bar{n}^* - \sigma(n)^*$  removes the left hand side as well, but still leaves us with short **ibis**. Top: In this step one complete connections is removed, as it does not have the required number of appositions. (d) The last step with  $a_3 = \frac{B^*}{B^2}$  leads to correct **ibis** and connection probabilities only slightly below reported values emerge. Top: One of the two remaining connections is (randomly) removed.

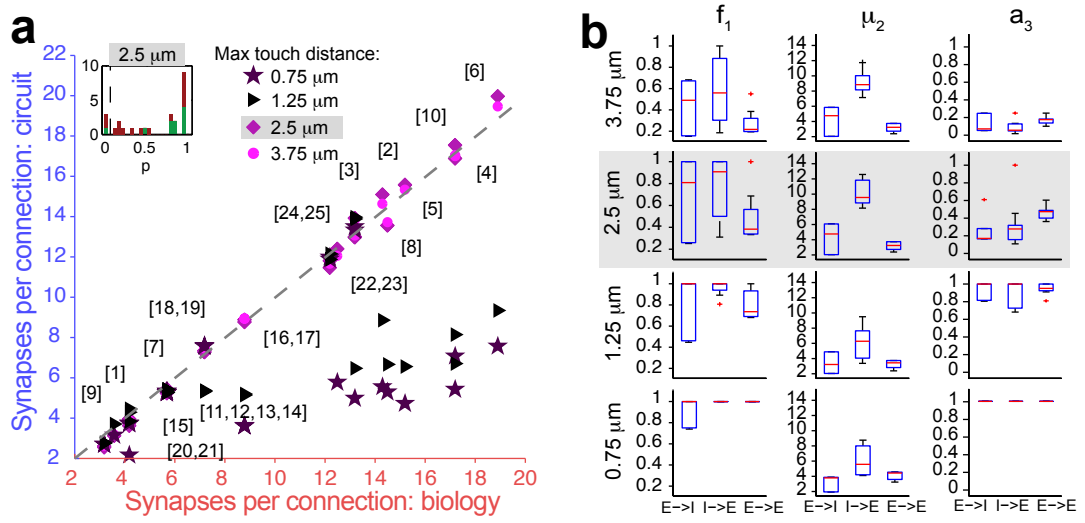


Figure 4.4 – Resulting synapse numbers and parameters

(a) Mean number of synapses per connection in pathways where available biological data on mean and standard deviation of synapse numbers as well as bouton densities could be used to fully constrain algorithm parameters. Numbers refer to pathways as listed in Table 4.2. Results for different maximal apposition distances: Stars: 0.75  $\mu\text{m}$ ; triangles: 1.25  $\mu\text{m}$ ; diamonds: 2.5  $\mu\text{m}$ ; circles: 3.75  $\mu\text{m}$ . Inset: Distribution p-values of a discrete KS-test comparing model and biology for the indicated pathways at 2.5  $\mu\text{m}$ . Where the actual samples of the biological data were available we compared them against samples from the model (green bars). Where they were unavailable, we compared against a gamma distribution with the published mean and standard deviation.  $p > 0.05$  for 22 of 25 pathways. (b) Boxplots of the parameter values determined by the biological parameterization procedure for excitatory to inhibitory (E→I), inhibitory to excitatory (I→E) and excitatory to excitatory (E→E) pathways and different touch distances (top to bottom). Red lines indicate the median, blue boxes the 25% and 75% percentiles and black whiskers the full data spread excluding outliers, which are indicated as red + signs.

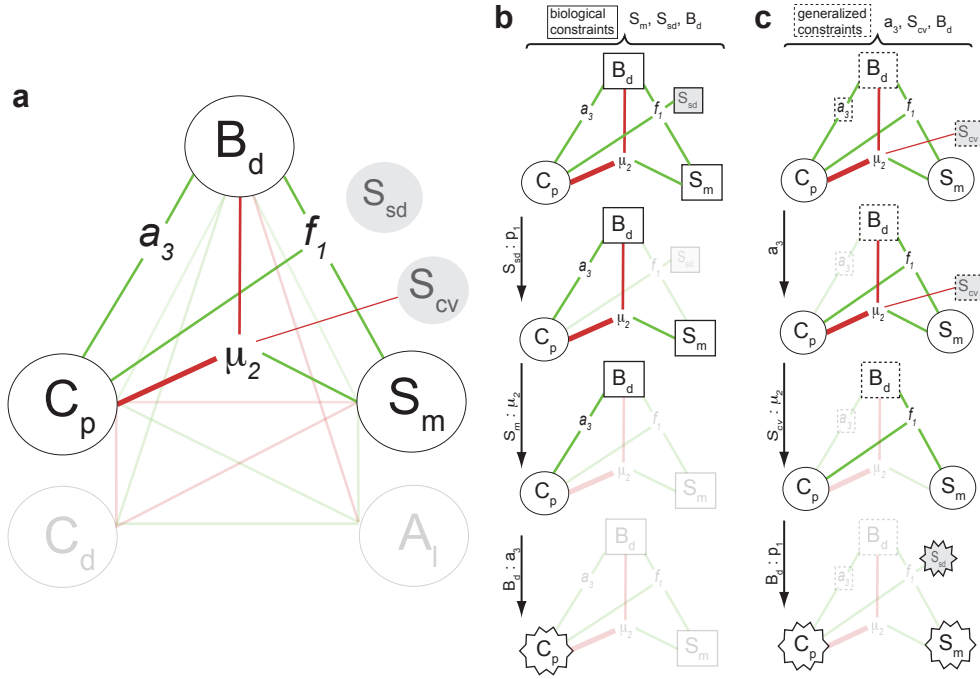


Figure 4.5 – Biological data and their inter-dependencies constrain synaptic pruning

(a) Dependency of metrics on the parameters of the pruning algorithm. Cell density and axonal length are experimentally provided and unaffected by pruning. Standard deviation of the number of synapses per connection ( $S_{sd}$ ) is assumed and serves as an additional metric. The coefficient of variation ( $S_{cv}$ ) is the ratio of standard deviation and mean ( $\frac{S_m}{S_{sd}}$ ). Green / red edges indicate that increasing the value of the parameter while keeping all else fixed, increases/decreases the metric. (b) Biological parameterization method: As  $S_{sd}$  is determined only by  $f_1$ , we can match the biological value by choosing  $f_1$ . The only remaining parameter that determines  $S_m$  is  $\mu_2$ . Finally, we can choose  $s_3$  to match  $B_d$ , leaving  $C_p$  as a prediction. (c) Derived parameterization method: After using a generalized value for  $a_3$  to allow a reservoir of multi-synapse connections, and choosing  $\mu_2$  to match a generalized  $S_{cv}$ , we determine  $f_1$  by matching a generalized  $B_d$ .  $C_p$ ,  $S_{sd}$  and  $S_m$  are all predictions.

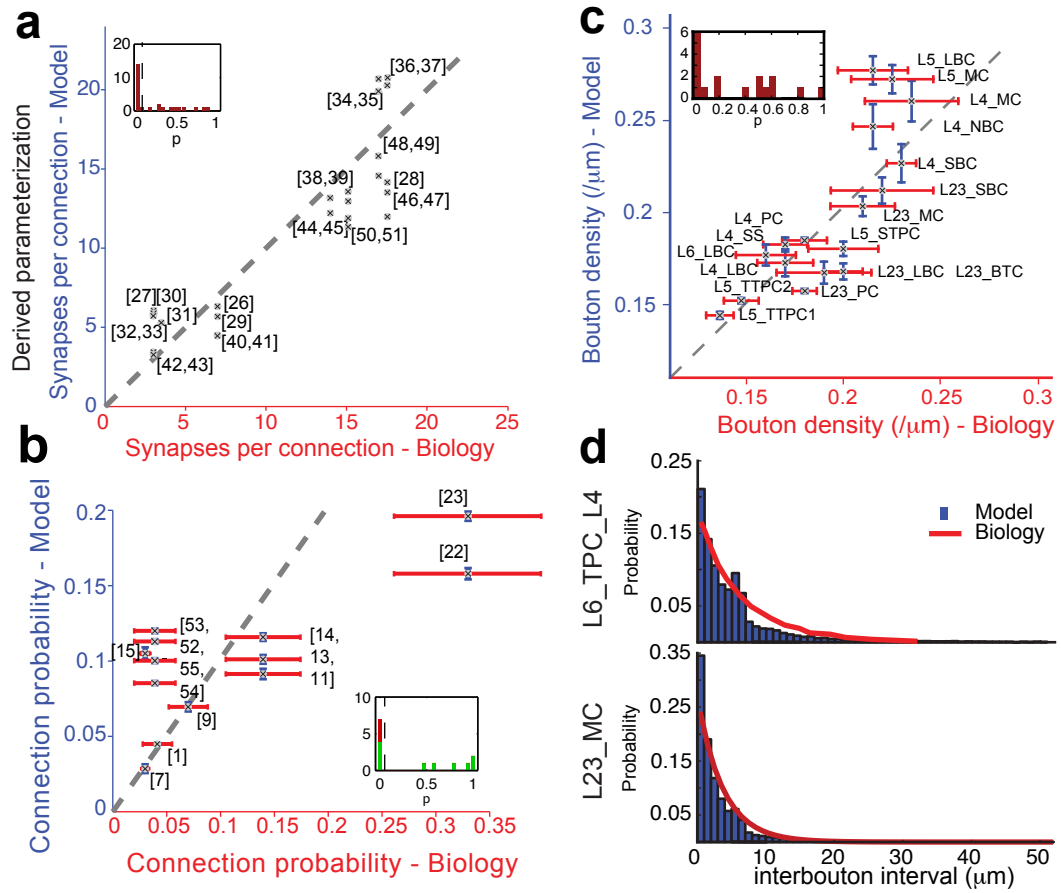


Figure 4.6 – Generalized and emerging results

(a) Comparison of the mean number of synapses per connection of pathways using the generalized parameter finding strategy to biology. Black x-marks: data, grey line: identity. Numbers refer to pathways as listed in Table 4.1. Inset: Distribution p-values of a discrete KS-test comparing model and biology for the indicated pathways (comparing against a gamma distribution with the published mean and standard deviation.) (b) Comparison of the mean connection probabilities for pairs closer than  $100\mu m$  in the model against biological data. X-marks indicate means, error bars the standard error of the mean. Specification of the numbered pathways in Table 4.1. (c) Comparison of bouton densities of a number of morphology types to biology. Purple circles: mean densities, red error bar: standard error of mean (SEM) of biological data, blue error bar: SEM of model data. Inset: Distribution of p-values of comparing the model data against biology (chi-squared goodness-of-fit test). (d) Distribution of inter-touch intervals (black bars), intervals between efferent synapses in the model (blue bars) and biological inter-bouton intervals (red lines) for two morphology times. Biological data from (Karube, Kubota & Kawaguchi, 2004) (L23\_MC) and (Anderson, Binzegger, Douglas & Martin, 2002) (L6\_PC).



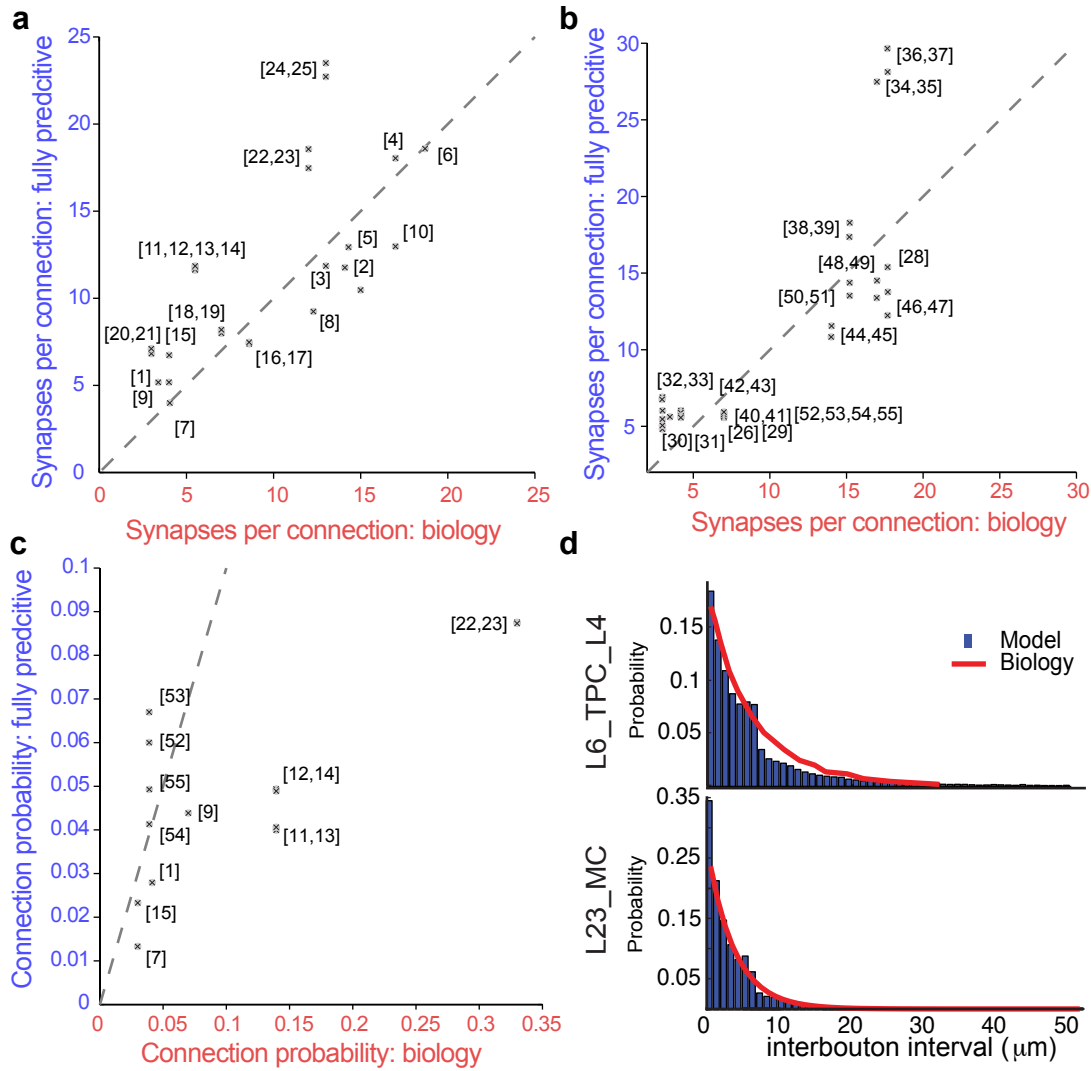


Figure 4.7 – Connectome derivation results in the near absence of biological data

Mean number of synapses per connection emerging when algorithm parameters are constrained by a single target bouton density for all cells and a mean number of synapses per connection predicted from the apposition based connectome. (a) For the pathways in Fig 4.4 a. (b) For the pathways in Fig 4.6 a. (c) Connection probabilities at  $100\mu\text{m}$  for the pathways in Fig 4.6 b. (d) Distribution of interbouton intervals as in Fig 4.6 d. Mean intervals are  $6.9\mu\text{m}$  for L6\_TPC\_L4, corresponding to a density of  $0.145\mu\text{m}^{-1}$  and  $4.2\mu\text{m}$  for L23\_MC, corresponding to a density of  $0.24\mu\text{m}^{-1}$ .

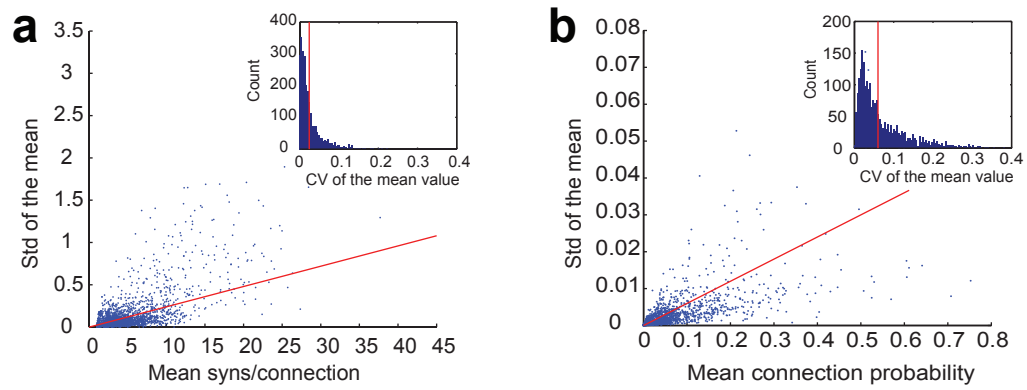


Figure 4.8 – **Robustness of emerging connectivity**

(a) Mean number of synapses per connection of all pathways in a microcircuit against the standard deviation of the mean across  $N=7$  microcircuits. Blue dots: data, red line: linear fit. Inset: Distribution of the coefficient of variation of the measurements of the mean, i.e. SD divided by mean. Red line: Mean CV. (b) Same, for the mean number of synapses per connection in pathways.

## Chapter 4. An Algorithm to Predict the Connectome of Neural Microcircuits

Pathway	3.75 $\mu m$	2.5 $\mu m$	1.25 $\mu m$	0.75 $\mu m$
L23_BTC to L23_PC	-	-	mean,std	mean,std
L23_LBC to L23_PC	-	-	mean,std	mean,std
L23_MC to L23_PC	-	-	mean,std	full
L23_NBC to L23_PC	-	-	mean,std	mean,std
L23_PC to L23_PC	-	-	std	mean,std
L4_BTC to L4_PC	-	-	mean,std	mean,std
L4_LBC to L4_PC	-	-	mean,std	mean,std
L4_NBC to L4_PC	-	-	mean,std	mean,std
L4_SBC to L4_PC	-	-	mean,std	mean,std
L4_SP to L4_SP	-	-	std	mean,std
L4_SS to L23_PC	-	-	mean,std	full
L5_LBC to L5_TTPC1	-	-	-	mean,std
L5_LBC to L5_TTPC2	-	-	-	mean,std
L5_MC to L5_TTPC1	-	-	-	mean,std
L5_MC to L5_TTPC2	-	-	-	mean,std
L5_STPC to L5_STPC	-	-	-	mean,std
L5_TTPC1 to L5_LBC	-	-	-	mean,std
L5_TTPC1 to L5_MC	-	-	mean,std	mean,std
L5_TTPC1 to L5_SBC	-	-	-	std
L5_TTPC1 to L5_TTPC1	-	-	-	mean,std
L5_TTPC1 to L5_TTPC2	-	-	-	mean,std
L5_TTPC2 to L5_LBC	-	-	-	mean,std
L5_TTPC2 to L5_MC	-	-	mean,std	mean,std
L5_TTPC2 to L5_SBC	-	-	-	std
L5_TTPC2 to L5_TTPC1	-	-	-	mean,std
L5_TTPC2 to L5_TTPC2	-	-	-	mean,std

Table 4.1 – **Overview of the failures to recreate biological connectivity measures for different maximal apposition distances.** Bouton density was the primary constraint, the mean number of synapses secondary, their standard deviation last. "std" indicates a partial failure where in order to reach the biological mean synapse number the standard deviation of their distribution had to be increased; "mean,std" indicates that the mean synapse number could not be reached at all with the specified bouton density; "full" indicates that even the bouton density could not be reached. Otherwise a full success was achieved.

#### 4.6. Figures, tables and legends

	Num	Presynaptic	Postsynaptic		Num	Presynaptic	Postsynaptic
<b>bio- logical</b>	1	L23_PC	L23_PC	<b>de- rived</b>	26	L23_PC	L23_LBC
	2	L23_NBC	L23_PC		27	L23_PC	L23_SBC
	3	L23_LBC	L23_PC		28	L23_SBC	L23_PC
	4	L4_NBC	L4_PC		29	L4_PC	L4_LBC
	5	L4_LBC	L4_PC		30	L4_PC	L4_SBC
	6	L4_SBC	L4_PC		31	L4_PC	L4_ChC
	7	L4_SS	L23_PC		32	L5_TTPC1	L5_NBC
	8	L23_MC	L23_PC		33	L5_TTPC2	L5_NBC
	9	L4_SP	L4_SP		34	L5_NBC	L5_TTPC1
	10	L4_BTC	L4_PC		35	L5_NBC	L5_TTPC2
	11	L5_TTPC1	L5_TTPC1		36	L5_SBC	L5_TTPC1
	12	L5_TTPC2	L5_TTPC1		37	L5_SBC	L5_TTPC2
	13	L5_TTPC1	L5_TTPC2		38	L5_BTC	L5_TTPC1
	14	L5_TTPC2	L5_TTPC2		39	L5_BTC	L5_TTPC2
	15	L5_STPC	L5_STPC		40	L6_TPC_L4	L6_LBC
	16	L5_TTPC1	L5_MC		41	L6_TPC_L1	L6_LBC
	17	L5_TTPC2	L5_MC		42	L6_TPC_L4	L6_SBC
	18	L5_TTPC1	L5_LBC		43	L6_TPC_L1	L6_SBC
	19	L5_TTPC2	L5_LBC		44	L6_LBC	L6_TPC_L4
	20	L5_TTPC1	L5_SBC		45	L6_LBC	L6_TPC_L1
	21	L5_TTPC2	L5_SBC		46	L6_SBC	L6_TPC_L4
	22	L5_MC	L5_TTPC1		47	L6_SBC	L6_TPC_L1
	23	L5_MC	L5_TTPC2		48	L6_NBC	L6_TPC_L4
	24	L5_LBC	L5_TTPC1		49	L6_NBC	L6_TPC_L1
	25	L5_LBC	L5_TTPC2		50	L6_BTC	L6_TPC_L4
					51	L6_BTC	L6_TPC_L1
					52	L6_TPC_L1	L6_TPC_L1
					53	L6_TPC_L1	L6_TPC_L4
					54	L6_TPC_L4	L6_TPC_L1
					55	L6_TPC_L4	L6_TPC_L4

Table 4.2 – Shorthands for synaptic pathways used in Figs 1, 4, 5, S4

## A Supplementary Material

### Supplementary figures

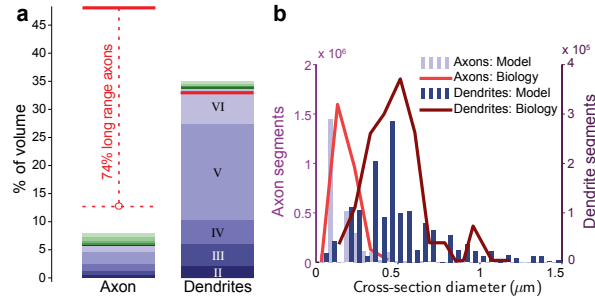


Figure S1 – Dendritic and axonal volume filling fractions

(a) Fraction of the volume occupied by axons or dendrites in a model microcircuit, surrounded by neighboring microcircuits (see methods). Contributions from cells residing in different layers are indicated by different shades of blue. Contributions from the surrounding microcircuits are stacked in different shades of green. Red solid horizontal lines indicate biological volume fractions in hippocampus from [Mishchenko et al., 2010]. The dashed red line indicates the expected axon volume fraction based on an estimated 74% long range connections (beyond  $500\mu\text{m}$ ; [Stepanyants et al., 2009]). (b) Distribution of diameters of axon and dendrite segments. Blue bars: model, red lines: biological data from electron microscopy [Mishchenko et al., 2010].

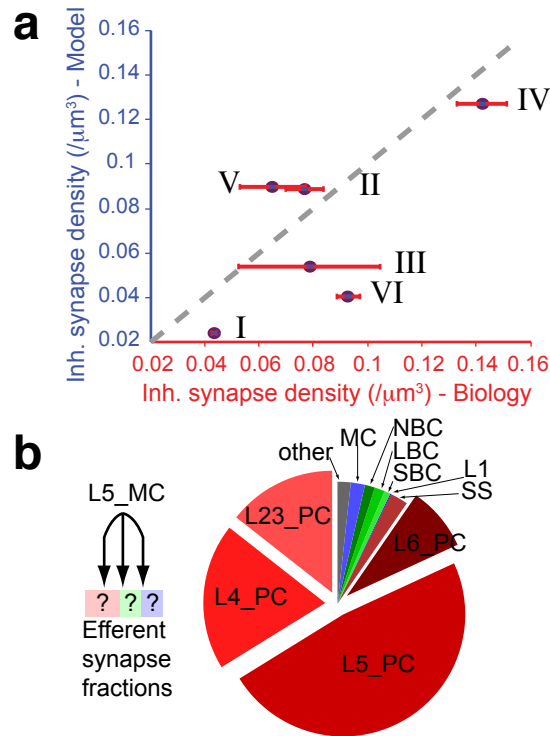


Figure S2 – Volumetric density and specificity of inhibitory synapses

(a) Density of inhibitory synapses in small ( $20 \times 20 \times 20 \mu\text{m}$ ) volumes placed in six layers and in the center of a column, surrounded by six further columns to reach full structural density (blue bars). Red bars indicate biological synapse densities measured through electron microscopy by (De Felipe et al. (2011 unpublished)). (b) Specificity of L5\_MC connectivity emerging from the pruning axonal appositions. The pie diagram depicts the fraction of efferent L5\_MC synapses on individual postsynaptic m-types.

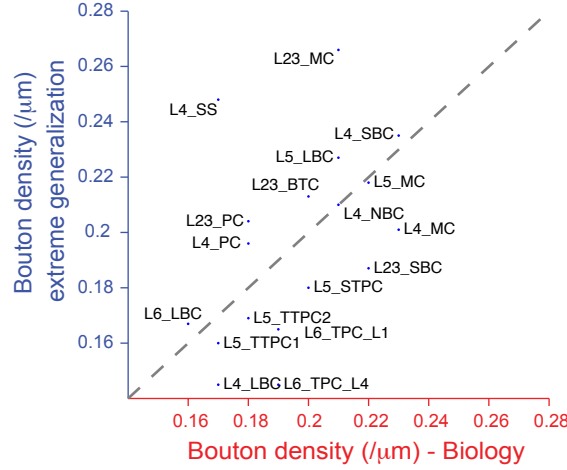


Figure S3 – Mean Bouton densities emerging from the extreme generalization approach

Comparison of mean bouton densities in a circuit using an extreme generalization approach to biology.

### Detailed derivation of parameters to metrics

We find parameters for the structural to functional conversion on a per-pathway basis. In the following section all experimental and model measurements as well as values for the parameters are meant to be considered for any single pathway, even when not explicitly mentioned.

Before conversion, we measure  $m_s$ , the mean of the distribution of structural touches per connection and the density of efferent synapses on the presynaptic morphology type. Later measurement is combined with the target bouton density to yield  $B^*$ , the target filling fraction, i.e. the fraction of structural touches converted to functional synapses.

In order to find the set of parameters –  $f_1$ ,  $\mu_2$  and  $a_3$  – that lead to the desired results, we consider that the distribution of touches per connection has the shape of a geometric distribution:

$$P(n_s = x) = (1 - p)^{x-1} \cdot p, \quad (\text{A.1})$$

$$\text{for } p = \frac{1}{mn_s}$$

The first filtering step removes a fraction of  $(1 - f_1)$  synapses. This reduces the mean and standard deviation of the distribution.

$$\bar{n}_1 = \frac{1-p}{p} \cdot f_1 + 1 \quad (\text{A.2})$$

$$\sigma(n)_1 = \frac{1-p}{p} \cdot f_1 + 0.5 \quad (\text{A.3})$$

For the second step, first let  $p'$  be the shape parameter of the geometric distribution after step 1:

$$p' = \frac{1}{\bar{n}_1} = \frac{1}{\frac{1-p}{p} \cdot f_1 + 1}, P(n_1 = x) = (1 - p')^{x-1} \cdot p' \quad (\text{A.4})$$

The second step cuts off the left side of the distribution. We see that under the slightly simplifying assumption that bins  $\geq \mu_2$  are admitted and bins  $< \mu_2$  are removed, this cutoff is equivalent to translating the distribution by  $\mu_2 - 1$  to the right. The normalization factor for the distribution after the cutoff is equal to 1 - the cumulative distribution of  $\mu_2 - 1$ :

$$\begin{aligned} P(n_2 = x) &= \frac{(1 - p')^{x-1} \cdot p'}{(1 - p')^{\mu_2-1}} = (1 - p')^{x-(\mu_2-1)-1} \cdot p' \\ &= P(n_1 = x - (\mu_2 - 1)), x \geq \mu_2 \end{aligned} \quad (\text{A.5})$$

This increases the mean accordingly, keeping the standard deviation unchanged:

$$\bar{n}_2 = \frac{1-p}{p} \cdot f_1 + \mu_2 = \frac{1-p'}{p'} + \mu_2 \quad (\text{A.6})$$

$$\sigma(n)_2 = \frac{1-p}{p} \cdot f_1 + 0.5 = \frac{1-p'}{p'} + 0.5 \quad (\text{A.7})$$

This means for the coefficient of variation of the distribution:

$$cv(n)_2 = \frac{\sigma(n)_2}{\bar{n}_2} = \frac{\frac{1-p'}{p'} + 0.5}{\frac{1-p'}{p'} + \mu_2} \quad (\text{A.8})$$

$$\Leftrightarrow \mu_2 = \frac{\frac{1-p'}{p'} + 0.5}{cv(n)_2} - \frac{1-p'}{p'} \quad (\text{A.9})$$

How many synapses are removed in the second step? To answer that, we first look at an alternative way to calculate the mean: The sum of each possible synapse number, multiplied with its probability:

$$\bar{n}_1 = \frac{1}{p'} = \sum_{i=1}^{\infty} (1 - p')^{i-1} \cdot p' \cdot i \quad (\text{A.10})$$

Similarly, the formula for the mean of the distribution after applying the cutoff at  $\mu_2$ :

$$\begin{aligned} \bar{n}_2 &= \frac{1-p'}{p'} + \mu_2 = \frac{1}{\sum_{i=\mu_2}^{\infty} (1 - p')^{i-1} \cdot p'} \cdot \sum_{i=\mu_2}^{\infty} (1 - p')^{i-1} \cdot p' \cdot i \\ &= \frac{1}{1 - \sum_{i=1}^{\mu_2-1} (1 - p')^{i-1} \cdot p'} \cdot \sum_{i=\mu_2}^{\infty} (1 - p')^{i-1} \cdot p' \cdot i \\ &= \frac{1}{(1 - p')^{\mu_2-1}} \cdot \sum_{i=\mu_2}^{\infty} (1 - p')^{i-1} \cdot p' \cdot i \end{aligned} \quad (\text{A.11})$$



$$\Leftrightarrow (1 - p')^{\mu_2 - 1} \cdot \left( \frac{1 - p'}{p'} + \mu_2 \right) = \sum_{i=\mu_2}^{\infty} (1 - p')^{i-1} \cdot p' \cdot i \quad (\text{A.12})$$

The factor before the sum serves as a normalization factor.

Finally, the fraction of synapses removed in the second step is:

$$\begin{aligned} R &= p' \cdot \sum_{i=1}^{\mu_2 - 1} (1 - p')^{i-1} \cdot p' \cdot i = \\ &= p' \cdot \left( \frac{1}{p'} - \sum_{i=\mu_2}^{\infty} (1 - p')^{i-1} \cdot p' \cdot i \right) \end{aligned} \quad (\text{A.13})$$

And inserting A.12:

$$\begin{aligned} R &= p' \cdot \left( \frac{1}{p'} - (1 - p')^{\mu_2 - 1} \cdot \left( \frac{1 - p'}{p'} + \mu_2 \right) \right) \\ &= 1 - p' \cdot (1 - p')^{\mu_2 - 1} \cdot \left( \frac{1 - p'}{p'} + \mu_2 \right) \\ &= 1 - p' \cdot \mu_2 \cdot (1 - p')^{\mu_2 - 1} - (1 - p')^{\mu_2} \end{aligned} \quad (\text{A.14})$$

The factor  $p'$  before the sum normalizes it to a maximal value of 1 because the series converges to  $\frac{1}{p'}$  (see equation A.10). Consequently, the fraction of touches *remaining* after step 1 and 2:

$$\begin{aligned} B^{1,2} &= f_1 \cdot (p' \cdot \mu_2 \cdot (1 - p')^{\mu_2 - 1} + (1 - p')^{\mu_2}) \\ &= \frac{p}{1 - p} \cdot \frac{1 - p'}{p'} \cdot (p' \cdot \mu_2 \cdot (1 - p')^{\mu_2 - 1} + (1 - p')^{\mu_2}) \\ &= \frac{p}{1 - p} \cdot \left( \mu_2 \cdot (1 - p')^{\mu_2} + \frac{(1 - p')^{\mu_2 + 1}}{p'} \right) \end{aligned} \quad (\text{A.15})$$

We use the equations derived above to find a set of parameters with one of the following two strategies.

### Matching mean, standard deviation and bouton density

Let  $\bar{n}^*$  and  $\sigma(n)^*$  be the target mean and standard deviation.  $p = \frac{1}{\bar{n}_s}$ . Follow the following steps:

1. Calculate  $\mu_2$ :

$$\mu_2 = 0.5 + \bar{n}^* - \sigma(n)^* \quad (\text{A.16})$$

2. Calculate  $p'$ :

$$p' = \frac{1}{\sigma(n)^* + 0.5} \quad (\text{A.17})$$

3. Calculate  $f_1$ :

$$f_1 = \frac{p}{1 - p} \cdot \frac{1 - p'}{p'} \quad (\text{A.18})$$

4. Calculate an appropriate bouton reduction factor after step 1 and step 2 are completed:

$$a_3 = \frac{B^*}{B^{1,2}} \quad (\text{A.19})$$

### Matching coefficient of variation, bouton density and active fraction

Let  $cv(n)^*$ ,  $B^*$  and  $a_3^*$  be the target coefficient of variation, bouton density reduction factor and value for  $a_3$ .  $p = \frac{1}{n_s}$ .

1. Calculate  $B_*^{1,2} = \frac{B^*}{a_3^*}$ , the target bouton density after the first two steps.
2. Solve the following equation for  $p'$ , for example using interval bisection with constraints  $\mu_2 > 1$  and  $p \leq p' < 1$ :

$$B_*^{1,2} = \frac{p}{1-p} \cdot \left( \mu_2 \cdot (1-p')^{\mu_2} + \frac{(1-p')^{\mu_2+1}}{p'} \right) \quad (\text{A.20})$$

where  $\mu_2 = \frac{\frac{1-p'}{p'} + 0.5}{\frac{cv(n)^*}{p'}} - \frac{1-p'}{p'}$  (see A.9)

3. Calculate  $f_1$  using A.18
4. Calculate  $\mu_2$ :

$$\mu_2 = \frac{\frac{1-p'}{p'} + 0.5}{\frac{cv(n)^*}{p'}} - \frac{1-p'}{p'} \quad (\text{A.21})$$

### Tables of detailed results

The column "Biology" is based on results from [Feldmeyer et al., 2006b, 1999, 2002, Le Bé et al., 2007, Perin et al., 2011, Markram et al., 1997, 2004, Silberberg and Markram, 2007, Petersen and Sakmann, 2000, Beierlein and Connors, 2002, Wang, 2002, Romand et al., 2011, Lübke, 2003, Larkman, 1991].

## Chapter 4. An Algorithm to Predict the Connectome of Neural Microcircuits

	Exact algorithm							
Pathway	Biology			Model			relevant literature	
	$P$	mean syns	std syns	$P$	mean syns	std syns	$a_3$	
	<b>E → E</b>							
$L23\_PC \rightarrow L23\_PC$	0.045	3.5	0.7	0.048	4.2	1.7	0.38	Feldmeyer et al 2006
$LA\_SP \rightarrow LA\_SP$	0.07	3.4	1.0	0.07	3.5	1.1	0.6	Feldmeyer 1999, Petersen and Sakmann 2000
$LA\_SS \rightarrow L23\_PC$	0.03	4.5	0.5	0.03	4.1	1.5	0.37	Feldmeyer 2002
$L5\_STPC \rightarrow L5\_STPC$	0.03	4.0	1.3	0.11	4.1	1.5	0.4	Le Be 07
$L5\_TTPC1 \rightarrow L5\_TTPC1$	0.14	5.5	1.3	0.09	5.6	2.0	0.48	Perin et al 2011, Markram 97
$L5\_TTPC1 \rightarrow L5\_TTPC2$	0.14	5.5	1.3	0.11	5.6	2.0	0.50	Perin et al 2011, Markram 97
$L5\_TTPC2 \rightarrow L5\_TTPC1$	0.14	5.5	1.3	0.11	5.6	2.1	0.50	Perin et al 2011, Markram 97
$L5\_TTPC2 \rightarrow L5\_TTPC2$	0.14	5.5	1.3	0.12	5.6	2.0	0.52	Perin et al 2011, Markram 97
	<b>E → I</b>							
$L5\_TTPC1 \rightarrow L5\_LBC$	-	7.0	3.0	0.06	7.6	3.2	0.17	Markram 2004
$L5\_TTPC2 \rightarrow L5\_LBC$	-	7.0	3.0	0.05	7.4	3.1	0.17	Markram 2004
$L5\_TTPC1 \rightarrow L5\_MC$	-	8.6	2.1	0.04	9.1	3.4	0.17	Silberberg 07
$L5\_TTPC2 \rightarrow L5\_MC$	-	8.6	2.1	0.05	9.2	3.4	0.16	Silberberg 07
$L5\_TTPC1 \rightarrow L5\_SBC$	-	3.0	1.0	0.11	3.0	1.2	0.61	Markram et al 2004
$L5\_TTPC2 \rightarrow L5\_SBC$	-	3.0	1.0	0.10	3.0	1.2	0.60	Markram et al 2004
	<b>I → E</b>							
$L23\_BTC \rightarrow L23\_PC$	-	15	5.0	0.05	15.9	5.1	0.25	Yun et al., unpublished
$L23\_LBC \rightarrow L23\_PC$	-	14	2.0	0.05	14.5	6.1	0.13	Markram et al., 2004
$L23\_MC \rightarrow L23\_PC$	-	12	6.4	0.12	12.7	4.1	0.45	Yun et al, unpublished
$L23\_NBC \rightarrow L23\_PC$	-	14.1	4.9	0.07	15.2	5.4	0.2	Yun et al, unpublished
$LA\_BTC \rightarrow LA\_PC$	-	17.0	7.4	0.05	18.0	6.2	0.17	Yun et al., unpublished
$LA\_LBC \rightarrow LA\_PC$	-	14.0	2.0	0.01	14.4	3.0	1.0	Markram et al., 2004
$LA\_NBC \rightarrow LA\_PC$	-	17.0	4.5	0.04	17.8	6.9	0.14	Markram et al., 2004
$LA\_SBC \rightarrow LA\_PC$	-	18.7	10.0	0.04	20.1	9.2	0.11	Markram et al., 2004
$L5\_LBC \rightarrow L5\_TTPC1$	-	14.0	2.0	0.13	13.8	5.3	0.3	Markram et al., 2004
$L5\_LBC \rightarrow L5\_TTPC2$	-	14.0	2.0	0.16	13.7	5.0	0.3	Markram et al., 2004
$L5\_MC \rightarrow L5\_TTPC1$	0.33	12.0	3.0	0.16	12.4	4.3	0.3	Silberberg 2007
$L5\_MC \rightarrow L5\_TTPC2$	0.33	12.0	3.0	0.19	12.5	4.6	0.31	Silberberg 2007

Table S1 – Emerging synapse numbers and connection probabilities compared to biology for pathways using biological parametrization

Pathway	Generalized algorithm							
	Biology			Model			relevant literature	
	$P$	mean syns	std syns	$P$	mean syns	std syns	$a_3$	
<b>E → E</b>								
<i>L6_TPC_L1 → L6_TPC_L1</i>	<b>0.04</b>	4.2	0.8	0.12	5.7	2.5	<i>0.5</i>	Berger et al., Beierlein & Connors 2002
<i>L6_TPC_L1 → L6_TPC_LA</i>	<b>0.04</b>	4.2	0.8	0.13	5.4	2.3	<i>0.5</i>	Berger et al., Beierlein & Connors 2002
<i>L6_TPC_LA → L6_TPC_L1</i>	<b>0.04</b>	4.2	0.8	0.07	5.7	2.4	<i>0.5</i>	Berger et al., Beierlein & Connors 2002
<i>L6_TPC_LA → L6_TPC_LA</i>	<b>0.04</b>	4.2	0.8	0.1	5.3	2.2	<i>0.5</i>	Berger et al., Beierlein & Connors 2002
<b>E → I</b>								
<i>L23_PC → L23_LBC</i>	-	7.0	3.0	0.04	6.2	2.9	<i>0.2</i>	Markram et al., 2004
<i>L23_PC → L23_SBC</i>	-	3.0	1.0	0.04	5.8	2.7	<i>0.2</i>	Markram et al., 2004
<i>LA_PC → LA_ChC</i>	-	3.5	1.5	0.03	5.4	2.8	<i>0.2</i>	Markram et al., 2004
<i>LA_PC → LA_LBC</i>	-	7.0	3.0	0.03	5.7	2.5	<i>0.2</i>	Markram et al., 2004
<i>LA_PC → LA_SBC</i>	-	3.0	1.0	0.02	4.5	2.1	<i>0.2</i>	Markram et al., 2004
<i>L5_TTPC1 → L5_NBC</i>	-	3.0	1.0	0.04	4.2	1.9	<i>0.2</i>	Markram et al., 2004
<i>L5_TTPC2 → L5_NBC</i>	-	3.0	1.0	0.04	4.1	1.8	<i>0.2</i>	Markram et al., 2004
<i>L6_TPC_L1 → L6_LBC</i>	-	7.0	3.0	0.08	3.9	2.7	<i>0.2</i>	Markram et al., 2004
<i>L6_TPC_LA → L6_LBC</i>	-	7.0	3.0	0.08	3.9	2.6	<i>0.2</i>	Markram et al., 2004
<i>L6_TPC_L1 → L6_SBC</i>	-	3.0	1.0	0.11	3.3	2.1	<i>0.2</i>	Markram et al., 2004
<i>L6_TPC_LA → L6_SBC</i>	-	3.0	1.0	0.08	3.3	1.9	<i>0.2</i>	Markram et al., 2004
<b>I → E</b>								
<i>L23_SBC → L23_PC</i>	-	18.0	10.0	0.04	14.3	5.7	<i>0.3</i>	Markram et al., 2004
<i>L5_BTC → L5_TTPC1</i>	-	15.0	7.3	0.03	13.0	5.0	<i>0.3</i>	Markram et al., 2004
<i>L5_BTC → L5_TTPC2</i>	-	15.0	7.3	0.05	13.6	5.6	<i>0.3</i>	Markram et al., 2004
<i>L5_NBC → L5_TTPC1</i>	-	17.0	4.5	0.10	21.0	8.9	<i>0.3</i>	Markram et al., 2004
<i>L5_NBC → L5_TTPC2</i>	-	17.0	4.5	0.12	20.9	8.7	<i>0.3</i>	Markram et al., 2004
<i>L5_SBC → L5_TTPC1</i>	-	18.0	10.0	0.05	21.7	9.1	<i>0.3</i>	Markram et al., 2004
<i>L5_SBC → L5_TTPC2</i>	-	18.0	10.0	0.05	21.9	9.4	<i>0.3</i>	Markram et al., 2004
<i>L6_BTC → L6_TPC_L1</i>	-	15.5	10.0	0.05	12.3	4.5	<i>0.3</i>	Markram et al., 2004
<i>L6_BTC → L6_TPC_LA</i>	-	15.5	10.0	0.08	11.8	4.2	<i>0.3</i>	Markram et al., 2004
<i>L6_LBC → L6_TPC_L1</i>	-	14.0	2.0	0.07	13.2	5.8	<i>0.3</i>	Markram et al., 2004
<i>L6_LBC → L6_TPC_LA</i>	-	14.0	2.0	0.08	12.3	5.0	<i>0.3</i>	Markram et al., 2004
<i>L6_NBC → L6_TPC_L1</i>	-	17.0	4.5	0.10	15.8	7.3	<i>0.3</i>	Markram et al., 2004
<i>L6_NBC → L6_TPC_LA</i>	-	17.0	4.5	0.10	14.6	6.5	<i>0.3</i>	Markram et al., 2004
<i>L6_SBC → L6_TPC_L1</i>	-	18.0	10.0	0.05	13.8	5.6	<i>0.3</i>	Markram et al., 2004
<i>L6_SBC → L6_TPC_LA</i>	-	18.0	10.0	0.08	12.2	4.9	<i>0.3</i>	Markram et al., 2004

Table S2 – Emerging synapse numbers and connection probabilities compared to biology for pathways using derived parametrization

m-type	Biology				Structural		Functional	
	Bouton density [/ $\mu\text{m}$ ]	Source	Spine density [/ $\mu\text{m}$ ]	Source	Bouton density [/ $\mu\text{m}$ ]	Exc. Aff. Syn. Dens. [/ $\mu\text{m}$ ]	Bouton density [/ $\mu\text{m}$ ]	Exc. Aff Syn. Dens. [/ $\mu\text{m}$ ]
L23_PC	0.18 $\pm$ 0.05 (63)	Wang <i>et al.</i> *	1.33 $\pm$ 0.19 (18)	Larkman '91	0.99 $\pm$ 1.04 (5100)	4.67 $\pm$ 0.07 (9341)	0.16 $\pm$ 0.109 (8408)	0.25 $\pm$ 0.00 (8379)
L23_LBC	0.19 $\pm$ 0.06 (6)	Wang <i>et al.</i> *	0.09 $\pm$ 0.05 (11)	Kawaguchi <i>et al.</i> '06	1.39 $\pm$ 0.68 (199)	10.98 $\pm$ 0.67 (283)	0.17 $\pm$ 0.137 (523)	0.7 $\pm$ 0.08 (254)
L23_NBC	0.21 $\pm$ 0.05 (18)	Wang <i>et al.</i> '02	0.04 $\pm$ 0.03 (18)		1.13 $\pm$ 0.54 (222)	8.77 $\pm$ 0.46 (373)	0.17 $\pm$ 0.141 (820)	0.56 $\pm$ 0.04 (376)
L23_SBC	0.22 $\pm$ 0.07 (7)	Wang <i>et al.</i> *	0.11 $\pm$ 0.06 (7)	Kawaguchi <i>et al.</i> '06	1.11 $\pm$ 0.61 (117)	11.28 $\pm$ 1.13 (176)	0.21 $\pm$ 0.155 (473)	0.87 $\pm$ 0.10 (196)
L23_BTC	0.2 $\pm$ 0.03 (9)	Wang <i>et al.</i> *			1.14 $\pm$ 0.53 (138)	9.75 $\pm$ 0.63 (256)	0.17 $\pm$ 0.124 (802)	0.58 $\pm$ 0.04 (326)
L23_MC	0.21 $\pm$ 0.06 (13)	Wang <i>et al.</i> *	0.29 $\pm$ 0.04 (9)	Kawaguchi <i>et al.</i> '06	1.31 $\pm$ 0.71 (246)	7.57 $\pm$ 0.37 (453)	0.20 $\pm$ 0.175 (1062)	0.58 $\pm$ 0.04 (593)
L23_ChC	0.3 $\pm$ 0.01 (2)	Wang <i>et al.</i> *			1.39 $\pm$ 0.67 (40)	7.87 $\pm$ 0.92 (48)	0.06 $\pm$ 0.049 (77)	0.28 $\pm$ 0.07 (32)
L23_DBC	0.29 $\pm$ 0.08 (8)	Wang <i>et al.</i> *	0.1 $\pm$ 0.05 (10)	Kawaguchi <i>et al.</i> '06	0.43 $\pm$ 0.22 (61)	11.20 $\pm$ 1.45 (74)	0.18 $\pm$ 0.093 (144)	0.59 $\pm$ 0.11 (55)
L23_BP	0.19 (1)	Wang <i>et al.</i> *			0.17 $\pm$ 0.08 (8)	6.48 $\pm$ 1.91 (21)	0.16 $\pm$ 0.067 (4)	0.17 $\pm$ 0.14 (9)
L23_NGC	0.23 $\pm$ 0.06 (2)	Wang <i>et al.</i> *	0.09 $\pm$ 0.07 (10)	Kawaguchi <i>et al.</i> '06	1.18 $\pm$ 0.08 (17)	4.39 $\pm$ 0.86 (41)	0.20 $\pm$ 0.136 (90)	0.58 $\pm$ 0.10 (56)
L4_PC	0.18 $\pm$ 0.06 (27)	Wang <i>et al.</i> *			1.36 $\pm$ 0.61 (3831)	5.49 $\pm$ 0.10 (6671)	0.18 $\pm$ 0.127 (7163)	0.24 $\pm$ 0.00 (8146)
L4_SS	0.17 $\pm$ 0.03 (7)	Wang <i>et al.</i> *	0.45 $\pm$ 0.11 (4)	Lübke <i>et al.</i> '03	1.44 $\pm$ 0.70 (463)	6.42 $\pm$ 0.33 (807)	0.18 $\pm$ 0.138 (1307)	0.27 $\pm$ 0.01 (1069)
L4_LBC	0.17 $\pm$ 0.05 (12)	Wang <i>et al.</i> *			1.17 $\pm$ 0.62 (74)	9.67 $\pm$ 0.94 (142)	0.17 $\pm$ 0.133 (327)	0.61 $\pm$ 0.08 (122)
L4_NBC	0.21 $\pm$ 0.04 (15)	Wang <i>et al.</i> *			1.77 $\pm$ 0.94 (91)	15.14 $\pm$ 1.41 (112)	0.24 $\pm$ 0.209 (298)	0.98 $\pm$ 0.14 (127)
L4_SBC	0.23 $\pm$ 0.02 (7)	Wang <i>et al.</i> *			2.19 $\pm$ 0.81 (50)	15.93 $\pm$ 1.55 (80)	0.23 $\pm$ 0.159 (234)	0.71 $\pm$ 0.09 (119)
L4_BTC	0.19 $\pm$ 0.03 (5)	Wang <i>et al.</i> *			3.63 $\pm$ 1.97 (37)	12.40 $\pm$ 1.17 (71)	0.18 $\pm$ 0.135 (258)	0.77 $\pm$ 0.12 (72)
L4_MC	0.23 $\pm$ 0.08 (11)	Wang <i>et al.</i> *			2.29 $\pm$ 1.32 (94)	9.23 $\pm$ 0.81 (160)	0.27 $\pm$ 0.201 (330)	0.91 $\pm$ 0.13 (136)
L4_ChC	0.22 (1)	Wang <i>et al.</i> *			1.91 $\pm$ 0.91 (18)	13.18 $\pm$ 1.71 (23)	0.21 $\pm$ 0.182 (71)	0.38 $\pm$ 0.09 (22)
L4_DBC	0.35 $\pm$ 0.19 (2)	Wang <i>et al.</i> *			0.60 $\pm$ 0.30 (15)	10.66 $\pm$ 2.16 (31)	0.19 $\pm$ 0.106 (94)	0.95 $\pm$ 0.41 (38)
L4_BP	0.19 $\pm$ 0.09 (2)	Wang <i>et al.</i> *			0.18 $\pm$ 0.09 (14)	3.95 $\pm$ 1.21 (9)	0.18 $\pm$ 0.108 (46)	0.23 (1)
L5_TTPC1	0.11 $\pm$ 0.04 (32)	Romand <i>et al.</i> '11	1.65 $\pm$ 0.26 (11)	Larkman '91	2.50 $\pm$ 0.98 (3863)	3.28 $\pm$ 0.07 (4937)	0.14 $\pm$ 0.09 2(4831)	0.23 $\pm$ 0.01 (5406)
L5_TTPC2	0.12 $\pm$ 0.05 (31)	Romand <i>et al.</i> '11	1.65 $\pm$ 0.26 (11)	Larkman '91	2.07 $\pm$ 0.97 (6520)	3.07 $\pm$ 0.05 (8410)	0.15 $\pm$ 0.102 (7002)	0.23 $\pm$ 0.00 (8464)
L5_STPC	0.2 $\pm$ 0.07 (15)	Wang <i>et al.</i> *	1.31 $\pm$ 0.41 (10)	Larkman '91	2.99 $\pm$ 1.40 (1277)	2.60 $\pm$ 0.11 (1662)	0.18 $\pm$ 0.125 (1016)	0.23 $\pm$ 0.01 (1663)
L5_LBC	0.21 $\pm$ 0.07 (7)	Wang <i>et al.</i> *			1.57 $\pm$ 0.89 (174)	8.11 $\pm$ 0.49 (306)	0.28 $\pm$ 0.224 (327)	0.98 $\pm$ 0.08 (316)
L5_NBC	0.18 $\pm$ 0.08 (3)	Wang <i>et al.</i> *	0.03 $\pm$ 0.03 (15)	Kawaguchi <i>et al.</i> '06	2.70 $\pm$ 1.42 (62)	9.45 $\pm$ 0.84 (119)	0.17 $\pm$ 0.141 (820)	1.01 $\pm$ 0.11 (165)
L5_BTC	0.14 $\pm$ 0.005 (2)	Wang <i>et al.</i> *			2.17 $\pm$ 1.11 (209)	5.65 $\pm$ 0.38 (326)	0.18 $\pm$ 0.135 (258)	0.50 $\pm$ 0.04 (341)
L5_MC	0.22 $\pm$ 0.06 (8)	Wang <i>et al.</i> *	0.23 $\pm$ 0.06 (8)	Kawaguchi <i>et al.</i> '06	2.66 $\pm$ 1.63 (197)	8.46 $\pm$ 0.64 (348)	0.28 $\pm$ 0.222 (834)	0.78 $\pm$ 0.06 (312)
L5_ChC	0.21 (1)	Wang <i>et al.</i> *			2.84 $\pm$ 1.73 (11)	10.56 $\pm$ 1.60 (19)	0.15 $\pm$ 0.144 (85)	0.53 $\pm$ 0.12 (18)
L5_DBC	0.22 $\pm$ 0.06 (4)	Wang <i>et al.</i> *			0.94 $\pm$ 0.51 (59)	4.94 $\pm$ 1.22 (85)	0.23 $\pm$ 0.159 (36)	0.31 $\pm$ 0.08 (58)
L5_BP	0.16 (1)	Wang <i>et al.</i> *			0.20 $\pm$ 0.10 (32)	4.36 $\pm$ 1.15 (50)	0.16 $\pm$ 0.076(16)	0.16 $\pm$ 0.04 (66)
L6_TPC	0.19 $\pm$ 0.08 (18)	Wang <i>et al.</i> *			2.51 $\pm$ 1.24 (2191),	1.95 $\pm$ 0.06 (2901)	0.16 $\pm$ 0.114 (2454)	0.14 $\pm$ 0.01 (2782)
					2.19 $\pm$ 1.04 (2058)	1.00 $\pm$ 0.07 (2376)	0.16 $\pm$ 0.103 (1780)	0.13 $\pm$ 0.01 (2569)
L6_IPC	0.18 $\pm$ 0.08 (19)	Wang <i>et al.</i> *			2.36 $\pm$ 0.99 (1982)	1.95 $\pm$ 0.07 (3084)	0.13 $\pm$ 0.103 (2074)	0.15 $\pm$ 0.01 (3207)
L6_BPC	0.2 $\pm$ 0.08 (17)	Wang <i>et al.</i> *			2.76 $\pm$ 1.32 (2509)	2.04 $\pm$ 0.07 (3169)	0.19 $\pm$ 0.104 (2066)	0.12 $\pm$ 0.01 (3384)
L6_LBC	0.16 $\pm$ 0.06 (15)	Wang <i>et al.</i> *			1.50 $\pm$ 0.76 (216)	6.09 $\pm$ 0.44 (246)	0.18 $\pm$ 0.152 (713)	0.53 $\pm$ 0.05 (261)
L6_NBC	0.13 $\pm$ 0.06 (5)	Wang <i>et al.</i> *			1.30 $\pm$ 0.67 (182)	6.03 $\pm$ 0.36 (288)	0.22 $\pm$ 0.123 (641)	0.66 $\pm$ 0.07 (272)
L6_SBC	0.15 $\pm$ 0.08 (4)	Wang <i>et al.</i> *			2.86 $\pm$ 1.48 (49)	4.95 $\pm$ 0.70 (66)	0.17 $\pm$ 0.109 (161)	0.26 $\pm$ 0.04 (71)
L6_MC	0.13 $\pm$ 0.05 (10)	Wang <i>et al.</i> *			1.80 $\pm$ 1.02 (173)	4.81 $\pm$ 0.47 (280)	0.19 $\pm$ 0.144 (470)	0.56 $\pm$ 0.05 (355)
L6_ChC					3.13 $\pm$ 1.30 (14)	6.02 $\pm$ 0.44 (16)	0.23 $\pm$ 0.177 (33)	0.26 $\pm$ 0.09 (4)
L6_DBC	0.08 (1)	Wang <i>et al.</i> *			0.53 $\pm$ 0.33 (21)	5.21 $\pm$ 1.25 (37)	0.12 $\pm$ 0.138 (77)	0.32 $\pm$ 0.10 (59)
L6_NGC	0.43 (1)	Wang <i>et al.</i> * * unpublished observations			0.53 $\pm$ 0.28 (15)	3.15 $\pm$ 0.57 (20)	0.16 $\pm$ 0.123 (14)	0.32 $\pm$ 0.21 (9)

Table S3 – **Structural functional and biological spine and bouton densities**

## **Acknowledgments**

Thanks to Mister James King for technical assistance. The financial support for CADMOS and the Blue Gene/P system is provided by the Canton of Geneva, Canton of Vaud, Hans Wilsdorf Foundation, Louis-Jeantet Foundation, University of Geneva, University of Lausanne and École Polytechnique Fédérale de Lausanne



## 5 Further Methods

This chapter serves to present a number of further refinements of the cortical microcircuit model introduced by me. The refinements, motivated by the deliberations outlined in Chapter 2, will be presented individually along with their validations and predictions derived from them. To review them in the context of the full cortical microcircuit model, refer to appendix C, where you can find the manuscript of the *magnum opus* of the Blue Brain Project: "Reconstruction of the Neocortical Microcircuit", submitted to Nature.

The methods described in this chapter have been developed by the thesis author with help from *Dr. Srikanth Ramaswamy, EPFL* and *Dr. Eilif Muller, EPFL*. Analysis and figure generation by the thesis author.

*In-vitro* data for extracellular stimulation experiments was provided by *Dr. Vincent Delattre, EPFL*.

### 5.1 Derivation of Synaptic Quantal Conductances

After obtaining synapse numbers and locations as described in Chapter 3, two more steps are required to functionalize the connectome:

1) Short term synaptic dynamics: Cortical synapses have a profile of short term facilitation or depression associated with them, increasing or decreasing the amplitude of the response to subsequent stimuli [Thomson et al., 1996, Thomson, 1997, Reyes et al., 1998, Feldmeyer et al., 1999, 2002, Tsodyks et al., 1998]. A strategy to reconstruct and extrapolate these dynamic properties is described in [Ramaswamy, 2011].

2) Unitary conductances: As described in Chapter 2, unitary synaptic conductances reported in the literature cannot be used uncorrected in a model because of the *space-clamp error*. We therefore developed a technique to reconstruct the conductances using less quantitatively problematic data: the reported amplitudes of postsynaptic potentials at the soma (PSPs). Assuming that synapse numbers, locations and short term dynamics are indeed biologically correct, it is the unitary conductance that decides PSP amplitude, matching it means matching the correct unitary conductance.



### 5.1.1 The approach to conductance prediction

Conceptually, there are two approaches to find the conductance leading to a given PSP amplitude: Analytically, using cable theory or numerically, running a simulation. While it is guaranteed to yield an exact value, the analytical approach comes with severe complications: The high degree of non-linearity in the ion channel models makes the approach costly and the high morphological variability in the model makes it hard to extract a general solution for a pathway. Besides, the conductances appear to have an intrinsic variability, indicated by a certain standard deviation reported in the literature [Thomson et al., 1996, Yoshimura et al., 1999]. Although it has been shown that the variability does not play a vital role [Ramaswamy, 2011, Ramaswamy et al., 2012], it indicates that the *exactness* of an analytical solution is not necessary. The numerical approach on the other hand leads to a long chain of trial and error until a sufficiently accurate value is found. We therefore propose a middle ground approach: Find an analytical solution in a greatly reduced model; then validate the predicted value numerically.

### 5.1.2 The prediction method

It is tempting to predict a linear relation between conductance and PSP amplitude. After all, Ohm's law postulates a linear relation between conductance and current, given a voltage. The current flow however changes the voltage, moving it closer to the reversal potential, thereby reducing the current. This is well known and can be seen in the saturating current strength upon charging a capacitor. In the case of synapses, this leads to a sub-linear dependence of PSP amplitude on conductance with the saturation effect being stronger for synaptic reversal potentials near resting (such as for inhibitory synapses) and for strong synapses. In other words, the relevant parameters are the PSP amplitude ( $A$ ), the synaptic reversal potential ( $e$ ) the resting membrane potential ( $r$ ) and the synaptic conductance ( $c$ ).

Without saturation effect, the amplitude scales proportional to the product of conductance and driving force, i.e. the difference between resting and reversal potential:

$$\frac{A_1}{A_2} = \frac{c_1 \cdot (e_1 - r_1)}{c_2 \cdot (e_2 - r_2)} \quad (5.1.1)$$

If there is saturation, we can assume that its strength is determined by how close the membrane voltage gets to the reversal potential:

$$S = \frac{\int (e - v(t)) dt}{\int (e - r) dt}, \quad (5.1.2)$$

where  $v(t)$  is the membrane voltage under a synapse at time  $t$  and  $S$  is a normalized measure of the saturation between 0 and 1.

The actual scaling is then weakened by the saturation:

$$\frac{A_1}{A_2} = \frac{c_1 \cdot S_1 \cdot (e_1 - r_1)}{c_2 \cdot S_2 \cdot (e_2 - r_2)} \quad (5.1.3)$$

To simplify the prediction, we make the following assumptions: 1) We can represent the PSP voltage trace by just its amplitude. 2) We can represent the PSP under the synapse by the one at the soma. As long as we only consider relative scaling and not absolute values, the first assumption can be made if scaling the driving force or conductance does not change the shape or time course of the PSP, only its

## 5.1. Derivation of Synaptic Quantal Conductances

strength. In that case the integral will be proportional to the amplitude. The second one can be made – again considering only scaling – if the attenuation from the synapse location to the soma is constant. Defining  $A = \max(v(t) - r)$  yields:

$$S = \frac{\int (e - r - (v(t) - r)) dt}{\int (e - r) dt} \propto \frac{e - r - A}{e - r} \quad (5.1.4)$$

$$\frac{A_1}{A_2} = \frac{c_1 \cdot (e_1 - r_1 - A_1)}{c_2 \cdot (e_2 - r_2 - A_2)} \quad (5.1.5)$$

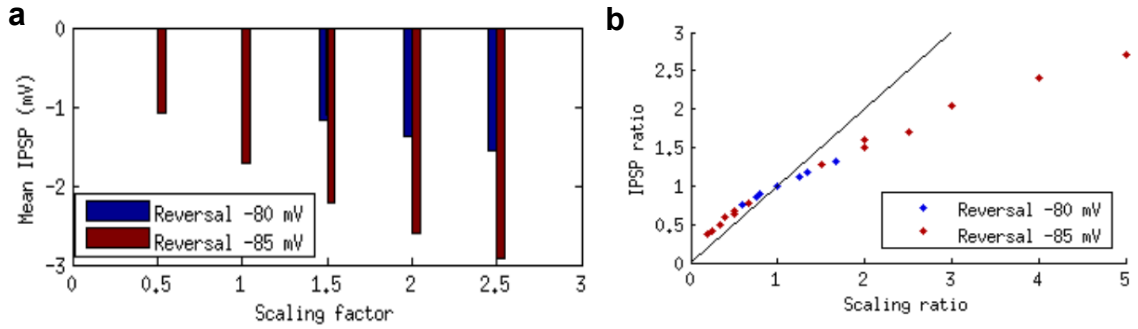


Figure 5.1 – Mean PSP amplitudes for different conductances / reversal potentials

a) Mean PSP amplitudes of N=417 L5\_MC to L5\_TTPC connections for a reversal potential of -80 mV (blue bars) and -85 mV (red bars). b) Conductance scaling ratio against resulting PSP amplitude ratio for  $5^2 = 25$  pairs of scaling factors at a reversal of -85 mV (red) and  $3^2 = 9$  pairs of scaling factors at -80 mV (blue).

### 5.1.3 Validating predictions

The prediction method rests on a number of simplifying assumptions and does not take into account non-linearities introduced by voltage gated channels on the dendrites, nor potential interactions between multiple synapses in a connections. To assess its accuracy, we tested the prediction on simulations of 417 inhibitory connected cell pairs (L5\_MC to L5\_TTPC). We chose inhibitory connections because the closeness of the inhibitory reversal potential to resting [Thomson et al., 1996, Silberberg and Markram, 2007] will lead to a more significant saturation effect. In the simulation the presynaptic L5\_MC cells were made to fire a single action potential and PSPs are recorded at the soma. The PSP amplitude was calculated as the difference between the minimum of the voltage trace (inhibitory connection!) and the voltage directly before the action potential. Connections were tested with 0.5, 1.0, 1.5, 2.0, 2.5 times the conductance reported in the literature [Thomson et al., 1996, Yoshimura et al., 1999] for a synaptic reversal potential of -85 mV and with 1.5, 2.0, 2.5 times the reported conductance for a reversal of -80 mV.

We found that PSP amplitude increases with synaptic conductance and driving force, but the scaling is not linear (see Fig 5.1a). Consistent with the saturation hypothesis, conduction (scaling) ratios  $> 1$  lead to sub-linear scaling of mean PSPs, ratios  $< 1$  to super-linear scaling (see Fig 5.1b).

Next, we compared PSP amplitude predictions to the actual amplitudes for individual cell pairs instead

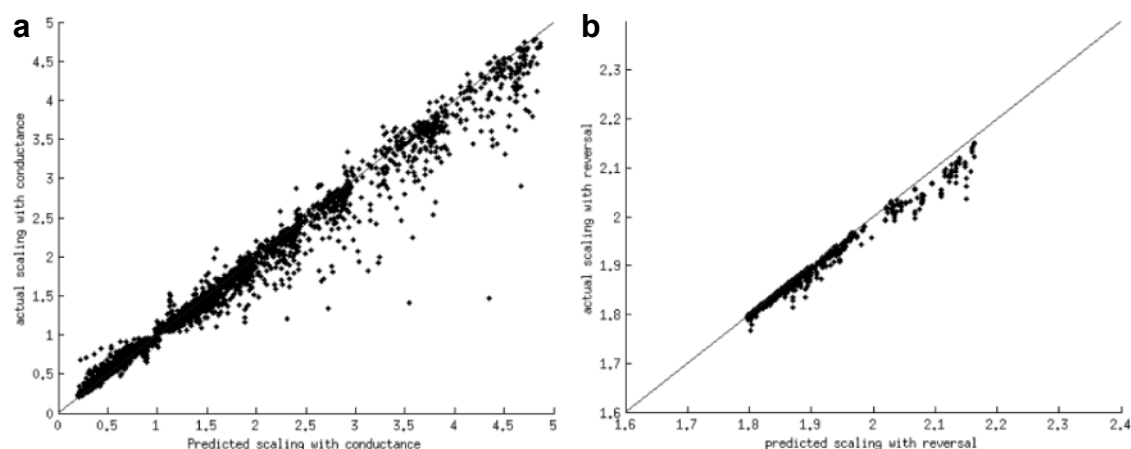


Figure 5.2 – Comparing predicted to actual PSP amplitude scaling

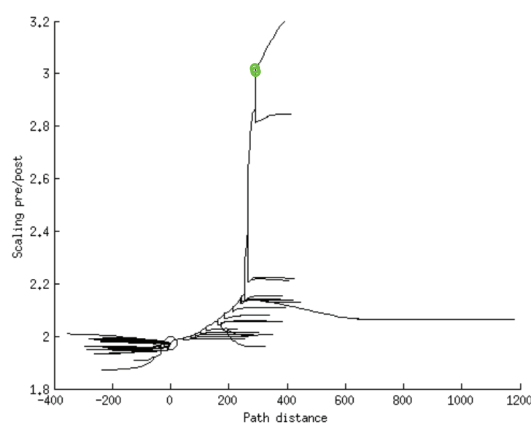
a) Predicted against actual PSP amplitude scaling upon changing the synaptic conductance. Each dot indicates one of 417 pairs  $\times$  (25 + 9) conductance combinations. b) Same, for scaling with reversal potential.

of averages (Fig 5.2). Since the method only allows us to predict the relative change upon adjusting a parameter, we split the analysis into two parts: Scaling upon adjusting synaptic conductance and scaling upon adjusting reversal potential. In both cases we found the predictions to be very accurate ( $R=0.98$  for scaling with conductance,  $R=0.99$  for scaling with reversal). Notably, there were significant differences in the scaling of individual pairs: For scaling with conductance, some went as high as a scaling factor of almost 5 (Fig 5.2a), while the maximum of the averaged data was around 2.5 (Fig 5.1b). Caused by individual differences in resting membrane voltage and PSP amplitude, these trends were accurately predicted.

While the prediction methods seems to accurately predict the sub-linearity caused by the satura-

Figure 5.3 – Super-linear PSP amplitude scaling in an excitatory connection

Relative increase in PSP amplitude (y-axis) plotted against path distance from the soma of the electrical compartments of an L23\_PC, conserving morphological structure of the cell. The data is for an up-scaling of synaptic conductance by a factor of 2. Green circles indicate the location of two synapses in close proximity on the apical tuft, causing the observed super-linearity.



tion effect, it does not take into account possible super-linearity due to local ion-channel activation in the dendrites. Indeed, we found an example pair of L23 PCs, where an up-scaling of synaptic conductances by a factor of 2 led to a increase of the local PSP amplitude in the dendrites by a factor of up

to 3.2 (Fig 5.3). Note, however that at the soma only a scaling factor  $< 2$  was reached, as predicted. In general, this kind of super-linear behavior was an exception, caused by a relatively dense cluster of strong synapses on a thin dendrite with a high input resistance. In the biologically relevant parameter range, this type of behavior will be unlikely to play a major role.

## 5.2 Cell Placement

### 5.2.1 Relevance

The preceding chapter discusses how a connectome can be predicted by selecting from a set of axo-dendritic appositions. Finding said appositions first requires the generation of a volume of neural tissue, i.e. placing reconstructed neurons in a volume. This placement is not completely arbitrary, not only do soma densities have to comply with biological data, but there are also constraints on the placement of any single cell. For example, they cannot be placed such that parts of the morphology land above the top of Layer I, as that part is filled with the meninges and eventually the skull.

Cell placement can be constrained even beyond those hard limits. Neuron morphologies tend to have certain regions of increased axonal or dendritic density that consistently within an m-type tend to land in specific layers (see Fig 5.5a. This can be speculated to be cause or effect of said m-type *targeting* that region for connections. As connectivity in the model is determined by axo-dendritic overlap, incorrect placement of these features will lead to a connectome inconsistent with biology.

The importance of cell placement becomes even larger when extracellular potentials are to be calculated. The weight of the contribution of a morphological section is determined by its distance to the sampling location. Unbiological placement would lead to incorrect and potentially biased distances, invalidating the results of the extracellular calculation.

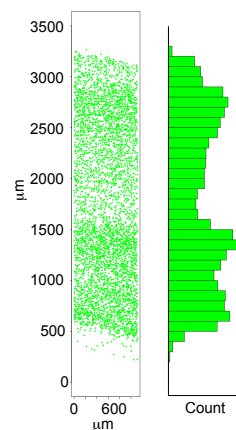


Figure 5.4 – Biological cell density depth profile

Left: Identified neuron soma positions in a NeuN stained slice of rat cortex. Right: Resulting cell counts per depth bin. Data from DeFelipe *et al* 2011

### 5.2.2 Method

Morphological density in the neocortex tends – with few exceptions [Woolsey and Van der Loos, 1970, Welker and Woolsey, 1974] – to be locally constant along a horizontal axis, i.e. parallel to layer boundaries. This is a result of neuronal morphologies of a given cell type being statistically rotational

symmetrical (with the potential exception of long range axonal projections). This symmetry lets place the morphologies with a random rotation at any location in a given x-z plane; it reduces the placement problem to placement along the y-axis, i.e. placement relative to layer boundaries, only.

At the same time, we find a very typical profile of soma densities along the y-axis *in-vitro* (see Fig 5.4a). To ensure that the model is consistent with this profile, we first determine a set of soma positions for each m-type matching the biological data. This turns the *placement* problem into a *selection* problem: For each pre-determined position we have to select a suitable morphology from the pool of reconstructions of the pre-determined m-type, based on the y-coordinate.

For the bulk of reconstructed morphologies used in the model the soma location relative to cor-

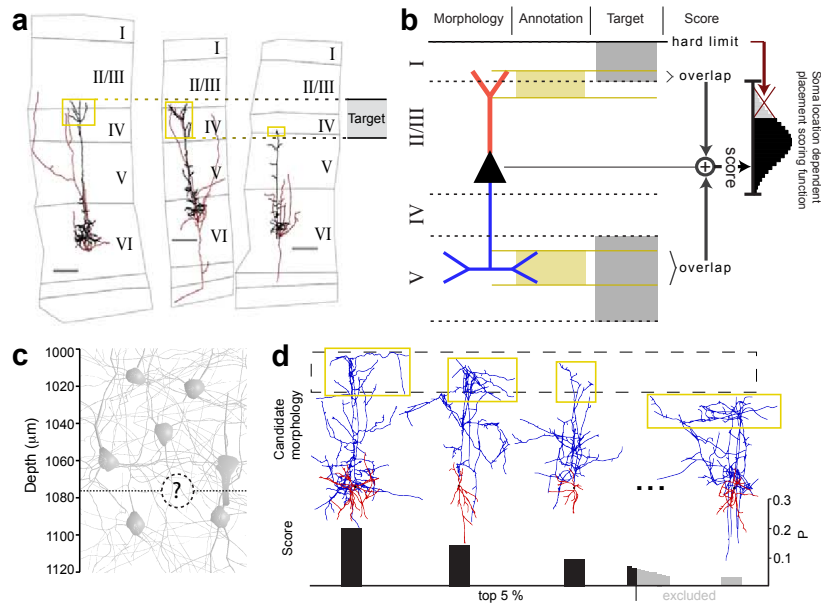


Figure 5.5 – Overview of selecting appropriate morphologies

Assigning morphologies to soma positions involves selecting the most appropriate reconstruction for a predefined soma position. (a) Annotating morphologies. Constraining rules for placing morphologies of each m-type are derived from experimental observed tendencies of dendritic and axonal clustering within and across layers. Clusters are manually annotated and their preferred laminar location are determined from experimental observations. Cluster annotation (yellow boxes) and laminar location (dashed lines) are illustrated for three representative layer six pyramidal cells. Analogous annotation was performed for m-types with observed laminar preferences (see Methods). (b) Schematic of the morphology-placement scoring algorithm. Above, the workflow of the algorithm. Morphology – placement of L23 PCs is illustrated. Annotation – the axonal and dendritic cluster extents are annotated. Target – the absolute target depth intervals are determined. Score – the overlap of annotated and target areas for a given soma position are summed. Violating hard limits, such as the dendrites extending above the pia, results in a zero score. (c) Soma position and m-type (m-type positions) is pre-determined. (d) Selection of a morphology instance. A score is calculated for all morphology instances at all m-type positions. For each position, an instance from the top 5% of candidates is selected with a probability proportional to the score. Morphologies (L5\_MC) are depicted according to descending scores from left to right for a given position.

tical layers was not recorded. This means we have to determine whether a morphology is suitable for a y-coordinate based on its features alone. As a first step, we identify for each m-type a number of conserved features – such as dendritic tufts or densities in the axonal arborisation – and identify their target layers. Next, these features are hand-annotated in each reconstructed morphology. Fig 5.5a shows an example of annotated tufts in L6 PCs and their target ranging from the top of 5% of layer 5 to the bottom 10% of layer 2/3. Combining these annotations with the prescribed layer boundaries of the model, we can calculate a *soma location dependent placement scoring function* (see Fig 5.5b). This is done by calculating for a given soma position the normalized overlap of the annotated feature with the layer target and summing the overlap of all annotations – the larger the overlap, the higher the score. A hard limit at the top of the volume sets the score to 0 if parts of the morphology go beyond the limit. During model building, we have to select a morphology for a given position (Fig 5.5c). We sort all candidates by their score for said position (Fig 5.5d) and select randomly from the top 5%, where the probability of choosing a morphology is proportional to its score.

This approach ensures that the placed morphology will be chosen from the best matches for a location and provides morphologies, even for location where no good fit is available. Since calculated overlaps are normalized, a morphology cannot score high for every location, automatically ensuring a balanced usage of different morphologies. Analyzing the soma location dependent scoring functions along an m-type allows us to identify locations with a scarcity of suitable candidates and direct future reconstruction effort towards it.

### 5.2.3 Results

Applying the result successfully ensures that identified features land in the correct layers. In the case of L5\_TTPC and L5\_MC cells for example, dendritic tufts or axonal densities cover layer 1 without going beyond it, for a wide range soma positions (see Fig 5.6a). Only for positions very low in layer 5 the dendrites / axons struggle to reach layer 1, indicating a lower quality placement. This indicates a lack of reconstructed morphologies from this part of the layer. An explanation might be that reconstruction effort is typically targeted at an m-type in a specific layer leading to a bias for cells from the center of that layer. This is confirmed in the overview of scoring of the two morphology types (Fig 5.6b). In both cases, the mean overlap of available morphologies as well as the number of suitable morphologies for different quality criteria is significantly reduced near the bottom of the layer.

In order to evaluate the overall placement of dendritic morphology, we predicted the volumetric spine density in the model and compared it to biological data. The prediction was obtained by multiplying total dendritic length in a sampled volume with an assumed spine density of  $1.05\mu m^{-1}$  (average of diverse estimates: Riccio and Matthews [1985], Larkman [1991], Datwani [2002], Bock et al. [2004], Mataga et al. [2004]) similar to [Stepanyants et al., 2009]. Since the spine density was assumed as constant, the free parameter of the prediction was dendritic length in the volume, making it a validation of dendrite placement.

The resulting prediction fits the profile of biological data remarkably well in five out of six layers. Only in layer III densities are about 50% underestimated. Yet, the overall trend of vertical density profile – increasing from layer I to layer II, decreasing in III, increasing to the maximum in IV, finally linearly decreasing to a minimum in VI – is exactly matched. In short, we conclude that both the overall cell density as well as placement is biologically accurate in the model.

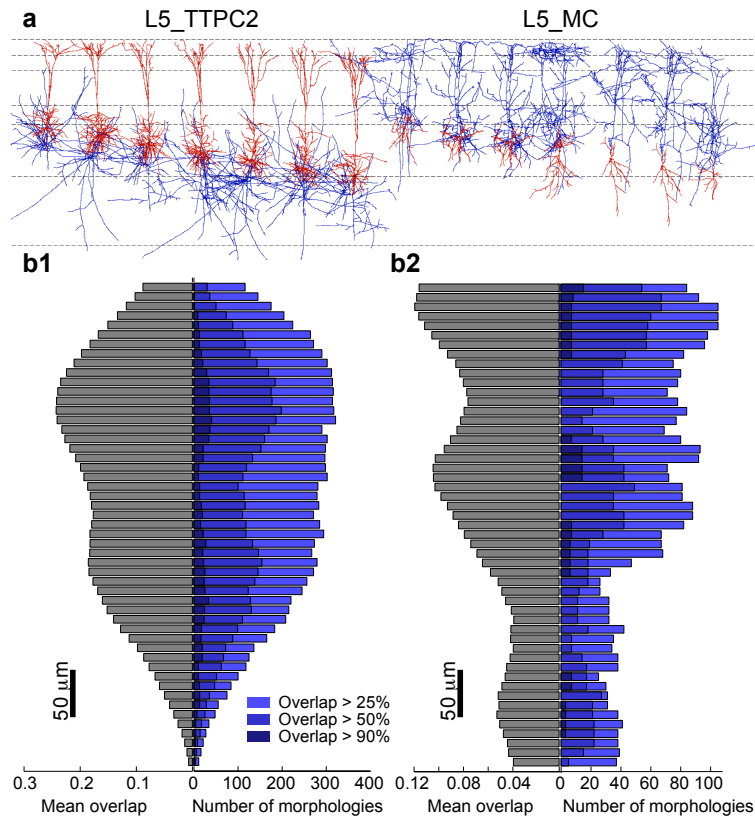


Figure 5.6 – Overview of scoring of L5\_TTPC2 and L5\_MC cells

(a) A collage of neurons at the depth they are placed in the microcircuit model. Seven L5\_TTPC2 (left) and seven L5\_MC (right) cells are depicted with their dendrites in red, axon in blue. Grey dashed lines indicate layer boundaries. (b) Mean overlap of annotated morphology features (grey, left) and number of morphologies scoring an overlap higher than 25 / 50 / 90% (shades of blue, right) at different depth in layer 5. b1: For L5\_TTPC2 morphologies, b2: For L5\_MC morphologies. Depth bins are 10  $\mu m$  wide and ranging from the border with layer 4 (top) to the border with layer 6 (bottom).

## 5.3 Input Generation

While the rat neocortical microcircuit of the BBP represents the state of the art in modeling of neural processes, it still only represents under 1  $mm^3$  of tissue. That means that it lacks a large fraction of the synaptic contacts present in an equivalent biological volume. As derived in Fig 6.3d, an estimated 80% of synapses are sent from outside the volume of a single unitary microcircuit.

In particular, the model lacks anything that can be qualified as input synapses that can be used to feed a controlled stimulus into the modeled system. This leads to a dilemma: How can we study the function of the microcircuit, when we have no way to systematically manipulate it?

### 5.3.1 Thalamocortical Input

A major source of inputs into neocortical microcircuits stems from the thalamus. While other cortical regions and brainstem nuclei provide significant input as well [Purves et al., 2001], the thalamus plays

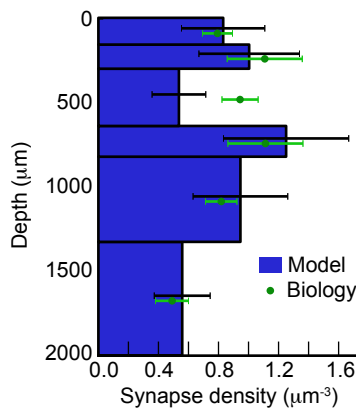


Figure 5.7 – Predicted synapse densities compared to biological data

Synapse densities in the model are predicted by multiplying the total length of dendrites in cubes at the centers of layers with an assumed spine density of  $1.05\mu m^{-1}$  and dividing by the volumes of the cubes. Blue bars with black error bars: Predicted means and standard deviations. Green: Biological data (mean and standard deviation) from DeFelipe *et al* 2011

a special role in perception as the last station on a route from peripheral receptors to the neocortex [Amaral, 2013]. This makes thalamo-cortical projections a prime candidate for input into the model that reflects a controlled external stimulus. There is significant neural processing happening within the thalamus [Chiaia *et al.*, 1991a,b] as well as interaction between cortical and thalamic neurons [Armstrong-James *et al.*, 1991, Scannell *et al.*, 1999] that will not be captured by considering it a simple input into the system. Still, it is at this stage the best candidate for a biologically relevant way of manipulating the model.

### 5.3.1.1 Method

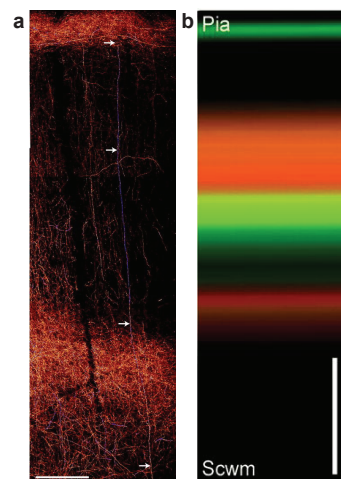


Figure 5.8 – Biological density profile of cortical synapses projected from two thalamic regions

Red: VPM (ventral posteromedial nucleus) projections. Green: POr (postero-medial nucleus) projections. Regions of overlap appear yellow. Taken from Wimmer *et al.* 2010.

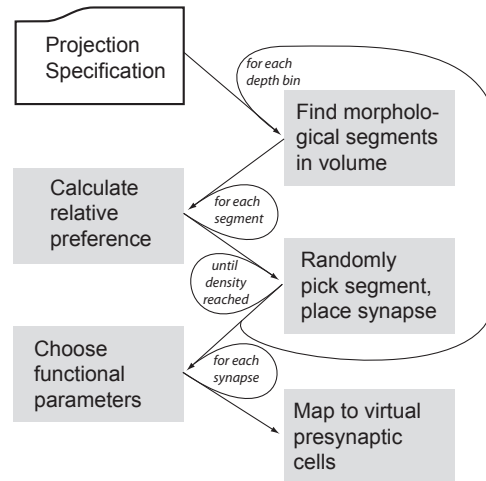
Thalamocortical neurons enter the cortex from the white matter below layer VI, ascending towards layer I. Along the way they form multiple synaptic contacts in specific layers that depend on the thalamic region they originate from [Wimmer *et al.*, 2010]. Our preferred method of placing synapses (see Chapter 3) depends on morphological reconstructions along with accurate cell placement (see Chapter 4.1). As long as axonal reconstructions of projecting cells are not available in sufficient number and quality, another method is needed.



Based on the ready availability of experimental data, we decided to constrain the placement of thalamo-

Figure 5.9 – Overview of thalamocortical projection generation

1) The .xml-formated projection specification ("recipe") defines a number of depth bins with associated horizontal extents and target synapse densities. 2) For each volume defined by a depth bin all contained morphological segments (somata, dendrites, axons) are found. 3) For each found segment a relative preference is calculated that is based on length (longer segments more likely to be picked) and recipe specified cell type and segment type preference. For example, projections could be limited to targeting only dendrites of pyramidal cells. 4) Segments are randomly picked with probabilities proportional to the relative preference until target density is achieved. 5) Each synapse is assigned functional parameters from recipe-defined distributions. 6) Each synapse is assigned a presynaptic identity based on its location.



mocortical synapses by their density profile. Fig 5.8a shows biological density profiles of inputs from two different thalamic regions. In order to be able to match depth profiles such as this, we developed a system that randomly selects for synapse placement morphological segments in a depth bin of the model until the specified density is reached.

Further constraints are needed to fully specify a projection:

1. Which cortical cells are target with which relative preference?
2. Which parts of neuronal morphology are targeted?
3. What are strengths and dynamics of the placed synapses?

In order to ensure maximal flexibility and compatibility with potential future plans to add other external projections, we devised a system allowing us to specify all those constraints in an .xml formatted file or *recipe*. An example of such a file is given in Appendix A.1. The full workflow for the generation of thalamocortical synapses is depicted in Fig 5.9:

For each specified depth bin, we gather all morphological segments of all cells inside the volume (i.e. their midpoint is inside the volume). Next the length of each segment is determined and multiplied with a preference factor based on its morphology type and segment type (i.e. is it part of apical or basal dendrites or an axon or a soma). The vector of resulting *total preferences* is normalized to yield the probabilities to choose each segment for synapse placement. We repeatedly draw randomly with replacement from the pool of segments with the assigned probabilities, placing synapses on each chosen candidate. Since the reconstructed segments are small compared to the electrical compartments used in the simulations of the model, the exact placement on the segment will hardly matter and we just place it at the center.

The synapse types are determined by the postsynaptic morphology and segment types according to specification in the recipe. This synapse type determines the distributions synapse strength and dynamic parameters are drawn from.

Finally, synapses are mapped to a virtual presynaptic cell: In biology, when a thalamic cell fires, all

its thalamocortical projection synapses will be activated at roughly the same time, only modulated by slightly differing axonal conduction delays, leading to a certain degree of correlation. In order to capture the correlation, we have to decide which synapses are grouped together by being innervated by the same presynaptic cell and prescribe an identifier to that cell. The process of defining input into the model is turned into defining spike times for each such virtual cell.

Biologically, the axons of projecting thalamic cells follow a vertical trajectory after entering the cortex with only limited horizontal range (see Fig 5.8b). This ensures that a topographical mapping in the thalamus will be preserved in the cortex [Jones et al., 1982, Georgopoulos et al., 2007]. To capture this behavior, we devised the following algorithm: We distribute locations for the assumed centers of 310 axonal trees evenly in the x-z plane of the microcircuit. The mapping of a placed synapse to the cells is random, with the probability proportional to a gaussian of the distance in the x-z plane between axonal center and postsynaptic location:

$$P(x = i) \propto e^{-\frac{|C_i - S|^2}{2\sigma^2}}, \quad (5.3.1)$$

where  $S$  and  $C_i$  denote the location of the synapse and  $i$ th center in the x-z plane. The parameter  $\sigma$  controls the amount of overlap between neighboring centers and was set to  $20\mu m$ .

Similar to the internal connectome of the model (see Chapter 3), the resulting distribution of synapses per thalamocortical connection has an exponential shape with most connections being formed by only one synapse (see 5.10a). This is incompatible with the available experimental data [Meyer et al., 2010a]. To obtain a biologically viable distribution of synapses per connection, we first increased the synapse densities to a multiple of the biological profile and applied a step of *multi-synapse-pruning* (see Chapter 3). The pruning removes selectively connections formed by a low number of synapses and reduces the density back to the biological target value.

#### 5.3.1.2 Results

We found that for an initial synapse placement at 3 times the biological density and subsequent multi-synapse pruning reproduces both the mean number of synapses per TC connection on L4 PCs and the biological density profile (see Fig 5.10). For connections on L5 PCs we predict a higher number of synapses per TC connections with a mean of 13.9. Similarly, the emerging distribution of PSP amplitudes matches biology exactly for connections on L4 PCs under *in-vivo*-like conditions and predicts higher values for connections on L5 PCs (mean = 0.72 mV).

Applying thalamic stimulation to a full microcircuit we can establish a stimulus-response relation (Fig 5.11a). A stimulus is applied to an increasing number of the most central thalamocortical axons, measuring the peak population firing rate in layer 4 as a response. The population firing rate is defined as 1000 times the number of spikes in a population in a 1 ms bin, divided by its size. As such, while it has the unit Hz, it does measure less the firing frequency of any single cell, but the fraction of the population that is activated by a stimulus and synchrony. At the same time, the mean population firing rate over a larger time window is equal to the mean single cell firing rate over the same time window.

We find an increase in response for increasing stimulus size with the shape of the increase depending on the simulated network state: Simulated *in-vitro* conditions led to an all-or-nothing type response with a sudden, sharp increase as the stimulus size reaches 9 fibers. Under *in-vivo* like conditions, the increase was more gradual, giving the response a much larger dynamic range.

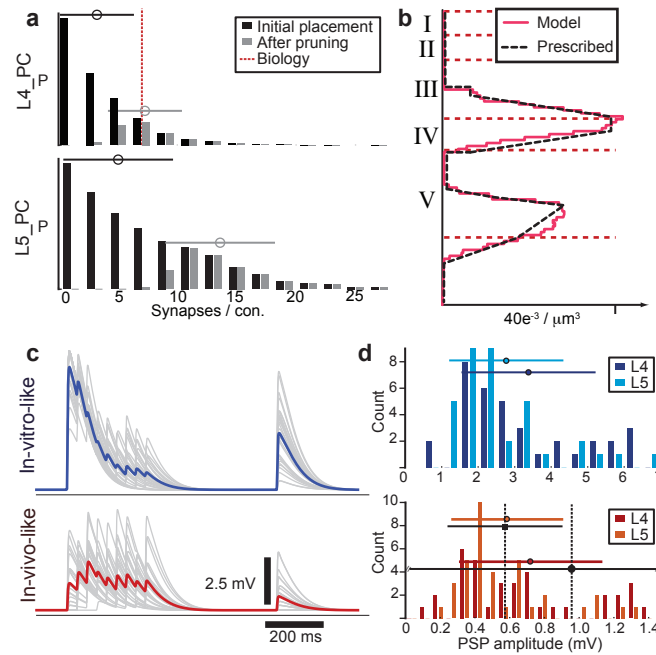


Figure 5.10 – Structure and physiology of in-silico thalamocortical projections

a) Distributions of the number of synapses per thalamocortical connection before application of the multi-synapse rule (black bars) and after (grey bars). Circles with error bars indicate the means and standard deviations. Top: For connections on L4 PCs, Bottom: For connections on L5 PCs. For L4 PCs the biological mean from [Meyer et al., 2010a] is indicated as a red, dashed line. b) Density of synapses after multi-synapse pruning to reach the mean number of synapses per connection on L4 PCs (red line) is compared to the prescribed values (black dashed line) from [Wimmer et al., 2010]. Red, dashed lines indicate layer boundaries. c) PSP responses at the soma of an L5\_PC upon 30 Hz activation of a single thalamocortical connection under simulated *in-vitro* (top, blue) and *in-vivo* like (bottom, red) conditions. Grey lines indicate individual traces, colored lines the mean. d) Distributions of unitary PSP amplitudes on L4 PCs (darker color) and L5 PCs (lighter color). Circles with error bars indicate means and standard deviations. Top: Under *in-vitro* conditions. Bottom: Under *in-vivo*-like conditions. Black circles and error bars indicate mean and standard deviations reported in the literature [Gil et al., 1999].

Under *in-vitro* conditions and super-threshold stimuli, the activation reached the full microcircuit population. The response spread from the center outward in a wave-like fashion (Fig 5.11b and c), indicating that structurally a topographical map in the thalamus would be preserved, feeding the input only into the center of the model as intended. Functionally however, the avalanche-like spread of activity under *in-vitro* conditions destroys any type of mapping, as any stimulus either fails to have any measurable result or activates the whole population.

Biologically, a similar type of wave-like activity spread has been observed in anesthetized mice upon whisker stimulation: A wave of depolarization originating from the somatosensory cortex representation of the whisker, spreading over the entire cortex over 60 ms ([Ferezou et al., 2007]).

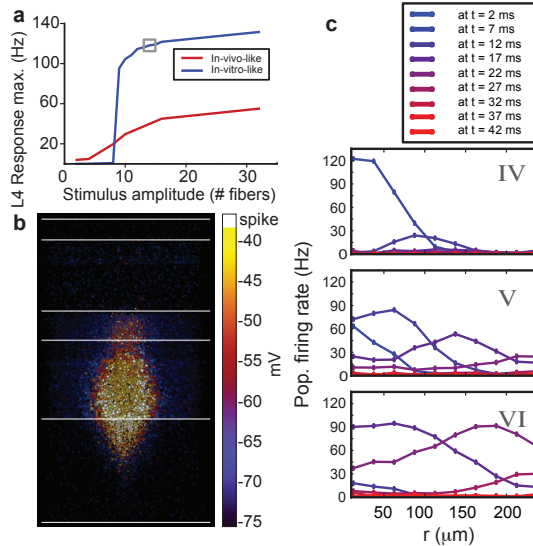


Figure 5.11 – Population response to in-silico thalamic stimulation

a) Maximal population firing rate (1000 times number of spikes in a 1 ms bin divided by the population size) in layer 4 upon simulated stimulation of different numbers of the most central thalamocortical fibers (5 spikes, 50 Hz). Blue line: Under *in-vitro* conditions. Red line: Under *in-vivo* like conditions. Grey box indicates the regime used in b and c. b) Soma voltage of cells in the model at  $t = 15ms$  after the stimulation. Stimulus condition as indicated in a. White lines indicate layer boundaries. c) Population firing rates of granular and sub-granular layers at different radial distances from the center. Stimulus conditions as indicated in a. Results in different time bins after the stimulus are indicated in different colors from blue (2 ms) to red (42 ms). We see the wave-like spread of activity from the center.

### 5.3.2 Simulated Extracellular Stimulation

While a thalamic input provides a cromulent, biologically motivated way of driving the circuit, other types of stimuli are more relevant *in-vitro*. In order to activate a whole microcircuit, *extracellular* stimulation is a widely used tool [Penfield and Boldrey, 1937, Ranck, 1981, Grill and McIntyre, 2001, Graziano et al., 2002]. Where extracellular measurements are used to deduct information about the state and activity of a microcircuit, extracellular stimuli systematically influence them. The NEURON simulation environment used in the BBP provides a mechanism to add an extracellular compartment for each cable compartment and set its voltage. We used the mechanism to investigate how extracellular stimuli activate neurons.

#### 5.3.2.1 Extracellular interaction in cable theory

The way in which extracellular voltages act on intracellular compartments is outlined in Fig 5.12. The voltages do not directly activate ion channels, instead they impose a gradient on the potential of intracellular nodes, leading to axial and trans-membrane currents which in turn change membrane voltages. If that change is large enough, it can cause a cell to fire. A prediction of this is that the strength of the effect is proportional not to the amplitude of the stimulus itself, but to its gradient. Morphological segments are hit most strongly if they point away from an extracellular electrode, orthogonal to it the direct effect is zero.

An actual morphology however is more complicated than a linear cable and indirect effects can affect even orthogonal segments. We therefore tested the effect by simulating extracellular stimulation of dendrites and soma of a single L2\_PC. We simulated a single square voltage pulse of an electrode placed near the cell by replaying the pulse into the voltage of the extracellular compartment of each

Figure 5.12 – Extracellular stimuli in cable theory

a) A cable at rest. Here, we assume no voltage gradient at rest. Extracellular space is assumed at 0 mV, the intracellular compartments have a potential equal to the voltage over the membrane ( $V^m$ ). b) An extracellular stimulus is applied. Membrane voltages are not directly affected, but the potential of the intracellular compartments is now the sum of extracellular ( $V^e$ ) plus membrane voltage. c) If the extracellular potential along the cable has a gradient, so does the intracellular potential. This leads to an axial current ( $I^a$ ) according to Ohms Law. d) Membrane currents ( $I^m$ ) are equal to the gradient in axial currents. Part of it will be in form of capacitive currents, charging or discharging the membrane voltage ( $\frac{dV^m}{dt}$ ).

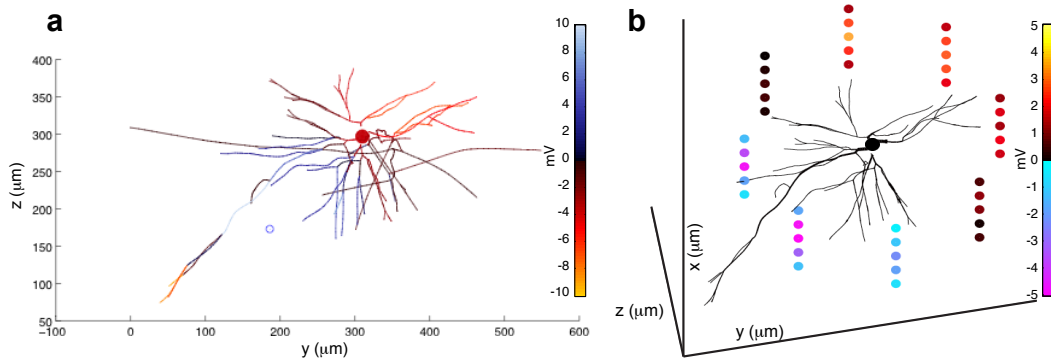
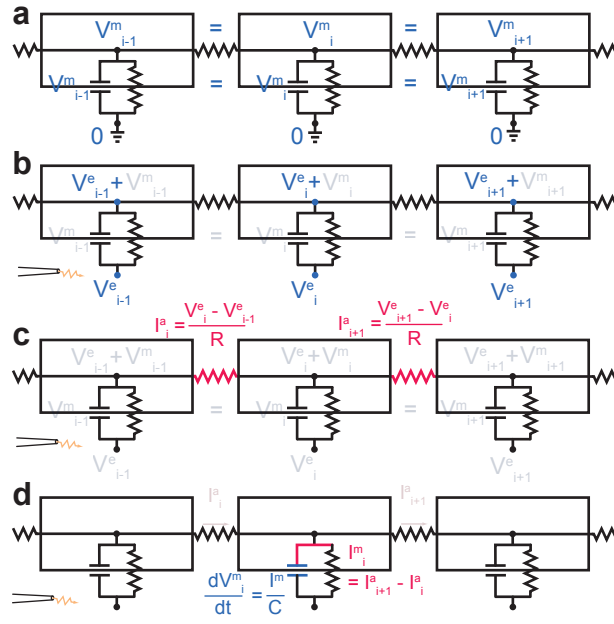


Figure 5.13 – In-silico effect of extracellular stimulation on a single cell

a) Maximal de- or hyperpolarization achieved in the dendrites and soma of an exemplar L2\_PC. The location of the simulated electrode is indicated as a blue circle near the apical dendrite (bottom left). Stimulus was a single  $500\mu V$  square pulse with a width of 1 ms. b) De- or hyperpolarizing effect at the soma for the same stimulus at different locations. Each colored disk indicates a tested stimulus location with the maximal effect at the soma color-coded. Each stimulus location was at the same distance in the y-z plane from the soma, but different x-coordinates (distance  $10\mu m$ ).

cable segment, scaled inversely proportional to its distance from the electrode.

The results (Fig 5.13) indicate that a single square pulse can have opposite effects on different parts of a neuron morphology, depolarizing some, hyperpolarizing others. In the case indicated in Fig 5.13a, the depolarizing occurs in the parts closest to the electrode, while the rest gets hyperpolarized. In *in-vitro* experiments, typically biphasic pulses containing a positive and a negative phase are used to ensure that each part gets depolarized once, thus maximizing the probability that an action potential is triggered [McIntyre and Grill, 2002].

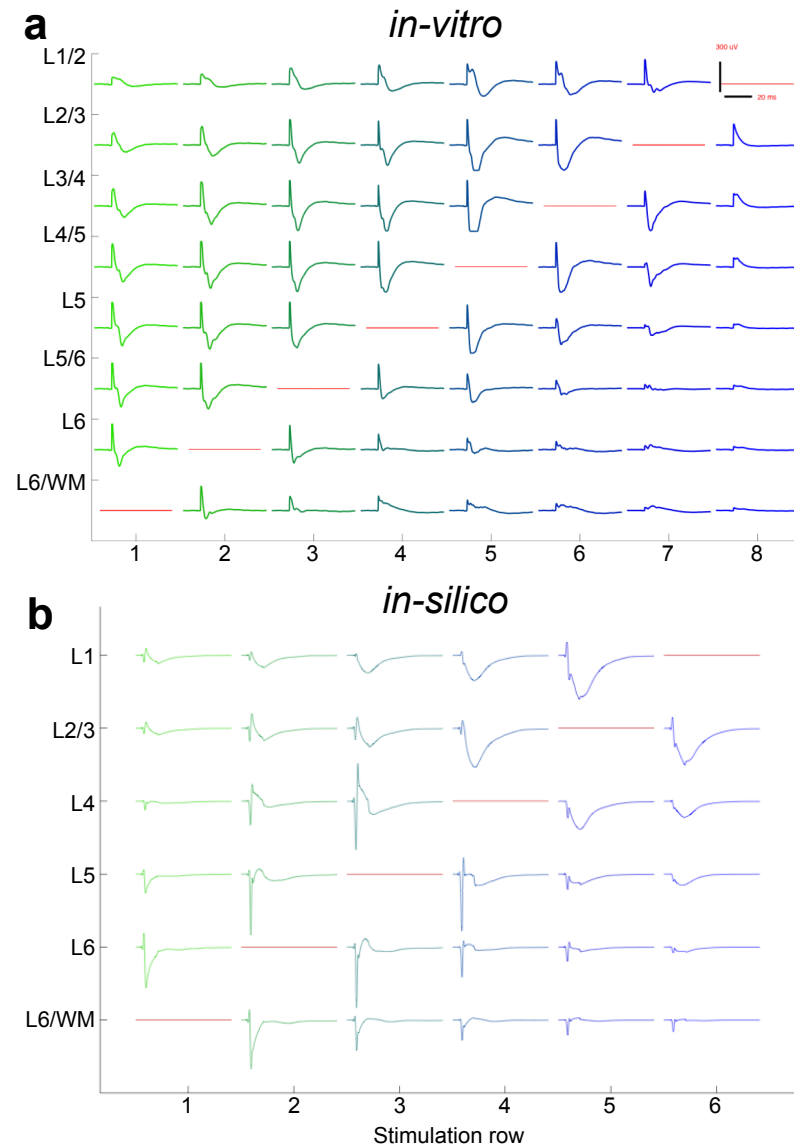


Figure 5.14 – Comparing in-vitro and in-silico effect of extracellular stimulation

a) *In-vitro* stimulation of a cortical slice with a single biphasic pulse of a full row of electrodes of a multi-electrode array (MEA). Positions of the electrodes relative to cortical layers were identified in a microphotograph and are indicated along the x and y axes of the plot. The row used for stimulation is varied along the x-axis, the one used for recording along the y-axis. Mean of  $N = 30$  stimulations is shown. Data recorded by Vincent Delattre. b) Attempt to re-create the experiment in a *in-silico*.

The morphology investigated has a very pronounced linear axis defined by its apical and parts of the basal dendrites. When investigating the effect for different stimulus locations (Fig 5.13b), it is found to be zero as predicted when the axis is oriented orthogonal to the simulated electrode location. These locations appear to be a 'blind spot' of the cell with respect to extracellular stimulation; it remains to be investigated to what degree a biphasic stimulus can penetrate it.

Using the extracellular stimulation protocol on the full microcircuit model, we attempted to re-create an *in-vitro* experiment *in-silico* (Fig 5.14). *In-vitro*, the stimulus is followed by a negative potential near the stimulus location that decays over roughly 20 ms. In layers further away from the stimulus a phase inversion occurs and the main response is positive. *In-silico*, this behavior is not fully reproduced: For example in the case of stimulation in layers 5 or 6, the electrodes closest to the stimulus report a positive potential after the stimulus and the potential in layer 1 is always negative. Differences between the *in-vivo* and the *in-vitro* case are not unexpected: It is thought that the main effect of extracellular stimulation lies in the triggering of action potentials in passing axons. As the cable-theory based simulations of the BBP exclude most of the axon, replacing it with a delay between action potential detection at the axon initial segment and efferent synapse activation, the axon-centric effect of extracellular stimulation cannot be captured.

Including the axon would increase the number of simulated electrical compartments and therefore the computational cost by over 150% and require the development of axonal ion-channel models reliably conducting an axon potential with biologically correct velocities. A more feasible strategy for the future may be to use single cell axon simulations to develop a simple model of the requirements for action potential triggering in axons. The model can then be used to activate synapses in full microcircuit simulations to add the axon-centric of extracellular stimulation.

# **Microcircuit Modeling Results**

## **Part III**





## **6 An Analysis of the Predicted Connectome of Neural Microcircuits**

*Contributions of the thesis author:*

Development and testing of the algorithm, analysis of results, figure generation and writing of the manuscript.

# A Predicted Connectome of the Neocortical Microcircuitry

Michael W. Reimann<sup>1</sup>, Eilif Muller<sup>1</sup>, Srikanth Ramaswamy<sup>1</sup> & Henry Markram<sup>1,†</sup>

<sup>1</sup> Blue Brain Project, Brain Mind Institute, Ecole Polytechnique Fédérale de Lausanne (EPFL),  
1015 Lausanne, Switzerland

<sup>†</sup> Corresponding author

Henry Markram

Blue Brain Project, Brain Mind Institute  
Ecole Polytechnique Fédérale de Lausanne (EPFL),  
1015 Lausanne, Switzerland  
Email: [henry.markram@epfl.ch](mailto:henry.markram@epfl.ch)

For submission to Nature Neuroscience

## 6.1 Abstract

We applied a data-driven algorithmic strategy to synaptically connect neurons in a model reconstruction of the neocortical microcircuit containing 31'000 neurons in 55 main morphological classes and obtained a first prediction of the complete connectome of the microcircuit. We identified 7 million connections that form 35 million synapses (65% excitatory, 35% inhibitory) in 2,258 pathways between morphologically different neurons. The predicted connectome into that the morphological diversity of inhibitory neuron types alone does not lead to target specificity of connections but that it leads to specificity of synaptic coverage of dendrites. Finally, we observed a power law of pathway strength and the emergence of a common-neighbor connectivity principle paralleling experimental findings in a majority of m-types.

## 6.2 Introduction

The connectome is a key determinant of the computational capability and capacity of the brain [Chklovskii et al., 2004, Hofer et al., 2009]. A neocortical microcircuit of neurons has been defined anatomically as the smallest volume of tissue where all the different morphologies of neurons can interact (all layers, about  $420\mu m$  in diameter) and contains 31,000 neurons, 55 morphological types (m-types) and 207 morpho-electrical types (me-types) [Markram, 2014]. This indicates that there are potentially 3,025 morphology specific pathways and 42'127 morpho-electrical pathways. Since the anatomical properties of only 25 of the morphology specific pathways have been characterized experimentally thus far, a data-driven algorithmic strategy was developed to predict the connectivity of the remaining pathways in the accompanying paper [Reimann et al., a]. The connectome algorithm implements a combination of statistical, multi-synaptic and plasticity principles and yields a first draft

map of all synapses formed between the neurons — the connectome of the microcircuit.

In this study, we present the predicted map of the connectome and some selected features. The connectome contains 35 million synapses formed between the neurons of the microcircuit (intrinsic synapses) in 7 million connections, forming 2,255 biologically viable synaptic pathways between morphologically different neurons, and 31'172 morpho-electrically specific pathways. The draft map allows first predictions of the pre-synaptic numbers and locations of the boutons and postsynaptic numbers and locations of synapses for all of these pathways. The space remaining on neurons after all intrinsic synapses are accounted for, allows prediction of the extrinsic input into the microcircuit.

Analysis of the connectome revealed a spectrum of novel properties and principles of neuronal connectivity: 1) The predicted connectivity reproduces the distance dependence of connection probabilities between the neurons, but not the hyper-reciprocity found experimentally [Perin et al., 2011], predicting that plasticity mechanisms drive hyper-reciprocity between nearest neighbors; 2) On the other hand, clusters of synaptically connected neurons — functional assemblies — found experimentally between layer 5 pyramidal neurons [Perin et al., 2011] were surprisingly reproduced in these same neurons, and were found to be ubiquitous amongst virtually all other morphological types of neurons in all layers, indicating that functional assemblies of neurons are originally geometrically prescribed; 3) The diverse set of axonal and dendritic morphologies do not seem to be exploited by neurons to form highly specific connections with other neurons, but rather to allow comprehensive coverage of synapses with significantly different domains of innervation, and; 4) The anatomical strength of synaptic pathways measured as the total number of synapses in the pathway follows a power law indicating that the connectome obeys scale invariance and universality and may reflect self-similarity and self-organized criticality.

## 6.3 Results

### Overview of the connectome

A set of connections between the same morphological types of neurons (m-types) is defined as a m-type specific synaptic pathway. With 55 main m-types, there are theoretically 3,025 synaptic pathways in the two week old rat neocortical microcircuit [Markram, 2014]. We found that 2,258 are biologically viable (Fig 6.1 a) in that they satisfy a set of anatomical constraints for connections to form between two neurons [Reimann et al., a] such as multi-synaptic connectivity (Fig 6.1 b1). For the remaining 767 potential pathways, the geometrical overlap was not extensive enough to reliably form connections with a sufficient number of synapses.

### Predicted anatomy of synaptic pathways

Of these 2,258 pathways, only the ones between thick-tufted pyramidal neurons in layer 5 (L5\_TTPC) has been comprehensively studied in terms of the number and locations of presynaptic boutons on the axon, number and location of postsynaptic synapses on the dendrites, soma and axon, and distant dependent connection probabilities while 24 others have been partly characterized (Fig 6.1 a; black circles) and the rest remain to be experimentally characterized (see [Reimann et al., a] for a list of characterized pathways and literature). A strategy to predict the connectome based on available biological data and principles of connectivity is therefore essential since it is rather unlikely that the remaining

pathways will be experimentally mapped and even more unlikely that such maps could be obtained across all ages, genders, strains, and brain regions. The algorithm that was developed provides a generic strategy to predict the connectome given any set of neurons. The algorithm reproduces the detailed anatomy of the characterized pathways with a high level of accuracy and predicts the detailed anatomy of the uncharacterized pathways. In addition to the mean number of synapses/connection (Fig 6.1 a) it predicts the full distribution of the number of synapses/connection (Fig 6.1 b2) as well as the fraction of appositions utilized to form functional synapses (Fig 6.1 b3).

The predicted connectome yields the full set of about 7 million connections than can now be analyzed individually in terms of the synapse locations, both on the pre-postsynaptic arbors and in euclidean space (Fig 6.2 a). Taking all connections participating in a pathway between two specific morphological types of neuron (m-type specific pathway) allows a comprehensive analysis of the anatomical properties of the pathway (Fig 6.2 b) including; 1) the distribution of branch order locations of synapses on the axon and dendrites (Fig 6.2 b1) or in Euclidian space (Fig 6.2 b2) providing a global overview of the innervation, 2) the distribution of the number of pre- and postsynaptic cells involved in the pathway (Fig 6.2 b3) providing an overview of the degree of convergence or divergence, 3) the fraction of total synapses involved in the pathway (Fig 6.2 b4, Fig S2) providing an overview of the relative contribution of the pathway in the connectome.

In addition, the precise location of efferent synapses on the axon can be used to predict the probability that a single bouton forms one or more synapses with different neurons. Electron microscopic studies have also reported more than one synapse formed by the same bouton onto different neurons (De-Felipe, unpublished data), but the prevalence of this phenomenon is not known. We found that the probability that a bouton forms two synapses is around 20% measured by a separation less than  $1\mu m$  of the appositions onto the arbors of two different neurons (Fig S3). This rate of double synapses may of course change if functional mechanism intervene with the statistical probability of how an axon passes by the dendritic arbors.

Due to the large number of m-type specific pathways, each will be fully illustrated in a public, internet accessible portal. The portal also provides a means to analyze the 31,278 morpho-electrical specific pathways and to challenge and refine each pathway to perfection since the connectome algorithm is designed to incorporate new principles and exceptions to any principles as they become available [Kandel et al., 2013, Markram, 2014].

### Predicted extrinsic connectivity

Since we can account for all synapses formed between the neurons of the microcircuit (Fig 6.3 a) we can make a general prediction of the number of synapses formed by neurons beyond the microcircuit (extrinsic synapses). We obtained experimental measurements of spine densities in a number of studies not necessarily in the same region, species or age and calculated the mean to determine the expected total number of excitatory synapses for each neuron (Fig 6.3 b, red dashed line). Assuming one excitatory synapse per spine, the free space on the dendrites indicates the number of extrinsic synapses (see methods). Fig 6.3 b provides the prediction of the average density of extrinsic synapses on the dendrites of the individual m-types. This method predicts 127 million extrinsic synapses making up 80% of all synapses. The layer dependent fractions of extrinsic synapses have been reported [Markram, 2014] and in principle the locations can be obtained through the portal.

### Predicted connection probabilities

The connectome algorithm predicts the connection probabilities ( $C_p$ ) between all the neurons [Markram, 2014, Reimann et al., a] (Fig 6.4). Fig 6.4 a displays the matrix of  $C_p$  while Fig 6.4 b displays the number of neurons in each m-type as well as the  $C_p$ . Experiments rarely control adequately for the distances and orientation between neurons and therefore obtain an average  $C_p$  across a range of distances which produce highly unreliable estimates [Reimann et al., a]. Nevertheless, the overall prediction matches reported  $C_p$  values significantly (see Reimann et al. [a]). The predicted connectome now allows estimates of  $C_p$  for any distance with an unbiased orientation (Fig S1). The overall trend of  $C_p$  in the microcircuit is that the values are highest within layers and still higher between like m-types (Fig 6.4), consistent with a trend found in experimental studies [Brown and Hestrin, 2009]. The average  $C_p$  for all connections in the microcircuit within  $100\mu\text{m}$  is 6.5%. While the distance-dependent unidirectional  $C_p$  profile is reproduced, the well-established hyper-reciprocity reported for the L5\_TTPC [Perin et al., 2011] and other cells [Song et al., 2005, Holmgren et al., 2003] is not reproduced by the connectome algorithm (Fig S4) and we therefore predict that functional mechanisms, such as microcircuit plasticity, or developmental mechanisms, such two cells arising from common progenitors, determine hyper-reciprocity.

### Predicted synaptic assemblies

Higher order clusters of synaptically connected neurons have been experimentally revealed by simultaneously patching up to 12 L5\_PC cells [Perin et al., 2011]. A rule was found that allowed calculation of  $C_p$  between any two neurons;  $C_p$  increases with the number of common neighbours between cells over what is expected from a random network. A common neighbour of a pair of cell is defined as a third cell connected to both of them. A high number of common neighbours indicates clustering of connectivity; i.e. a partial segregation of the network into a number of tightly interconnected functional assemblies.

We found that by sampling the connected microcircuit in the same way in which the experimental patch recordings were obtained (number and location of recorded sets of neurons), the predicted relationship between  $C_p$  and the number of common neighbours matched the biological data (Fig 6.5 a). The number of pairs with more than 2 common neighbours in the sampled sub-networks of 8-12 cells is more than 10 times the expected value in a random network with the same overall  $C_p$ . The  $C_p$  increases from 0.1 for no common neighbours to 0.24 for three common neighbours, almost exactly mirroring what was found in the experiments (Fig 6.5 b).

The predicted connectome allows testing the various hypotheses underlying the common neighbour rule. While experiments are limited with respect to the number of cell pairs that can be sampled, the connected microcircuit allowed us to analyze the full connectivity of over 4300 L5\_TTPCs (more than 16 million pairs) across a range of distances. To quantify the increase in  $C_p$  for higher numbers of common neighbours, we analyzed connected and unconnected cell pairs separately, because Bayes Theorem dictates that a higher  $C_p$  for high numbers of common neighbours conversely means a higher mean number of common neighbours for connected cell pairs.

To test the various hypotheses, we compared the results to random networks created by different rules; 1) A random network with the same distance dependent  $C_p$  as in the reconstruction. 2. A network where, in addition to conserving the distance dependent  $C_p$ , the number of outgoing connections of each cell is held constant, but the recipients of the connections are chosen randomly from within the same distance bins.

The first hypothesis is that the common neighbour rule can be explained by the distance-dependent  $C_p$  alone. If two cells are close to each other, not only are they more likely to be connected, but also both are more likely to be connected to other close neighbours, i.e. they have graph-theoretical common neighbours mainly because they are neighbours in euclidean space. The profile of the number of common neighbours is highly distance-dependent (Fig 6.5 c; solid lines), which is expected, but the number of common neighbours for connected pairs is also higher than for unconnected pairs across all distances (green vs grey line for the reconstruction). This is a feature that a random network with the same distance-dependent  $C_p$  can not exhibit (dashed green and grey lines with asterisk marks overlaid) and the number of common neighbours is well below that of the reconstruction. A random network with distant-dependent  $C_p$  can therefore yield some tendency to exhibit the common neighbour rule, but not even close to the extent found in the reconstruction.

The second hypothesis is that the common neighbour rule can be explained by the presence of super-connected cells (i.e. cell with a much higher  $C_p$  than the rest). The presence of any super-connectors would increase the number of common neighbours and the  $C_p$  and therefore establish a dependence of the  $C_p$  on the number of common neighbours. We randomized the connectivity in the reconstructed microcircuit but preserved the distance-dependent  $C_p$  and the number of outgoing connections of each cell thus retaining any potential super-connectors in the network (see methods). Indeed, in this randomized network, we found an increased number of common neighbours for connected pairs. However, the effect is weaker than in reconstructed network and once more the overall number of common neighbours is lower in the random network than in the original reconstruction for distances up to  $250\mu m$  (unconnected pairs) or for all distances (connected pairs) (Fig 6.5 c, x-marked dashed lines). We also performed the same test preserving the number of incoming instead of outgoing connections and found very similar results (not shown). This indicates the while some cells are strong connectors, their presence alone does not explain the common neighbour rule.

The third and remaining hypothesis is that the common neighbour rule arises during the pruning of appositions. We first tested whether the common neighbour rule was expressed before the pruning was applied. We therefore examined the apposition-based connectome with the same method (Fig 6.5 d), and did find an increased number of common neighbours for connected pairs. However, the ratio of the mean number of common neighbours of connected vs all pairs at all distances was only 1.15 before the algorithm was applied (i.e. pure apposition-based connectivity) compared to 1.55 after (i.e. predicted synaptic connectivity). The number of common neighbours in apposition-based connectivity was also only marginally higher than in randomized apposition-based connectivity that preserved distance-dependence and number of connected cells. This indicates that a combination of the super-connector effect and the distance dependence can fully explain the slight common neighbour bias in apposition-based connectivity, but no longer after pruning. The pruning as described in [Reimann et al., a] therefore explains the common neighbour rule.

As an overall measure of the effect of the common-neighbour rule, we defined the common-neighbour bias as the ratio of the mean number of common neighbours of connected vs all pairs. Analyzing the data of [Perin et al., 2011] in this way led to a factor of 1.6 (Fig 6.5 e). This factor was exceeded for connectivity between 24 of 55 m-types and significantly greater than in a random networks for 36 m-types. The m-types that did not follow the common neighbour rule were those with an overall connectivity that is too low to give rise to a significant number of common neighbours. The common-neighbour rule is therefore a ubiquitous feature of most neocortical neurons.

### Morphological diversity does not enable connection specificity

We have shown examples of an analysis of synapse fractions in a pathway, i.e. the percentage of synapses that a given pathway contributes to the total number of synapses on the pre- or postsynaptic m-type (Fig 6.2 a4, Fig S2). This is a measure of the degree of specificity of the connections to or from a m-type. For example, one type might form connections predominantly on one particular m-type with high specificity, another one might connect to all types more equally. As the predicted connectome begins with the set of incidental axo-dendritic overlap [Hill et al., 2012, Reimann et al., a], such specificity would be tightly linked to any specificity in the morphology of neurons (i.e. the axonal or dendritic arborizations). In fact, specific m-type targeting might provide an answer to the question as to why we find such a wide variety of different morphologies [Stepanyants et al., 2004, DeFelipe et al., 2013].

To test this hypothesis, we went beyond the fraction of synapses in a particular pathway and calculated the probability distribution of m-types in the pre- and postsynaptic populations of all m-types in 7 full microcircuits, each containing 31,000 cells (Fig 6.6). That is, we calculated for each m-type ( $m_i$ ) the probabilities that a randomly picked pre-/postsynaptic cell ( $c$ ) is of a particular m-type ( $m_x$ ):

$P_{pre}(M(c) = m_x | M_i)$  and  $P_{post}(M(c) = m_x | M_i)$  respectively, where  $M$  denotes a function returning the m-type of a cell. We first calculated this distribution for each cell, then averaged over the cells of a certain m-type. Examples of postsynaptic distributions can be found in Fig 6.6 a. The distributions peak for excitatory neurons because of their higher numbers present (see Markram [2014]). We therefore normalized the distribution with the number of cells in a given m-type, thereby eliminating the bias towards excitatory neurons (Fig 6.6 b). The two exemplary m-types (L4\_MC, L5\_TTPC2) differ substantially in the distribution of the postsynaptic m-types of their efferent synapses.

We see that for example L4\_MCs have a tendency to connect to L4 PCs that is almost three times that of connections onto L5\_TTPC2s, but conversely they are only half as likely to connect to L6\_BPCs. To quantify the difference in such distributions, we developed an information theoretical distance measure. The distance was defined as the mutual information between the probability distributions of pre and postsynaptic m-types. i.e. how much do we learn about the m-type of a cell by revealing the m-type of a cell pre- or postsynaptically connected to it (see methods). If morphological diversity leads to specific connectivity, one would expect a large amount of information would be gained while in a uniform randomly connected network, no information would be gained.

To obtain a relative specificity for each m-type we measured the distance between the pre- or postsynaptic distribution of an m-type from the overall distribution for all 31,000 cells in the network (Fig 6.6 c). This provides a relative connection specificity measure for the axons (red, presynaptic specificity) and dendrites (blue, postsynaptic specificity) of each m-type. This measure revealed a high level of connection specificity for all m-types with the highest input and output specificity in layer 1 and a gradient of increasing output specificity and decreased input specificity with cortical depth. Layers 1-3 therefore get their specificity mainly from their inputs and Layers 5-6 mainly from their outputs.

We then analyzed the input/output specificity relative to the neurons only in the same layer and found that while the trends identified above remain, the specificity dropped significantly. It is therefore the laminar structure and not the morphological diversity that confers most of the connection specificity.

Finally, we calculated the whole matrix of pairwise distances for all  $55 \times 55 = 3,025$  pairs of m-types. We calculated a phenetic tree from the matrix of pairwise distances using established methods (sequential neighbor joining, see [Saitou and Nei, 1987]) as a novel way of visualizing the relations between m-types (Fig 6.6 d). The tree revealed large distances between layers, but almost none within a layer, further demonstrating that the laminar structure of the cortex adds to connection specificity (Fig 6.6 e). This



does not exclude the possibility that individual cells of an m-type display a large degree of specificity, nor a specificity imposed by molecular mechanisms such as in the case of Chandelier cells [Somogyi, 1977, Somogyi et al., 1982, Howard et al., 2005].

### Morphological diversity enables domain specific synaptic innervation

A characteristic of the neocortex is that inhibitory neurons, which occupy the smallest fraction of the cells, are the most morphologically diverse. The microcircuit reconstruction defines 42 different inhibitory types compared to only 13 excitatory types [Markram, 2014] although in total, only between 10 and 30% of neurons are inhibitory [Meyer et al., 2011, DeFelipe et al., 2002]. It is known that the typical arbours of axonal trees of interneurons can lead to synapses forming on different parts of the postsynaptic morphology [Lübke, 2003, Staiger et al., 2000, Hill et al., 2012], for example Martinotti Cells (MCs) are known to be targeting the distal parts of a pyramidal cells dendritic tree, Basket Cells (BCs) the proximal parts [Markram et al., 1997, Wang, 2002]. This targeting can have significant functional consequences. For example, inhibitory synaptic conductance, in addition to hyperpolarizing the cell, leads to a local decrease in input resistance, making nearby excitatory synapses temporarily less effective [Gidon and Segev, 2012]. Such local synaptic interactions — in addition to other interactions occurring in active dendrites [Koch and Segev, 2000, Hausser, 2000, Euler, 2001] — may suggest an alternative hypothesis for inhibitory morphological diversity: that it leads to differential innervation of domains of the postsynaptic neuron and hence different functions. Simply measuring the synapse densities from exemplary inhibitory m-types already reveals larger difference with L5\_LBC synapses largely restricted around somata, L5\_MCs distributed across most of the dendritic arbor, and L1\_NGCs restricted to the apical tuft (Fig 6.7 a). There is virtually no overlap between inhibition from Layer 1 and L5 BCs.

To rigorously test the hypothesis we assessed whether the different inhibitory innervation profiles are significantly different using a variant of the distance measure established above. We performed this analysis on the L5\_TTPCs cells because they receive input from virtually all type of inhibitory neurons. We calculated the pairwise differences between inhibitory innervation profiles (Fig 6.7 b, see methods) revealing four clear clusters of inhibitory innervation: Chandelier Cells (ChCs), Layer 1, Basket Cells in Layer 2/3 (L23\_BC) and the rest. Arguably, the latter cluster could be split further. The differences between Layer 1 inhibition and the rest or Chandelier Cell inhibition and the rest approach 1 bit, the theoretical maximum. In the case of ChCs this is purely a consequence of the connectome derivation, where appositions on the axon initial segment are selectively permitted and not a consequence of its specific axonal arborization. We once more converted the distances into a phenetic tree (Fig 6.7 c), as described above. Unlike for m-type targeting, the tree no longer simply recreates the laminar structure, instead clusters emerge with a subset of m-types within a layer or spanning several layers.

We then determined the overall specificity for each m-type (Fig 6.7 d) as before, which revealed highest innervation specificity for Layer 1 cells and ChCs and generally a high specificity for different types of Basket Cells and even some dendritic targeting cells. Martinotti cells for example are highly non-specific when compared to the overall distribution indicating that they target most of the dendritic arbor.

Overall there is higher degree of specificity for domain targeting as compared to m-type targeting ( $0.34 \pm 0.06$  against  $0.29 \pm 0.05$ ). This measure only reflects the specificity onto one m-type in one layer and adding other types can only increase the domain targeting specificity.

### A power law governs pathway strength

The anatomical strength of a synaptic pathway rests on both the  $C_p$  (determines the number of connections for a given cell density) and the average number of synapses/connection. We therefore examined the connectivity in terms of the mean number of synapses per pair of neurons, which is equivalent to the product of the  $C_p$  and the mean number of synapses per connection (Fig 6.8 a). Fig 6.8 b displays the number of neurons in each m-type as well as the anatomical strength. We converted the anatomical strength into a distance measure between m-types proportional to the inverse of the sum of strengths in both directions, i.e. the larger the number of synapses/pair in either direction, the closer a pair of m-types is placed to each other. We calculated a phenetic tree from the matrix of pairwise distances as described above (Fig 6.8 c, see methods). We found the root of the tree is formed by the L5 PCs and the base mainly centered around m-types in layers 4 and 5, with layer 6 sitting on a separate branch and layer 2/3 along with layer 1 on another branch.

Most of the 2,258 anatomically viable pathways are characterized by extremely low  $C_p$  and/or synapse numbers. In other words, most pathways had an anatomical strength near 0 (Fig 6.8 d). Consequently, we defined an anatomically relevant pathway as one which has an anatomical strength higher than 5% of the strongest pathway; 522 pathways fulfilled that criterion (Fig 6.8 d).

We also found that the anatomical strength of pathways follows a power law indicated by a linear plot of quantiles of the log transformed data against corresponding quantiles of an exponential distribution (Fig 6.8 d, inset). Remarkably, we found an exponent of the power law (maximum likelihood) of exactly -1, i.e. the number of pathways in a bin was proportional to the inverse of the anatomical strength of that bin. This indicates that the product of pathway strength and number is therefore constant (i.e. all the weakest pathways together are as strong as the strongest pathways together). Such a power law is an indication of a small-world property of a network that has been hypothesized to characterize neural circuits before [Sporns and Zwi, 2004, Bassett and Bullmore, 2006], but this is the first time it has been quantitatively predicted in a full cortical microcircuit.

## 6.4 Discussion

The morphological variability, and even more so the morpho-electrical variability of neocortical microcircuits produce a daunting number of potential pathways, each one potentially with their own characteristics. Considering the experimental work required to characterize a single pathway (currently requires paired recordings and anatomical reconstruction), an algorithmic strategy is essential to predictively map connectome. The predicted connectome generates first estimates of synapse numbers, fractions, and locations for all pathways given any set of neurons. These estimates have been demonstrated to be largely invariant with respect to the exact morphologies chosen and their exact locations as long as the inter-laminar architecture remains intact [Reimann et al., a]. The estimates are also robust against changes of touch distances, as long as they remain above a critical value around  $2\mu\text{m}$ .

While the connectome described is only a first draft, it guides future experiments to challenge and hence refine the predictions. Since the algorithmic strategy leverages multi-constraint principles, it is not anticipated that a large number of missing pathways will need to be mapped experimentally to converge on a final definitive connectome. To enable collaborative refinement, we have made the connectome and related tools available online.

### Functional assemblies are geometrically determined

It is generally accepted that connectivity is shaped by experience [Chklovskii et al., 2004, Hofer et al., 2009, Holtmaat and Svoboda, 2009, Wilbrecht et al., 2010]. Potentially even the wiring diagram of a microcircuit, i.e. the presence or absence of a connection between pairs of cells can be changed [Lamprecht and LeDoux, 2004, Neves et al., 2008, Chklovskii et al., 2004, Holtmaat and Svoboda, 2009]. Microcircuit plasticity could therefore form higher order connectivity features that can be described graph-theoretically [Sporns and Zwi, 2004, Bassett and Bullmore, 2006].

But do what degree are plasticity mechanisms needed to explain the emergence of these features? We have found that a higher order connectivity pattern of three or more cells emerges from reducing the set of axo-dendritic appositions via three simple filtering steps. Each of these steps is agnostic with respect to the emerging pattern, meaning the the pattern is also a consequence of cell morphological structure.

At the same time we found a comparatively simple pattern – increased reciprocal connectivity – that does not emerge that easily. While this does not rule out the possibility that a different filtering algorithm leads to greater reciprocal connectivity, it suggests that plasticity plays a crucial role in the emergence of this particular pattern.

In the context of the computational function of a microcircuit in the whole brain, plasticity will be even more important. Even matching the biological metrics, the model microcircuit will likely not be able to play a useful computational role, due to the large degree of randomness in pruning, in particular during the last step selecting a final wiring diagram from viable multi-synapse connections. A function can emerge only after subjecting the model to periods of plasticity. Still, the process of going through microcircuit plasticity can be thought of as an optimization problem: Find the wiring diagram that best solves a certain task. And it is well established that incremental optimization techniques have a higher success rate and converge faster, if one starts with a proposed solution close to the optimum. This means that a connectome derivation aiming to recreate biological data such as this is preferred even if plasticity is required to give it the final touch.

### The role of morphological diversity

The availability of detailed pathway information allowed us to evaluate to what extent the diversity in axonal and dendritic morphology enables neurons to form specific connections with other neurons, and the extent to which it allows domain-specific targeting. While other, so far uncharacterized mechanisms – such as molecular triggers for synapse formation – may increase specificity in one or both cases, we were able to evaluate to what degree the two types of specificity provide explanations for the large variety, especially of inhibitory m-types in neocortical microcircuits. We found very little information in the morphological identity about which neurons are connected within a given layer, but a significant amount of information across layers, suggesting the laminar structure and not morphological diversity is exploited to form specific connectivity. On the other hand, we found that morphological diversity contributes to domain specific targeting and together ensure comprehensive coverage of the neuron with inhibitory synapses.

## 6.5 Methods

### Prediction of extrinsic input

The amount of extrinsic input into the microcircuit was predicted in a microcircuit surrounded by 6 further microcircuits to maximize axonal density in its center. Next, the density of excitatory synapses onto cells in the center of the microcircuit was measured by first identifying all somata in a cylinder with radius  $50\mu m$  at the center and spanning all layers. For the identified cells, the total number of excitatory synapses onto dendrites divided by the total dendritic length yielded an estimate of the "intrinsic" spine density. By comparing the mean intrinsic spine density to biological estimates of total spine densities, we identified the missing fraction of excitatory input needed to increase the density to biological values. That fraction constitutes our estimate of extrinsic input.

### Generation of random and randomized networks

Random networks for the evaluation of common neighbour related hypotheses were generated in one of three ways. 1) A completely random network with a given connection probability  $P$  was generated by drawing random numbers between 0 and 1 for all  $N \cdot (N - 1)$  cell pairs. Only if the number was  $\leq P$  a connection was placed. 2) A network preserving the distance dependent connection probability of a given connectome was generated by first binning all cell pairs according to their inter-soma distance (bin size  $25\mu m$ ). For each bin connections were randomly placed or not as described above. 3) A given connectome was randomized preserving distance dependence and the number of efferent connections of each cell by first binning cell pairs as described above. Next, for each cell the recipients of all its efferent connections in all distance bins were randomly shuffled within a given distance bin. Similarly, the number of afferent connections could be preserved by shuffling the afferent connections.

### Distance measurements for m-type targeting and innervation patterns

#### Deriving structural innervation patterns

In order to obtain an average inhibitory innervation profile for a postsynaptic cell, we built a microcircuit containing a large number of copies of an exemplary L5\_TTPC2 morphology at different locations with different rotations. After deriving the connectome of the circuit, each copy will receive a slightly different, but biologically relevant inhibitory innervation profile and we can average across all of them to obtain the *typical structural inhibition profile of an L5\_TTPC2 neuron*.

#### Computing domain-specificity of an innervation profile

In order to quantify the specificity of inhibition or the difference between two innervation patterns, we developed an approach grounded in information theory. After normalization, an innervation pattern can be interpreted as probability distributions: The probability to find a randomly selected synapse at a given location. We define the divergence of two such profiles  $a$  and  $b$  as the mutual information between the profiles  $C$  and inhibitory type  $T$ :

$$I_{a,b}(C; T) = \sum_{0 \leq i < N, j \in \{a,b\}} P(C_i, T_j) \cdot \log_2 \left( \frac{P(C_i, T_j)}{P(C_i) \cdot P(T_j)} \right), \quad (6.5.1)$$

where  $C$  refers to a normalized innervation pattern as described above and  $T$  to an m-type. Similarly, we define the domain-specificity of an m-type as the mutual information between its profile and the profile derived from using *all* synapses of *all* types.

### Computing specificity of m-type targeting

We quantified the specificity of m-type targeting in a similar manner. We calculated for an m-type the probability distribution of the m-types of a randomly picked afferent or efferent synapse  $P(T_{post}(S) = T_x | T_{pre}(S) = T_j)$  or  $P(T_{pre}(S) = T_x | T_{post}(S) = T_j)$  respectively, where  $T_{post}(S)$  refers to the m-type of the postsynaptic cell of a synapse  $S$ ,  $T_{pre}(S)$  to the presynaptic m-type. Using the shorthand  $T_{post}^i$  for  $T_{post}(S) = T_i$ , the divergence is then defined as:

$$I_{a,b}(W; T) = \sum_{0 \leq i < N, j \in \{a,b\}} P(T_{post}^i, T_{pre}^j) \cdot \log_2 \left( \frac{P(T_{post}^i, T_{pre}^j)}{P(T_{pre}^j) \cdot P(T_{post}^i)} \right) \quad (6.5.2)$$

### Recreating a connectivity sampling experiment

In-vitro, connectivity is typically investigated by randomly sampling pairs of cells in slice of brain tissue and probing for the presence of a connection between them. A *connection probability* can then be expressed as the ratio of established connections to cell pairs investigated. This approach comes with methodological problems: Not only can the connectivity be altered by the slicing process [Stepanyants et al., 2009], but it leaves open the question how exactly the pairs are selected: Is it truly random with a uniform probability, or is the selection biased?

One possible bias lies in the distance between the somata. Few publications [Holmgren et al., 2003, Perin et al., 2011] account for it by calculating a distance-dependent connection probability, showing a clearly reduced probability for higher distances. Geometrically, the number of potential cell pairs increases with the square of the distance, the experimental data on the other hand [Holmgren et al., 2003] shows more sampled pairs for low distances. Another potential bias lies in the direction of the potential connection. With some morphology types, such as pyramidal cells having highly asymmetrical dendritic and axonal trees, it seems possible that the connectivity depends on the arrangement of the pair relative to an axis perpendicular to the layer boundaries, even within a layer.

Consequently, the actual connection probability in a model, i.e. the number of connections divided by the number of cell pairs, or even the actual distance dependent connection probability cannot be expected to reflect the results of in-vitro experiments. Therefore, we investigated connectivity by attempting to recreate the sampling of an in-vitro experiment. We used the coordinates of the patch pipettes of [Perin et al., 2011] by placing the 43 sets of  $8.7 \pm 2.7$  coordinates (mean distance:  $105 \mu m$ ) inside the model volume with a random offset and picked the cells of the morphology type under investigation closest to that location. When comparing to the literature, we expanded or contracted distances in the coordinate sets to match the mean soma distance, if that value was reported. Connectivity was then investigated for all  $\frac{N \cdot (N-1)}{2}$  pairs in a set. If pre- and postsynaptic morphology type of the pathway were different, we randomly picked half of the coordinates to belong to the presynaptic type, the other half to the postsynaptic.

From the sampled sets of cells we calculate a connection probability in the following way: If the publication we are comparing to lists a distance dependent connection probability profile, we compare the interpolated value at  $100\mu m$  to the connection probability of sampled pairs between  $90$  and  $110\mu m$ . If no distance dependent profile was published, we compare the listed number to the connection probability of all sampled pairs.

### Circular connectivity diagrams

Circular connectivity diagrams in Figures 3,4 and S1 were generated using Circos software [Krzywinski et al., 2009].

## 6.6 Figures, tables and legends

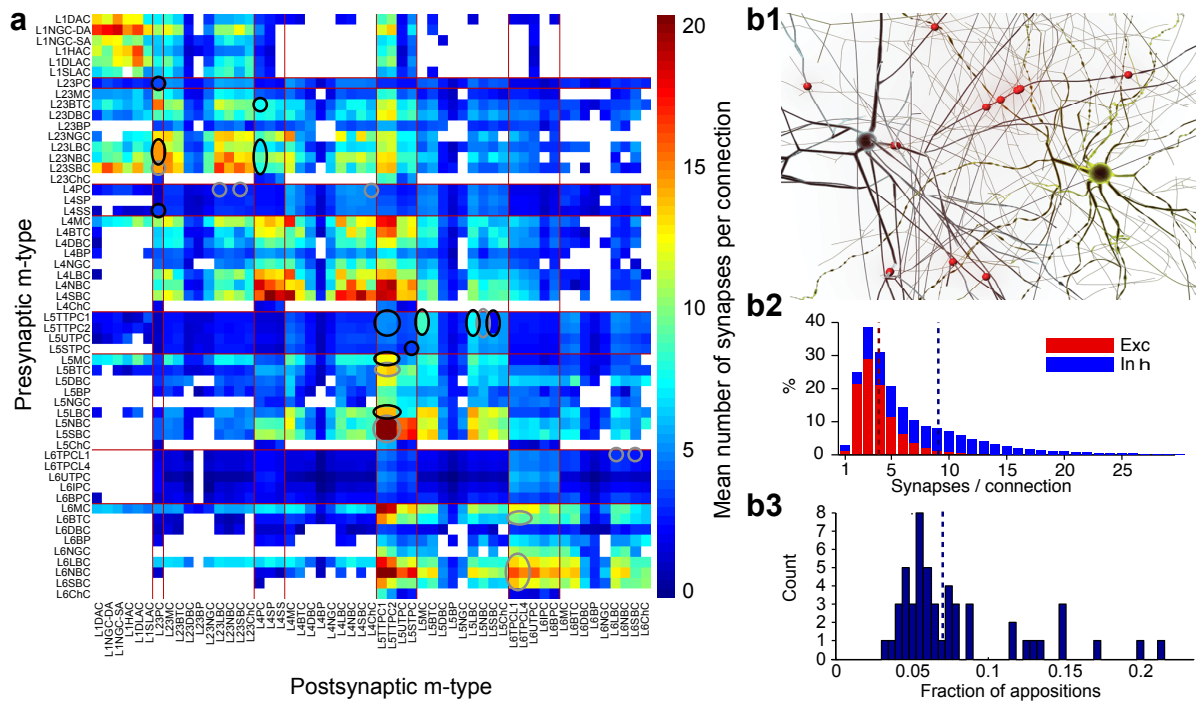


Figure 6.1 – Multi-synapse connections in the predicted connectome

(a) Mean number of synapses per connection for all 2258 m-type specific pathways. Pathways where the biological mean was used to constrain algorithm parameters are indicated by black circles. Red lines surround excitatory morphology types. White areas indicate the absence of a pathway (no connected pair in at least one of  $N=7$  modeled microcircuits). (b1) Example of a multi-synaptic connections emerging from axo-dendritic overlap. (b2) Emerging distribution of the number of synapses per connection in excitatory (red) and inhibitory (blue) pathways. (b3) Fraction of axonal appositions used for synapse placement in the 55 individual m-types.

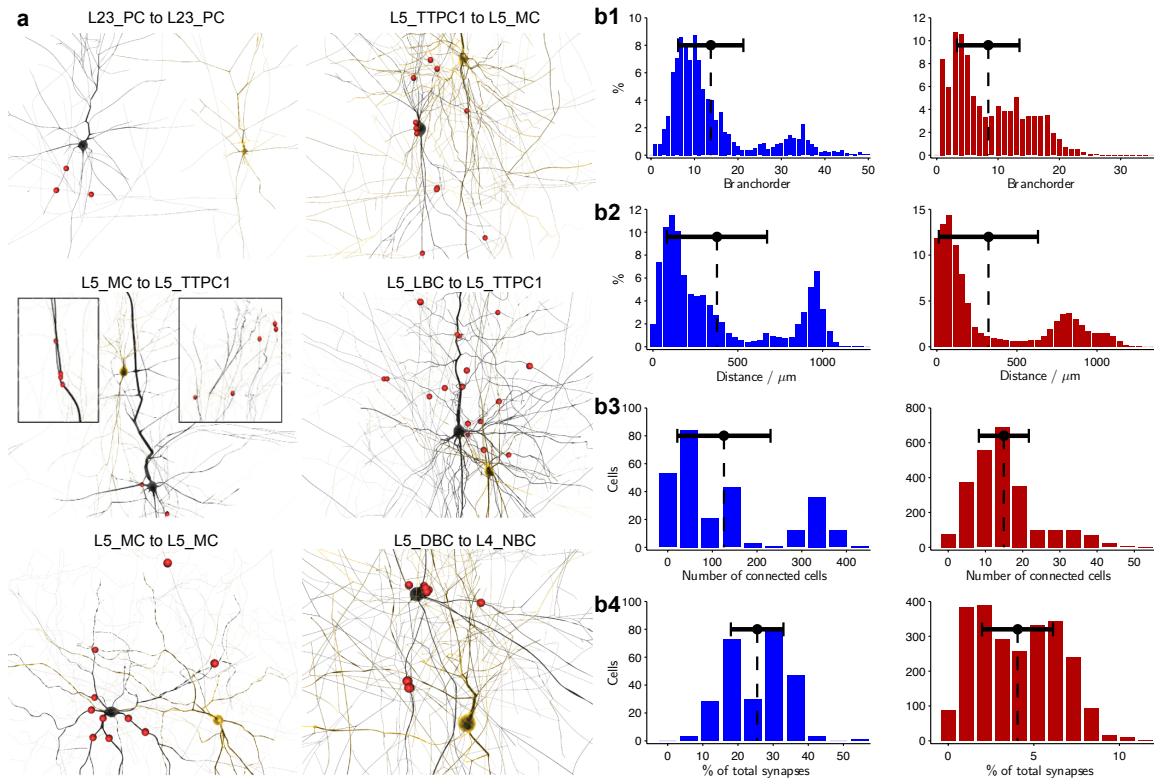


Figure 6.2 – An example of pathway specific connectivity metrics

(a) Examples of connected cell pairs in individual m-type specific pathways. Yellow: presynaptic cell, black: postsynaptic cell, red spheres: synaptic contacts. (b1-b4) Analysis of synapse locations and numbers in the L5\_MC to L5\_TTPC2 pathway. Left column / blue bars: analysis of axonal locations / on the presynaptic side. Right column / red bars: analysis of dendritic locations / on the postsynaptic side. (b1) Branchorder of synapse locations. (b2) Euclidean distance of the synapse from the soma of the pre- or postsynaptic cell. (b3) Number of cells of the post- / presynaptic m-type connected to a cell of the pre- / postsynaptic m-type. (b4) Percentage of all synapses that connect to / from the post- / presynaptic m-type.

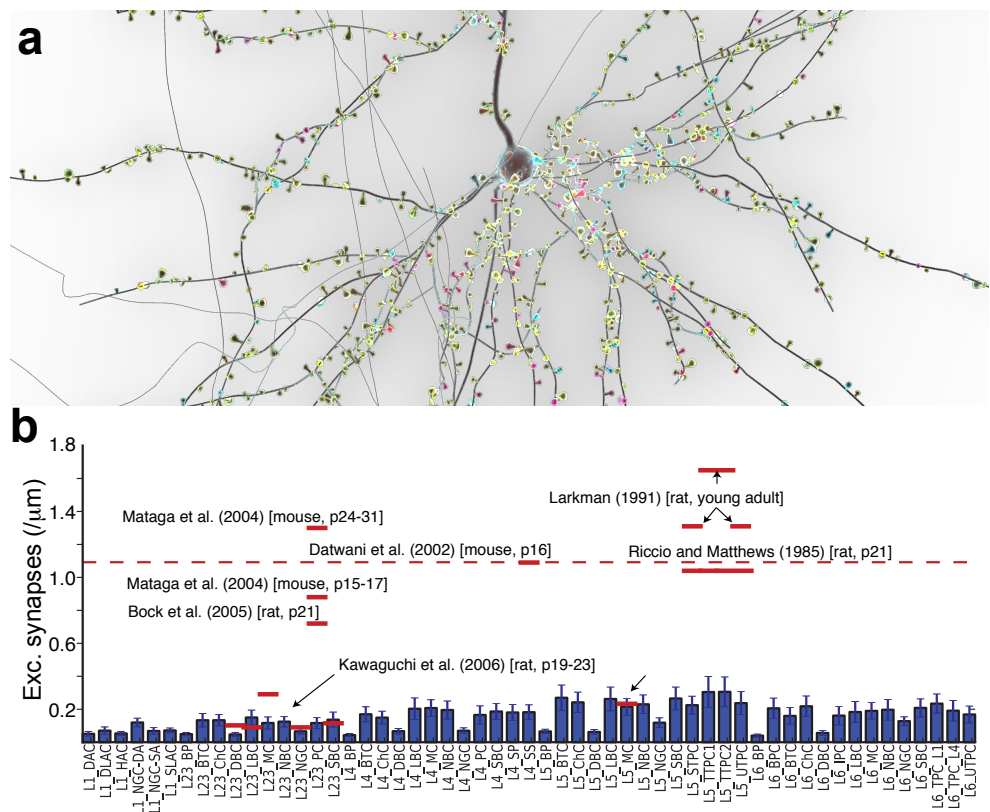


Figure 6.3 – Predicting external input

(a) An exemplary L5\_UTPC with all afferent synapses highlighted. Different colors indicate different presynaptic m-types. (b) Comparing the density of excitatory synapses across the entire dendritic tree for 55 m-types in the reconstructed connectome (blue bars) against biological data (red lines, data from: [Riccio and Matthews, 1985, Larkman, 1991, Datwani, 2002, Bock et al., 2004, Mataga et al., 2004, Kawaguchi, 2006]). The dashed line indicates the mean of the biological data, with the lower outliers excluded.



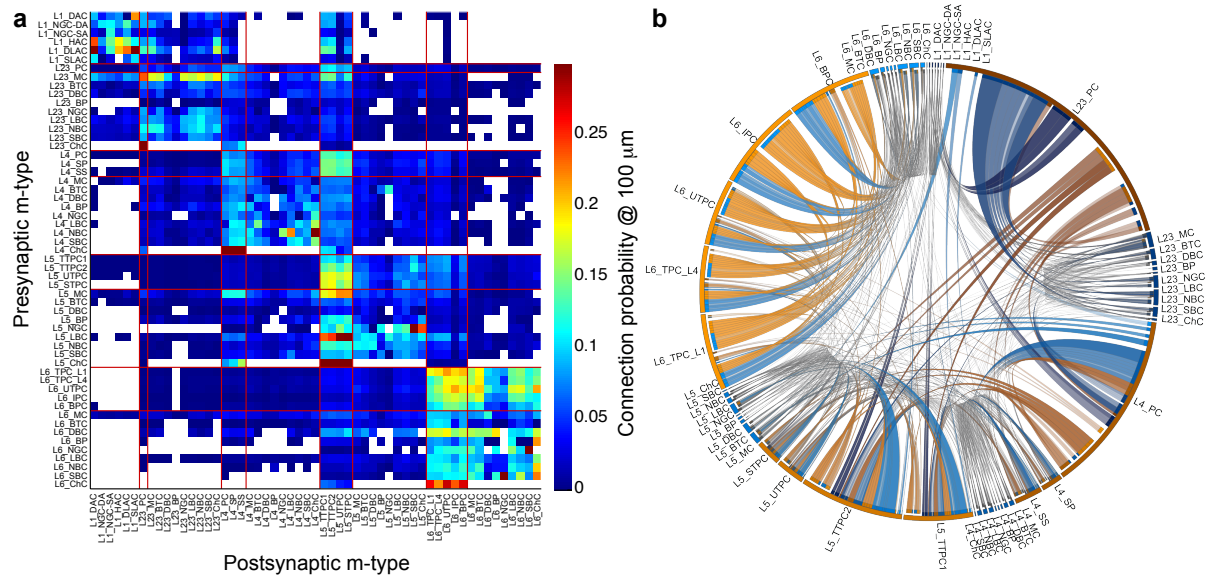


Figure 6.4 – Emerging connection probabilities

(a) Connection probability for pairs closer than  $100 \mu\text{m}$  for all 2258 m-type specific pathways. Red lines surround excitatory morphology types. White areas indicate the absence of a pathway (no connected pair in at least one of  $N=7$  modeled microcircuits). (b) Alternative visualization of the connection probabilities: The size of each sector of the circle is proportional to the number of cells in the m-type the sector corresponds to. Ribbons represent connections, with the width of ribbons connecting to an m-type proportional to the connection probability. For each m-type, afferent connections come clockwise before the efferent connections. Excitatory connections orange, inhibitory connections blue.

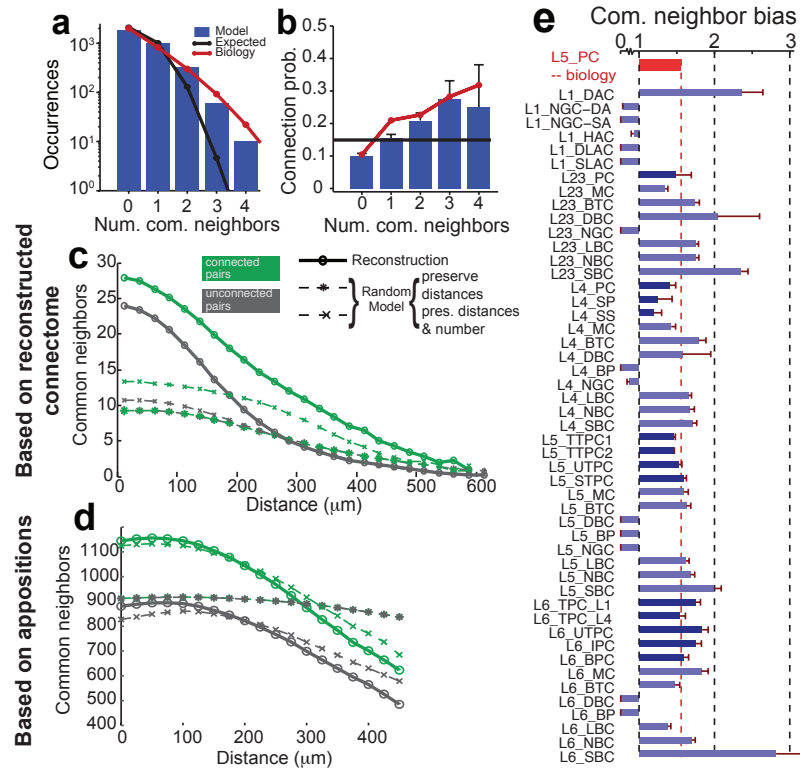


Figure 6.5 – Predicting the common neighbor rule for most pathways

A multi-patch experiment and analysis [Perin et al., 2011] was mimicked in silico using the reconstructed connectome. (a) Distribution of the number of common neighbors of L5\_TTPC pairs. Black line indicates relationship expected in a random network with independent uniform connection probability. (b) Connection probability vs the number of common neighbors of L5\_TTPC pairs. Black line as in (a). (c) The number of common neighbors between connected (green) and unconnected (grey) pairs sampled from a full network of 2450 L5\_TTPCs. Thick solid line indicates data from the reconstructed connectome; dashed line with asterisks data from a random network with the same distance dependent connection probability; dashed line with x marks the data from a random network that in addition to the distance dependent connection probability also conserves the number of outgoing connections of each cell. (d) As in (c) but for connectivity based on all appositions. (e) The common neighbor bias, i.e. the relative increase of the number of common neighbors for connected pairs over all pairs, for connections within a population. Only data for populations with more than 500 connections in total is shown. Red bar: biological value for L5\_PCs calculated from the data of [Perin et al., 2011].



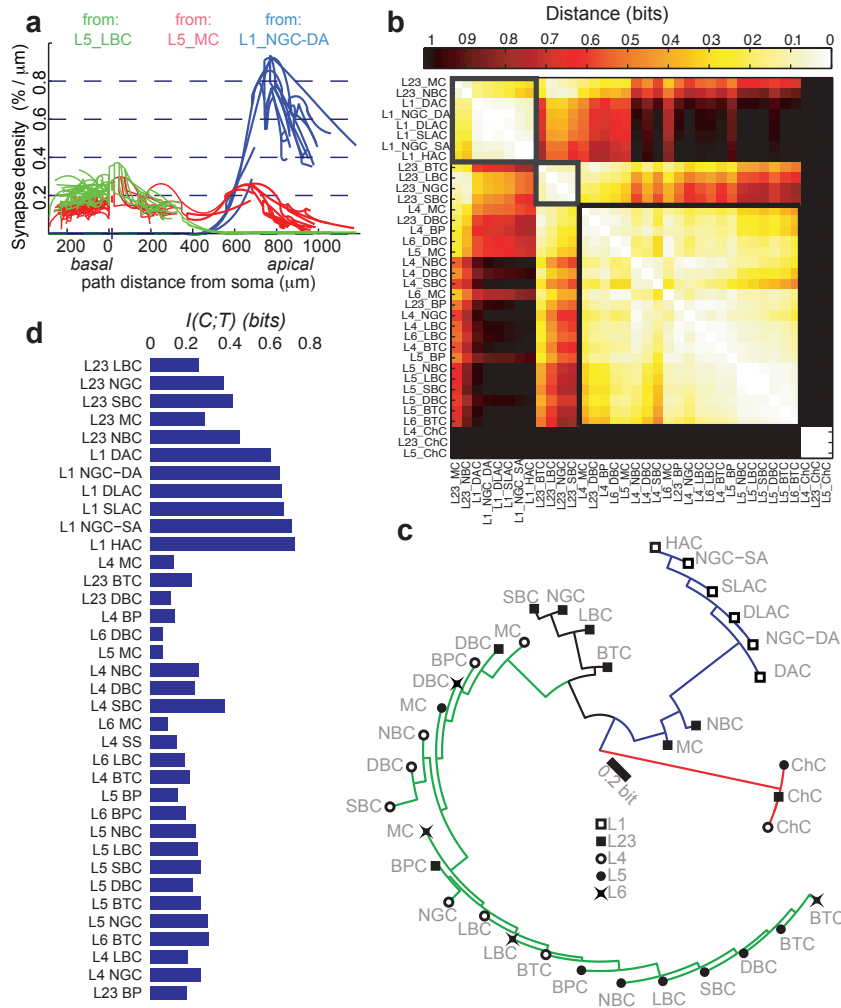
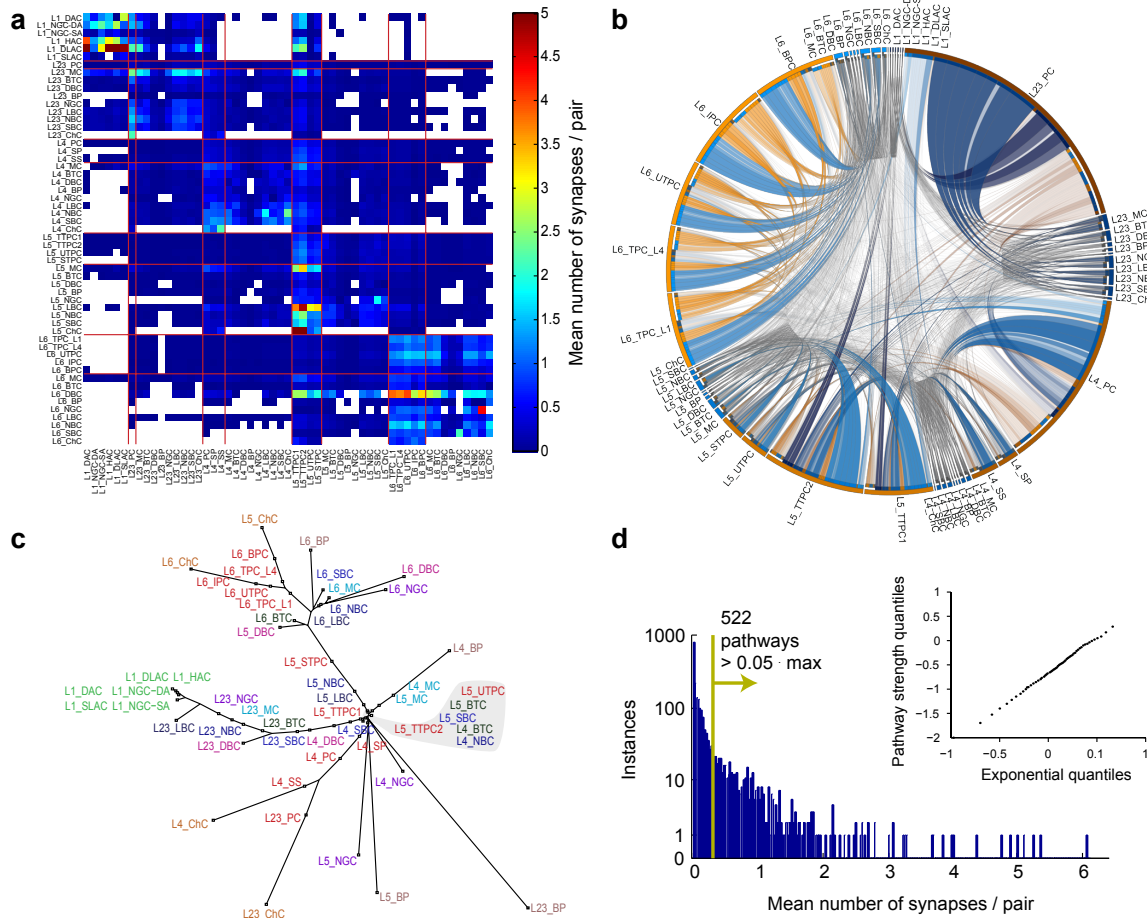


Figure 6.7 – Specificity of structural innervation patterns of inhibitory synapse types

(a) Mean structural coverage against path distance from the soma of the dendritic tree of an exemplary L5\_TTPC with synapses from three exemplary inhibitory cell types (blue: L1\_NGC-DA, red: L5\_MC, green: L5\_LBC). Profiles calculated from over 10,000 connections each. (b) Matrix indicating the distances, calculated as mutual information, between the structural inhibition profiles of different morphology types on L5\_TTPCs (see Methods). Four emerging clusters are outlined in black. (c) A phyletic tree reconstructed from the distances in (b). The distance between pairs is roughly proportional to the total path length along radial edges between two types/nodes (see scale bar). Accurate to within 5% due to distance averaging in the tree reconstruction process. (d) Mean specificity of layers (d1) and m-type groups (d2), calculated as the distance — defined as above — between their mean innervation profile and the mean profile of all types.



**Figure 6.8 – The relative structural strength of pathways follows a power law**

(a) The predicted mean number of synapses per cell pair, i.e. the product of the number of synapses per connection and the connection probability as a measure of structural pathway strength. Red lines surround excitatory morphology types. White areas indicate the absence of a pathway (no connected pair in at least one of  $N=7$  modeled microcircuits). (b) Visualization of the number of synapses per cell pair as in Fig 6.4 b. (c) The connectome visualized as a reconstructed tree. The tree was reconstructed from a distance matrix, calculated as the inverse of the mean number of synapses per cell pair, using a sequential neighbor joining algorithm. (d) Distribution of the number of synapses per cell pair in a semi-log plot. Yellow line indicated the cutoff used for the main matrix plot. The data follows a power law with an exponent of exactly -1.

## A Supplementary Material

### Supplementary figures

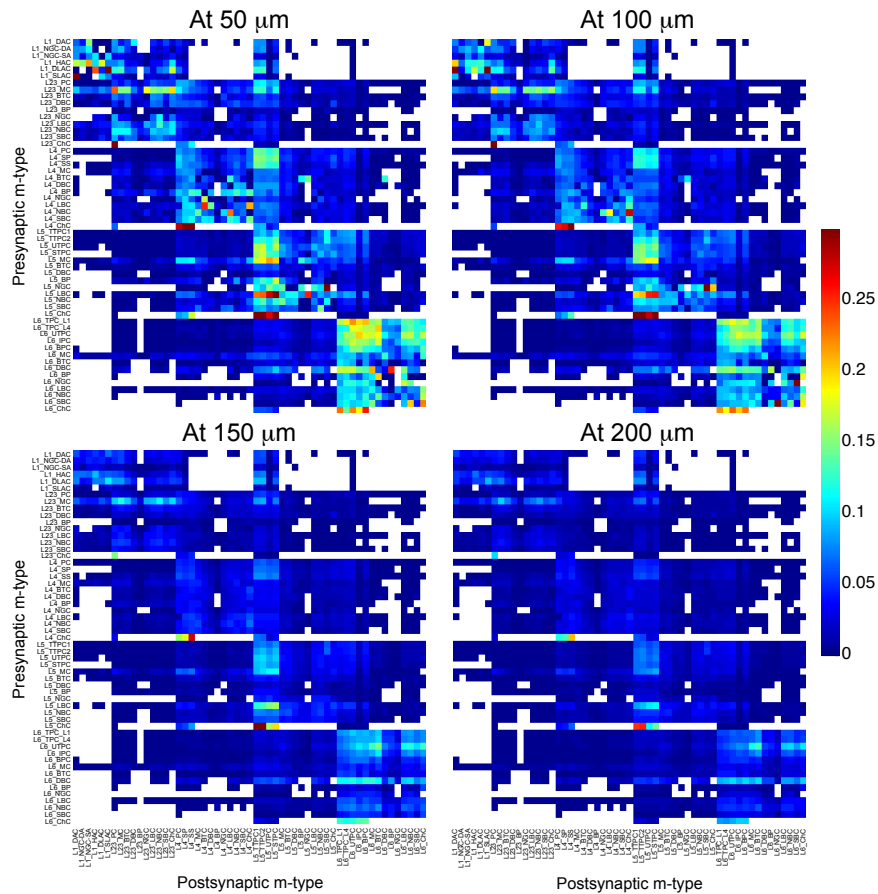


Figure S1 – Predicted connection probabilities at different distances

Overview of connection probabilities as in Fig 6.4 a, but for soma distances of (from top left to bottom right): 50 $\mu\text{m}$ , 100 $\mu\text{m}$ , 150 $\mu\text{m}$ , 200 $\mu\text{m}$ .

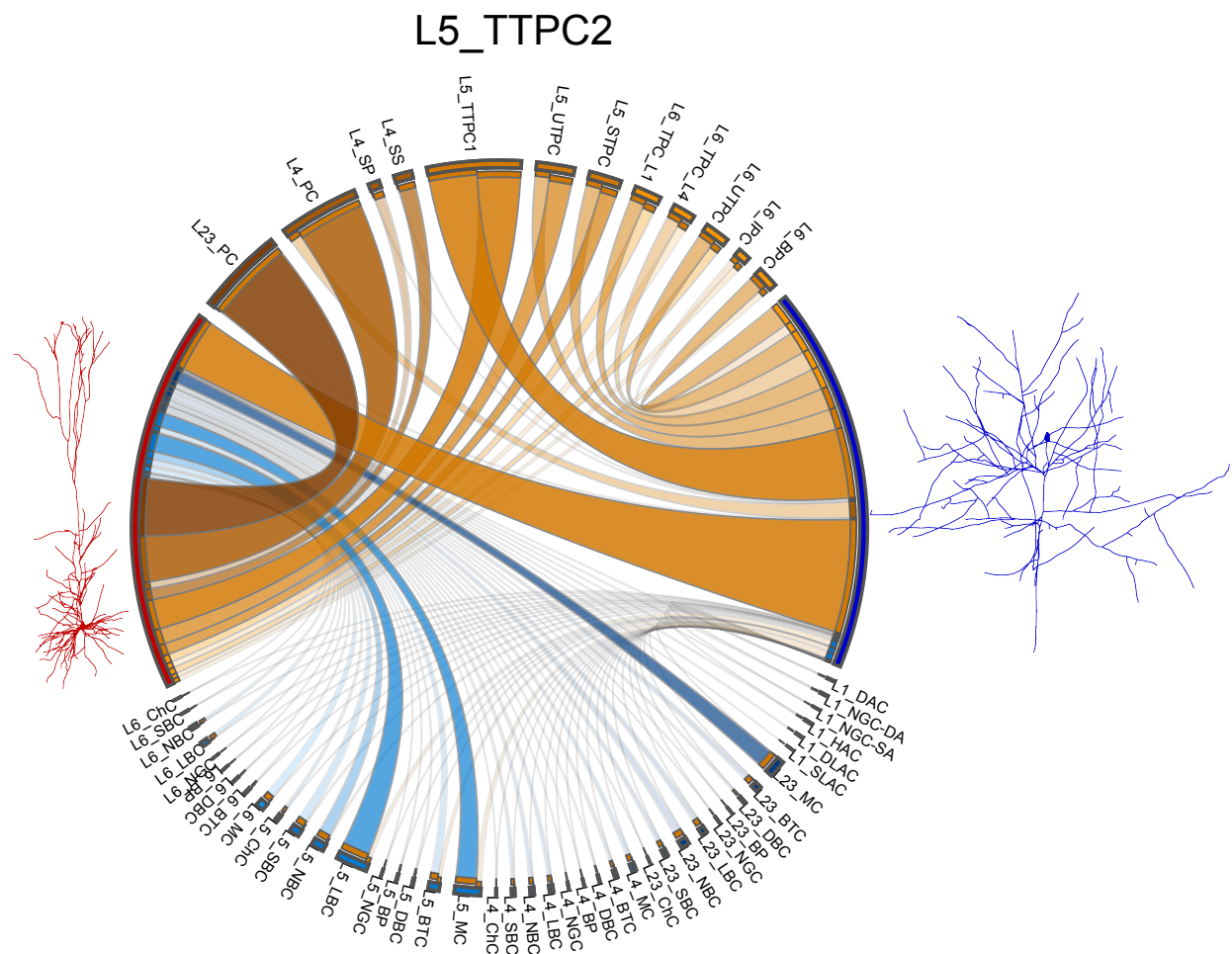


Figure S2 – Distribution of m-types of synaptic contacts to / from L5\_TTPC2 cells

Distribution of the m-types at the other end of synaptic contacts on L5\_TTPC2 dendrites (left side, indicated by exemplary dendritic morphology in red) and of contacts made by L5\_TTPC2 axons (right side, indicated by exemplary axonal morphology in blue). Width of ribbons is proportional to the total number of synapses. Blue ribbons indicate inhibition, orange ribbons excitation.

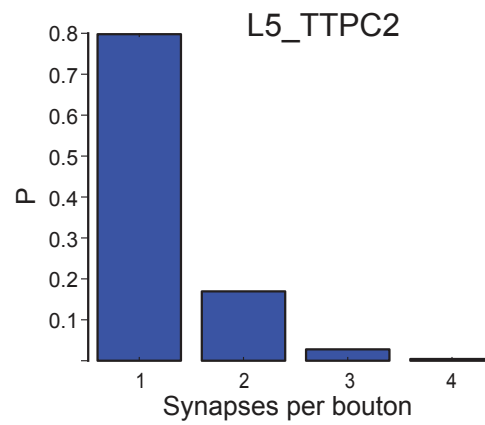


Figure S3 – **Distribution of the predicted number of efferent synapses per bouton**

Histogram of the number of efferent synapses per bouton under the assumption that 2 synapses, separated by less than  $1\mu m$  would form only one bouton on the axon.



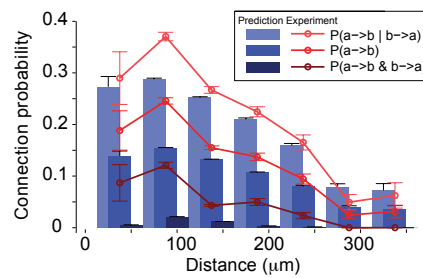


Figure S4 – **Emerging distance-dependent connection probabilities**

Comparison of the distance dependent connection probability of the L5\_TTPC to L5\_TTPC pathway in the model to biology (shades of blue: model, red: data from [Perin et al., 2011]). Three types of connection probability are shown with increasing lightness: Reciprocal connection probability (dark), unidirectional connection probability (medium) and undirected connection probability (light).

## Acknowledgments

Thanks to Mister James King for technical assistance. The financial support for CADMOS and the Blue Gene/P system is provided by the Canton of Geneva, Canton of Vaud, Hans Wilsdorf Foundation, Louis-Jeantet Foundation, University of Geneva, University of Lausanne and École Polytechnique Fédérale de Lausanne

## 7 In-silico measurements of extracellular potentials

### 7.0.1 Overview

The simulation of neural activity on a cellular level, typically employs *cable-theory* as its theoretical background [Hodgkin and Rushton, 1946, Hodgkin and Huxley, 1952, Koch and Segev, 1998]. Combining its view of dendrites as capacitive cables with Hodgkin-Huxley type models of active ion-channels, it allows the researcher to make accurate predictions about the membrane voltage traces of cells under different conditions. As in any good (efficient) model, only the scale and phenomena needed for an accurate predictions of the variable of interest (membrane voltage) are considered. Irrelevant variables are ignored or they are simplifying assumed to be constant and uniform.

In the case of the model of the Blue Brain project – as is the standard for such simulations [Holt and Koch, 1999, Hong et al., 2012, McTavish et al., 2012] and others – the extracellular space is treated as such: It is assumed to be an infinite space with a constant potential of 0. In order to get an in-silico estimate of extracellular potentials, the simulation had to be amended. As a theoretical backend, we chose volume conductor theory [Malmivuo and Plonsey, 1995, Plonsey, 1969, Stevens, 1966]. The theory simplifies the extracellular space to be a homogeneous, uniformly resistive medium, which will not take into account small variations in potential due to biomembranes and other obstructions. On a spatial scale  $> 1\mu\text{m}$  however, it provides accurate predictions.

### 7.0.2 Implementing a volume conductor based calculation of extracellular potentials

In particular, the method described in [Holt and Koch, 1999] was a prime candidate: It makes the calculation of extracellular potentials a separate step, leaving the the actual simulation unchanged. In order to calculate the extracellular potential, first the trans-membrane currents are recorded during a simulation with the usual assumption of zero extracellular potential. Then the potential is calculated using volume conductor theory which predicts that the potential is proportional to the sum of current sources with the weight being proportional to the distance from the simulated extracellular electrode.

Implementing this model in the architecture of the Blue Brain Model posed its own set of challenges. In particular, the immense scale of the model made availabel computing time and file size a serious constraint. This led to the four stage design of extracellular in-silico experiments and analysis,

## Chapter 7. In-silico measurements of extracellular potentials

Step	Description	Implementation	Hardware	Space	Time
1.	Cable theory based simulation	.hoc (NEURON)	$\geq 4096$ processors on a BG/P supercomputer	$\frac{1TB}{s}$	$\frac{1h}{s}$
2.	Calculate contributions of individual cells based on volume conductor theory	c++	Shared memory computer cluster	$\frac{1GB}{s \cdot N}$	$\frac{30mins}{s \cdot N}$
3.	Sum up the contributions of a population of interest	Python	regular PC	$\frac{40KB}{s \cdot N}$	$\frac{2mins}{s \cdot N}$
4.	Analyze traces	MATLAB	regular PC	-	$\leq 5$ mins

Table 7.1 – Overview of the steps in *in-silico* extracellular experiments. 's' refers to the number of simulated seconds, 'N' to the number of extracellular locations considered. Numbers are for a sampling frequency of 10 KHz. Frequency can be decreased or increased at will.

characterized by subsequently smaller file sizes and less powerful machines detailed in Table 7.1. In an alternative implementation we utilized the BG/P supercomputer to directly calculate extracellular potentials while running the cable theory simulation, thus merging steps 1 and 2. We found however, that keeping the cable theory and volume conductor theory based separate came with a number of practical advantages:

It allows us to calculate the potentials at any number of extracellular locations, even post-hoc. If the outcome of an analysis directed our attention at a particular location, it could be sampled with a higher resolution without re-running the cable-theory simulation. Also, keeping them separate made it easy to immediately take advantage of improvements in the simulator without first evaluating potential conflicts with the volume-conductor based code.

After a simulation, the extracellular potential at a time step is calculated as a weighted sum of the transmembrane currents of all cable compartments in that step. Weights are inversely proportional to the distance of a compartment, i.e. a part of neuron morphology, to the extracellular location sampled from. Since the distance is constant – we assume neither the "virtual electrode" nor the neurons are moving – it can be pre-calculated and re-used in each time step. This turn the whole calculation into a large matrix multiplication operation outlined in Fig 7.1:

$$V_e = C \cdot W, \quad (7.0.1)$$

where  $C$  is a  $T \times N$  matrix holding the membrane currents, with  $T$  being the number of time steps and  $N$  the number of compartments;  $W$  is a  $N \times 1$  matrix holding the weights; consequently  $V_e$  is a  $T \times 1$  matrix — the extracellular trace.

For reasons of practicality, we separated the process into two further steps (2 & 3 above): First calculate the *contribution of each cell* separately, then sum up the contribution of a cell population of interest. This allowed easy study of questions like which cell types contribute how much to the total signal under different conditions. Conceptually changes the weight matrix  $W$  to a  $N \times M$  matrix, where  $M$  is the number of cells. In each row of  $W$ , only the entries for compartments of one particular cell have values

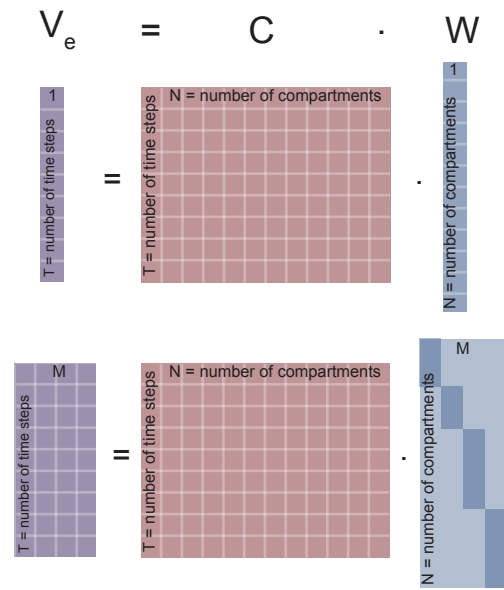


Figure 7.1 – Extracellular as a matrix multiplication

The calculation of extracellular potentials according to volume conductor theory can be conceptualized as a matrix multiplication of the matrix of membrane currents ( $C$ , one entry per time step ( $T$ ) and compartment ( $N$ )) with the matrix of distance dependent weights ( $W$ ). In the case of direct computation of the total potential  $W$  has one entry per time step ( $T$ , top). In the case of per-cell computation it has one entry per time step ( $T$ ) and neuron ( $M$ ). In the later case only one entry of each row of  $W$  has values  $\neq 0$  indicated slightly darker.

$\neq 0$ . This ensures that the sum of  $W$  along the second dimension and therefore the total extracellular potential is constant in both cases.

Using these methods, we obtained the insights outlined in the following two chapters.



# **8 A Biophysically Detailed Model of Neocortical Local Field Potentials Predicts the Critical Role of Active Membrane Currents**

*Contributions of the thesis author:*

Development and testing of the extracellular calculations; design, setup and running of neural simulation; analysis of results and figure generation.

# A detailed biophysical model of neocortical LFPs emphasizes the critical role of active membrane currents

Michael W. Reimann<sup>1,\*</sup>, Costas A. Anastassiou<sup>2,\*†</sup>, Rodrigo Perin<sup>1</sup>, Sean Hill<sup>1</sup>, Henry Markram<sup>1</sup> & Christof Koch<sup>2,3</sup>

<sup>1</sup> Blue Brain Project, Brain Mind Institute, Ecole Polytechnique Fédérale de Lausanne (EPFL), 1015 Lausanne, Switzerland

<sup>2</sup> Division of Biology, California Institute of Technology, 91125 Pasadena, California, U.S.A.

<sup>3</sup> Allen Institute for Brain Science, Seattle, Washington, U.S.A.

\* These authors contributed equally to the work.

† Corresponding author  
Costas A. Anastassiou

Division of Biology, California Institute of Technology  
1200 East California Boulevard, 91125 Pasadena, California, U.S.A.  
Tel: +1-626-626-395-8965  
Fax: +1-626-796-8876

Published in NEURON

## 8.1 Summary

Brain processing generates extracellular voltage fluctuations recorded as local field potentials (LFPs). While much has been reported about LFPs, they remain mysterious. Here we bridge the gap between intracellular and transmembrane processing at the single compartment/neuron level and LFPs through unique, biophysically faithful, large-scale simulations. We simulated the LFP in a model of the rodent cortical column composed of 12,000, fully reconstructed, multi-compartmental and spiking cortical layer 4 and 5 pyramidal neurons and basket cells, including millions of dendritic and somatic compartments with voltage- and ion-dependent currents, realistic connectivity and probabilistic AMPA, NMDA and GABA<sub>A</sub> synapses. We found that the LFP reflects local processing with a length scale that depends on synaptic, morphological and membrane properties. Active membrane conductances substantially impact LFPs and the spatiotemporal constellation of extracellular sinks and sources. Importantly, active dendritic processes and their binding to somatic processes critically shape the spatiotemporal profile of LFPs even at low frequencies ( $< 50$  Hz).

### Running title

Simulating the LFP

### Highlights

1. Large-scale model of realistic and interconnected neurons computing LFPs bottom-up
2. LFPs reflect local, within-layer neural processing
3. Active membrane conductances substantially impact LFPs and CSDs
4. Spike and spike-related events are reflected in the low bandwidths of the LFP



## **8.2 Introduction**

Extracellular voltage recordings ( $V_e$ ) – the voltage difference between a point in the extracellular space and a reference electrode – are the primary method of monitoring brain processing *in vivo*. Such recordings are high-pass filtered to isolate unit spiking activity. Slower  $V_e$ -fluctuations (typically <300 Hz) referred to as local field potentials (LFPs), reflect the summed electric activity of neurons and associated glia and provide experimental access to the spatiotemporal activity of afferent, associational and local operations [Buzsáki, 2004]. The relationship between electric activity of nerve and (presumably) glia cells and the LFP has remained mysterious (for a review, see [Buzsáki et al., 2012]). LFPs have traditionally been viewed as a reflection of cooperative postsynaptic activity [Mitzdorf, 1985, Lindén et al., 2011]. Yet, even when synaptic activity is blocked, neural populations can show emergent activity associated with large LFP deflections [Jefferys and Haas, 1982, Chrobak et al., 2000, Buzsáki, 2002] – the precise source of these fluctuations is not understood. What is clear is that nonsynaptic events can greatly affect the recorded LFP [Buzsáki et al., 2012, Chrobak et al., 2000, Anastassiou et al., 2010, 2011]. Moreover, other processes such as the spike afterpotential [Belluscio et al., 2012, Ray and Maunsell, 2011, Zanos et al., 2011, Schomburg et al., 2012] and intrinsic oscillatory membrane currents [Chrobak et al., 2000] also contribute to LFP-generation.

To what extent do such processes impact the LFP? To address this question manipulation of brain network activity and dissection of the individual LFP-contributors during various brain states is required. While relevant interventionist tools are becoming available [Cardin et al., 2009], biophysical modeling lends itself to such manipulation and dissection [Gold et al., 2006, Pettersen et al., 2008, Lindén et al., 2011, Schomburg et al., 2012]. In particular, models emulating realistic morphology, physiology and electric behavior as well as connectivity can provide useful insights into the origin of different kinds of extracellular signals since they allow precise control and access of all variables of interest. Here we use a large-scale model consisting of roughly 12,000 morphologically and functionally realistic neurons connected with each other based on rules that capture many aspects of measured connectivity [Perin et al., 2011, Hill et al., 2012]. In particular, we account for the presence of neocortical (somatosensory cortex, hindlimb area) excitatory (layer 4, L4, and layer 5, L5, pyramidal neurons) and inhibitory (L4 and L5 basket cells) neurons. We investigate the impact of relatively slow (approximately 1 Hz) external activity impinging on neurons and its effect on the resulting extracellular LFP-signature.

Such slow activity is relevant, for example, in the case of the most prominent of cortical LFP rhythms, slow wave activity (SWA, 0.1-1 Hz). SWA is observed both in humans [Achermann and Borbely, 1997] and animals [Steriade et al., 1993c,a,b, Destexhe et al., 1997] and involves large areas of the neocortex, along with various subcortical structures, that are synchronized into cyclical periods of global excitation followed by widespread silence [Steriade et al., 1993c,a,b, Contreras et al., 1996, Timofeev and Steriade, 1996, Destexhe et al., 1997, Stern et al., 1997, Lampl et al., 1999, Sanchez-Vives and McCormick, 2000, Timofeev et al., 2000, Shu et al., 2003, Dickson et al., 2003]. SWA is a defining characteristic of slow wave sleep (deep or non-REM sleep) but also occurs under anesthesia and in isolated cortical preparations. Neocortical cells discharge during the trough of the LFP and remain silent during the peak of the LFP recorded from deep layers of cortex. Active and silent periods of this slow oscillation are referred to as UP (high conductance) and DOWN (low conductance) states. This robust neocortical oscillation coordinates various other rhythms, including spindles and delta waves [Steriade et al., 1993c,a,b] and faster activity in the beta-gamma range [Mukovski et al., 2006].

Notably, while we do not attempt to emulate all biophysical details of SWA that involves a multitude of internal and external inputs, our large-scale, bottom-up biophysical model provides insights into the

origin and functionality of the LFP-signal, in the presence of active membrane conductances, realistic neural morphologies and network connectivity patterns.

### 8.3 Results

Based on hundreds of morphologically and functionally reconstructed neurons [Hay et al., 2011] (Fig. S1), the network model was built to capture many aspects of connectivity [Perin et al., 2011, Hill et al., 2012]. Neural membrane processing of every compartment of every neuron is reflected in  $V_e$  by superposing membrane current contributions from each neural compartment using the line source approximation [Holt and Koch, 1999]. That is,  $V_e$  at every location in extracellular space results from the linear summation of all membrane currents throughout the volume, scaled (to a first order inversely) by the distance to the current source. In the present study, we focus on how the microscopic currents across each membrane sum to give rise to the macroscopic LFP signal and neglect any contributions that the LFP, in turn, might have on the voltage across each membrane [Anastassiou et al., 2010, 2011, Jefferys, 1995].

Comparison between the extracellular action potential (EAP) traces elicited during simulated administration of brief (10 ms) intracellular somatic current injections (Fig. 8.1) and simulation as well as experimental observations [Gold et al., 2006, Anastassiou et al., in preparation] demonstrates that our single-neuron representations accurately reproduce the EAP waveform even though their reconstruction was optimized to reproduce intracellular rather than extracellular events [Hay et al., 2011]. In fact, accurate simulation of the EAP waveform can be used as an additional (and often stricter) measure for the quality of the reconstruction of a neuron, especially for perisomatic compartments [Gold et al., 2007].

The prevailing view is that the LFP primarily reflects postsynaptic currents for frequencies lower than approximately 100–150 Hz [Mitzdorf, 1985], which stems from the recognition that extracellular currents from many individual compartments must overlap in time to induce a measurable signal, with such overlap primarily occurring for synaptic events [Logothetis and Wandell, 2004]. This assumption, in turn, has motivated the study of LFPs using models that account for morphologically realistic but passive neurons with the statistics of postsynaptic currents and their spatial distribution emulating experimental observations. Yet, the presence of active conductances along the neural membrane is a highly nonlinear (either voltage- or ion-dependent) contributor of extracellular currents that cannot be accounted for via passive elements.

Fig. 8.2 shows the outcome of a large-scale simulation in which slow (1 Hz) external excitatory (*AMPA* and *NMDA*) and inhibitory (*GABA<sub>A</sub>*) synaptic activity impinged along both L4 and L5 pyramidal neurons (Fig. 8.2 a). For the active membrane simulation, this elicits spiking (Fig. 8.2 b), which, in turn, gives rise to local and global postsynaptic activity (Figs. 8.2 c, d). We define the depolarizing (hyperpolarizing) part of the external 1 Hz stimulation as UP (DOWN) state. The spike frequency (Fig. 8.2 d) of the different cell types considered in our simulations agrees with experimental observations in rodents during SWA [Sanchez-Vives and McCormick, 2000, Haider et al., 2006, Luczak et al., 2007, 2009, Fanselow and Connors, 2010].

## Chapter 8. A Biophysically Detailed Model of Neocortical Local Field Potentials Predicts the Critical Role of Active Membrane Currents

---

### LFP is not determined by postsynaptic currents alone

To understand the different components contributing to the LFP, we considered three scenarios, each of which has identical spatiotemporal postsynaptic currents (PSC). We define the PSC to be the postsynaptic membrane current flowing at the synapse in response to the synaptic-associated conductance change,  $I_{syn}(t) = g_{syn}(t)(V_m - V_{rev})$ , with  $g_{syn}$  being the synaptic conductance,  $V_m$  is the membrane potential, and  $V_{rev}$  is the reversal potential. In the first scenario, we only consider the LFP caused by these currents from the roughly 15 million synapses (Fig. 8.2 e) by ignoring all nonsynaptic currents in the calculation of the LFP. Thus, the simulation reflects purely PSC activity and only accounts for the way synapses are arranged in space in the absence of neurons. In Fig. 8.2 f, we replay the identical PSC input along every neuron as in the full simulation (Fig. 8.2 g) but, in a more complex scenario than in Fig. 8.2 e, compute the LFP contributed by synapses plus the morphologically accurate but passive cables. Finally, the last scenario includes synapses as well as the morphology supplemented by all active membrane conductances (Fig. 8.2 g).

If we compute the LFP only from synaptic conductances (Fig. 8.2 e), excitatory input (mainly along the basal dendrites) [Hill et al., 2012] on L4 and L5 pyramids gives rise to a negative LFP deflection extending across L4 and L5 at the onset of UP. The LFP negativity attenuates during the UP state due to synaptic depression. During the DOWN state, synaptic activity is much reduced, resulting in an LFP close to zero.

How do morphological features of neurons impact the LFP? In Fig. 8.2 f, we replayed the pattern of PSC activation of Fig. 8.2 e, but this time we included morphologically detailed neurons (Figs. 8.1 and S1) with passive membranes. In this setup, the LFP contributors are by definition limited to PSC and related passive “return” currents, i.e., currents induced along the neural membrane by impinging synaptic input due to charge conservation. (Notably, the impact of return currents is absent in the simulation shown in Fig. 8.2 e.) All sodium, potassium, and calcium currents have been blocked. Oscillatory external inputs (Fig. 8.2 a) give rise to oscillatory intracellular depolarization (similar to Fig. 8.2 c). Yet, LFP features, such as the amplitude or the temporal width in the two layers, change drastically compared to Fig. 8.2 e. The presence of passive membranes markedly attenuates the amplitude and the temporal width of the LFP waveform (note the voltage scale bar in Fig. 8.2 e is 5-fold larger than in Figs. 8.2 f and g). This reduction is due to the impact of return currents of opposite sign that cancel out the extracellular impact of locally impinging synaptic input and low-pass filtering of passive membranes. In particular, the LFP waveform changes as a function of depth. This is especially true during the first 50–100 ms of UP.

### Active membrane conductances of within-layer pyramidal neurons crucially shape the LFP

How do voltage- and ion-specific membrane conductances found in all of these neurons shape the LFP? The short answer is a lot, in particular, compared to the passive cable simulation (Fig. 8.2 f). The LFP amplitude in the active case (Fig. 8.2 g; mid L5 at approx. 1, 100  $\mu m$  cortical depth; mean amplitude: 0.8 mV (active) versus 1.3 mV (passive); mean half-wave width: 60 ms (active) versus 130 ms (passive); see also upcoming sections and Fig. 8.4) is substantially attenuated. This is caused by the active conductances giving rise to a leakier membrane, especially at the onset and during UP, that, in turn, manifests itself in spatially extended extracellular multipoles of smaller amplitude (Fig. S2). During DOWN, the difference between active and passive membrane leakiness is much attenuated because the membrane conductances in the state of near absence of synaptic input are almost identical (Fig. S2). In general,

adding return currents (via the inclusion of passive morphologies) and, in a subsequent step, increasing membrane leakiness (via the inclusion of active membrane conductances) leads to attenuation of the LFP amplitude and spatiotemporal width.

Given the linearity of the extracellular resistive milieu (Anastassiou et al. [2011], Logothetis et al. [2007], but see Bédard et al. [2004]), the LFP plotted in Figs. 8.2 e–g is the sum of extracellular contributions from synapses and neurons distributed across two layers. In Fig. 8.3, we segregate the LFP contribution of each neural type (top to bottom: L4 pyramids, L5 pyramids, L4/5 basket cells) for the case shown in Fig. 8.2 g. We observe that the LFP contributors within both layers are currents associated with L4 and L5 pyramids. More specifically, in L4, L4 pyramids contribute  $46\% \pm 18\%$  of the LFP (L5 pyramids contribution:  $45\% \pm 18\%$ ), whereas in L5, L5 pyramids contribute  $52\% \pm 20\%$  (L4 pyramids contribution:  $39\% \pm 18\%$ ). These results support the view that, under the conditions studied here, the LFP does not reflect only local population processing but also outer-layer activity (Figs. 8.3 a and 8.3 b), especially in L4. The LFP in L5 is larger than in L4 due to the large size of L5 pyramidal neurons as well as the powerful synaptic drive they receive along their basal (mainly) and apical dendrites (Fig. 8.2 g). This elicits membrane currents along the whole depth axis (Fig. 8.3 b) so that, while perisomatic compartments still contribute mostly to the LFP, the apical dendrites of these neurons also contribute to the LFP in L4, especially during the transition from DOWN to UP, i.e., during the highly synchronous barrage of excitation impinging on L5 pyramidal neurons.

Comparatively, L4/5 basket cells, making up only 13% of all cells with their temporally narrow EAPs (Fig. 8.1, bottom) [Schomburg et al., 2012] and fairly symmetric and localized dendritic arbors, contribute very little to the LFP in either layers (basket cell contribution is  $9\% \pm 2\%$  in L4 and  $9\% \pm 6\%$  in L5; Fig. 8.3 c). The negligible contribution of L4/5 basket cells to the LFP is in stark contrast to their particularly high level of activity (their spiking rate reaches up to 75 Hz during UP; Fig. 8.2 d), compared to L4 and L5 pyramidal neurons in our simulations.

The simulated LFP contributions of L4 and L5 pyramids capture a common experimental observation: the positive LFP deflections in the perisomatic region and the negative LFP deflection along basal and apical dendrites during somatic depolarization periods (especially at UP onset; see also Fig. 8.4) can be attributed to the location of excitatory and inhibitory conductances along the elongated morphology of neurons in combination with the presence of return currents.

### Active membrane conductances alter LFP and CSD amplitude, spatial width, and constellation

To quantify differences in the spatial extent of the LFP between the passive (Fig. 8.2 f) and active membrane (Fig. 8.2 g) simulations, we fit the sum of two, spatially displaced, Gaussian functions (independent variable: location along the depth axis) of opposite sign to the mean LFP depth profile during UP (Figs. 8.4 a–c) and determined the amplitude, peak location, and the LFP length scale (described by the half width of each of the Gaussians). We found that the amplitude changes by approx. 50%–300%, the location by 100–300  $\mu m$ , and the spatial width by 30%–40% (values determined 50 ms after onset of UP; Fig. 8.4 d). Differences between active and passive are even greater during the first 50 ms of UP states (Fig. 8.4 a), but we chose to compare LFP depth profiles after synaptic activity had propagated throughout the network. Thus, in both layers, the presence of spiking and spike-related currents drastically alters LFP depth characteristics (amplitude, spatial, and temporal constellation), with differences being more pronounced in L5 especially during the first 100 ms of UP (Fig. 8.4 a). On

## Chapter 8. A Biophysically Detailed Model of Neocortical Local Field Potentials Predicts the Critical Role of Active Membrane Currents

---

the other hand, in L4, the LFP traces for the active and passive simulation are more similar, suggesting that the LFP there reflects not only active membrane processing but also synaptic and passive processes.

Current source density (CSD) analysis estimates the negative second-order spatial derivative of the LFP along the depth axis of the recordings. Per definition, the CSD represents the volume density of the net current entering or leaving the extracellular space [Nicholson and Freeman, 1975] and is used as a measure of synaptic input eliciting so-called current sinks (for excitatory inputs) and sources (for inhibitory inputs). In contrast to the LFP that is a distance-weighted superposition of currents within a small volume, the CSD crucially depends on local events along the depth axis. Thus, it is a better measure for processes occurring along the extent of L4 and L5 pyramids.

We calculated the one-dimensional CSD along the 1 mm depth axis covering L4 and L5 (Figs. 8.2 e–g and 8.3; sinks are in blue, and sources are in red). In the presence of active membrane conductances, sodium influx and potassium efflux associated with spiking gives rise to sinks and sources, respectively, in the vicinity of cell bodies. The oscillatory pattern of impinging synaptic inputs gives rise to a temporally oscillatory CSD of the same frequency as well as an intricate spatial structure of the waxing and waning of two sources (one in each layer) and one sink (in L5) with a length scale of approximately  $250\mu\text{m}$ . The aforementioned LFP differences (amplitude, spatial, and temporal variance) are also reflected in the CSD characteristics with passive membranes resulting in temporally wider CSD and differential sink-source constellation along the depth axis (Figs. 8.2 f and g). Notably, a current source is present in deep L5 for active membranes at UP onset (Fig. 8.2 g, red areas) that vanishes in the passive case. More generally, passive membranes exaggerated the strength and spatial reach of the induced multipoles along pyramidal neurons (Figs. 8.2 f, g, and 8.4a–d). Examination of the CSD contribution of the individual neural types (Figs. 8.3 and S3) revealed that the presence of active versus passive membranes altered the overall sink-source constellation and individual neural type contributions. Yet, for the stimulation scenarios examined in this paper, the contribution of L5 pyramids continues to dominate also in terms of CSD (Figs. 8.3 b and S3 b).

### Experimentally measured sink-source constellation replicated by simulations

Which CSD, passive (Fig. 8.2 f) or active (Fig. 8.2 g), is closer to CSDs obtained in vivo? Answering this question involves comparing CSDs during various brain states that can differ greatly. Riera et al. [2012] recently conducted detailed experiments in rat somatosensory barrel cortex and measured the CSD along the depth axis of barrel cortex during single whisker deflections. In Fig. 8.4 e, we plot the CSD for (left to right) the passive simulation (mean of the data shown in Fig. 8.2 f aligned at UP onset; Fig. 8.4 a), the active membrane simulation (mean of the data shown in Fig. 8.2 g aligned at UP onset; Fig. 8.4 a) and the grand average measured by Riera and colleagues (their Fig. 8.3). We observe how at UP onset and during the first 10–20 ms, sink-source constellation in L4 and L5 is similar to in vivo experiments. Subsequently, following synaptic depression in L5 attributed to particularly synchronous spiking, the two scenarios differ markedly for the next 10–20 ms with the sink-source constellation inverting. Finally, after equilibration of synaptic weights in L4, the active membrane simulation becomes almost identical to experiments. Notably, the resemblance between simulated and measured CSDs is greatly diminished when assuming identical synaptic input but passive membranes (Fig. 8.4 e, left), with the sink in L5 being exaggerated and the source almost absent from L4. (The resemblance becomes even poorer when comparing the experimental CSD to the PSC case shown in Fig. 8.2 e.) Although this comparison needs to be extended across multiple brain states, it suggests that active membrane conductances have a powerful influence on the CSD.

### Synaptic input correlation differentially reflected in sink-source features, depending on membrane conductances

How do LFP characteristics change with input statistics? Synaptic input correlation crucially impacts the spatial extent of the LFP [Lindén et al., 2011, Pettersen and Einevoll, 2008, Schomburg et al., 2012]. We performed simulations in which we either eliminated (“uncorrelated” case; Figs. 8.5 a-c) or further enhanced (“super-synchronized” case; Figs. 8.5 d-f) the temporal correlation of impinging synaptic input compared to the simulations shown in Fig. 8.2 g (termed the “control” case). Importantly, the “uncorrelated” and “supersynchronized” simulations have an identical number of PSCs impinging at the same locations as the “control” simulation. Only their timing is shifted, reflecting a decrease or an increase in input correlation (see Methods; Fig. S4). As synaptic drive becomes more correlated, the LFP amplitude increases (Fig. 8.5 c versus 8.5 f). To quantify such differences, we use the same method as introduced in Fig. 8.4 and report amplitude, location, and spatial width of the two spatially displaced Gaussian functions 50 ms after UP onset (Figs. 8.5 g and h; see also Table S1).

For example, the amplitude of the LFP negativity (fit by a Gaussian),  $A_{neg}$ , increases with input correlation: 0.12 mV (uncorrelated) versus 0.36 mV (control) versus 0.50 mV (supersynchronized) (Table S1). We see that the extent of the amplitude decrease for passive versus active membranes depends on cell type, with the greatest effect observed for L5 pyramids due to their size and strong synaptic drive. As witnessed by Figs. 8.2, 8.4, and 8.5, identical synaptic input causes larger LFP amplitudes for passive than for active membranes for almost all input correlation scenarios considered. For example, for the “control” simulation, identical synaptic activity gave rise to  $A_{neg} = 0.99$  mV and  $A_{pos} = 0.68$  mV for passive membranes versus  $A_{neg} = 0.50$  mV and  $A_{pos} = 0.46$  mV for active membranes (Table S1). Increased input correlation generally resulted in an increase in the length scale of the LFP, both for active and passive membranes, with L5 pyramids most strongly affected (compare spatial width  $w$  in Fig. 8.5 g versus h; Table S1). Again, passive membrane simulations have a larger spatial extent than active ones (manifested in the negative slope in almost all  $w$ -related panels in Figs. 8.4 d, 8.5 g and h).

So far our analyses have focused on the LFP and CSD features along the cortical depth axis. Assuming extracellular recording sites are situated along the center of the cortical disk, how do LFP characteristics change along the radial axis, that is, tangential to the cortical sheet? In Fig. 8.6, we segmented the population into concentric cylinders of radii  $R$  and calculated the LFP amplitude contributed in the center of L4 (left column) and L5 (right column) as a function of  $R$ . Accounting only for the  $V_e$  contribution of pyramidal neurons within a certain layer, we adopted the approach introduced in Lindén et al. [2011] (their Figure 5) to calculate the LFP contribution for the uncorrelated (stars) and control (circles) case for active (red) and passive (black) membrane conductances. Briefly, we defined the LFP amplitude  $\sigma$  as the SD of the LFP signal (Figs. 8.6 a and b) and the LFP saturation distance  $R^*$  (Figs. 8.6 c and d; blue triangles) as the radius at which the LFP amplitude reaches 95% of its maximum value with neurons located farther from  $R^*$  having a small contribution to the LFP signal. (Importantly, LFP amplitude  $\sigma$  is not the same as  $A$  reported in Figs. 8.4 d, 8.5 g, and h). Similar to Lindén et al. [2011], we found that increasing input correlation increased  $R^*$ . Yet, as for the analyses along the cortical depth axis, the presence of active membranes reduced  $R^*$  (active versus passive in L4: uncorrelated, 89 versus 184  $\mu\text{m}$ ; control, 187 versus 278  $\mu\text{m}$ ; L5: uncorrelated, 212 versus 249  $\mu\text{m}$ ; control, 315 versus 319  $\mu\text{m}$ ), especially in L4. Interestingly, for uncorrelated input in L5 and passive membranes,  $R^*$  from our simulations (249  $\mu\text{m}$ ) is in agreement with the value reported by Lindén et al. [2011] (approximately 200  $\mu\text{m}$ ; their Figure 5c).

## Chapter 8. A Biophysically Detailed Model of Neocortical Local Field Potentials Predicts the Critical Role of Active Membrane Currents

---

### LFP composition is transient and state dependent

So far, we focused on the LFP contribution of different cell types. Given the critical role of active membranes, which channels impact the LFP most and under which conditions? To address this question, we calculate the LFP contribution of synaptic input as well as the specific ions sodium (Na), potassium (K), and calcium (Ca) of the different cell types separately and show them for two cases, “uncorrelated” and “control” (Fig. 8.7). (Performing the same analyses for the “supersynchronized” case yields very similar results to “control”.) Specifically, we define the normalized portion of the LFP signal attributed to the current passing from a particular conductance integrated over the time bin (resulting in charge) as LFP contribution. We calculated the LFP contribution of specific conductances in two locations, the center of L4 and L5. For the “uncorrelated” case (Fig. 8.7 a), synaptic excitatory and inhibitory currents contribute under 15%–20% to the LFP. Fast sodium currents, especially from local pyramidal neurons, contribute about 30%, with the rest of the contribution stemming from slower potassium currents. Interestingly, whereas L5 pyramids expectedly (due to the presence of thick apical dendrites) contribute to the LFP recorded in L4, L4 pyramids also contribute to the LFP recorded in L5, mainly via K-related currents. The main contribution of L4/5 basket cells is in L5, where sodium and potassium currents constitute about 30% of the total current, yet it needs to be pointed out that the LFP amplitude for uncorrelated input is small (see Fig. 8.5 g and traces in Fig. 8.7).

How do these contributions change with input correlation? For the “control” case (Fig. 8.7 b), we observe how spiking Na and K currents from L5 pyramids dominate the LFP 20–40 ms from UP onset, both in L4 and L5. In fact, in L4, the LFP contribution from postsynaptic input impinging on L5 pyramids is larger than the LFP contribution of postsynaptic input impinging along L4 pyramids. Concurrently, there is a strong activation of Na- and K-related currents through spiking of L5 pyramids that prominently contribute to the LFP in L4. It is after the initial transient of 40 ms that synapses of L5 pyramids depress at which point Na- and K-related currents of L4 pyramids begin dominating (approx. 60%–80%) the LFP signal in L4. In L5, within-layer pyramids dominate the LFP throughout the UP-DOWN cycle with two main differences to L4 activity: first, synaptic currents contribute more (approx. 15%–20%) than in any other case during UP, and second, L4/5 basket cells have a significant (even if short-lived) impact on the LFP 50 to 70 ms from UP onset (approx. 30%–40%), where dense local connectivity (Fig. 8.1) and the massive bolus of postsynaptic activity induces high spiking rates (Fig. 8.2). Finally, we found IPSCs to contribute approximately 10% of the total (excitatory and inhibitory) synaptic contribution, i.e., under the conditions studied here excitatory input dominates the synaptic contribution.

### Frequency and distance scaling of LFPs is determined by active membrane currents

Temporal frequency (“1/f”) and distance (“1/r”) scaling of LFP signals can reveal aspects of neural processing [Pritchard, 1992, Bédard et al., 2006, Milstein et al., 2009, Miller et al., 2009, Buzsáki et al., 2012]. Which sort of scaling do our simulations exhibit? Using the  $V_e$  traces recorded in depths ranging from 500 to 1,700  $\mu\text{m}$  (representative  $V_e$  traces shown in Fig. 8.8 a; blue: PSC only, black: passive membranes, red: active membranes), we initially calculated the power spectral density (PSD)  $P$  (“control” simulations in Fig. 8.8 b; line: mean, shaded area: SD). We calculate the best fit (see Table S2) to  $P(f) \propto \frac{1}{f^\alpha}$  with  $f$  being the frequency and  $\alpha$  the scaling exponent for two bandwidths: <40 Hz (Fig. 8.8 c, bottom) and 40–1,000 Hz (Fig. 8.8 c, top).  $\alpha$  is consistently smaller across all cases of input correlation for low frequencies compared to high ones (circles: mean; error bars: SEM), with the differences in  $\alpha$  between

all cases being small for <40 Hz (Table S3). For 40–1,000 Hz,  $\alpha$  is similar between PSC and passive membrane simulations, while substantially reduced for active membranes (Table S3). For example, for the "control" simulation with active membranes,  $\alpha = 2.0 \pm 0.4$ , whereas for passive membranes,  $\alpha = 3.7 \pm 0.1$ . (For <40 Hz, for the "control" simulation,  $\alpha = 1.0 \pm 0.2$  and  $0.9 \pm 0.1$ , respectively.) Notably, experimental recordings exhibit  $\alpha$  close to two [Milstein et al., 2009, Miller et al., 2009], with  $\alpha$  smaller at lower frequencies [Miller et al., 2009]. We conclude that  $\alpha$  is crucially shaped not only by postsynaptic currents but also by membrane characteristics in the 40–1,000 Hz range.

How do individual neurons and the associated microvariables give rise to such frequency-scaling evident in the macrovariables, i.e., the LFP? To address this question, we defined a single-cell frequency scaling exponent for all L5 pyramidal neurons (the population with the strongest LFP contribution), where  $P(f) \propto \frac{1}{f^\beta}$ , and calculated the mean  $V_e$  of all 5,364 L5 pyramidal neurons at three different locations relative to the soma (Figs. 8.8 d and 8.8 e shows the "control" simulation). The PSD as well as its frequency scaling differs substantially depending on whether only PSC, passive cable structures, or active membranes contribute to the LFP. PSC and passive membranes consistently give rise to steeper scaling and larger  $\beta$  (approx. 2.5–3; Figs. 8.8 e and f; Table S4) for all simulations, whereas for active membranes  $\beta$  is smaller (approx. 1–2; Table S4). The PSD decreases drastically as a function of frequency for passive membranes and decreases much less so for active membranes (Fig. 8.8 e). More surprisingly, differences in PSD as well as frequency-scaling for active versus passive membranes persist for frequencies <100 Hz (Fig. 8.8 e). This suggests that spiking and spike-related currents contribute to low LFP bandwidths traditionally considered to reflect purely synaptic activity, an observation that agrees with experiments demonstrating LFPs generated via nonsynaptic events [Buzsáki et al., 2012, Chrobak et al., 2000, Anastassiou et al., 2010, 2011].

The spatial extent of LFPs changes substantially between cases (Figs. 8.4 and 8.5). We analyzed the LFP contribution of L5 pyramids to three bandwidths (<50, 50–100, and 800–1,000 Hz; Fig. 8.8 g), as a function of distance  $r$  between the soma and the electrode, i.e.,  $P(r) \propto \frac{1}{r^\gamma}$ , with  $P(r)$  as the distance-dependent PSD in a particular bandwidth, and  $\gamma$  is the distance-dependent exponent (Figs. 8.8 g–i). In agreement with Lindén et al. [2011], Pettersen and Einevoll [2008], and Schomburg et al. [2012], we found that for passive membranes,  $\gamma < 2$  for  $r < 100\mu m$ , increasing to  $\gamma \approx 3$  for larger distances (Fig. 8.8 i). This observation was robust for all bandwidths and input correlations we examined. In the presence of active membrane conductances, PSD distance scaling changed substantially closer than  $100\mu m$  (Figs. 8.8 h and i), with  $\gamma \approx 3$  for all distances and input correlation scenarios. This suggests that active membrane conductances in L5 pyramids consistently generate extracellular multipoles [Pettersen and Einevoll, 2008, Riera et al., 2012]. Notably, PSC simulations, consistent with the point-like nature of synaptic input, give rise to monopoles close to the recording electrode and dipoles when measured farther away. As illustrated in Fig. 8.8 h (and already suggested by Figs. 8.8 band e), PSD not only differs in the higher bandwidths, where spiking currents dominate, but, surprisingly, also below 50 Hz. Given the identical synaptic activity between PSC, passive and active membrane simulations, these differences are attributed to the active membrane properties that not only give rise to a leakier membrane but fundamentally alter the sink-source constellation.

## 8.4 Discussion

We use a large-scale computational model with more than five million compartments to study the extracellular signature of active brain tissue, the LFP. The model accounts for biophysically characterized and morphologically reconstructed neurons interconnected based on rules supported by experimental



## Chapter 8. A Biophysically Detailed Model of Neocortical Local Field Potentials Predicts the Critical Role of Active Membrane Currents

---

data. Traditionally, the LFP has been assumed to reflect postsynaptic currents and associated passive return currents, with the final extracellular field mainly shaped by neural morphology and synaptic input. Our simulations challenge this picture. With identical synaptic input waxing and waning at 1 Hz, active membrane conductances cause markedly different LFP signatures than passive cable structures or only postsynaptic activity without any passive or active membranes. These differences are not merely due to the amount of current flowing through the membrane but also by the radically altered spatial constellation of extracellular sinks and sources. In agreement with recent work [Pettersen et al., 2008, Lindén et al., 2011, Schomburg et al., 2012], we find that the LFP length scale depends on the temporal coordination of the oscillatory inputs. Importantly, spiking and spike-related currents impact the LFP not only in the higher bandwidths but also in lower ones (<50 Hz) traditionally thought to reflect purely postsynaptic activity.

We found that L4 pyramids impacted the LFP and CSD within both layers, with their extracellular contribution greatly affected by the presence or absence of active membranes. Conversely, L5 pyramids with their large somata, thick apical dendrites, and strong synaptic input contribute not only to the LFP within L5 but also to the LFP in L4, especially at the onset of coordinated synaptic input. Given their large size and powerful synaptic input, it is conceivable that L5 pyramids could also contribute to the LFP in other layers, such as L2/3 or L6, not simulated here. Thus, whereas the LFP reflects processing of neurons whose cell bodies are situated within that layer, the extended nature of pyramidal neurons gives rise to multipoles that reach into nearby layers. Importantly, we found this to be broadly true in simulations exhibiting varying degrees of input correlation.

In agreement with others [Pettersen et al., 2008, Schomburg et al., 2012], we find that L4/5 basket cells with their fairly low density (compared to excitatory neurons), localized and symmetric dendritic arbor, spatially uniform synaptic input, the small temporal width of their somatic spikes, and lack of strong afterpotentials have only a small impact on the LFP and CSD, even though their spike frequency is substantially higher than that of their excitatory neighbors (Fig. 8.3 c). Of course, this does not suggest that extracellular action potentials from individual basket cells are small.

When considering LFP characteristics, such as amplitude and spatiotemporal width, we observed that these are markedly shaped by the impinging pattern of postsynaptic currents and membrane characteristics. Increasing model complexity from only postsynaptic to using fully reconstructed active neurons attenuates the LFP amplitude, alters its spatiotemporal width and changes the sink-source location. Additionally, our findings regarding the LFP length scale (depending on input correlation, approximately 200–600  $\mu\text{m}$  along the cortical depth and 100–300  $\mu\text{m}$  tangentially) points to the necessity of large-scale models to study the origin and functionality of the LFP.

How do these observations compare with LFPs recorded during whisker stimulation [Riera et al., 2012]? Such stimulation triggers prominent thalamocortical input into L4 in somatosensory cortex. At UP onset, and during the first 10–20 ms, the sink-source constellation in L4 and L5 was similar to experiments. Following the onset of synaptic depression in L5, the CSD became markedly different for the next 10–20 ms, with sink-source constellation inverting. Finally, after equilibration of synaptic weights in L4, the simulated CSD became almost identical to experiments. Given that the synaptic activation in our network was not designed to emulate whisker stimulation, we are led to the conclusion that while network computation requires inclusion of synaptic, morphological, and membrane characteristics, connectivity patterns, and features of synaptic dynamics, such as plasticity rules, are crucial not only for network processing but also to fully account for extracellular sinks and sources.

Sodium and potassium currents prominently contribute to the LFP in both layers with K currents dominating (approx. 40%–60%) the LFP during the UP-DOWN cycle. Although fast Na currents of local neurons contribute less than K ones, their contribution to the LFP is greater (approx. 10%–20%) than that of postsynaptic currents (<10% in most cases). Thus, it is true that synaptic input is reflected in the LFP in that it initiates and sustains the intracellular and membrane currents along neurons, but our simulations show that the LFP signal does not directly reflect synaptic activity. Instead, it predominantly reflects active membrane conductances activated by impinging postsynaptic input.

This observation challenges the classic view that LFPs are primarily a reflection of synaptic currents based on the number of activated synapses within a volume of brain tissue being typically much larger than the number of spikes (per unit time) within the same volume. Why do our simulations show such strong contribution of active membrane currents? The main reason is that during an individual spike, charge fluxes across the neural membrane at the perisomatic region (axon initial segment, soma, etc.) are much stronger than individual PSCs [Koch and Segev, 1998]. While the strongest charge fluxes occur within 1–2 ms of every spike (according to the standard Hodgkin-Huxley model), a cascade of slower spiking currents (mainly K- but also Ca-dependent) with much longer time scales is coactivated. These slower active membrane conductances crucially contribute to the LFP as observed in Fig. 8.7. On the other hand, fast synaptic currents (*AMPA*- and *GABA<sub>A</sub>*-type) die out rapidly, while the slower ones (*NMDA*-type) have a fairly small contribution (the *AMPA* versus *NMDA* component of every excitatory synapse is about 1 to 0.7; Ramaswamy et al. [2012]). (Notably, not all presynaptic inputs give rise to PSCs; Markram et al. [1997] and Ramaswamy et al. [2012].) Finally, active conductances contribute much more to the LFP than passive ones because they are mainly located in the perisomatic region along large compartments (i.e., low axial resistance), such as the soma and near dendrites (especially for L5 pyramidal neurons), so that the associated return currents are spread along the whole morphology of the neuron. As a consequence, EAP amplitude is approximately proportional to the sum of the dendritic cross-sectional areas of all dendritic branches connected to the soma. Therefore, neurons with thick dendrites connected to the soma produce large EAPs and have the largest “radius of visibility” [Pettersen and Einevoll, 2008]. At the same time, PSCs are mainly located along thin dendrites (i.e., much higher axial resistance), preventing return currents from spreading along the whole neural morphology.

Another important observation stemming from our simulations is the input specificity of the LFP composition. Although the LFP during the first 50–80 ms from UP onset is dominated by K currents originating from L5 pyramids for temporally coordinated input (Fig. 8.7 b), this switches to K currents from L4 pyramids for uncorrelated input (Fig. 8.7 a). Moreover, basket cells generally do not contribute markedly to the LFP, but this changes briefly 50 to 70 ms after UP onset. Thus, the LFP composition is not static but time- and state-dependent and is crucially impacted by the impinging input and the sort of subthreshold and spiking activity it induces (especially proximally to the recording site).

What are the functional (computational) ramifications of these observations? Coherence between spiking and specific LFP bands has been used to infer the relationship between synaptic input (hitherto considered to be reflected in the LFP) and neural output (spiking) and thereby specific mechanisms of information processing within and across brain regions [Montgomery et al., 2008, O’Keefe and Recce, 1993, Rutishauser et al., 2010]. This raises the question of the extent to which the locally generated LFP (or particular bandwidths of it) represent actual synaptic input impinging on local neurons rather than spiking output [Buzsáki et al., 2012]. For example, it was recently shown that spiking coherence

## Chapter 8. A Biophysically Detailed Model of Neocortical Local Field Potentials Predicts the Critical Role of Active Membrane Currents

---

to ripples during sharp waves in CA1 is partly attributed to spiking currents shaping the ripple signal [Belluscio et al., 2012, Schomburg et al., 2012].

Another question arises regarding how perturbing rhythmic LFP activity such as theta with tetanic stimulation at particular phases of theta induces potentiation or depression of synaptic strength [Holscher et al., 1997, Hyman et al., 2003, Pavlides et al., 1988]. Other studies relate cognitive alteration to perturbation of neocortical UP-DOWN states [Marshall et al., 2006] or hippocampal sharp waves [Girardeau et al., 2009]. Our population model does not attempt to reproduce any particular LFP rhythm, but it does link the LFP to biophysical processing. Thus, it can become a useful tool toward addressing the involvement of particular mechanisms during particular LFP bandwidths and phases and how perturbing them crucially alters other processing and, ultimately, cognitive function.

When modeling the impact of active membranes on LFP power scaling, we found an inverse power law [Miller et al., 2009, Milstein et al., 2009] with scaling exponent  $\alpha$  depending on input correlation and bandwidth of interest. Passive membrane consistently resulted in larger exponents for higher bandwidths (40–1,000 Hz). When zooming in to the level of individual L5 pyramids by calculating the scaling exponent  $\beta$ , active membrane contributions differ substantially from passive membrane ones not just for higher bandwidths but, importantly, down to low frequencies (<50 Hz). Interestingly,  $\beta$  compares much better to  $\alpha$  in the 40–1,000 Hz range than below 40 Hz for synaptic only and passive membranes. Yet, in the presence of active membrane conductances,  $\beta$  becomes comparable to  $\alpha$ , both in the lower and higher bandwidth (especially so for the control and supersynchronized scenarios), suggesting very similar scaling between the entire population and L5 pyramidal neurons, regardless of their exact location within L5.

We also looked at PSD distance scaling (exponent  $\gamma$ )—within a  $100\mu m$  radius, PSD scales with  $\gamma \approx 2$ , characteristic of a dipole. For larger distances,  $\gamma \approx 3$ . A recent study elegantly illustrated that as long as  $\gamma > 2$ , the contribution of successive more distant populations of neurons to the LFP saturates, that is, the LFP has a finite spatial reach [Lindén et al., 2011]. In our simulations, for active membranes, PSD consistently scales with distance as  $\gamma \approx 3$ . To generalize, for smaller distances, postsynaptic currents contribute as monopoles ( $\gamma \approx 1$ ), the presence of passive membranes gives rise to return currents and an additional pole ( $\gamma \approx 2$ ), and active conductances give rise to leakier membranes, resulting in a third pole ( $\gamma \approx 3$ ). For larger distances, power scaling of active and passive membranes is similar ( $\gamma \approx 3$ ). Concurrently, an increase in input correlation results in an increase in LFP amplitude and, importantly, length scale. Thus, whereas the LFP is a good estimator of local neural processing, the volume it is representative for (within the same layer) can change substantially.

The present biophysical model does not include glial and astrocytic processes likely to be important for slowly fluctuating components of the LFP and we do not include nonmyelinated presynaptic axonal compartments (though Gold et al. [2006] and Schomburg et al. [2012]; and our own modeling indicate they contribute minimally to the LFP). Likewise, we neglected contributions of presynaptic terminals; given their small size, it is likely that the associated local return currents will render their contribution nugatory. Diffusion was also excluded in our simulations, which can lead to  $\frac{1}{f}$ -scaling [Bédard and Destexhe, 2009]. Finally, in our simulations we assumed a purely resistive and homogeneous extracellular medium. There is evidence in favor of a purely ohmic extracellular medium for frequencies <500 Hz, but at least one study has emphasized a capacitive component [Bédard et al., 2004], which, if true, may alter some of the findings in terms of the LFP contributions of all processes involved. Moreover, even for the purely resistive case, conductivity experiments have shown that the extracellular

medium is inhomogeneous, i.e., resistivity gradients exist [Goto et al., 2010]. Although the model can be extended to account for such observations, our primary goal is to account for the conventional biophysical processes related to LFP generation and the impact of active membrane conductances in particular.

Despite these limitations, our model reproduces a number of observations. First, external synaptic input gives rise to spike frequencies compatible with *in vivo* observations during slow-wave activity. The simulated EAP waveforms from our pyramids and basket cells agree with experimental observations [Gold et al., 2006]. Our simulations suggest the LFP contribution of fast spiking basket cells is small, as also shown in Lindén et al. [2011] and Schomburg et al. [2012]. Furthermore, our active simulations generate LFPs and CSDs that agree, both in terms of spatial constellation [Riera et al., 2012] and spectral content [Miller et al., 2009, Milstein et al., 2009], with *in vivo* observations, especially after UP onset. Using passive morphologies, we were able to reproduce the observation that LFP power scales differently within versus outside a  $100\mu\text{m}$  radius from the recording electrode [Lindén et al., 2011]. This changed substantially in the presence of active membranes. Finally, increasing input correlation resulted in larger LFP amplitudes and length scales, both for active and passive membranes. Richard Feynman once famously wrote: “what I cannot create, I do not understand.” It is our belief that the present approach is a necessary step toward unraveling the biophysics of LFPs and the workings of brain circuitry, in general.

## 8.5 Methods

### The core simulation

The model and simulations were developed using the software and hardware infrastructure of the Blue Brain Facility which includes data, models and workflows for modeling the cortical microcircuitry of somatosensory S1 cortex of the young (P12-16) rat. Each network simulation was performed using NEURON software, running on a Blue Gene P supercomputer on 1024 nodes and 4096 CPUs, and took approximately 3 hours to complete for 4 seconds of simulated time. Simulations of the cortical column relied on the NEURON simulation package [Hines and Carnevale, 1997]. A collection of tools and templates written in HOC and NMODL [Hines and Carnevale, 2000] were employed to handle the setup and configuration on the parallel machine architecture [Hines et al., 2008]. In addition, a reporting library written in C++ handled the parallel gathering of data and output to disk [Press, 1999].

### Electrophysiology and morphological reconstruction

Electrophysiology and reconstruction protocols are described in [Hay et al., 2011]. Briefly, the firing response was obtained from *in vitro* whole-cell patch clamp recordings in rat somatosensory cortex. For L4 and L5 pyramidal neurons, protocols were identical to [Hay et al., 2011]. For the basket cells, we used some additional (but very similar) stimulation protocols for their characterization [Toledo-Rodriguez et al., 2004]. After the experiment, brain slices were fixed and incubated overnight. Morphological reconstruction was performed from well-stained neurons that exhibiting only few cut neurite branches.

## Chapter 8. A Biophysically Detailed Model of Neocortical Local Field Potentials Predicts the Critical Role of Active Membrane Currents

---

### Computational reconstruction of neurons

Computational modeling of the neurons is described in [Hay et al., 2011]. Briefly, neurons were represented as a compartmental, conductance-based model using detailed reconstructed morphologies of cells from rat primary somatosensory cortex. The compartments were separated in 4 zones: axon initial segment (AIS), soma, basal dendrites and apical dendrites (Fig. 8.1). For interneurons there was only one dendritic zone. The full axon was not simulated, only the AIS (Fig. 8.1, bottom row). In the network simulation, action potentials were detected in the AIS, and the information was sent with a delay to the synapses at the postsynaptic cells. Passive membrane capacitance was set to  $1 \mu\text{F}/\text{cm}^2$  for the soma, AIS and dendrites, while for pyramids it was  $2 \mu\text{F}/\text{cm}^2$  for basal and apical dendrites to correct for dendritic spine area. Axial resistance is  $10 \text{ k}\Omega \text{ m}$  for all compartments. Input resistance  $R_{in}$  was  $225 \pm 41 \text{ M}\Omega$  for L4 pyramids and  $74 \pm 35 \text{ M}\Omega$  for L5 pyramids [Le Bé et al., 2007, Stuart and Spruston, 1998]. For basket cells,  $R_{in} = 379 \pm 210 \text{ M}\Omega$  [Kawaguchi and Kubota, 1993].

Up to 10 active membrane conductance types were accounted for that are known to play role in neocortical neurons, with kinetics taken from the published ion channel models or from published experimental data (transient sodium [Colbert and Pan, 2002], persistent sodium [Magistretti and Alonso, 1999], transient potassium [Korngruen and Sakmann, 2000], persistent potassium [Korngruen and Sakmann, 2000], m-current [Adams et al., 1982], h-current [Kole et al., 2006], high voltage-activated calcium [Reuveni et al., 1993], low voltage-activated calcium [Avery and Johnston, 1996], Kv3.1 [Rettig et al., 1992], d-type potassium [Shu et al., 2007], stochastic potassium [Diba et al., 2006], SK calcium-activated potassium [Köhler et al., 1996]). Kinetics of ion conductances that were characterized in room temperature ( $21^\circ\text{C}$ ) were adjusted to the simulation temperature of  $34^\circ\text{C}$  using Q10 of 2.3 and those taken from experiments where junction potential was not corrected for were shifted by  $-10 \text{ mV}$ . The reversal potentials for sodium and potassium were  $50 \text{ mV}$  and  $-85 \text{ mV}$ , respectively, and  $-45 \text{ mV}$  reversal potential was used for the  $I_h$  current. Ion currents were modeled using Hodgkin-Huxley formalism. In simulations with passive cells, the active conductances were set to zero.

### Network connectivity

Connectivity patterns were implemented based on the methods presented in [Hill et al., 2012]. Briefly, randomly picked instances of the reconstructed cells from L4 and L5 were placed in a hexagonal volume with a radius of  $320 \mu\text{m}$ . Subsequently, every instance of an axon coming closer than  $3 \mu\text{m}$  to a dendrite is detected and synapses are placed at a subset of 5% of those appositions [Reimann et al., a]. The subset is chosen such that the number of synapses per connection and bouton densities are matching known biological values [Silberberg and Markram, 2007, Feldmeyer et al., 2006a, Markram et al., 1997]. The spatial distributions of synapses placed in such manner on the soma, dendrites and axon are known to match biological distribution for a number of pyramidal-to-pyramidal neuron, pyramidal-to-interneuron and interneuron-to-pyramidal neuron connections with a mean error  $< 8\%$  [Hill et al., 2012]. Based on these methods, resulting soma densities (for all neurons) are approx.  $240,000 \text{ per mm}^3$  in L4 and  $90,000 \text{ per mm}^3$  in L5, consistent with biological data provided by DeFelipe *et al.* (2011, unpublished observations).

### Synaptic dynamics

AMPA- and NMDA-type synapses accounted for excitation. For AMPA receptor (AMPA) kinetics, the synaptic conductance was  $0.3 \pm 0.2 \text{ nS}$  [Yoshimura et al., 1999, Sarid et al., 2007, Rinaldi et al., 2007a].

The rise and decay time constants were  $0.2 \pm 0.05$  ms and  $1.7 \pm 0.18$  ms, respectively [Häusser and Roth, 1997]. For NMDA receptor kinetics, conductance was set to  $0.2 \pm 0.1$  nS, with rise and decay times being  $0.29 \pm 0.23$  ms and  $43 \pm 1.2$  ms, respectively [Sarid et al., 2007]. The reversal potential of AMPAR and NMDAR was set to 0 mV. For inhibitory GABA<sub>A</sub> synapses, the mean conductance was  $0.66 \pm 0.2$  nS with the rise and decay time constants being  $0.2 \pm 0.05$  ms and  $8.3 \pm 2.2$  ms. Time constant for recovery from depression and time constant for recovery from facilitation were adopted from several data sources and assigned to each putative inhibitory synaptic location identified by the collision-detection algorithm [Angulo et al., 1999, Gupta et al., 2000, Ling and Benardo, 1999]. The GABA<sub>A</sub> reversal was set to -80 mV [Silberberg and Markram, 2007]. External input is mediated by distributing additional excitatory and inhibitory synapses randomly (uniform distribution) across all cells and activating them independently with a temporally modulated frequency. These external synapses were less than 5% of the total number of synapses. In the control case, stochastic model synapses were activated after online detection of action potentials of the presynaptic cell and a conduction delay that was computed using the axonal path distance to the soma (assuming AP conduction velocity  $300 \mu\text{m/ms}$  [Stuart et al., 1997]). In all other cases, synapses were activated by pre-recorded spike trains accounting for the conduction delay. For passive morphologies, the spike train of the control case was used; in cases with increased / decreased synchrony that spike train was further modified.

### Spiking synchrony

As a measure of spiking synchrony, we calculated the mean of the normalized joint peri-stimulus time (PST) histogram [Aertsen et al., 1989] at a lag of 0 ms, *i.e.*, the mean cross-covariance of PST histograms of cell pairs, normalized by the product of their standard deviations. To generate the histograms, we used a bin width of 1 ms. As the covariance would be affected by the change in firing rates between simulated UP- and DOWN-states (see [Brody, 1999]), we limited the analysis to spikes elicited during the UP-state. To remove synchrony from the simulation (uncorrelated case), we first generated artificial spike trains by moving all spikes of the control case to times randomly chosen between 0 and 4000 ms (= duration of simulations). This generated independent, stationary Poisson spike trains with the same number of spikes per cell as in the control case. This spike train was then used to drive synapses in a simulation (see *Synaptic dynamics*). The external input was also present, but with a constant rate equal to the mean of the rate in the control case. To increase synchrony (super-synchronized case), we moved all spike times of the control case to the nearest multiple of 5 ms. The external input in this case was identical to the control case.

### Extracellular field calculation

Custom written software in C++ was used to calculate the extracellular contribution of all cells from the transmembrane currents of all their electrical compartments using the line-source approximation [Holt and Koch, 1999, Gold et al., 2006, Pettersen et al., 2008] (approx. 410 compartments per cell, > 5,000,000 in total). As the extracellular medium was assumed to be homogeneous and purely resistive ( $3.5 \Omega \text{ m}$ ) [Logothetis et al., 2007, Goto et al., 2010, Anastassiou et al., 2011] (but see [Bédard et al., 2010]), the extracellular potential is proportional to the sum of the contributions from each compartment, weighted by the inverse of the distance between the compartment and the sampling point. This calculation took place on a separate computer cluster (SGI, Fremont, CA). Full calculation of the extracellular field from the data supplied by NEURON took approximately 1 hour. In this first-order active model, we neglect any feedback – in the form of ephaptic interactions [Anastassiou et al., 2011] – from the field onto the

## **Chapter 8. A Biophysically Detailed Model of Neocortical Local Field Potentials Predicts the Critical Role of Active Membrane Currents**

---

transmembrane potential of individual neurons.

### **Acknowledgments**

This work was supported by grants from the US NINDS, the Human Frontiers Sciences Program, the Swiss National Science Foundation, the Mathers foundation and the funding to the Blue Brain Project by the ETH Board and the Ecole Polytechnique Fédérale de Lausanne (EPFL). Financial support for the CADMOS and Blue Gene/P system is provided by the Canton of Geneva, Canton of Vaud, Hans Wilsdorf Foundation, Louis-Jeantet Foundation, University of Geneva, University of Lausanne, and EPFL. Special thanks go to E. Schomburg, A. Shai, Y. Billeh and J. Taxidis for comments on the manuscript and methodology as well as all members of the Blue Brain Consortium, in particular Michael Hines, James King, Eilif Müller, Srikant Ramaswamy, Felix Schürmann and Werner van Geit.

## 8.6 Figures

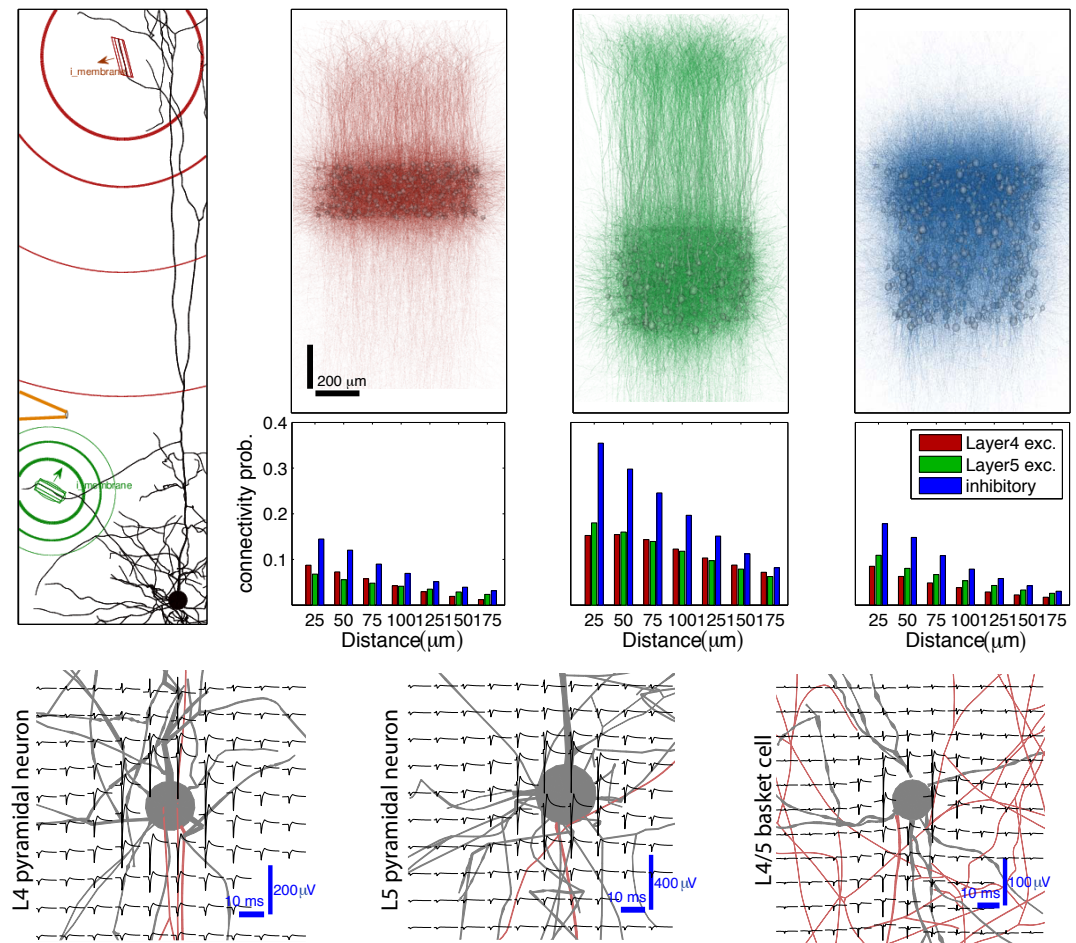


Figure 8.1 – Intracellular and extracellular biophysics of individual neurons

**Figure 1:** Intracellular and extracellular biophysics of individual neurons. (First row) Neural populations and connection probabilities. Populations of morphologically reconstructed and interconnected (left to right) L4 pyramids (green;  $n=5,471$  cells), L5 pyramids (brown;  $n=5,364$  cells) and basket cells (blue;  $n=1,700$  cells). Circles indicate soma location. (Second row) Connectivity probability (bars) as a function of inter-somatic distance and neural type (corresponding to the top row). For example, the probability that a basket cell is connected to a L4 pyramidal neuron located within 25  $\mu\text{m}$  is approximately 0.16 (blue bar). (Bottom row) Extracellular correlates of spiking for the three neural types considered (left to right: L4 pyramids, L5 pyramids, L5 basket cell) induced via a brief (10 ms) intracellular somatic current pulse as a function of location (grey: soma and dendrites; red: axons; see Methods). (Left panel) Transmembrane currents along the neural morphology give rise to extracellular electric fields that induce extracellular voltage fluctuations measured by an electrode (circles: isopotentials arising from two dendritic current sources).



**Chapter 8. A Biophysically Detailed Model of Neocortical Local Field Potentials Predicts the Critical Role of Active Membrane Currents**

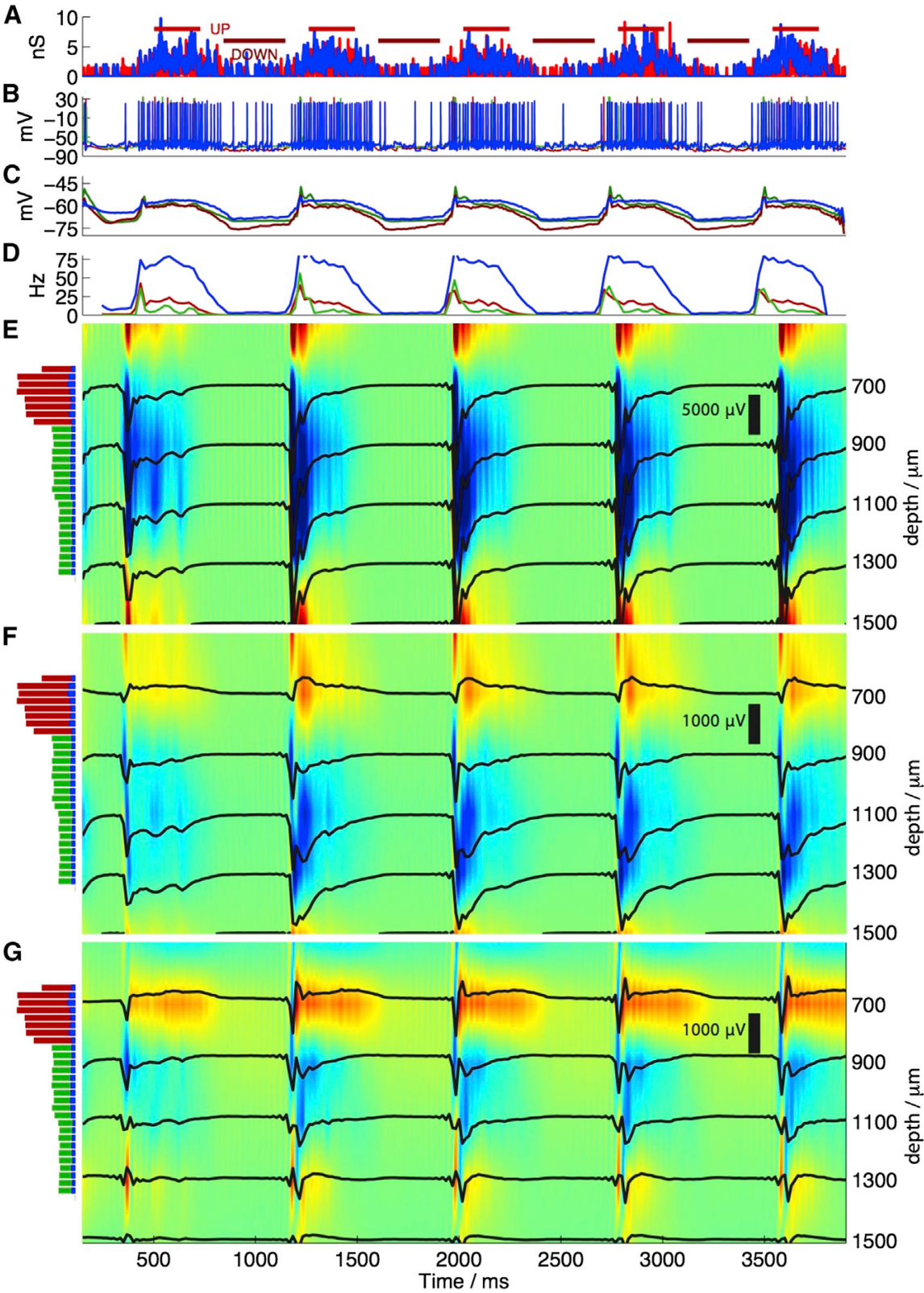


Figure 8.2 – Extracellular potentials under simulated network activity

**Figure 2:** Simulated network activity. (a) External excitatory (red) and inhibitory (blue) synaptic input to a L5 pyramid, placed along its morphology [Hill et al., 2012]. Synapses were activated by independent Poisson processes with a rate – fluctuating at 1 Hz – between 3 and 15 events per second for excitation and 0.3 and 1.5 events for inhibition. This input, given to all L5 pyramids, drives network activity. (b) Intracellular potential of three individual neurons (red: L4 pyramid; green: L5 pyramid; blue: L4 basket cell). (c) Mean intracellular somatic potential and (d) spiking frequency (time bin: 25 ms) as a function of time for all L4 (red), and L5 pyramids (green) and basket cells (blue). (e-g) LFP- and current source density (CSD)-dynamics for postsynaptic excitatory and inhibitory currents (e) in the extracellular space, (f) impinging along morphologically realistic neurons with passive membranes and (g) impinging along morphologically realistic neurons with active membranes. LFP-traces in solid black at different locations along the depth axis. CSD shown along the depth axis (blue: sink; red: source; CSD-scale:  $\pm 25$  mV/mm<sup>2</sup>). (Left) Soma density of L4 (red), L5 (green) pyramids and basket cells (blue) ( $10^5/\mu\text{m}^3$ ) as a function of depth to indicates layering. The numbers on the right indicate the depth in  $\mu\text{m}$ . Time axis, on the bottom, is identical for all panels.

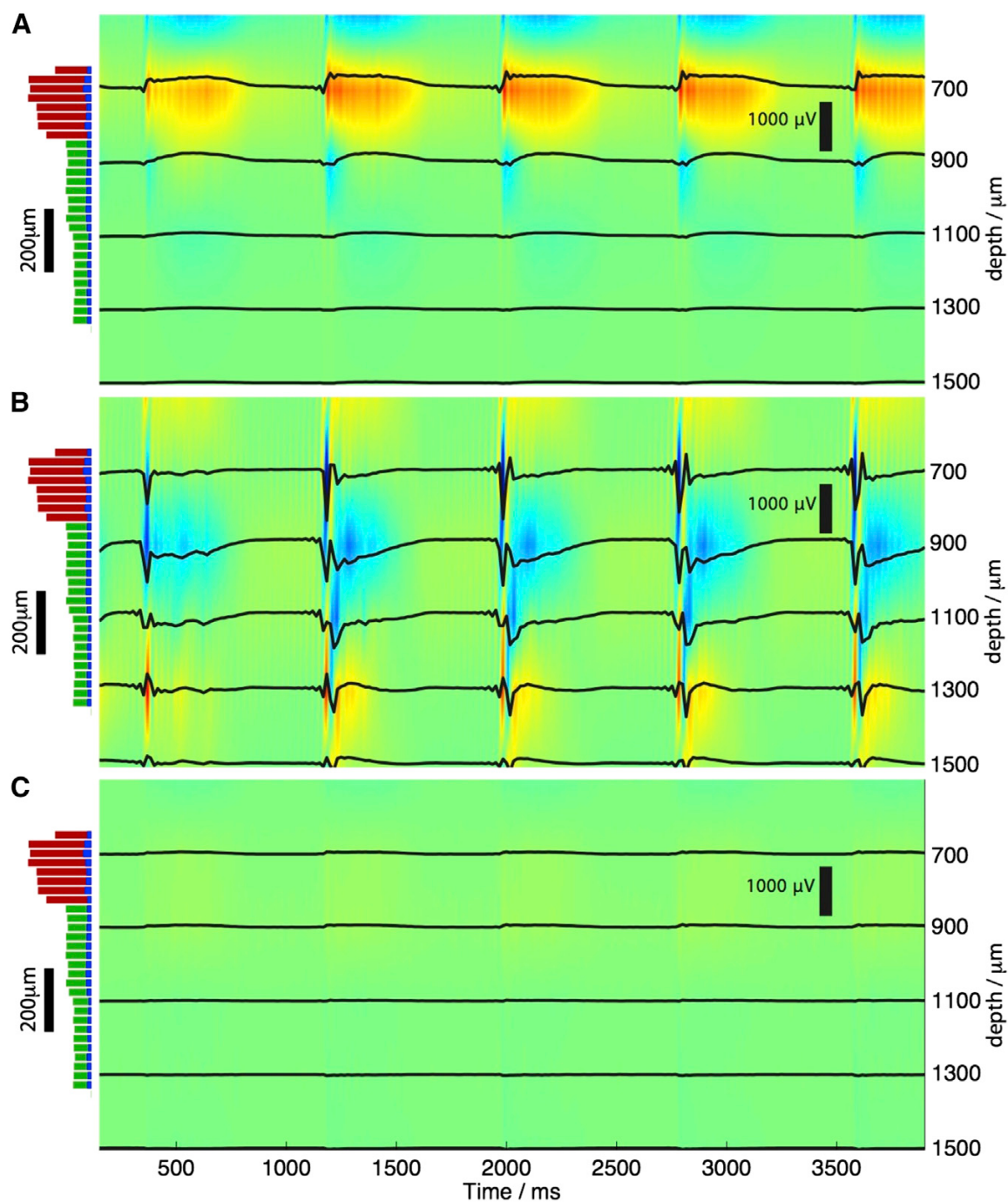


Figure 8.3 – LFP- and CSD-contribution of individual cell populations

**Figure 3:** LFP- and CSD-contribution of individual cell populations. For the active conductance simulation shown in Fig. 8.1g, the LFP- and CSD-contribution of (a) L4 pyramidal neurons, (b) L5 pyramidal neurons and (c) L4/5 basket cells as a function of depth. CSD shown along the depth axis (blue: sink; red: source; CSD-scale:  $\pm 25 \text{ mV/mm}^2$ ).

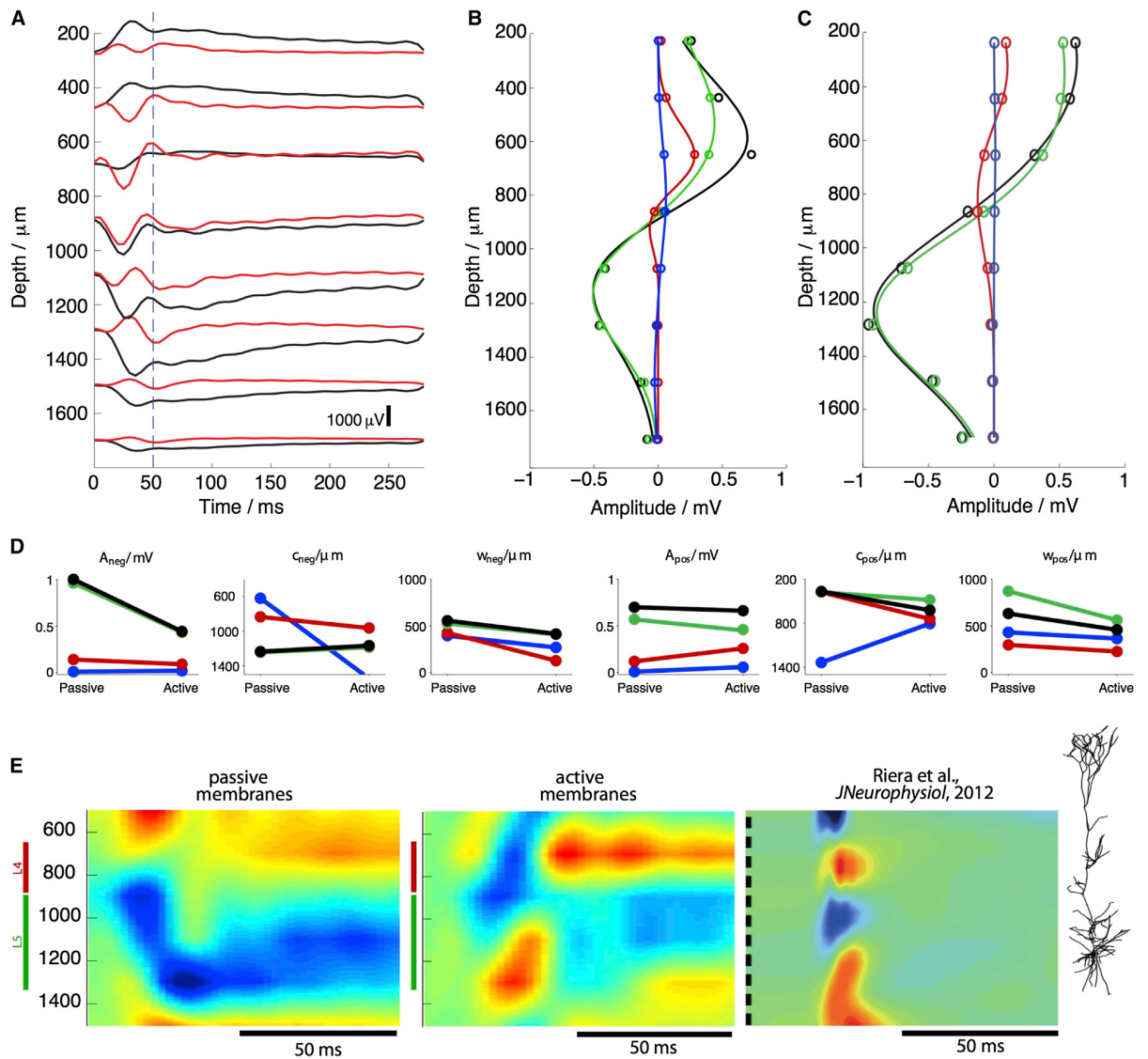


Figure 8.4 – Comparison of the LFP depth profiles between active and passive membranes

**Figure 4:** Comparison of the LFP depth profiles between active and passive membranes. (a) Average LFP-trace as a function of depth during the mean UP-state (mean calculated over the five UP-states in Fig. 2 8.2) for passive (black; simulation in Fig. 8.2f) and active (red; simulation in Fig. 8.2g) membranes. The blue line indicates the 50 ms instant that analyses shown in panels b-d are based on. (b) The contribution of different neural types (black: all neurons; red: L4 pyramidal neurons; green: L5 pyramidal neurons; blue: L4/5 basket cells) as a function of depth (circles: simulation results; line: best fit with double Gaussian function) in the center of the neural population for active membranes. (c) Same as panel b but for passive membranes. (d) Amplitude of the negativity ( $A_{neg}$ ) and positivity ( $A_{pos}$ ), location ( $c_{neg}$  and  $c_{pos}$ , respectively) as well as the half-width of the LFP negativity ( $w_{neg}$  and  $w_{pos}$ , respectively) of the double Gaussian fits for active (red) and passive (black) membranes (see also Table S1). Color coding as in panels (b) and (c). (e) Comparison of network simulations with

## Chapter 8. A Biophysically Detailed Model of Neocortical Local Field Potentials Predicts the Critical Role of Active Membrane Currents

---

experimental data. (e, left) Mean CSD of simulation (time zero: UP-onset; Fig. 8.4a) with purely passive membrane conductances (simulation shown in Fig. 8.1f). (e, middle) Mean CSD of simulation including active membrane conductances (simulation shown in Fig. 8.1g). (e, right) Grand average ( $n=13$  rats) CSD from recordings in rat somatosensory barrel cortex during single whisker deflections from Riera and co-workers [Riera et al., 2012]. The dashed vertical line on the left indicates the time instant for the whisker deflections. The position of L4 (red) and L5 (green) is indicated. The right panel is partly adopted from Riera *et al.* [Riera et al., 2012] and aligned to the simulation CSDs so as to show the same depth coordinates.



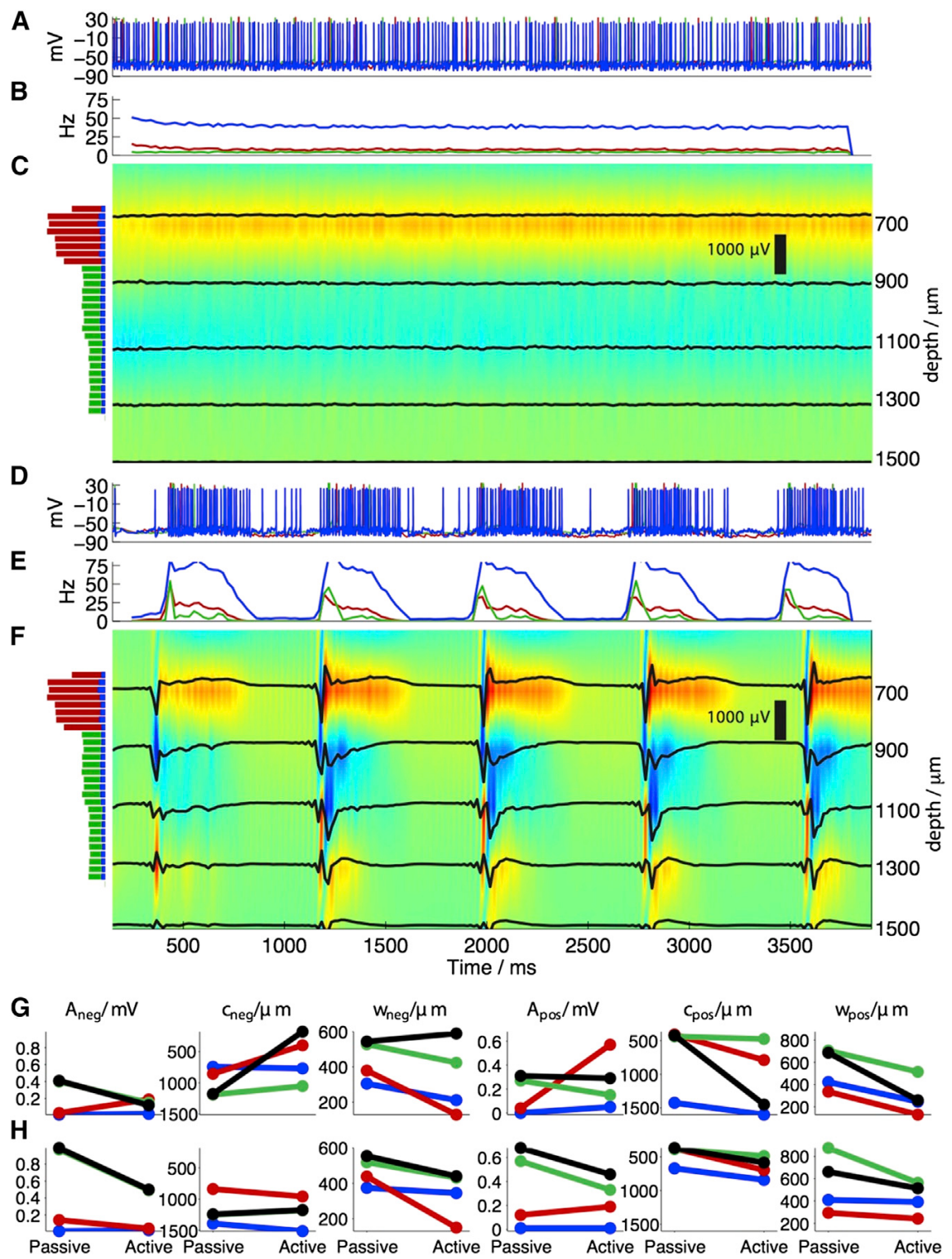


Figure 8.5 – Two cases with altered synaptic input correlation

## Chapter 8. A Biophysically Detailed Model of Neocortical Local Field Potentials Predicts the Critical Role of Active Membrane Currents

**Figure 5:** Two cases with altered synaptic input correlation driving L5 pyramidal neurons (compared to ‘control’ in Fig. 8.2): one with decreased (‘decorrelated’, panels a-c and g) and one with increased input correlation (‘super-synchronized’, panels d-f and h). (a) Intracellular potential of three individual neurons (red: L4 pyramid; green: L5 pyramid; blue: L4 basket cell). (b) Spiking frequency as a function of time for all L4 (red) and L5 pyramids (green) and basket cells (blue). (c) LFP- and current source density (CSD)-dynamics with impinging along morphologically realistic neurons with active membranes. (d-f) Same as panels a-c, respectively, for the ‘super-synchronized’ case. (g, h) Amplitude of the negativity ( $A_{neg}$ ) and positivity ( $A_{pos}$ ), location ( $c_{neg}$  and  $c_{pos}$ , respectively) as well as the half-width of the LFP negativity ( $w_{neg}$  and  $w_{pos}$ , respectively) of the double Gaussian fits for active (red) and passive (black) membranes (see also Table S1) for the (g) decorrelated and (h) super-synchronized case (same color coding as in Fig. 8.4d). Notably, simulation parameters were chosen such as to give rise to the same mean synaptic input being received by all neurons as in the simulations in Figs. 8.2 and 8.3, but the temporal patterning is absent.

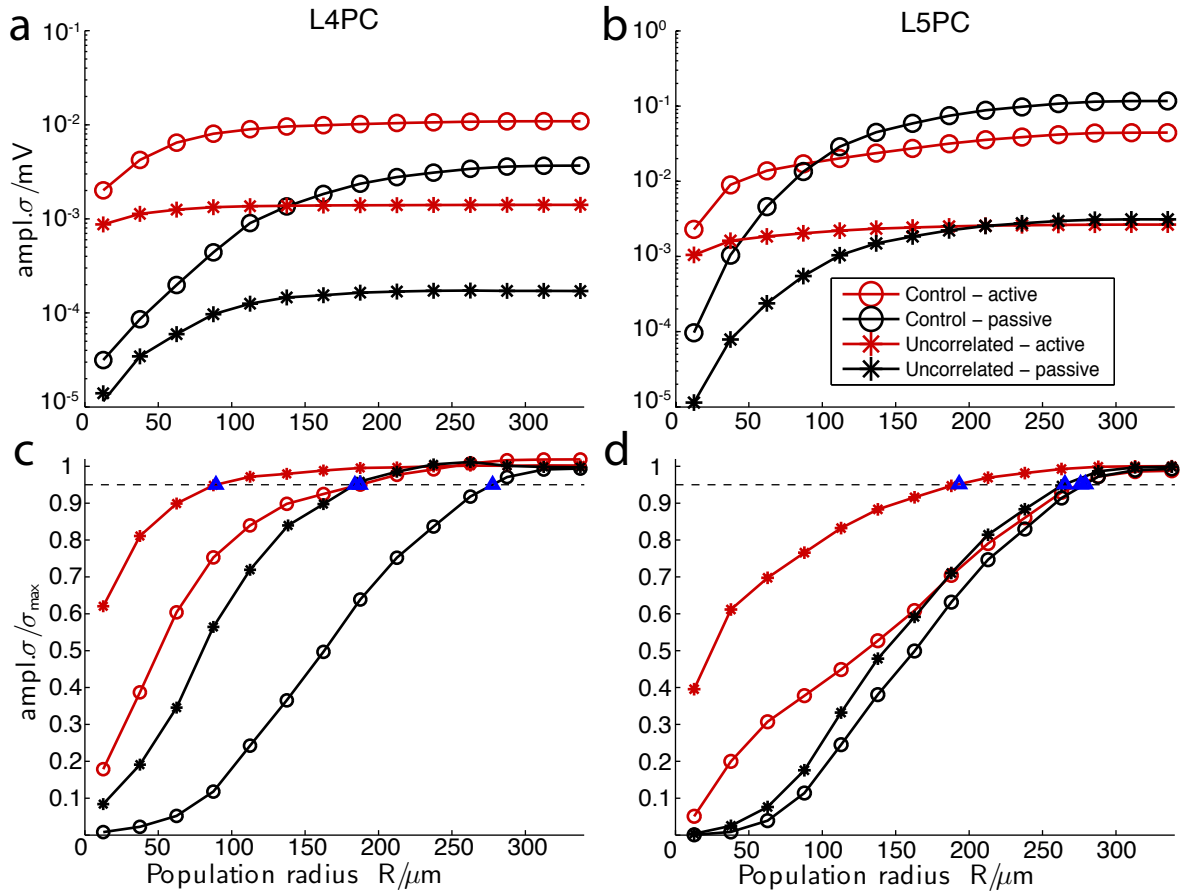


Figure 8.6 – Horizontal reach of extracellular population signals

**Figure 6:** Horizontal reach of extracellular population signals. (a–d) (Left) L4 and (right) L5 pyramidal neuron population was separated in concentric cylinders of radii  $R$ . (a and b) Cumulative contribution of each additional cylinder to the LFP amplitude measured in the center of each population (red: active membranes; black: passive; circle: control input; star: uncorrelated input) with  $\sigma$  defined as the SD of the LFP signal during four UP states. (Notably,  $\sigma$  differs from the LFP amplitude definition in Figs 7.4

and 7.5.) (c and d) Rescaled version of panels (a) and (b) with the LFP amplitude expressed as fraction of the asymptotically reached amplitude (95% of the maximum value). The vertical distance  $R^*$ , where the LFP amplitude equals 95% of the asymptotically reached LFP amplitude is designated by blue triangles.



**Chapter 8. A Biophysically Detailed Model of Neocortical Local Field Potentials Predicts the Critical Role of Active Membrane Currents**

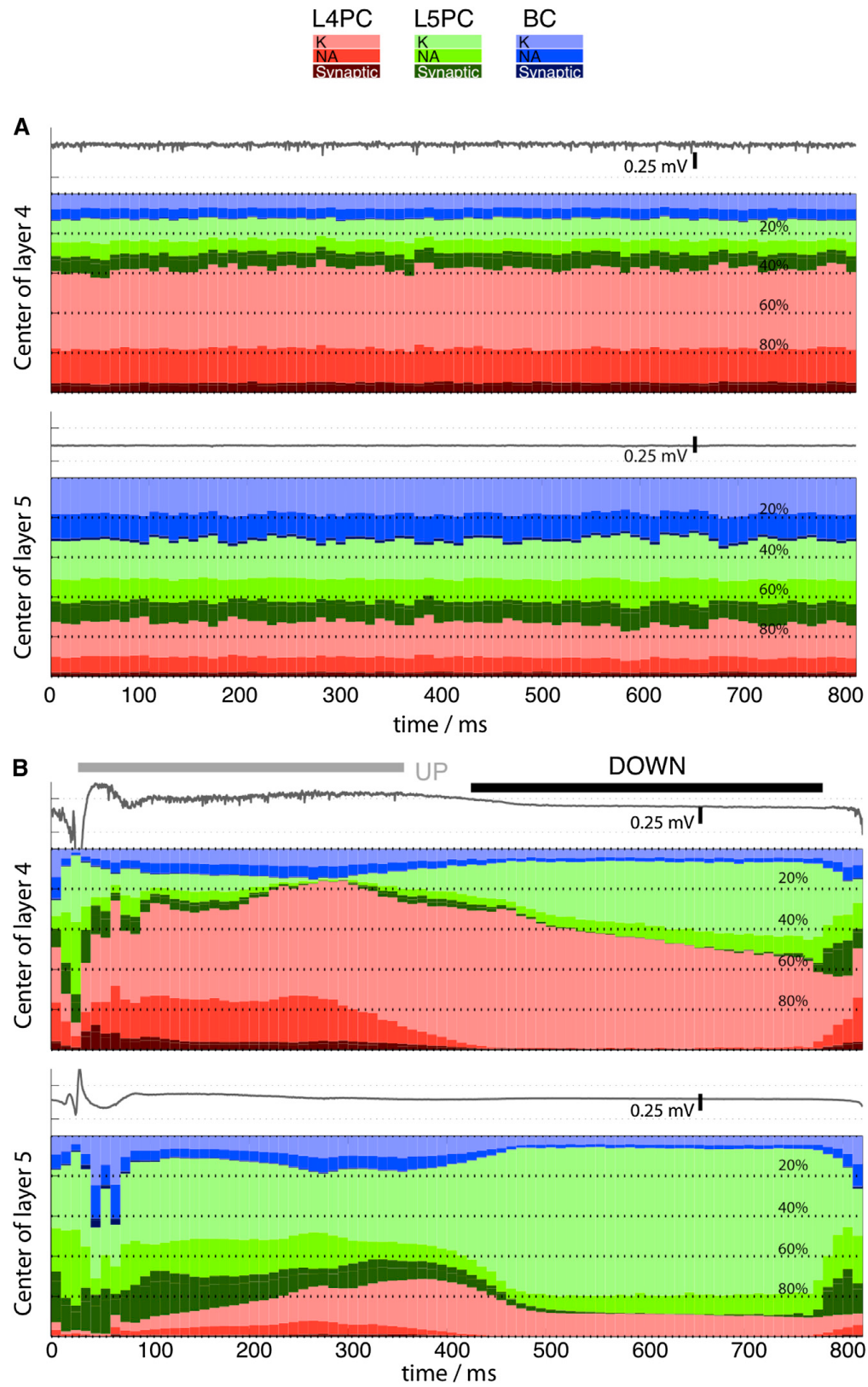


**Figure 8.7 – Ionic Contributions to the LFP**

**Figure 7:** Ionic Contributions to the LFP. (a and b) Three types of LFP contributions are considered: excitatory and inhibitory postsynaptic currents (synaptic) as well as Na-related (NA) and K-related (K) membrane currents as measured in the center of L4 (top) and L5 (bottom). Ca-related currents were also calculated, but their contribution was small (less than 2.5%) and is neglected. Temporal binning is 10 ms. To calculate the contribution at the time bin of interest, the synaptic and active charge contribution (return currents are not included) of a particular neural population is weighted by the distance. In a second step, we normalized the contribution to the LFP amplitude generated by the population as shown in Fig. 7.3. (The reason for the second step is to ensure that the sum of Na, K, and synaptic contributions of a cell type population equals the total contribution of that population to the overall LFP.) For example, the contribution of Na-related conductances of L5 pyramids is the total charge moved across the membrane via active Na-conductances during a particular time bin weighted by the inverse of the distance to the electrode. Then we divide the charge contributed by Na-related conductances by the total charge contributed by all conductances of L5 pyramids. The contribution of the three cell types is considered separately: L4 pyramidal neurons (red), L5 pyramidal neurons (green), and basket cells (blue). The data are presented in form of relative (stacked) percentual contributions. (a) The results for the "uncorrelated" simulation (Figs. 7.5a-c). (b) The results for the "control" simulation (Fig. 7.2f). Notably, inhibitory postsynaptic currents contribute approximately 10% of the total synaptic contribution, i.e., excitatory input dominates the synaptic contribution.

# Chapter 8. A Biophysically Detailed Model of Neocortical Local Field Potentials Predicts the Critical Role of Active Membrane Currents

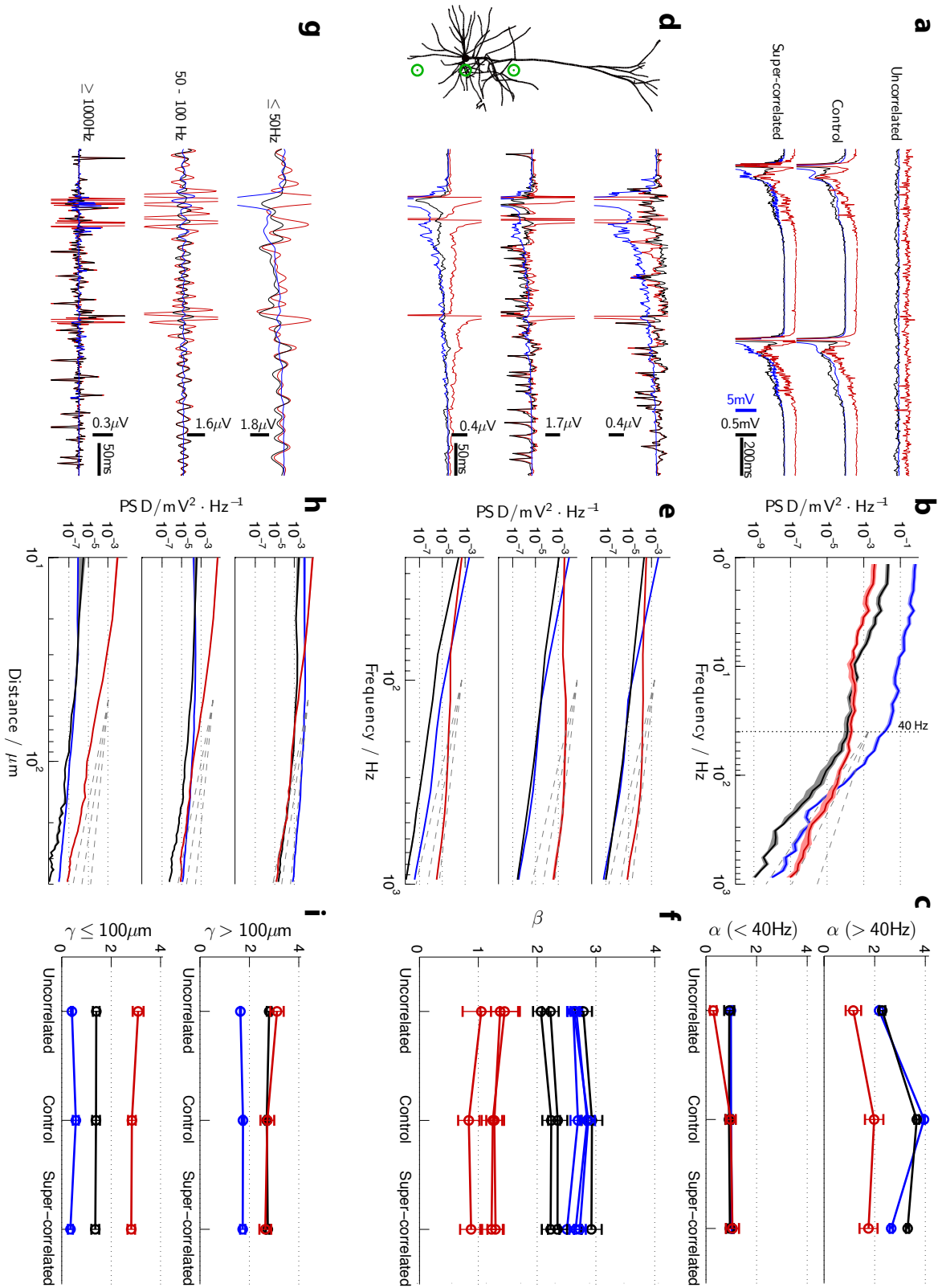


Figure 8.8 – Frequency- and distance-scaling of LFP

**Figure 8:** Frequency- and distance-scaling of LFP. (a) A 2 s long period of the  $V_e$ -recording conducted in the middle of L5 for (top to bottom) uncorrelated, control and super-correlated input (red: active membrane; black: passive membrane). (b) PSD frequency scaling for the control input simulation (line: mean PSD of seven recordings from L4 and L5; see Fig. 8.2; shaded line: std). Broken lines indicated slopes of 2 and 4. (c) PSD frequency scaling-exponent  $\alpha$  as a function of network state (linear fit from 40 to 1000 Hz; circle: mean; error bar: std). (d)  $V_e$ -recordings from three locations within L5 where the extracellular signal is only contributed by a single L5 pyramidal neuron located in the middle of L5 (traces are clipped to follow subthreshold events). (e) PSD frequency scaling of individual L5 pyramidal neuron  $V_e$ -contribution (line: mean; shaded area: std; broken lines show slopes of 2, 3 and 4) for the three locations shown in panel (d). (f) The value of frequency scaling exponent  $\beta$  indicates the frequency scaling of L5 pyramidal neurons at the single-neuron level as a function of network state (circle: mean; error bar: std). (g)  $V_e$ -signal originating from a single L5 pyramidal neuron (same as in the middle of d) filtered at (top to bottom) <50 Hz, 50-100 Hz and high pass (>800 Hz). (h) The PSD of the filtered  $V_e$  traces shown as a function of distance of the recording electrode from each L5 pyramidal neuron (line: mean; shaded area: std). It is observed how for passive membranes PSD scales differently as a function of distance for distances larger vs. smaller than 100  $\mu\text{m}$ . (i) Distance scaling exponent  $\gamma$  indicates distance scaling of the  $V_e$ -contribution of L5 pyramidal neurons at the single-neuron level as a function of network state (circle: mean; error bar: std) for distances larger (top) or smaller (bottom) than 100  $\mu\text{m}$ .

## **A Supplementary Material**

## A. Supplementary Material

	$A_{neg}$	$c_{neg}$	$w_{neg}$	$A_{pos}$	$c_{pos}$	$w_{pos}$	$A_{neg}$	$c_{neg}$	$w_{neg}$	$A_{pos}$	$c_{pos}$	$w_{pos}$
Control case												
Active membrane						Passive membrane						
All	0.36	1167	415	0.43	622	459	1.00	1236	557	0.70	366	633
L5PC	0.35	1187	409	0.26	483	563	0.96	1245	526	0.57	377	872
L4PC	0.09	964	128	0.26	742	226	0.14	835	427	0.12	377	297
BC	0.02	1545	270	0.06	805	365	0.01	619	395	0.01	1336	431
Uncorrelated input												
Active membrane						Passive membrane						
All	0.12	180	589	0.29	1450	259	0.41	1179	544	0.31	424	686
L5PC	0.15	1054	424	0.15	476	515	0.40	1190	528	0.27	438	705
L4PC	0.19	400	130	0.57	790	130	0.03	855	379	0.04	408	336
BC	0.02	770	212	0.05	1600	247	0.01	745	305	0.00	1425	422
Super-synchronized input												
Active membrane						Passive membrane						
All	0.50	1173	440	0.46	585	514	0.99	1242	555	0.68	366	662
L5PC	0.49	1178	431	0.33	485	563	0.97	1249	518	0.57	385	876
L4PC	0.04	957	150	0.19	694	241	0.14	838	438	0.12	375	294
BC	0.02	1510	345	0.01	840	391	0.01	1390	374	0.01	670	410

Table S1 – Parameters of the LFP-depth profile in Figs. 7.2, 7.3, 7.4, 7.5

**Table S1:** The depth profiles are fit using a double Gaussian function  $A_{neg} \cdot N(x, c_{neg}, w_{neg}) + A_{pos} \cdot N(x, c_{pos}, w_{pos})$  with  $N$  being the normal probability density function. Reported in this table are the amplitude of the negativity ( $A_{neg}$ , in  $mV$ ), its location ( $c_{neg}$ , in  $\mu m$ ) and the half-width ( $w_{neg}$ , in  $\mu m$ ). The same parameters corresponding to the positivity are designated via the subscript 'pos'.

	Normalized RMS					
	< 40 Hz			40-1000 Hz		
	uncorrelated	control	super-synchr.	uncorrelated	control	super-synchr.
<b>Synaptic only</b>	0.088	0.056	0.068	0.061	0.035	0.147
<b>Passive</b>	0.035	0.065	0.062	0.033	0.046	0.063
<b>Active</b>	0.067	0.101	0.092	0.073	0.056	0.115
	Correlation					
	uncorrelated	control	super-synchr.	uncorrelated	control	super-synchr.
<b>Synaptic only</b>	0.973	0.989	0.988	0.976	0.992	0.948
<b>Passive</b>	0.989	0.985	0.986	0.996	0.995	0.993
<b>Active</b>	0.943	0.927	0.937	0.948	0.965	0.883

Table S2 – Quality-of-fit parameters associated with Fig. 7.8

**Table S2:** Normalized RMS is the square root of the mean square error normalized by the range (RMS=0 is perfect fit). Correlation quantifies the strength of the linear relationship between two variables (correlation=1 is perfect fit). As observed, the fits are good so that  $\alpha$  values accurately depict power-scaling in the designated frequency bandwidths.

**Chapter 8. A Biophysically Detailed Model of Neocortical Local Field Potentials Predicts the Critical Role of Active Membrane Currents**

	$\alpha$ (mean $\pm$ s.e.m.)					
	$< 40Hz$			$40 - 1000Hz$		
	<b>uncorrelated</b>	<b>control</b>	<b>super-synchr.</b>	<b>uncorrelated</b>	<b>control</b>	<b>super-synchr.</b>
<b>Synaptic</b>	$0.98 \pm 0.05$	$0.98 \pm 0.01$	$1.03 \pm 0.01$	$2.17 \pm 0.03$	$3.94 \pm 0.03$	$2.67 \pm 0.06$
<b>Passive</b>	$0.92 \pm 0.20$	$0.91 \pm 0.15$	$0.94 \pm 0.15$	$2.30 \pm 0.12$	$3.66 \pm 0.10$	$3.23 \pm 0.06$
<b>Active</b>	$0.29 \pm 0.13$	$0.98 \pm 0.20$	$1.04 \pm 0.26$	$1.15 \pm 0.31$	$1.98 \pm 0.36$	$1.80 \pm 0.30$

Table S3 – Power-scaling exponent  $\alpha$  as calculated for Fig. 7.8

	$\beta$ (mean $\pm$ s.e.m.)		
	<b>uncorrelated</b>	<b>control</b>	<b>super-synchr.</b>
<b>Synaptic</b>	$2.67 \pm 0.10$	$2.85 \pm 0.13$	$2.66 \pm 0.11$
<b>Passive</b>	$2.78 \pm 0.15$	$2.93 \pm 0.18$	$2.92 \pm 0.18$
<b>Active</b>	$1.37 \pm 0.34$	$1.27 \pm 0.14$	$1.29 \pm 0.14$

Table S4 – Power-scaling exponent  $\beta$  for the location closest to the soma as calculated for Fig. 7.8

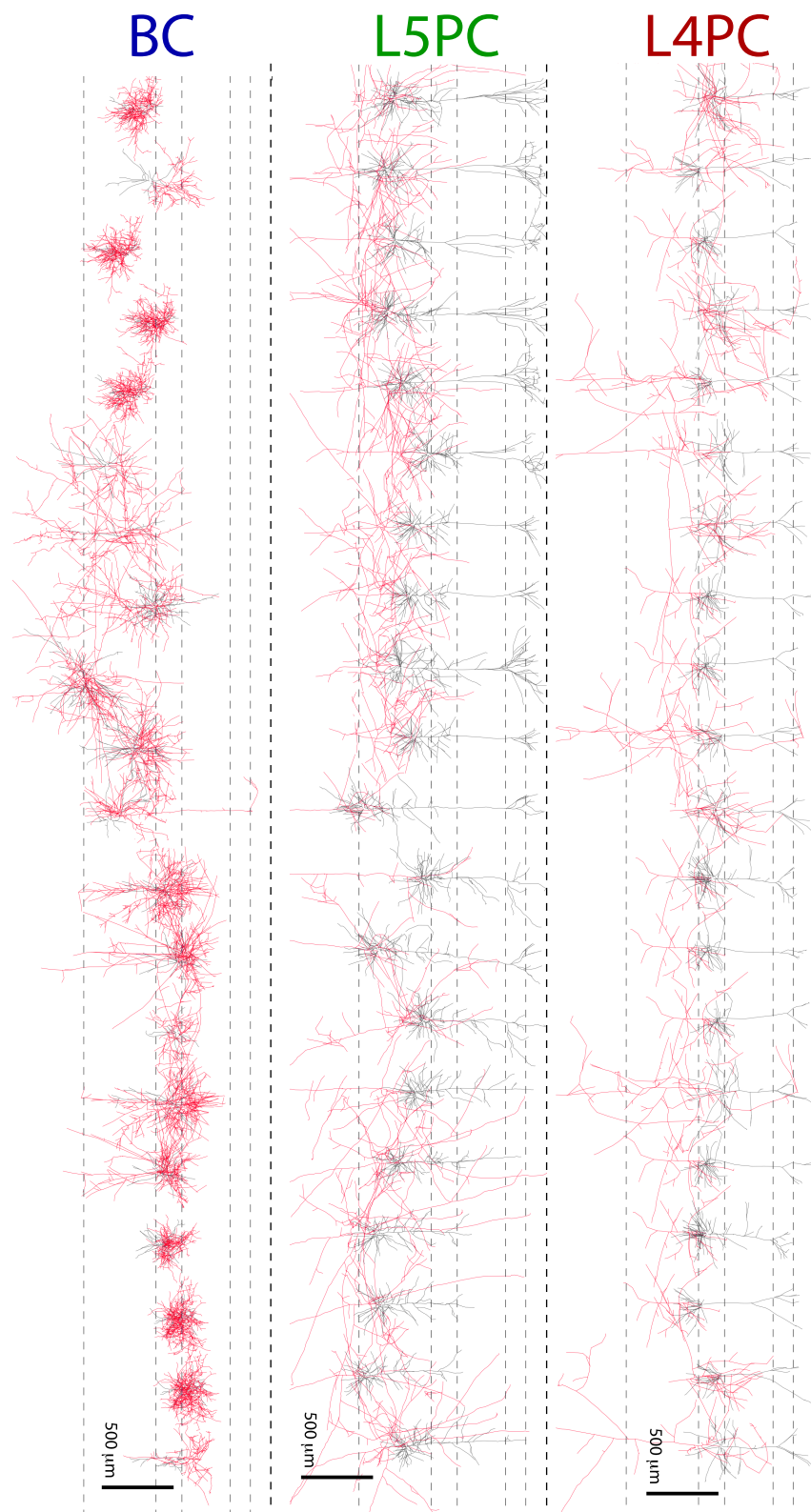


Figure S1 – Exemplary morphologies



## **Chapter 8. A Biophysically Detailed Model of Neocortical Local Field Potentials Predicts the Critical Role of Active Membrane Currents**

---

**Figure S1:** Neural morphologies related to Figs. 7.1 and 7.2. Twenty unique morphologies from (top to bottom) L4 pyramidal neurons, L5 pyramidal neurons and L4/5 basket cells. Somatic and dendritic compartments are shown in black while axonal arborizations in red. Dashed lines indicate the location of L1 to L5.

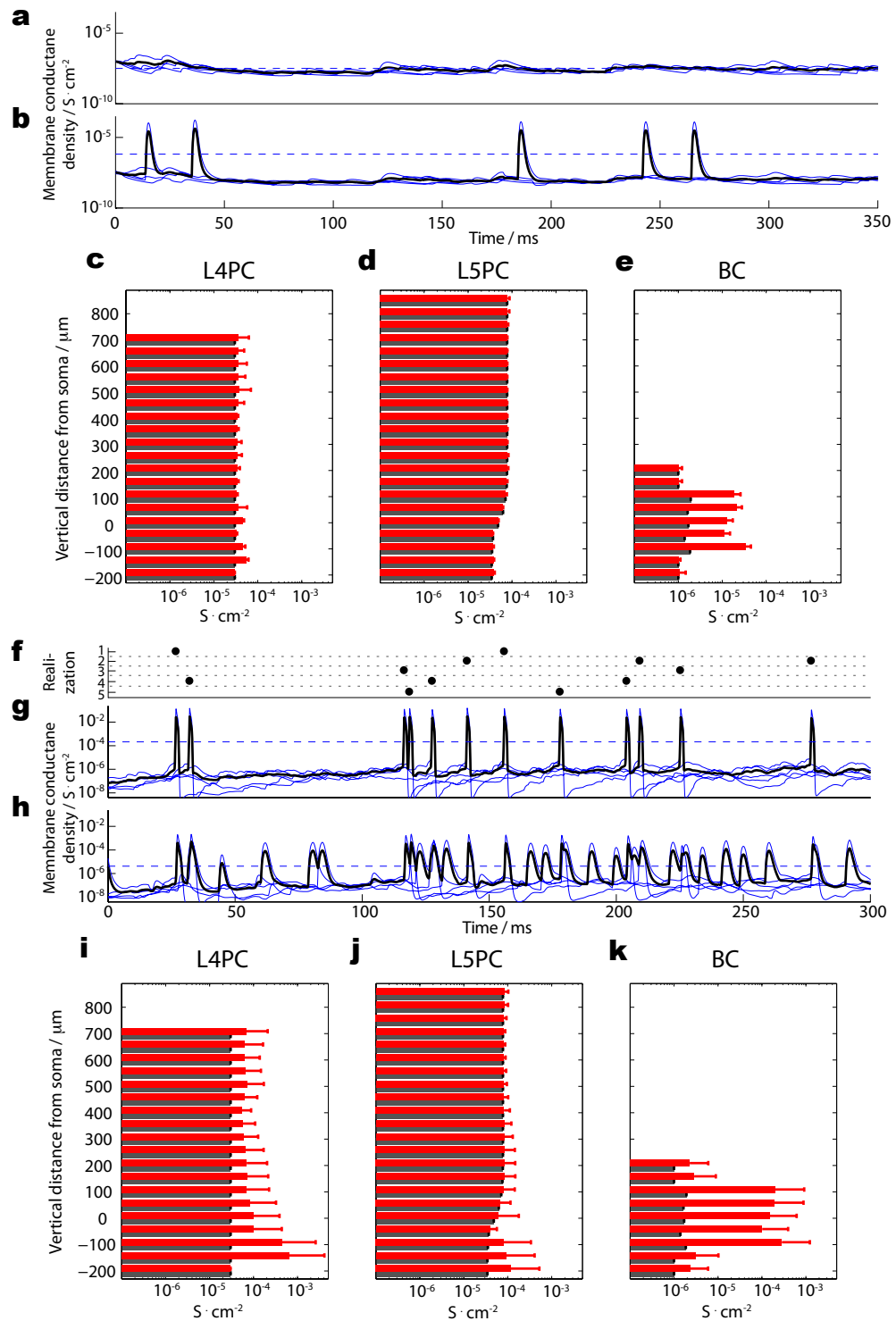


Figure S2 – Comparing membrane conductance on active and passive morphologies

## Chapter 8. A Biophysically Detailed Model of Neocortical Local Field Potentials Predicts the Critical Role of Active Membrane Currents

---

**Figure S2:** Membrane conductance along neurons during UP and DOWN, related to Figs. 7.2-7.5. (a) Membrane conductance density (membrane conductance of a particular compartment divided by the compartment's surface area) measured at the axon initial segment of the L5 pyramidal neuron (blue: individual runs; black: mean membrane conductance over five realizations; dashed blue: overall mean). (b) As in panel (a) but for a compartment in the apical dendrite,  $200\mu m$  from the soma. Transient deflections in membrane conductance (e.g. between 0 and 50 ms) are induced by impinging postsynaptic currents which fail to lead to somatic spiking (see panel a). (c-e) Mean active (red) and passive (black) membrane conductance density during DOWN (five realizations; duration: 300 ms from UP-onset) as a function of distance (along the somadendritic axis) from the soma in (c) 15 L4 pyramids, (d) 15 L5 pyramids, and (e) 12 basket cells (bars: mean over five DOWN and number of cells; error bars: std). During DOWN, conductance for active and passive membrane simulations is very similar for L4 and L5 pyramidal neurons (compare red and black bars) while basket cells remain active (see Fig. 7.2b). Under such conditions, given that basket cells only minimally impact the LFP and CSD, sink-source constellation between active and passive membrane simulations is expected to be very similar. (f) Raster plot of the first 300 ms of five consecutive UP-states for the same L5 pyramidal neuron (circles: spikes; y-axis: realization number) as in panels (a, b). (g-k) Identical panel structure as panels (a-e) but for 300 ms of five consecutive realizations of UP (time 0: UP-onset). As observed in panel (h), in the apical dendrite, transient increases of membrane conductance are observed shortly after each somatic spike indicating backpropagating APs (e.g. see membrane conductances deflections in panels (g) and (h) between 25 and 40 ms). Panels (i-k) depict the fact that during UP membrane conductance increases drastically compared to DOWN, especially in the presence of active membrane conductances. This is particularly true in the perisomatic region of L4 and L5 pyramids (compare panels (c-d) with (i-j)) where membrane conductance density can be as much as ten-fold larger for active than for passive membranes. As during DOWN (panels c-d), membrane conductance remains fairly constant for passive membranes along the somatodendritic axis (i-j). Moreover, membrane conductance density std is approximately ten-fold larger for active than for passive membranes indicating increased neuron-to-neuron variability attributed to spike-related currents and temporally varying spiking.

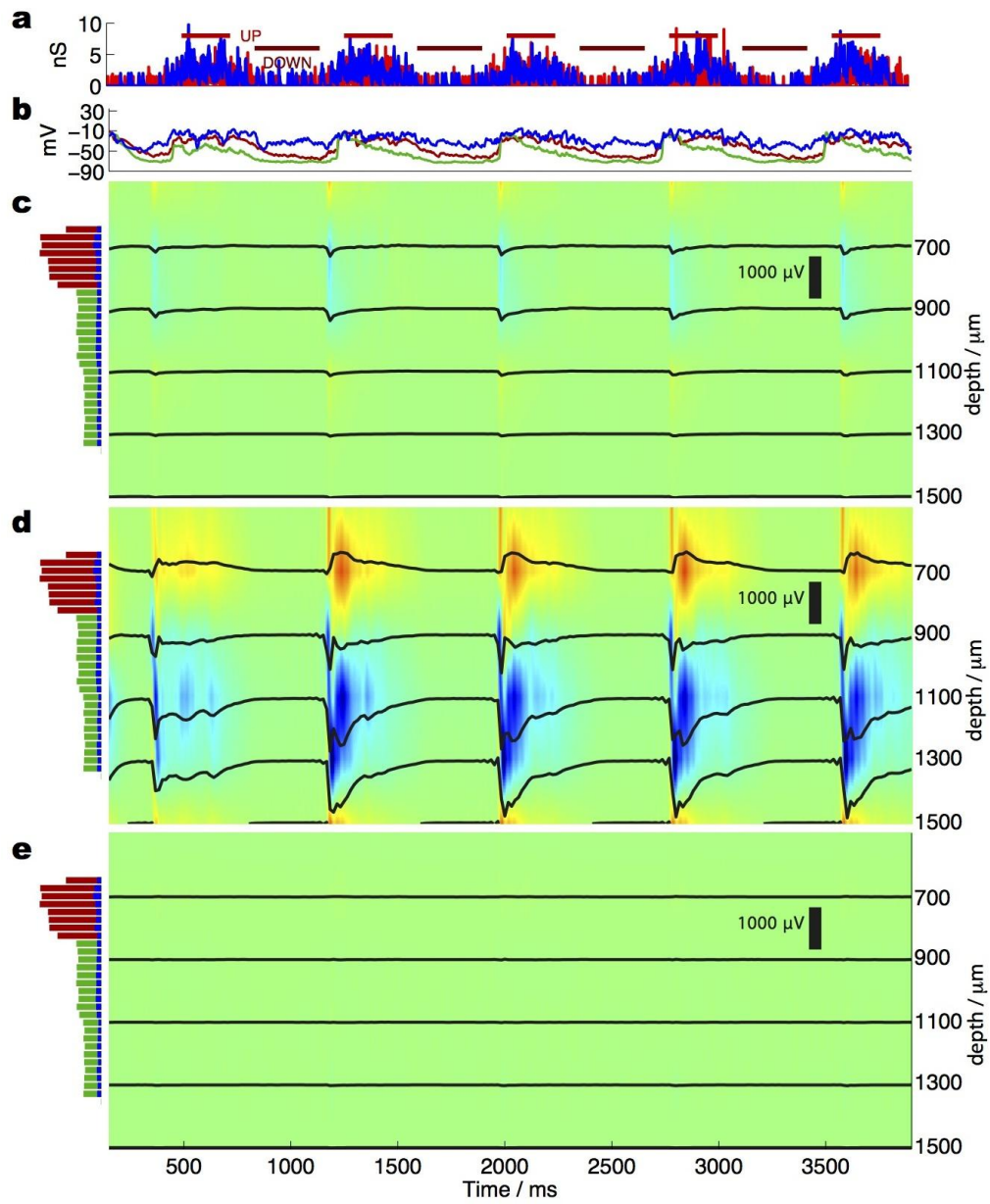


Figure S3 – LFP- and CSD-contribution of individual cell populations for the passive membrane simulation

## Chapter 8. A Biophysically Detailed Model of Neocortical Local Field Potentials Predicts the Critical Role of Active Membrane Currents

---

**Figure S3:** LFP- and CSD-contribution of individual cell populations for the passive membrane simulation shown in Fig. 7.2f related to Figs. 7.2 and 7.3. (a) External excitatory (red) and inhibitory (blue) synaptic input to the same L5 pyramid as in Fig. 7.2a. Yet by design, the postsynaptic events (external as well as generated within the network) are identical. (b) Intracellular voltage traces of the same three neurons (red: L4 pyramid; green: L5 pyramid; blue: L4 basket cell) as in Fig. 2b. The LFP- and CSD-contribution of (c) L4 pyramidal neurons, (d) L5 pyramidal neurons and (e) L4/5 basket cells. CSD calculated along the depth axis (blue: sink; red: source).

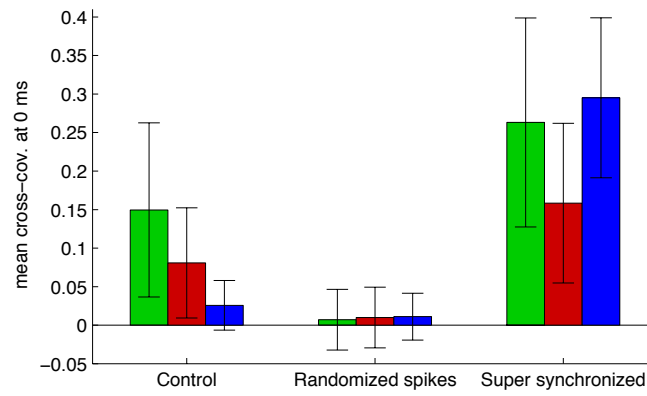


Figure S4 – **Input correlation statistics for the three network cases**

## Chapter 8. A Biophysically Detailed Model of Neocortical Local Field Potentials Predicts the Critical Role of Active Membrane Currents

---

**Figure S4:** Input correlation statistics for the three network cases shown in Figs. 7.2 and 7.5 where correlation among the external synaptic input driving L4 and L5 pyramids is varied ('control', 'uncorrelated' and 'super-synchronized'). As a measure of spiking synchrony, the mean (box) and std (error bar) of the normalized joint peri-stimulus time (PST) histogram is calculated at a lag of 0 ms, that is, the mean cross-covariance of PST histograms of cell pairs, normalized by the product of their standard deviations (see Methods; red: L4 pyramidal neurons; green: L5 pyramidal neurons; blue: L4/5 basket cells).

## 9 Further Results

### 9.1 The limits of spike detection in extracellular signals

#### 9.1.1 Introduction

One important use of extracellular recordings lies in the detection of spikes of cells in the vicinity of the electrode. Under *in-vivo* conditions, spikes of between 1 and 7 cells ("single units") can be isolated from a single location; this number can be increased to between 3 and 9 when four are used in conjunction [Gray et al., 1995]. But it is impossible to tell much more about those cells, beyond their spiking activity: Exactly where they are located relative to the electrode and their morphological type remain unknown. Also, it is hard to estimate the reliability of the approach: what fraction of spikes is missed? More than one electrode can be used in conjunction to increase the reliability of detection and add the capability to triangulate cell positions from spike amplitudes. This comes however with another question: How can the electrodes be ideally positioned with respect to each other to yield maximal reliability? In this section I compare spikes isolated from simulated extracellular traces to the known actual spiking activity of all cells (i.e. *ground truth*) to answer some of these questions.

#### 9.1.2 Spike detection and mapping methods

Most of the complication in the theory of spike sorting is derived from ways to attribute the spikes to individual neurons by clustering certain features of their waveform [Abeles and Goldstein, 1977]. The simulation method simplifies that problem to some degree, as we have direct access to the spike waveform of every single cell. For example, Fig 9.1 depicts the mean extracellular waveform of the action potential of two different types of pyramidal cell around the soma. The shape of the extracellular action potential is characterized by a strong and short negativity, followed by a slower and weaker positive potential near the soma. For locations above the soma an initial positive potential appears, eventually dominating the trace for distances  $> 250\mu m$ . The amplitude is clearly dependent on the distance to the soma, although it falls off more quickly laterally than vertically.

To isolate spikes, we first detected the large deflection they left in the high-pass filtered extracellular traces by finding local extrema with an amplitude  $> 2.5 \cdot$  the standard deviation (Fig 9.2a). This method reliably detected all spikes in extracellular traces generated by single cells, i.e. without noise (see Chapter 5), at any distance. Next, we mapped each spike back to an individual cell in the model by



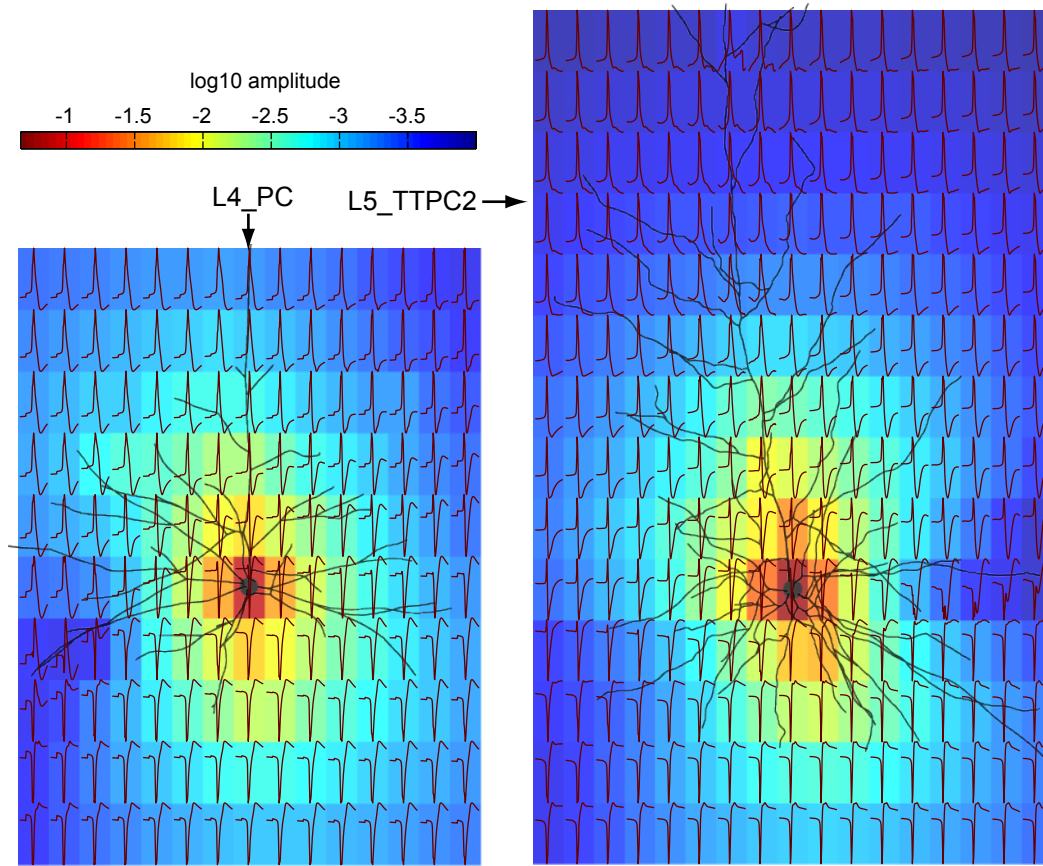


Figure 9.1 – Shape and amplitude of extracellular spikes of pyramidal cells

The shape of the mean extracellular action potential of a L4\_PC (left) and a L5\_TTPC2 (right) at locations in a grid around the soma (red lines, mean of  $N = 100$  APs). The waveforms are normalized to fully fill each box, actual amplitudes (maximum - minimum) are indicated by the color of a box (note the logarithmic color scale), duration is 1 ms. Each box is  $100\mu\text{m}$  high and  $50\mu\text{m}$  wide. Neuron morphology is drawn in black.

comparing the waveforms. *In-vitro* spike waveforms need to be compared to each other to identify clusters [Abeles and Goldstein, 1977], assuming that they are constant for a given cell, or at least that variability between cells exceeds the one within a cell. However, [Anastassiou et al., 2013, 2011] have shown that the extracellular waveform varies significantly depending on the inter-spike interval. *In-silico*, we have access to the individual contributions of single cells to the extracellular potential (see Chapter 5), i.e. the signal generated by a single cell in isolation as it receives identical input and consequently fires identical spikes. This allowed us to match not only against an average extracellular waveform (Fig 9.1), but against the actual trace of individual cells as the spike occurs.

After spike detection in a trace of population activity (Fig 9.2a), the mapping was performed for each detected event in three steps: First we found candidate cells that fired an (intracellularly detected) action potential within 1 ms of the event in question. Then we compared the extracellular contribution of an individual candidate to the full population trace in a time window around the event (Fig 9.2b). If it was the contribution of a certain candidate that generated the event, we expect a strong overlap

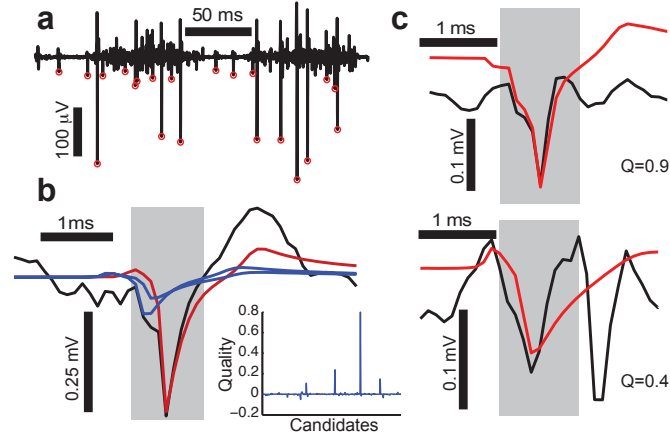


Figure 9.2 – Mapping of detected extracellular events to intracellular spikes

(a) 250 ms of a highpass-filtered (100 Hz) trace of *in-silico* extracellular population activity. Detected spikes are indicated as red circles. (b) A detected extracellular event and the extracellular contributions of the three most likely candidates to have caused the event. The contribution of the most likely candidate (red line) shows a very large overlap with the full extracellular trace (black line) leading to a quality of fit (see methods) of 0.8. The next two candidates (blue lines) show significantly less overlap and have scores of only 0.22 and 0.19. The grey shaded area shows the time window over which the overlap is calculated. Inset: Distribution of quality score of all cells that fired 1 ms around the event. (c) Example of a good fit (top, quality 0.9) and a bad fit (bottom, quality 0.4) that is rejected as a false positive because the quality is  $< 0.5$ . Black lines: full extracellular traces, red lines: individual contributions.

of individual contribution and population trace (red and black traces in Fig 9.2b). In particular, we calculated the cross-covariance at lag 0 between individual and population trace in a time window of 1 ms around the event, normalized by the variance of the population trace:

$$Q_i = \frac{\int_{t_e-0.5}^{t_e+0.5} (V_p(t) - \bar{V}_p) \cdot (V_i(t) - \bar{V}_i) dt}{\int_{t_e-0.5}^{t_e+0.5} (V_p(t) - \bar{V}_p)^2 dt}, \quad (9.1.1)$$

where  $t_e$  denotes the time of the detected extracellular event,  $V_p$  the trace of population activity,  $V_i$  the contribution of an individual cell  $i$  and  $\bar{V}$  the mean of  $V$  in the time window  $[t_e - 0.5, t_e + 0.5]$ . This yields a dimensionless indicator of the quality of fit between -1 and 1 (since the variance of the population trace was always larger than the variance of the individual contribution); it takes on values near 1 for a good fit of both amplitude and shape.

Finally, we excluded all events where the maximal quality of fit was below 0.5 (Fig 9.2c, bottom), considering them false positives instead. This happened for under 1% of all detected events.

### 9.1.3 Results

In a trace of the extracellular contribution of a single cell, every single spike could be detected and mapped correctly with a quality of 1. That is because considering an individual contribution only is an idealized situation with not a single source of noise. In reality, there are two sources of noise to be considered: The ongoing activity of other neurons and the internal noise of the measuring system.

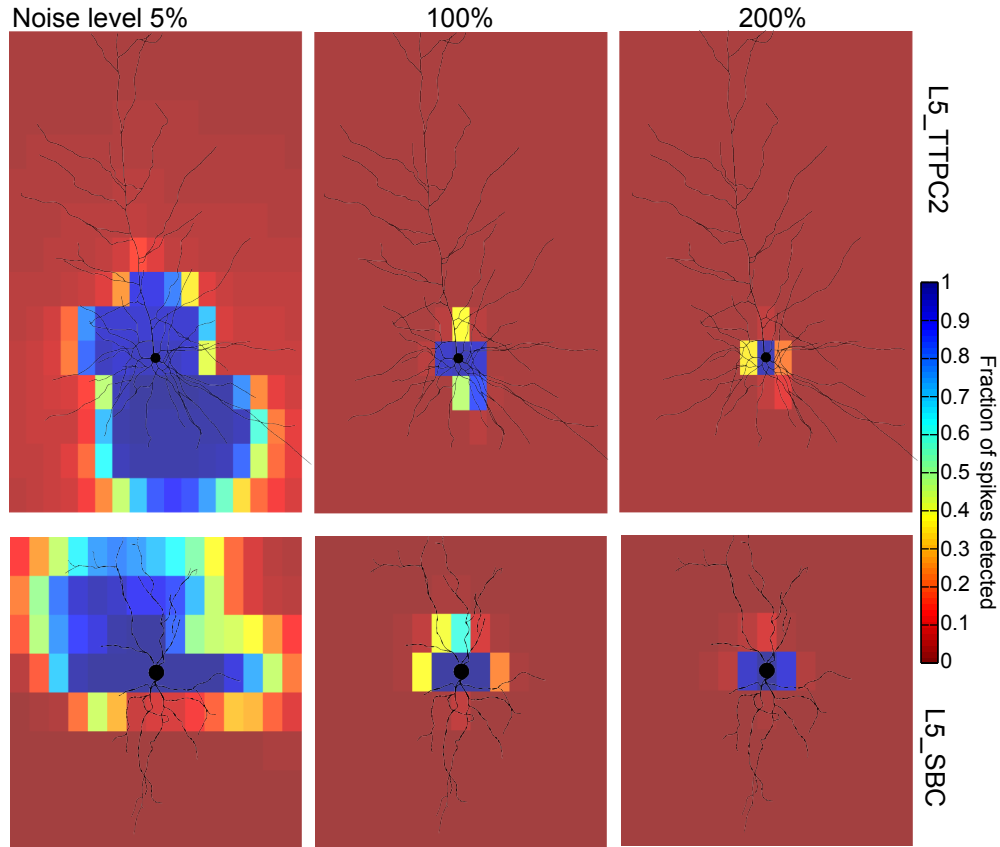
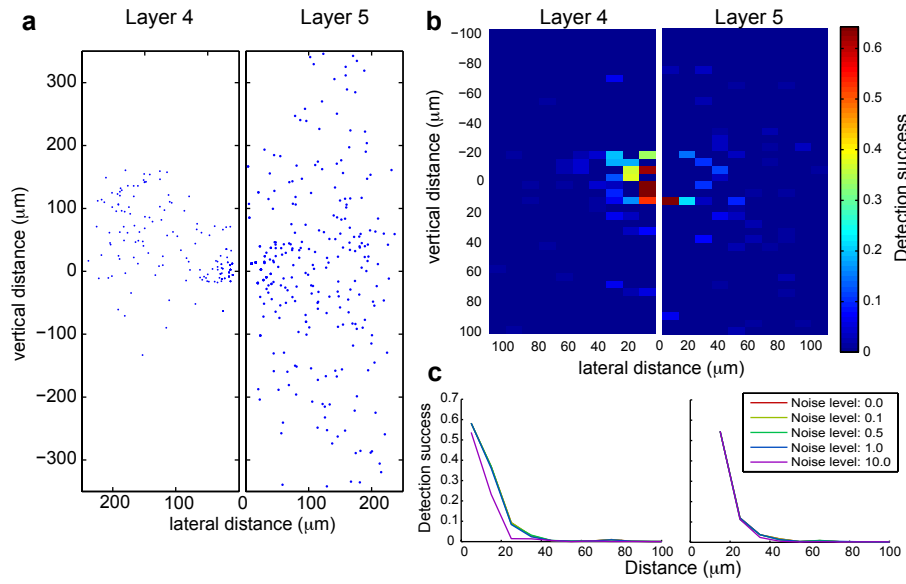


Figure 9.3 – Extracellular detection of isolated spikes in the presence of electrode noise  
We calculated the fraction of spikes detected in the extracellular contribution of a single cell spiking at pseudo-random times, when electrode noise at different levels is added to it. Noise was obtained from an *in-vitro* recording in saline and multiplied with (from left to right): 0.05, 1.0 or 2.0. The fraction detected when recording from the center of a rectangle is depicted in the rectangles color. Each rectangle is  $50\mu\text{m}$  wide and  $100\mu\text{m}$  high. Top: for an exemplary L5\_TTPC2 cell, bottom: for an exemplary L5\_SBC cell.

To assess the role of internal noise, we used an *in-vitro* trace of an extracellular electrode in saline, adding parts of it to the *in-silico* recording of an individual, spiking cell. We made the chosen cell spike 100 times at pseudo-random times, added a randomly chosen snippet of *in-vitro* noise multiplied by a factor to it and attempted to detect the spikes. This experiment was repeated for 10 different snippets and at 3 different noise levels for extracellular locations in a grid around the cell (Fig 9.3). Already noise at a quarter of the realistic level reduces the range of reliable detection to approximately  $100\mu\text{m}$ . For the L5\_TTPC, the vertical range is higher than the lateral one with almost  $200\mu\text{m}$ . At realistic noise levels, the range is quickly reduced to  $50\mu\text{m}$ , after which further increasing it does very little. In particular, it is striking how much the detection tends to be an *all-or-nothing* process, where detection rates are either 100% or quickly fall to zero.

To assess the role of ongoing activity, we calculated the extracellular potential in a full population of  $N = 31000$  cells under two conditions: External synaptic input was given to cells in either layer 4 or 5,



**Figure 9.4 – Extracellular spike detection during ongoing full population activity**  
(a) The location of all cells that caused at least one detected extracellular spike during 5.5 seconds of activity in a full microcircuit model is indicated as blue dots. The location relative to the locus of the extracellular recording is indicated: Lateral distance (within a layer) and vertical distance (across layers). Left: Activity is induced as synaptic input into layer 4 and measured in the center of that layer. Right: induced and measured in layer 5. (b) We calculated the fraction of spikes that were successfully detected in an extracellular trace of full microcircuit activity. The fraction for spatial bins relative to the recording site is indicated. Left: activity induced and recorded in layer 4, right: in layer 5. (c) The fraction successfully detected spikes at different distances when additional *in-vitro* noise is added. The noise of an electrode in saline is added with different multipliers, 1.0 indicates the originally recorded noise level. Left, right as in (b).

modulated with 1 Hz. This caused a cycle of phases of high activity and consequently a high level of noise interspersed with relative silence at 1 Hz. In both cases, the extracellular potential was calculated in the center of the layer receiving the input.

In both cases, spikes are picked up from cells from most cells closer than  $40\mu\text{m}$  to the recording location (Fig 9.4a), but also from a number of cells further away at distances up to  $350\mu\text{m}$ . Considering that the number of cells increases linearly with lateral distance however,<sup>1</sup> indicates that spike detection at those distances is an exception rather than the norm. The apparent longer vertical reach in the layer 5 case is purely due to the lower width of layer 4: There simply are fewer cells actually firing beyond the layer boundaries.

Detection at large distances is just an exception occurring in phases of low activity. This becomes abundantly clear, once the fraction of successful spike detection at different locations is considered (Fig 9.4b): Detection under these circumstances is only reliable for distances up to  $20\mu\text{m}$ . More than rate of success over 50% was achieved for only 6 cells in layer 4 and 3 cells in layer 5. The 100% increased number of reliably isolated cells in layer 4 over layer 5 is proportional to the overall higher cell density in

1. The number of cells at a lateral distance of  $x\mu\text{m}$  is proportional to the circumference of a circle with radius  $x$ :  $2 \cdot \pi \cdot x$

that layer ( $240,000mm^{-1}$  against  $105,000mm^{-1} \Rightarrow 128\%$  increase in the microcircuit model), indicating that it is caused by a larger number of cells being close enough to the recording site, not an intrinsic property of layer 4 cells.

When electrode noise at different levels was added to the full extracellular traces, it mattered very little for the spike detection reliability measurement at close ranges (Fig 9.4c). Only at 10 times the realistic noise level did we find a noticeable drop in reliability, but only for layer 4. Adding noise at realistic levels did however completely remove the occasional spike detection at larger distances (result not shown). This further indicates that the long range detection events were only possible for isolated spikes fired at periods of relative quietness.

### 9.1.4 Conclusions

We have used *in-silico* extracellular potentials to assess the spatial limits of extracellular spike detection. We found that a theoretically almost unlimited range under idealized conditions is drastically reduced by noise due to ongoing activity as well as internal noise of the recording apparatus. While the low levels of ongoing activity occasionally may increase the range, a reliable detection can only be achieved for a handful of cells closest to the recording site ( $< 25\mu m$ ). In contrast, the presence of recording noise alone still allows reliable detection at distances of  $100\mu m$ , indicating that efforts to decrease that source of noise would not be helpful for investigating population activity.

Detection has a slightly larger range vertically than laterally (especially in layer 4), indicating that placing multiple electrodes along a vertical axis adds the most redundancy to the detection (if high reliability is needed) and placing them laterally increases the number of cells covered.

This work covered only the question of the range and prerequisites of detecting a spike in an extracellular trace at all. As we are confident that our technique correctly maps extracellular spikes back to neurons, we can use it in the future to assess the accuracy of different spike sorting algorithms, such as feature clustering.

## 9.2 Comparing Structural and Functional Inhibition under In-Vitro and In-Vivo Conditions

*Contributions of the thesis author:*

Methods, theory, design and analysis by the author in conjunction with *Albert Gidon, HUJI, Jerusalem*

### 9.2.1 Introduction

One striking feature of cortical microcircuits is their great variety of morphological interneuron types [Stepanyants et al., 2004, DeFelipe et al., 2013]. The BBP model defines 42 different inhibitory types compared to only 13 excitatory types although in total, only between 10 and 30% of neurons are inhibitory [Meyer et al., 2011, DeFelipe et al., 2002]. It is known that the typical shapes of axonal trees of interneurons can lead to them placing synapses on different parts of the postsynaptic morphology [Lübke, 2003, Staiger et al., 2000], for example Martinotti Cells (MCs) are known to be targeting the distal parts of a pyramidal cells dendritic tree, Basket Cells (BCs) the proximal parts [Markram et al., 1997, Wang, 2002].

## 9.2. Comparing Structural and Functional Inhibition under In-Vitro and In-Vivo Conditions

This targeting can have significant functional consequences. Inhibitory synaptic conductance, in addition to hyperpolarizing the cell, leads to a local increase in input resistance, making nearby excitatory synapses temporarily less effective [Gidon and Segev, 2012]. This type of local synaptic interaction may be the key to understanding inhibitory diversity: It is possible that different functions of inhibitory neuron types are implemented by targeting different parts of the postsynaptic morphology, leading to different interactions with excitatory input. For example, MCs targeting the tuft of Pyramidal Cells may act as a gating mechanism for excitatory input on the apical dendrite (such as POM projections (Fig 5.8) or from L23 PCs).

Testing that hypothesis requires us to first assess whether the inhibition profiles of different inhibitory types are significantly different at all. We use the derived Connectome (see Chapter 3) to investigate this question for the postsynaptic L5\_TTPCs, as this morphology type receives input from most inhibitory types (Fig 3.7).

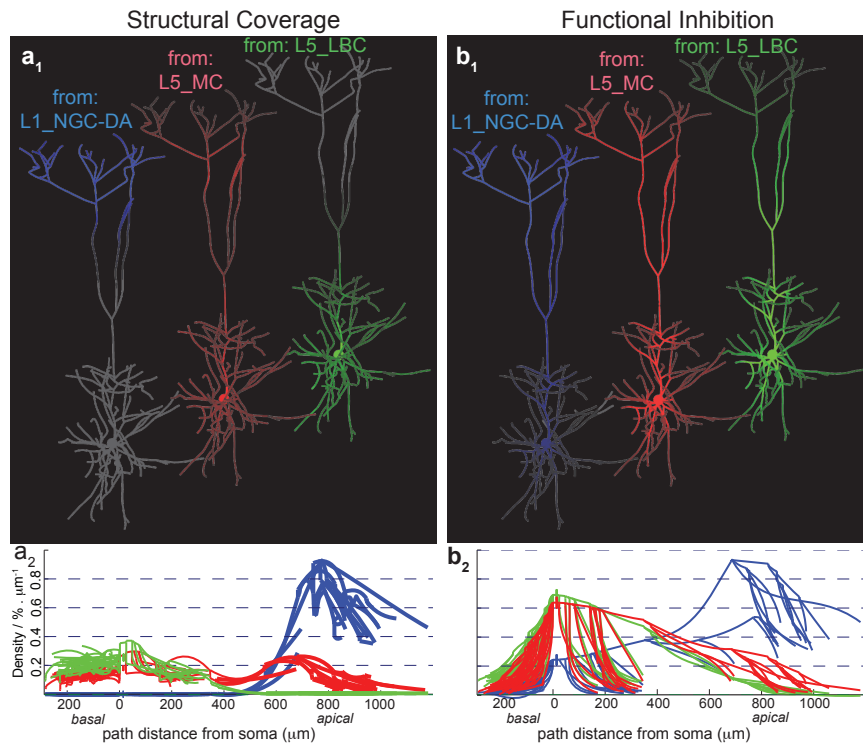


Figure 9.5 – Structural and functional inhibition of an L5\_TTPC

a) Mean structural coverage of the dendritic tree of an exemplary L5\_TTPC with synapses from three exemplary inhibitory cell types. Profiles calculated from over 10,000 connections each. Top: Coverage color coded with high saturation indicating high coverage and different colors different presynaptic types as labeled in the figure. Bottom: Coverage against path distance from the soma for inhibition from the same inhibitory types. Colors indicate different types as in top. b) Same for functional inhibition calculated as the average shunt level calculated from the structural coverage in a.

### 9.2.2 Methods

#### 9.2.2.1 Structural innervation profile

In order to obtain an average inhibitory innervation profile for a postsynaptic cell, we built a microcircuit containing a large number of copies of an exemplary L5\_TTPC2 morphology at different locations with different rotations. After running the Connectome algorithm (Chapter 3), each copy will receive a slightly different, but biologically relevant inhibitory innervation profile and we can average across all of them to obtain the *typical structural inhibition profile of an L5\_TTPC2 neuron*.

#### 9.2.2.2 Functional innervation: The shunt level

When discussing the functional relevance of inhibitory types, we have to consider the actual functional impact of the types. As mentioned above, inhibitory synapses have a *shunting* effect on their immediate neighborhood, i.e. they decrease the PSP amplitudes of synapses around them. This type of non-locality can logically only decrease the specificity of inhibition, turning the structural profile into an upper boundary.

We calculated the relative shunt level  $\frac{\Delta R_i}{R_i}$  using an analytical solution for calculating the input resistance in compartmental neuron models described in [Koch and Segev, 1998]. We compared baseline input resistances to the one when all synapses formed by an individual presynaptic interneuron are activated. Finally, we averaged across presynaptic neurons of a given type to get the *typical functional inhibition profile* of that type.

#### 9.2.2.3 Computing domain-specificity of inhibition

In order to quantify the specificity of inhibition or the difference between two inhibition profiles, we developed an approach grounded in information theory. After normalization, both the structural as well as the functional inhibition profile can be interpreted as probability distributions: The probability to find a randomly selected synapse or quantum of shunting at a given location. We define the divergence of two inhibition profiles  $a$  and  $b$  as the mutual information between the profiles  $C$  and inhibitory type  $T$ :

$$I_{a,b}(C; T) = \sum_{0 \leq i < N, j \in \{a,b\}} P(C_i, T_j) \cdot \log_2 \left( \frac{P(C_i, T_j)}{P(C_i) \cdot P(T_j)} \right) \quad (9.2.1)$$

Similarly, we define the specificity of an inhibitory type as the mutual information between its profile and the profile derived from using *all* inhibitory synapses of *all* types.

### 9.2.3 Results

Fig 9.5a shows that as expected, large differences between inhibitory types are evident with structural BC innervation not extending beyond basal dendrites, MC innervating almost the whole dendrite and innervation from Layer 1 exclusively the tuft. There is virtually no overlap between inhibition from layer 1 and from BCs. Functionally (Fig 9.5b), the difference is diminished, showing around 50% overlap of the profiles.

## 9.2. Comparing Structural and Functional Inhibition under In-Vitro and In-Vivo Conditions

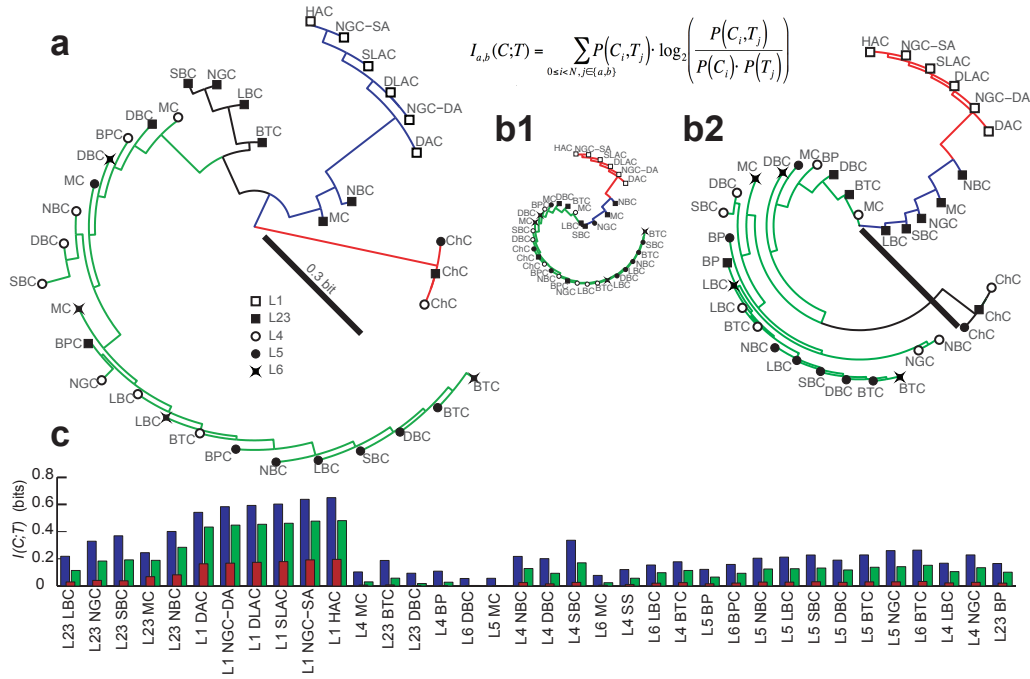


Figure 9.6 – Domain specificity of structural and function inhibition

a) A phenetic tree indicating the distances, calculated as mutual information, between the structural inhibition profiles of different morphology types. The distance is roughly proportional to the total path length along radial edges between two types/nodes (see scale bar). Accurate to within 5% due to distance averaging in the tree reconstruction process. b) Same for the functional inhibition profiles under *in-vitro* (left, b1) and *high-conductance* (right, b2) conditions. All three trees are on the same scale. c) Specificity of inhibitory types, calculated as the distance between its specific inhibition profile and the average inhibition profile, structurally (blue bars), under *in-vitro* (red bars) and *high-conductance* (green bars) conditions.

We calculated the pairwise differences between inhibition profiles as described above and visualized the results as a phenetic tree using an established method to reconstruct a tree from distance matrices (sequential neighbor joining, see [Saitou and Nei, 1987], Fig 9.6a). Structurally, four clear clusters of inhibition emerge: Chandelier Cells (ChCs), Layer 1, Basket Cell in Layer 2/3 (L23\_BCs) and the rest. Arguably, the last cluster could be split once more. The differences between Layer 1 inhibition and the rest or Chandelier Cell inhibition and the rest approach 1 bit, the theoretical maximum. Functionally (Fig 9.6b1), the differences are drastically reduced, in particular the very specific nature of ChC inhibition is completely lost; only the specificity of Layer 1 inhibition remains.

Those results are however for derived from simulated *in-vitro* conditions, characterized by high input resistances due to low ongoing activity; during "up states" under *in-vivo* conditions, it falls significantly [Destexhe et al., 2003], (although see [Waters, 2006]). We increased the conductance of membranes until the somatic input resistance falls to approximately  $15M\Omega$  to simulate such a *high-conductance state*. As a result, the reach of shunting inhibition is decreased and the specificity consequently partly recovered (Fig 9.6b2). In particular, Layer 1 still forms a cluster and ChCs once more cluster separately, although no longer near the 1 bit distance they have structurally. Surprisingly, the distances within the cluster formed by the rest of inhibitory types seems to have recovered relatively well, leading to a large



degree of variability within that cluster under *high-conductance like* conditions.

Comparing the innervation to the average one formed by pooling *all* inhibitory synapses (Fig 9.6c) reveals specific inhibition – aside from Layer 1 and ChCs – mainly from different types of Basket Cells with dendrite targeting cells (MC, BP, DBC) very unspecific.

### 9.2.4 Conclusions

We introduced an information-theoretical measurement of innervation difference and specificity and explored it for postsynaptic L5\_TTPCs. We found that based on the inhibitory coverage, distinct roles for Chandelier Cells and cells in Layer 1 can be predicted, although a *high-conductance* state is required for Chandelier specificity.

While only Layer 1 specificity remains under *in-vitro* conditions, a large part can be recovered in a *high-conductance* state. Especially the differences between inhibitory types in layer 2-6 recover well and as a result – relative to the overall level of specificity – they cover a larger range of specific inhibition patterns in that state. This indicates that the functionality of different types of inhibition will have to be studied under *in-vivo* conditions.

The lack of specificity of dendrite targeting cells compared to Basket Cells may already indicate a distinct role as a global gain control mechanism, while BCs operate with higher granularity modulating more specific types of input. Overall, the specific inhibitory patterns found support a view of dendrites as not just a passive cable leading to the soma, but an active site of input integration, potentially increasing the computational capability of a single cell.

## **Concluding Remarks** **Part IV**



## 10 Context and Relevance of This Work

In this thesis I described a number of significant improvements of the cortical microcircuit model of the Blue Brain Project and a number of insights and predictions made possible by simulations of neural activity using the improved model. Of the improvements, the most prominent one is the derivation of the local connectome, as it is not only the first attempt at reconstructing cell-to-cell connectivity on such a large scale, but it will be central to every future use of the model, as the recurrent connectivity is one of the main determinants of circuit dynamics.

Further, the connectome derivation algorithm describes a very general method utilizing any available data and generalizing for the vast majority of missing data points. As such, it will likely be compatible with future modelling efforts of different microcircuits, such as other animals, brain regions, or pathological phenotypes.

The insights and predictions are related to the improvements, either directly – in the case of information theoretical connectome analysis – or indirectly – in the case of extracellular potentials. They have the potential to improve our understanding of microcircuits and their activity or – a more hands-on result – at the very least improve our interpretation of extracellular signals.

Beyond the relevance of the individual results, this work as a whole gives an example of how research in complex models of neural systems inherently moves between *quality management* and *model use*. With the Human Brain Project in the start-up phase at the time of writing and several other large scale modelling efforts underway Jones et al. [2009], Kandel et al. [2013], we have to address the question how exactly simulation based research is executed most efficiently.

The Human Brain Project explicitly states its goal to provide a platform for continuing integration of experimental data, i.e. the goal is not a final 'perfect' model. In other words, the steps of building the model and using the model are not temporally separated as in traditional modelling projects. This thesis shows the power of an approach that does not even keep them conceptually separated.

On a high level, we can identify six different types of work with the microcircuit model mentioned in this thesis:

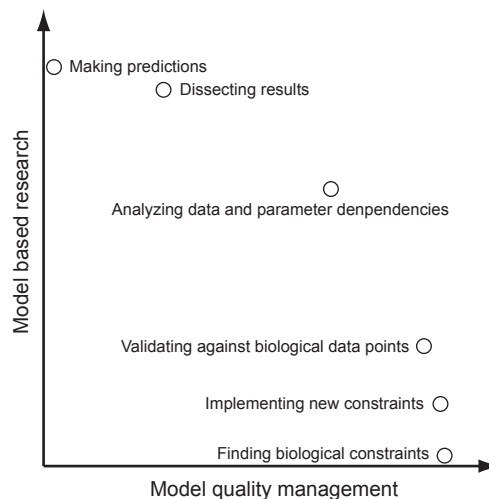
1. **Finding biological constraints:** This refers to identifying, extracting and interpreting biological data point constraining the model, either from the literature or original research. For example, a new result about biological synapse numbers in a certain pathway will have to be integrated into the constraints for the connectome algorithm.
2. **Implementing new constraints:** At this stage, new synapse number constraints can be easily used in the model by editing an xml-formatted text file. That was not the case before the de-

velopment of the connectome algorithm in its present form. Similarly, if we identify the need to consider a new modality of constraints – such as the attenuation of the extracellular action potential – we will have to "make room" for the constraints in the model building process.

3. **Analyzing data and parameter dependencies:** Certain data point are intrinsically related, such as functional and structural strength of a synaptic connection. For example, in section 3, we analyzed the relation between different connectivity measures, cell densities and axon length. On the one hand, this allows one to find a minimal set that fully constrains the model. On the other hand, this leads to predictions about potential effects of modified measures, for example in models of pathological phenotypes.
4. **Validating against biological data points:** Not every biological result can have an explicitly constraining role in the building process. Still, in order to validate the model it has to be compared against them by re-creating *in-vitro* or *in-vivo* experiments.
5. **Dissecting results:** After a successful validation, i.e. if we re-create a certain biological finding in the model, we can ask the question what are the underlying causes that give rise to that particular result. The *in-silico* approach allows us to fully dissect the model until the root causes have been identified, such as we dissected extracellular contributions in sections 6 and 7.
6. **Making predictions:** Finally, once we are convinced that the model is validated sufficiently, we can subject it to new conditions to predict the response. For example, we predicted a common neighbor rule to shape the connectivity of more than just L5\_PCs in section 3 and we predicted the response of the microcircuit to different input frequencies in section 7.

Figure 10.1 – Types of work required for continuous usage of an integrative model

Six different types of work have been identified and ranked according to how much they are relevant for *model based research*, i.e. generating original, publishable research, and *model quality management*, i.e. the continuous updating of the model itself. Ranking is the subjective opinion of the author.



If we arrange these activities with respect to how much they manage the quality of the model against actually using it for research (Fig 10.1), we find that it covers the whole spectrum. Additionally, all of them are linked to each other in various ways, as demonstrated in this thesis: It was the attempt to validate extracellular potentials that led to a number of biological constraints that had to be correctly implemented as a prerequisite (see section 2). In implementing them we not only gathered the relevant biological data, but also identified the dependencies to find a fully constraining set (see section 3). Validations led to the opportunity of dissecting the extracellular potential contributions (see section 6) and finally changing input conditions to predict the response to different frequencies (see section 7). This demonstrates that the quality management and actual research related activities are ideally not to be separated. Where such a separation is inevitable, for example if model complexity grows beyond a certain threshold, effective communication between the two arms has to be facilitated.

## 11 Ongoing and Future Work

Compared to what is covered in this thesis, a several orders of magnitude higher volume of research using the cortical microcircuit model is in the future. With **Reconstruction of the Neocortical Microcircuit** (see Appendix) nearing its publication, not only will the productivity of internal collaborators be boosted, but the model is opened up to external collaborators for their own projects.

Some of the next steps will be logical extensions, continuations or even replacements of the research described in this thesis.

The **connectome derivation** described in section 3 has been proven to be a flexible algorithm robustly reproducing any biological measurement used to constrain it. The next step will be to use it in models beyond a rat neocortical microcircuit – other species, brain regions or in pathological models. Autism for example has been characterized by an increase in local neocortical connection probability Courchesne and Pierce [2005], this has been found to be accompanied by a decrease in synapse numbers in a rat model: This change corresponds to a single parameter ( $a_3$ ) in the connectome algorithm. We will explore whether we can build an *in-silico* reconstructed microcircuit that also reproduces functional aspects of the model (PSP amplitudes, spiking, etc).

Further refinements can be made to the algorithm as well. In particular, at the first and third stage of the algorithm we employ a completely random pruning, i.e. one with uniform probabilities. Instead, the pruning can be more targeted in order to re-create more biological measurements: (1) In the first stage, the pruning can be made *touch-distance dependent*: Biologically, most synapses span only a fairly short gap between axon and dendrite Arellano [2007], (Benavides, DeFelipe, unpublished observations). While the maximal distance is roughly equal to the one used in the model, only very few actually reach the maximum. In the model on the other hand, due to elementary geometrical considerations, most synapses are at maximum. By introducing touch-distance dependent pruning, the biological distance profile can be re-created. (2) As shown in section 3, the microcircuit model does not re-create the biological increase in reciprocal connection probability. This can be remedied by preferably pruning non-reciprocal connections in step 3 of the algorithm.

As outlined, the third pruning step creates room for rewiring: By not activating all viable multi-synapse connections, some of them can be added later on from this pool according to structural plasticity rules (and others removed). Currently ongoing is work to implement and tune this kind of plasticity in the model.

The calculation of **extracellular potentials** is a versatile tool that can be used in a number of different studies in the future. The first one — already in preparation — will be to use it for a characterization of

the full microcircuit and under a more diverse set of inputs.

Still, further improvements will have to be made. The algorithm to calculate extracellular potentials is based on volume conductor theory with the assumption that extracellular resistance is uniform and isotropic. While these assumptions are standard in the field Pettersen and Einevoll [2008], Pettersen et al. [2008], Lindén et al. [2011], we will investigate in the future the impact of a layer-dependent extracellular resistance. A step further in the future will be the implementation of anisotropic, i.e. direction dependent resistances. Since the model has the full dendritic density (albeit not full axonal density), the direction dependence can be calculated based on the preferred direction of neurite morphology in the immediate vicinity. For example, the prominent vertical alignment of apical dendrites may lead to higher horizontal than vertical resistance. Still, for that endeavour an extensive set of experimental data will be needed for calibration.

# **A Supplementary Material**

## **A.1 Example of a thalamocortical projection specification**

As used in Chapter 4.3.1



```

<!--
Thalamocortical VPM projection
Densities based on Fig 1, Meyer et al., Cer cortex 2010
Author: Michael Reimann, Srikanth Ramaswamy, June, 2012
-->
<Projections>
  <Projection id="thalamocortical -- VPM" type="volume projection">
    <!-- volumes are axis aligned rectangular for now -->
    <Volume>
      <Boundaries>
        <!-- defines top of the volume -->
        <Boundary which="y_max" type="layer" id="3" rel="0.5"/>
        <!-- defines bottom -->
        <Boundary which="y_min" type="layer" id="4" rel="0"/>
        <Boundary which="x_min" type="mosaic" hex="2"/>
        <Boundary which="x_max" type="mosaic" hex="2"/>
        <Boundary which="z_min" type="mosaic" hex="2"/>
        <Boundary which="z_max" type="mosaic" hex="2"/>
      </Boundaries>

      <!-- specify density profile with y coordinates relative too the volume -->
      <DensityProfile type="y_rel">
        <bin height="0.05" density="0.01" unit="/micron^3"/>
        <bin height="0.15" density="0.02" unit="/micron^3"/>
        <bin height="0.25" density="0.03" unit="/micron^3"/>
        <bin height="0.35" density="0.04" unit="/micron^3"/>
        <bin height="0.45" density="0.04" unit="/micron^3"/>
        <bin height="0.55" density="0.04" unit="/micron^3"/>
        <bin height="0.65" density="0.03" unit="/micron^3"/>
        <bin height="0.75" density="0.02" unit="/micron^3"/>
        <bin height="0.85" density="0.01" unit="/micron^3"/>
        <bin height="0.95" density="0.01" unit="/micron^3"/>
      </DensityProfile>

      <!-- Which postsynaptic cells and regions are valid? -->
      <Targets>
        <target preference="1.0">
          <cell_type mType="Mosaic" />
          <region secType="DENDRITE"/>
          <region secType="APICAL_DENDRITE"/>
          <!-- Synaptic dynamics, specified in Synapses block -->
          <synType id="projectionSynapse1" fraction="1.0"/>
        </target>
      </Targets>
    </Volume>
  </Volume>
  <Volume>
    <Boundaries>
      <!-- defines top of the volume -->
      <Boundary which="y_max" type="layer" id="5" rel="0.6"/>
      <!-- defines bottom -->
      <Boundary which="y_min" type="layer" id="6" rel="0.85"/>
      <Boundary which="x_min" type="mosaic" hex="2"/>
      <Boundary which="x_max" type="mosaic" hex="2"/>
      <Boundary which="z_min" type="mosaic" hex="2"/>
      <Boundary which="z_max" type="mosaic" hex="2"/>
    </Boundaries>

    <!-- specify density profile with y coordinates relative too the volume -->
    <DensityProfile type="y_rel">
      <bin height="0.05" density="0.005" unit="/micron^3"/>
      <bin height="0.15" density="0.01" unit="/micron^3"/>
      <bin height="0.25" density="0.015" unit="/micron^3"/>
      <bin height="0.35" density="0.02" unit="/micron^3"/>
      <bin height="0.45" density="0.0225" unit="/micron^3"/>
      <bin height="0.55" density="0.025" unit="/micron^3"/>
    </DensityProfile>
  </Volume>

```

```

        <bin height="0.65" density="0.0275" unit="/micron^3"/>
        <bin height="0.75" density="0.03" unit="/micron^3"/>
        <bin height="0.85" density="0.015" unit="/micron^3"/>
        <bin height="0.95" density="0.005" unit="/micron^3"/>
    </DensityProfile>

    <!-- Which postsynaptic cells and regions are valid? -->
    <Targets>
        <target preference="1.0">
            <cell_type cell_target="Mosaic" />
            <region secType="DENDRITE"/>
            <region secType="APICAL_DENDRITE"/>
            <!-- Synaptic dynamics, specified in Synapses block -->
            <synType id="projectionSynapse1" fraction="1.0"/>
        </target>
    </Targets>
</Volume>

    <!-- Describes how the synapses are grouped into groups that are activated by the same gid -->
    <InputMapping type="MapToMiniColumns" sigma="20" exclusion="60"/>
</Projection>
<!-- synapse dynamics SR-->
<Synapses>

    <SynapseType label="projectionSynapse1" id="120">
        <!-- synaptic parameters are mainly derived from Amitai, 1997; Castro-Alamancos &
        Connors 1997; Gil et al. 1997; Bannister et al. 2010 SR -->
        <!-- peak synaptic conductance SR -->
        <parameter id="gsyn" mean="0.4" std="0.2"/>
        <!-- decay time constant SR -->
        <parameter id="dtc" mean="1.74" std="0.2"/>
        <!-- Absolute synaptic efficacy - not used, but a placeholder
        continuing from legacy nrn.h5 SR -->
        <parameter id="Ase" mean="1" std="0.01"/>
        <!-- Analogous to transmitter release probability SR -->
        <parameter id="Use" mean="0.75" std="0.02"/>
        <!-- Time constant for recovery from depression SR -->
        <parameter id="D" mean="671" std="17"/>
        <!-- Time constant for recovery from facilitation SR -->
        <parameter id="F" mean="17" std="5"/>
    </SynapseType>
    <!-- for now we prescribe the same parameter set for
    both VPM and P0m innervation until specific data sets become available SR -->
    <SynapseType label="projectionSynapse2" id="120">
        <parameter id="gsyn" mean="0.4" std="0.2"/>
        <parameter id="dtc" mean="1.74" std="0.2"/>
        <parameter id="Ase" mean="1" std="0.01"/>
        <parameter id="Use" mean="0.75" std="0.02"/>
        <parameter id="D" mean="671" std="17"/>
        <parameter id="F" mean="17" std="5"/>
    </SynapseType>
</Synapses>
</Projections>

```



# B A Brief Introduction into the Underlying Neuroscientific Concepts

In this thesis, I will presume some general concepts and terms to be known, at least superficially. For interested readers from outside the field I will give a brief and non-comprehensive explanation of the most fundamental themes in this chapter.

## B.1 From Brain to Neocortex to Microcircuits

The brain is fundamentally an information processing system: It takes up information sent by the periphery and turns it into an appropriate reaction. This fundamentally splits neural activity into a sensory (input) and a motor (output) part and theoretically, when a vertebrate reacts to a stimulus we can track a flow of information from sensory organs into the brain and out again to muscles effecting a behavioral pattern. For example, when a driver encounters a red traffic light the light with a wavelength of  $650\text{nm}$  hits the retina, exciting cone cells. That sensory signal is carried into the brain, where it is transformed into a motor signal sent out to the muscles in the leg, causing the foot to be placed on the brake.

The biggest unknown in this flow is the transformation at the center: A decision has to be made, whether the red is actually a traffic light or just a red car and whether it is relevant for the currently occupied lane. While the early stages can be readily studied given total control over the stimulus and the late stages because of readily measurable macroscopic behavior, the place in between has remained a "black box" to some degree.

One of the brain regions responsible for the transformation is the neocortex. It is the seat of perception, memory storage, cognition, consciousness and even personality [Kandel et al., 2005], the functions relevant for selecting an appropriate response to stimuli. The relative fraction of the brain volume taken up by the neocortex is a good predictor of the complexity of the behavior an animal is capable of, reaching 80% in the case of humans.

It is organized in six distinct layers, starting from the surface of the brain (layer I), going down into its depth. Horizontally, we find a *columnar organization* of the neocortex [Mountcastle, 1997], i.e. similar groups of neurons spanning all six layers are repeated over and over again across the whole surface. As the pattern is repeated only horizontally, the number of these groups is proportional to the surface area of the cortex. This leads to the formation of grooves and wrinkles on the surface of the brain of primates, increasing its surface area.

The columnar groups can be thought of as functional units of cortical computation, each being slightly different depending on the specific function it has taken over, while coarse trends are preserved between them. This can be compared to the memory banks of a RAM module in a computer: Each identical in hardware, but slightly different while in use representing the information stored in them.

### B.2 About Extracellular Measurements in Neural Tissue

Brain activity is fundamentally electrical. That fact is well known since the experiments of Luigi Galvani [Piccolino, 1997]. But while it was fairly simple to stimulate nerves to elicit a twitch as Galvani did, recording the naturally occurring activity was much harder, due to the comparably weak voltages. It took until the early 20th century, before the first recording from single nerve fibers could be achieved [Adrian, 1928]. Today, extracellular measurements are recorded with various methods, including glass micropipettes, tungsten or platinum microelectrodes or multi-electrode arrays (MEAs).

These techniques measure a time series of the electric potential at a point inside neural tissue to draw conclusions on the activity of neurons around that point. As mentioned above, the activity of neurons as they process information is electrically encoded, and part of this electrical activity can be measured in their vicinity. What is picked up by an electrode is the compound signal of hundreds or thousands of neurons around its location. It can be a robust indicator of the overall activity in that population, although the reduction of so many cells to a single signal comes with a loss of information – just like the ambient noise in a full stadium can tell us whether the crowd is happy or unhappy with the activity on the playing field even if individual voices are drowned out <sup>1</sup>.

The interpretation of these signals is therefore mainly driven by experience, correlating certain frequencies with the macroscopic state of the organism, for example sleep. Well established is the interpretation of strong, high-frequency deflections as (extracellular) *action potentials* (APs), reflecting the output of one of a handful of cells in the immediate vicinity of the electrode. In the allegory of the crowded stadium this corresponds to the handful of spectators closest to the observer that can be individually understood at least intermittently.

---

1. In fact this work well even if we do not understand the language of the crowd at all

# C Reconstruction of the Neocortical Microcircuit

*Contributions of the thesis author:*

Figures:

- C.2  
Development of the method to calculate mean fiber density 'clouds'. Figure generation.
- C.4  
Development of the unbiased method to calculate the unitary microcircuit size. Figure generation.
- C.9, C.10  
Development of the connectome algorithm and validation. Figure generation
- C.18  
Calculation of spiking correlation profile. Figure generation
- C.20, C.21  
Development of the algorithm to place external synaptic input. Functional validation of thalamocortical input. Figure generation.
- C.S.3  
Development of the morphology selection method. Figure generation.
- C.S.4  
Anatomical analysis of pathways. Figure generation
- C.S.12  
Detection of structural assemblies. Calculation of synchrony. Figure generation

Manuscript:

Participated extensively in manuscript writing related to the sections listed above.

# Reconstruction of a Neocortical Microcircuit

The Blue Brain Consortium

For submission to Nature

## Abstract

We present a digital reconstruction of a prototypical neocortical microcircuit. A novel strategy enabled a first draft of a full reconstruction from partial anatomical and physiological data on the cellular and synaptic organization of the somatosensory cortex of a two-week old rat. This first draft cellular-level map of the microcircuit is  $0.28\text{mm}^3$  in volume and contains 31,000 neurons belonging to 55 morphological neuron types and 207 morpho-electrical types distributed across 6 layers. The reconstruction predicts the number of neurons of each type per layer (the neurome) with around 7 million intrinsic and 26 million extrinsic connections forming around 35 and 127 million synapses, respectively (the connectome). The reconstruction predicts the detailed anatomy and physiology of 2,258 unique synaptic pathways between neurons of different morphological types, 31,628 unique pathways between neurons of different morpho-electrical types, 600 intra-laminar and 1,618 inter-laminar pathways. The complete map of intrinsic synapses for all neurons is also predicted (the synaptomes). In silico simulations revealed a robust activity spectrum, ranging from synchrony to asynchrony (SA spectrum). Modulating synapses, neurons and layers shift the network along the spectrum. Network properties differ along this SA spectrum, including the specific neuron assemblies participating in the activity, the network response to input, and the propagation of the activity beyond the microcircuit. The reconstruction is freely available for independent investigation and to facilitate collaborative refinement of the predictions.

## C.1 Introduction

The neocortex originated in a mammalian ancestor approximately 250 million years ago and its evolution has been critical for the emergence of human cognition and behavior. The types of neurons and their local synaptic connectivity in different parts of the neocortex appear to be variations on stereotypical circuit properties [Szentágothai, 1975, Peters, 1987, White, 1989, Nieuwenhuys, 1994, Somogyi et al., 1998, Silberberg et al., 2002]. Lorente de No (1938) first suggested that “vertical chains” of neurons traversing the six layers of the neocortex formed elementary functional units: “all the elements of the cortex are represented in it, and therefore it may be called an elementary unit, in which theoretically, the whole process of the transmission of impulses from the afferent fibre to the efferent axon may be accomplished” (Lorente de No, 1938). Subsequent studies by Vernon Mountcastle and colleagues showed that different neurons separated by a horizontal distance of less than a millimeter, respond to brief sensory stimuli to their peripheral receptive fields in a similar manner [Mountcastle, 1957, Powell and Mountcastle, 1959]. The seminal studies of Hubel and Wiesel demonstrated functional cortical columns with a diameter of around 0.5 mm [Hubel and Wiesel, 1977]. Later studies showed that different patterns of stimuli result in more complex functional architectures [Mountcastle, 1998]. The manner in which spatio-temporal patterns in the input influence functional architectures and network dynamics has been studied extensively, but we still do not understand how neurons interact locally to shape the network response.

The foundations for mapping local networks of neurons in the neocortex (defined as a microcircuit) were laid down over a century ago by Santiago Ramón y Cajal [y Cajal, 1909]. Since then, we have made significant progress in characterizing the types of neurons involved and the connections they form, but we are far from completing the map [Douglas and Martin, 2007]. There are still large gaps in our knowledge of the complete set of neurons involved and their densities (the neurome), their connectivity (the connectome), and the full complement of synapses associated with any given neuron (the synaptome).



## Appendix C. Reconstruction of the Neocortical Microcircuit

---

The obstacles to obtaining this map include dispersed data from different groups working on different neocortical regions in animals belonging to different species, strains, ages, and genders, and under different experimental conditions. The lack of consensus on the definitions of cell types, synapses, or the volume of the microcircuit itself is also a significant barrier. By far the biggest obstacle however is the insurmountable number of high quality experiments necessary to fully map the microcircuit experimentally. Reductionism applied to this complex system therefore seems hopeless.

As a way forward, we developed a multi-level, multi-constraint process that pragmatically uses the available data to reconstruct the microcircuit in the form of computer models. (see below). We used this process to reconstruct a microcircuit from the somatosensory cortex of two-week old Wistar (Han) rats. This model system was chosen not only because it is one of the best-studied microcircuits in the neocortex, but also because experimental data on its cellular and synaptic organization are accessible. In what follows, we present this first draft cellular-level map of the neocortical microcircuit as well as simulations that demonstrate some of its emergent behavior. The reconstruction is consistent with most of what we know about the neocortical microcircuit and provides an array of experimentally testable predictions about its structure and function. This is the first detailed map of a local circuit of neurons – a microcircuit. To further facilitate community efforts to challenge, improve and interpret the map, an Internet-accessible Neocortical Microcircuit Collaboration portal (NMC portal) was developed, providing access to the necessary data, literature, data processing and modeling tools and methods (NMC portal - <https://bbp.epfl.ch/portal/unifyingNCC>).

### C.2 Biological Reconstruction Process

We developed a reconstruction process that guarantees a systematic evolution of a model towards a high fidelity and biologically accurate representation of a target biological system. The reconstruction process is based on a fundamental hypothesis that a compound model composed of embedded levels of component models (in our case; circuit behavior, circuit design, neurons & ion channels), maintains generalization power and minimizes over-fitting if (1) the component models and parameters at a particular level of organization are chosen such that they are constrained by a necessary and sufficient (i.e. minimal) experimental dataset and account for all their (i.e. maximal) observed phenomena, and (2) refitting the component models is prohibited when integrating them into the immediately higher level compound model.

Rather than requiring a dense experimental characterization at any given level, this hypothesis redirects the reconstruction process towards identifying a) the minimal dataset for reconstruction (i.e. the data containing the most information), b) the fundamental organizing principles (i.e. optimal regularization assumptions), and c) any available data at that level for validation (i.e. a theory at that level that accounts for all observables at that level).

In the ideal case, the process protects against error amplification as components are integrated into higher levels of the compound model, thus preserving generalization power at higher levels. In cases where the compound model fails validation, a curation process is triggered for component models only at the immediately lower level, in which the accuracy of the biological data (defining the parameters) and validity of the biological principles (defining the regularization assumptions) are challenged. To reduce the danger of over-fitting and evolve the reconstruction towards biological accuracy, it is necessary to forbid top-down bias. In other words, the triggered curation process may not consider any error in validation at higher levels to prescribe biological refinement (i.e. changing of parameters &

assumptions to reproduce higher level phenomena). The outcomes of alternative hypotheses about the parameters and assumptions may however be compared against experimental data at higher levels only as a exploratory guide, but refinement is only allowed using new experimental data at the curation level. This defines the biological reconstruction process. The process reflects principles analogous to "validate early and often" [Boehm, 1988] and test-driven development fundamental in computer science for assembling complex software systems that are reliable and robust. If this hypothesis is true, then the reductionist approach to characterizing complex systems is in general not hopeless.

### **C.3 Morphological diversity**

As the first step, we recorded, labeled and reconstructed neurons constituting the microcircuit, obtaining a core experimental dataset for use in the reconstruction process. Using patch-clamp electrodes in *in vitro* slices, we identified, recorded and labeled 14,045 neurons from all 6 layers in the somatosensory cortex of P14 male Wistar (Han) rats (see Figure 1).

In 2,052 cases, the anatomical staining of the axonal and dendritic arbours of neurons was sufficiently complete to allow classification into different morphological types (m-types). We did not develop a new classification or naming system for neuron morphologies. Established morphological criteria and names that have been given over the last century were used [Somogyi et al., 1982, Fairen et al., 1984, Kisvarday et al., 1985, Connors and Gutnick, 1990, DeFelipe, 1993, Hestrin and Armstrong, 1996, Kawaguchi and Kubota, 1997, Svoboda et al., 1997, Somogyi et al., 1998, Staiger et al., 2004, Szabadics et al., 2007, Oberlaender et al., 2012, DeFelipe et al., 2013]. In some cases, an m-type name reflects a semantic equivalent of multiple given names for the same morphology (see also The Reconstructed Neocortical Microcircuit as an *in silico* Resource, in preparation). We added a prefix to the established names to distinguish the layer of origin (e.g. a Layer 4 Pyramidal Cell is labeled L4\_PC).

The 3D morphologies of 1005 of these neurons were digitally reconstructed, creating a sample of reconstructed neurons for the different m-types. This process yielded 55 distinct m-types (13 excitatory and 42 inhibitory), all of which had been previously reported in the literature (Figure 2). At this stage, the m-type classification is strictly related to the properties of the local morphology and layer. It does not for example reflect known sub-types of any one m-type that project to or from different brain regions (i.e. a target sub-type or m-type) because a) there is not sufficient data available to sub-divide all m-types and b) we cannot yet integrate all projections to and from the rest of the brain. Deeper levels of morphological sub-types of a particular m-type were introduced only in cases where there was sufficient morphological data for clearly separate the neurons based on their local morphology (e.g. L5\_TTPC1 and L5\_TTPC2; see below). Similarly, L2 and L3 are considered together in this first draft reconstruction because there is insufficient local morphology data to distinguish between m-types in these layers. The reconstruction process does, however, position individual representative morphologies obtained from experiments in L2 and L3 within their appropriate layers (see below).

We developed three applications to analyze, repair and clone reconstructed neurons, available through the collaboration portal, together with the raw data used in the reconstruction. NeuroM performs a morphometric analysis of the axonal and dendritic morphology, objectively classifies a neuron as one of the 55 m-types and provides a measure of confidence in the classification. NeuroR uses the morphometric results generated by NeuroM to identify and repair arbours that have been cut during slice preparation (Figure S1). The third application (NeuroC) generates clones of the repaired neurons (Figure S2), incorporating random statistical variations in the arbours of each clone. This technique generates an unlimited number of morphological instances of the same m-type, each with statistical variations within the distributions obtained from the reconstructed neurons. In rare cases where the

## Appendix C. Reconstruction of the Neocortical Microcircuit

---

original dataset did not contain sufficient exemplars for a particular layer, we used exemplars of the same m-type from the immediately adjacent layer (L5&6 NGC, L5&6 BP, and L2/3&4 NGC). Two rare m-types are not included in the reconstruction because we do not have sufficient data to reconstruct and clone these neurons (horizontal L6 pyramidal neurons and sub-plate neurons lying in the white matter at the bottom of L6).

With unlimited exemplars for each m-type, the total number of neurons in the microcircuit and the numbers of neurons belonging to different m-types were then determined (Figure 3). When a first microcircuit was reconstructed using neuron densities published in the literature (40'000-80'000 cells/ $mm^3$ , Cragg [1967], Peters [1987], Beaulieu and Colonnier [1983], Schüz and Palm [1989], Beaulieu et al. [1992], DeFelipe et al. [2002], Lefort et al. [2009], Meyer et al. [2010b]), it failed validation at a higher level; a) failed to reproduce the mean distance between cells measured in in vitro IR-DIC images (not shown) and, b) failed to account for inhibitory synapse densities when synaptic connections were formed (see below). Exploratory reconstructions of the microcircuit with different hypothesized cell densities predicted about 50-100% higher cell densities than all previous reports. In accordance with the reconstruction process, a curation process was triggered. A re-examination of the methods employed in previous cell counting studies revealed that all studies used only thin sections, which may not adequately correct for slicing errors. Anatomical experiments were therefore performed on tissue blocks independently in two separate laboratories. Immunofluorescence was used to label neurons (NeuN for all neurons and GABA to separate between all cells and GABAergic ones) for counting and calculating their densities in each layer [DeFelipe et al., 2002, Lefort et al., 2009, Meyer et al., 2010b] (Figure 3a).

These studies yielded overall cell densities that were much higher than the values reported in previous studies and validated the prediction from hypothesized reconstructions (in cells/ $mm^3$ : DeFelipe lab 110,700±500). At these densities, a mini-column of 100 neurons spanning over the 6 layers as previously defined [Mountcastle, 1997, 2003] would have a diameter of approximately 24 $\mu m$ , a value consistent with anatomical estimates [Peters and Yilmaz, 1993, Mountcastle, 1997, 1998, Buxhoeveden et al., 2000, Silberberg et al., 2002, Mountcastle, 2003, DeFelipe, 2005]. The studies also showed that cell densities in L4 were almost twice that in the next densest layer (L2/3). This finding matches previous reports that cell densities in L4 are higher than in any other layer [DeFelipe et al., 2002, Lefort et al., 2009]. Overall, 85% of neurons were GABA-immuno negative and 15% GABA-immuno positive (Figure 3b), also consistent with the literature for this age, species and region [DeFelipe et al., 2002] and similar to other ages, species and regions [Lefort et al., 2009, Meyer et al., 2010b].

The sample of 2,052 morphologically classified neurons was used to estimate the proportion of m-types in each layer (Figure 3C). In general, the values found were consistent with the literature [Markram et al., 2004, Meyer et al., 2010b, 2011]. Around half of all GABAergic interneurons are basket cells and that the second most common m-type in layers 2-6 are Martinotti cells.

The next step was to define the dimensions of the neuronal microcircuit. Since neocortical neurons interact across all 6 layers, the height of the microcircuit is given necessarily by the combined height of all layers - approximately 2 mm in the somatosensory cortex at this age. If only cells in a minicolumn are considered as a microcircuit then the neuropil volume will not be filled and not all m-types will be represented. Therefore, to objectively define the diameter of the microcircuit, we began with a single minicolumn with a radius of 24 $\mu m$  (Figure 4a) [Mountcastle, 1997, Buxhoeveden et al., 2000, Mountcastle, 2003, Silberberg et al., 2002], and gradually increased the radius of the circle adding minicolumns surrounding a single minicolumn, until the volume occupied by dendrites in the neuropil at the center minicolumn, reached a plateau. The radius of the microcircuit was defined as the radius at

which the volume of dendrites in the neuropil saturated (95% of the plateau value;  $210\mu\text{m}$ ; Figure 4b). Finally, the minicolumns were arranged in a hexagonal shape (diameter:  $420\mu\text{m}$ ) that conserved the area of the original circle to allow tiling of multiple microcircuits (Figure 4b). An analogous procedure based on the horizontal extent of the dendrites of the largest neuron in the microcircuit (the thick-tufted L5 Pyramidal Cell - L5\_TTPC) yields a similar diameter for a neocortical microcircuit (not shown).

In the next step, a digital 3D volume with the dimensions defined above was generated. Application of the estimated cell densities for each layer provided an estimate of the total number of neurons (approximately 31,000) and the total number of minicolumns (310) in the microcircuit (Figure 4c). A space-filling algorithm was then used to position minicolumns in that volume and then to randomly position neurons in each minicolumn in such a way as to respect the measured densities and ratios of excitatory to inhibitory cells (Figure 4d) [DeFelipe et al., 2002, Binzegger et al., 2004, Lefort et al., 2009]. Since some layers of the rat neocortex do not display pronounced minicolumnar arrangement [Mountcastle, 1998], Gaussian distributions were used to relax the possible positions of excitatory and inhibitory cells around the center of minicolumns (Figure 4d).

Once the positions of the cells were established (Figure 4e), a second algorithm 1) chose each position in sequence, 2) scanned the database of cloned neuron morphologies to identify a pool of optimal morphologies for the selected location, 3) randomly selected one of these morphologies and 4) placed the selected morphology in the target position (Figure 4f). The pool of optimal morphologies was determined by scoring morphologies according to the match between the distribution of their cross-laminar projections with targets determined from layer annotated reconstructions, or from literature (Figure S3 a,b).

Figure 5 provides an impression of the microcircuit at this stage of reconstruction. Each inhibitory m-type is shown in a specific colour, independent of layer. The reconstruction allows a first prediction of the total length of axons (344 m, 7 reconstructions; mean: 11.1 mm/cell) and dendrites (208 m - mean: 6.7 mm/cell).

To assess the biological accuracy of the reconstruction, we mimicked *in vitro* immunohistochemical techniques to label each neuron with one or more commonly used neuronal markers (calcium binding proteins and neuropeptides, Figure 6a). Labels were guided by previously published probabilities of gene expression in specific m-types (Figure 6b) [Wang, 2002, Wang et al., 2004, Toledo-Rodriguez et al., 2005]. The corresponding *in vitro* stains were then obtained experimentally (Figure 6c). Since the *in vitro* stains were performed on  $30\mu\text{m}$  sections, the reconstructed microcircuit was sliced similarly into equivalent *in silico* sections. The *in vitro* and *in silico* stained cells across all layers were thus compared against each other (Figure 6d). Gene expression data is noisy and genes do not translate equally to marker expression, nonetheless a highly significant correspondence between the two stains was found (Figure 6d,e). The layer-dependent pattern of stained cells is also consistent with a large body of literature reporting previous staining experiments with these markers [DeFelipe, 1993, Kawaguchi and Kubota, 1993, 1997, 1998, Kawaguchi and Kondo, 2002, Dumitriu et al., 2007, Ascoli et al., 2008, Gentet et al., 2010, McGarry et al., 2010, Packer and Yuste, 2011, Gentet et al., 2012] (NMC portal). The reconstruction constrained by cell densities, fractions of morphologies in different layers, and positions of individual morphologies to respect inter-laminar target preferences, therefore reproduces global properties observed in biological tissue not used in the reconstruction process (overall  $P = 0.8$ ). Since the number of different markers used may not be sufficient to fully test the cellular composition, the composition may refine as the reconstruction is challenged with additional markers and hence should be considered as a first draft.

### C.4 Morpho-electrical diversity

Neurons differ in terms of their location in the brain, morphology, electrical properties, local, proximal and distal target preferences, afferent inputs, and their proteins and genes expressed. Taking each property as a dimension, the potential combination implies an immense diversity of cell types. Given the lack of sufficient data for each dimension, a first draft of the neurome was only attempted at the resolution of the morphological and electrical properties. To obtain the full morpho-electrical diversity we recorded and analyzed discharge patterns of 3,974 neurons across all layers in response to a standardized set of stimulation protocols (Figure 7a). The discharge patterns were classified based on their responses to step current pulses. In general, neurons were classified using the criteria established by the Petilla convention [Ascoli et al., 2008], with the exception for stuttering cells, which were instead considered as a separate class. This classification scheme yielded 11 electrical types (e-types; Figure 7b; also see Figure 8). Alternative approaches based on objective clustering of spiking features [Cauli et al., 2000, Druckmann et al., 2013] and profiles of ion channel expression [Toledo-Rodriguez et al., 2004, Khazen et al., 2010] categorized cells in a similar manner. All m-types expressed multiple e-types (Figure 7b), consistent with numerous previous observations [Cauli et al., 2000, Toledo-Rodriguez et al., 2005, Ascoli et al., 2008] (NMC portal). On this basis, 207 morpho-electrical types (me-types) were present in the neocortical microcircuit (Figure 7c). A dataset of 2,109 electrically classified neurons was used to determine the fraction of each e-type for a given m-type in the microcircuit (Figure 7c; colour coded).

The absolute number of neurons for each me-type in the microcircuit was estimated by multiplying these e-type fractions by the number of neurons in a given m-type. The result constituted an initial draft of the neurome at this level of resolution for defining a neuron type (location, morphology and electrical behavior), which will elaborate as further dimensions are added. Although there is already a large literature describing and discussing specific aspects of the neurome, this first integrated view reveals a long-tailed distribution of me-types and all e-types are present in all layers 2-6.

### C.5 The Connectome

The next step was to reconstruct the synaptic connectivity between neurons. Analyzing published data from our own group, unpublished data on L6, and data from other groups revealed four fundamental principles of synaptic connectivity. First, it has been shown that synapses are located at incidental appositions between neurons [Hill et al., 2012, Kalisman, 2005], i.e. at locations where axons and dendrites collide when neurons are placed randomly with respect to each other. Indeed, the only anatomical difference found experimentally between the location of appositions in connected and unconnected pairs of pyramidal neurons is the presence or absence of boutons [Kalisman, 2005, Stepanyants and Chklovskii, 2005a]. There are only a few exceptions to this principle (see below) and they indicate chemotactic guidance mechanisms such as the axon of Chandelier cells guided down the axon initial segment. Second, synapses only form at a low fraction of appositions [Hellwig, 2000, Stepanyants & Chklovskii, 2005a, Kalisman et al. 2005]; in some locations, the fraction is zero because some types of synapses are never formed (e.g. excitatory synapses do not form on the somata of excitatory neurons despite appositions). Third, without exception, all synaptic connections between connected pairs of neurons involve multiple synapses [Thomson et al. 1993, Deuchars & Thomson, 1995, Buhl et al. 1997, Markram et al. 1997, Tamas et al. 1997, Feldmeyer et al. 1999, Gupta et al. 2000, Feldmeyer et al. 2002, Silver et al. 2003, Lübke et al. 2003, Feldmeyer et al. 2005, Bremaud et al. 2007, Silberberg & Markram, 2007]. Fourth, only a fraction of multi-apposition connections form multi-synapse connections, leaving a reservoir of potential connections, whereby additional multi-synapse connections can form in an

activity-dependent manner (i.e. microcircuit plasticity) [Le Be & Markram, 2006; see also Holtmaat et al. 2006. Holtmaat & Svoboda, 2009, Wilbrecht et al. 2010].

The accompanying paper demonstrates that Peters' rule [Peters and Feldman, 1976] is insufficient to explain biological connectivity and that these four principles are essential, hence fundamental. These principles of synaptic connectivity were therefore implemented by a structural connectivity and apposition-pruning algorithm (the regularization assumptions; see Biological Reconstruction Principle). The structural connectivity algorithm, described previously yields appositions [Kozloski et al., 2008], and the pruning algorithm, described in the accompanying study yields synapses (The Connectome Algorithm, in preparation).

The structural connectivity algorithm identifies all possible axonal appositions between neurons (i.e. no dendro-dendritic appositions). An apposition was defined as a collision or near collision between axons and dendrites, where the distance between these arbours is less than or equal to  $2.5\mu\text{m}$  (for post-synaptic excitatory neurons) or  $0.5\mu\text{m}$  (for post synaptic inhibitory neurons). These apposition distances are consistent with biological data for the formation of excitatory and inhibitory synapses [Ballesteros-Yanez et al. 2006, Arellano et al. 2007, Kawaguchi et al. 2006, for reviews see Nimchinsky et al. 2002, Yuste & Bonhoeffer, 2004, see also Yuste, 2010]. The effect of changing the criteria for apposition distances is explored in the accompanying paper (The Connectome Algorithm, in preparation).

The apposition-pruning algorithm first excludes appositions where biological data indicates a lack of synapses with specific postsynaptic elements. For example, statistical connectivity cannot recreate the specific innervation of the axon initial segment of pyramidal cells by Chandelier axons [Somogyi, 1977, Somogyi et al., 1982, 1998]. The algorithm deals with this exception by ignoring appositions that form on dendrites and relocating appositions that form on somata of pyramidal cells onto their axon initial segment. Excitatory axonal appositions with excitatory somata are also prohibited. In this way, all retained appositions are located at biologically viable locations for synapses to form. In seven instantiations of the microcircuit we found  $600 \pm 45$  million such appositions.

The pruning algorithm then solves a multi-constraint problem. The multiple constraints arise from a fundamental relationship between five circuit properties; 1) cell density, 2) axonal density of each neuron, 3) bouton density, 4) mean number of synapses/connection, and 5) connection probability (The Connectome Algorithm, in preparation). Appositions between all neurons must be pruned simultaneously to fully constrain the parameters for any individual connection (i.e. the algorithm is valid only when given a set of morphologically reconstructed neurons at their biological densities). This approach utilizes the interdependencies between parameters to enforce constraints on the synaptic parameterization for all connections even when a single biological data point is introduced for one connection, making it theoretically plausible to reconstruct the connectome from partial data. The accompanying paper demonstrates that the minimal dataset required to predictively reconstruct the connectome given a set of neurons is a) the relationship between the appositions/connection and synapses/connection and b) an average bouton density (The Connectome Algorithm, in preparation).

Since the pruning algorithm satisfies multiple constraints for all m-types simultaneously, the outcome is a test, not only of the structural connectivity and pruning algorithms, but also of the whole reconstruction including cell densities, the m-type composition of the circuit, the positioning of neurons belonging to different m-types, and the quality of the morphological reconstructions (i.e. a validation test for the compound model up to this level).

## Appendix C. Reconstruction of the Neocortical Microcircuit

---

The reconstructed circuit reproduces a) overall differences in connection probabilities [Thomson et al. 1993, Markram et al. 1997, Feldmeyer et al. 1999, Petersen & Sakmann, 2000, Beierlein & Connors, 2002, Feldmeyer et al. 2002, Song et al. 2005, Feldmeyer et al. 2006, Silberberg et al. 2007, Le Be et al. 2007, Perin et al. 2011], b) the different numbers of synapses/connection for pairs of neurons belonging to specified m-types [Markram et al. 1997, Feldmeyer et al. 1999, Petersen & Sakmann, 2000, Feldmeyer et al. 2002, Beierlein & Connors, 2002, Lübke et al. 2003, Markram et al. 2004, Feldmeyer et al. 2005, Feldmeyer et al. 2006, Silberberg & Markram, 2007, Le Be et al. 2007, Frick et al. 2007, Bremaud et al. 2007], c) layer by layer densities of glutamatergic and GABAergic synapses obtained from confocal and electron microscopy (EM) studies [Beaulieu & Colonnier, 1985; Beaulieu et al. 1992; DeFelipe et al. 2002], d) axon bouton densities and distributions established from EM studies [Wang et al. 2002, Lübke et al. 2003, Karube et al. 2004, Markram et al. 2004, Kawaguchi et al. 2006, Romand et al. 2011], e) dendritic spine densities and distributions [Larkman, 1991, Lübke, 2003, Kawaguchi, 2006, Romand et al., 2011], f) data showing densely synaptically clustered neurons from 12-patch recordings [Perin et al., 2011], g) and data on the approximate fraction of extrinsic synapses from tract tracing studies [Killackey & Ebner, 1972, Cusick et al. 1985, Agmon & Connors, 1991, White & Hersch, 1992, Cauller & Connors, 1994]. These and further validations are fully described and quantified in the accompanying paper (The Predicted Connectome of the Neocortical Microcircuit, in preparation).

To characterize the properties of the predicted connectome, we generated a central microcircuit surrounded on all sides by six microcircuits to avoid boundary effects in the central microcircuit (total of seven microcircuits). A detailed characterization is provided in the second accompanying paper (The Predicted Connectome of the Neocortical Microcircuit, in preparation). Briefly, each circuit contained  $35 \pm 1$  million ( $N = 7$ ; mean  $\pm$  SD) intrinsic synapses formed by neurons within the microcircuit forming  $7 \pm 0.2$  million connections with an average of 5.2 synapses/connection (average of 8.5 synapses for inhibitory connections, 4.3 for excitatory connections). The sample circuits contained 2,258 unique types of connections between pairs of neurons belonging to specific m-types (Figure 10a), and 31,628 types of connections between neurons of different me-types. On average, any one neuron in the microcircuit innervated  $217 \pm 199$  other neurons belonging to  $35 \pm 6\%$  ( $N = 217,000$ ) of the m-types present in the circuit, forming an average of  $1,129 \pm 1050$  synapses in total. Each neuron received input from  $46 \pm 8\%$  of all m-types present. As a population, m-types innervated  $75 \pm 15\%$  of other m-types.

The space remaining on postsynaptic neurons following the formation of intrinsic synapses predicts the number of synapses formed by fibres originating outside the circuit (extrinsic synapses). On this basis, we were able to predict that around 127 million synapses (78% of all synapses in the circuit) are formed by around 25 million incoming fibres (extrinsic synapses; assuming an average of around 5 synapses/connection). Figure 10b shows predictions of extrinsic innervation for each layer. The reconstruction also enabled prediction of the number of GABAergic synapses forming on somata for all m-types in all layers (see NMC portal). As an example, the predicted number of GABAergic synapses on L5 pyramidal neurons ranges between 100 - 200 (Figure 10c). We tested this prediction by performing EM experiments and found overlapping values (Supplementary Table Z).

The predicted map of connectivity reveals a spectrum of additional connectivity features: 1) only about 6% of possible appositions are converted to synapses, 2) Excitatory connections have far more excess appositions ( $110 \pm 74\%$ ) than inhibitory connections ( $47 \pm 66\%$ ) 3) different m-types have different numbers of excess appositions predicting different number of multi-synapse connections held in reserve and suggesting differences in their potential for microcircuit re-wiring, 4) for excitatory connections, about 50% of potential multi-synapse connections are actually functional – allowing

the maximum possible number of configurations of connected neurons. The accompanying paper provides further detailed predictions of connectivity for each m-type (The Connectome Algorithm, in preparation) and the NMC portal provides predictions for connectivity for all e- and me-types and for individual neurons in the microcircuit (NMC Portal).

The connectivity map not only predicts general connectivity properties, but detailed connectivity between any two neurons. As an example, synaptic connections between L5 thick-tufted PCs in the reconstructed microcircuit showed no evidence of significant differences against available experimental data upon statistical comparisons of the mean number of synapses/connection and their incidental locations along the presynaptic axons and postsynaptic dendrites [Ramaswamy et al., 2012, Hill et al., 2012, Reimann et al., a]. Predictions on the anatomy of in silico synaptic connections between L5 Martinotti cells and L5 thick-tufted PCs (Figure S4) are further compared against available experimental data [Silberberg and Markram, 2007]. The NMC portal not only provides the detailed anatomy for all 2,258 synaptic pathways but also allows the study of any other pathway (e.g. pathways between me-types) and neurons involved in polysynaptic pathways forming known motifs.

## C.6 Neuronal Physiology

With the reconstructed neurome and connectome of the microcircuit, we began reconstructing the physiology of the neurons and synapses. A series of algorithms and an automated workflow made it possible to model the physiology of the different me-types of neurons [Druckmann et al., 2007, Hay et al., 2011]. This process captured the diversity of electrical behavior displayed by different m-types and their morphological variants (Figure 11).

At this stage of the reconstruction we face insufficient data to satisfy the first principle of the fundamental hypothesis and are required to proceed in a non-ideal manner. In order to reconstruct the diversity of me-types in the microcircuit, the ideal experimental dataset includes; 1) the various ion channel kinetics and 2) the combinations of ion channels expressed in any of the different neurons, 3) their distribution profile along the neuronal arbours, and 4) their absolute density. However, given that data on the kinetics and combinations of ion channels are largely missing, we modeled 14 principal ionic mechanisms known to contribute to electrical behavior (13 ion channel models to capture the diversity of dynamics exhibited by known ion channel families and a model of intracellular  $Ca^{2+}$  dynamics; Figure S5). The kinetics of ion channel models were not adjusted in order to match experimentally characterized neuronal physiology. Where available, biological data on distribution profiles was applied and otherwise a uniform distribution was assumed. All ion channel classes were then used in all neuron types and only their individual densities were adjusted to recreate the target electrical behavior (Figure 11) (see also, Druckmann et al. [2007]; Hay et al. [2011]).

Specifically, as the first step, a single reconstructed morphological instance of an m-type was loaded (step 1). Hodgkin-Huxley (HH) type models of 13 known classes (Figure S5) of ion channels were added (step 2). The ion channel models were distributed along the neuronal arbours as described above (step 3).

The raw experimental traces of responses to step currents for a selected e-type (step 4) were analyzed to extract salient spiking features (step 5). A multi-objective feature optimization algorithm computed the vector of ion channel conductance densities that best reproduced spiking features (step 6) and transplanted the resulting vector of densities onto all variants of that m-type (step 7). Models were mass-produced in this manner and those with the highest generalization power were retained. The generalization power was tested using a battery of stimulus protocols that were additionally applied in



the *in vitro* experiments (Figure 8a). Models whose responses fell within or outside the observed range of statistical variation in the biological recordings were accepted or rejected respectively (step 8). The fitting scores for all model neurons were examined as a further test of this quality control process (step 9).

The workflow provides a generic method for reconstructing the electrical behavior of an unlimited number of neurons of any e-type (Figure S6). In total, we reconstructed 171,602 model neurons (see Experimental Data-sets for Reconstructing a Neocortical Microcircuit, in preparation; The Reconstructed Neocortical Microcircuit as an *In silico* Resource, in preparation; NMC portal to download the models). In most cases, transferring a vector of conductances to different variants of the same m-type and or to a different m-type accurately captured the target physiology. This suggests, contrary to previous reports, that e-types are largely insensitive to morphological variations within an m-type.

Since the first principle was not ideally applied, we cannot guarantee that there are regimes of activity where the neurons do not fire as in biology. Indeed, there is no unique solution for the vector of conductances (Figure S7). Nevertheless the generalization is shown to be sufficient to reproduce the morpho-electrical diversity. This is because a broad validation dataset was available and because only models with a demonstrated generalization power were retained.

The active dendritic properties of model neurons were optimized to reproduce experimental observations of back-propagating action potentials as part of the fitting procedure (Figure 12a, a1; [Stuart & Sakmann, 1994, Nevian et al. 2007]). As a further validation, the dendritic properties of the models were examined for the attenuation of synaptic potentials (Figure 12b,b1), which were found to be consistent with experimental observations [Berger et al. 2001, Nevian et al. 2007].

Based on the above, propagating the neuron models to the next level of the reconstruction (circuit behavior) allows the role of m-types in circuit activity to be examined, but the role of ion channels in circuit activity cannot be determined.

### C.7 Synaptic Physiology

In the final step of the reconstruction process, we set out to predict the physiology of the 35 million intrinsic synapses in the microcircuit. We again relied on published paired-recording data, mining the literature for previously reported synaptic properties (conductances, post-synaptic potentials (EPSPs/IPSPs), latencies, rise and decay times, failures, release probabilities, etc.; see NMC portal). We first attempted to predict the value for synaptic conductances and then the transmission dynamics for different synapse types.

Since the model neurons capture the passive and active properties of biological neurons and synapses are formed in biologically accurate numbers and locations (especially for well characterized m-type to m-type pathways), we hypothesized that model synapses using unitary synaptic conductances reported in the literature would automatically reproduce *in silico* evoked post-synaptic potentials (PSPs) (Figure 13a; Benardo & Ling, 1999, Feldmeyer et al. 1999, Angulo et al. 1999, Gupta et al. 2000, Yoshimura et al. 2000, Sarid et al. 2007, Rinaldi et al. 2008). Instead, the resulting PSPs were found to be far too small. Therefore, the synaptic conductances were progressively increased until simulated somatic PSPs matched the experimental levels [Thomson et al. 1996, Markram et al. 1997, Feldmeyer et al. 1999, Angulo et al. 2001, Feldmeyer et al. 2003, Feldmeyer et al. 2006, Silberberg & Markram, 2007, Le Be et al. 2007]. The results suggested that the reported conductances were about 3 fold too low for

excitatory pathways (N=4 pathways) and 2 fold too low for inhibitory pathways (N=3 pathways) (Table S1). In accordance with the reconstruction process this discrepancy triggered a curation step at this level. The biological data in the literature was revisited. We concluded that the discrepancy with these studies [Angulo et al. 1999, Feldmeyer et al. 1999, Benardo & Ling, 1999, Yoshimura et al. 2000, Gupta et al. 2000, Rinaldi et al. 2008] is due to inadequate correction for space clamp errors and dendritic filtering in experiments. Indeed, experiments have demonstrated a similar level of underestimation of synaptic conductances under these conditions [Williams & Mitchell, 2008, Sarid et al. 2007].

The reported conductances for specific m-type to m-type pathways were scaled by the error calculated for each known pathway to reproduce the experimentally measured amplitudes of synaptic potentials (Figure 13b; N=21). However, synaptic data is missing for the vast majority of pathways and a generalization strategy is required. The corrected mean synaptic conductance for broader classes of pathways (excitatory-excitatory, excitatory-inhibitory, inhibitory-inhibitory, and inhibitory-excitatory) was calculated as the average of pathways in each class where the conductance was corrected (see above). To test whether these class-specific means generalized to m-type specific conductances, the resulting amplitudes of *in silico* PSPs were compared against *in vitro* PSPs in a different set of pathways where only synaptic potentials were measured experimentally (Figure 13c; N=17). Similar to the mean, the standard deviation of the distribution of synaptic conductances was scaled to preserve the experimentally measured c.v. values in the synaptic connection type (Figure 14; Table S1) yielding unique conductances for individual synaptic contacts.

For a majority of pathways, the results suggest a lack of sufficient evidence for significant differences in mean PSPs measured *in silico* and *in vitro* (Figure 13b, inset, discrete KS test,  $p = 0.1$ ; Figure 13c, inset, discrete KS test,  $p = 0.17$ ). The class-specific corrected conductance values were applied to all pathways for which no experimental data was available (Figure 13d). This yields a prediction of the synaptic conductances of the 2,258 m-type to m-type and 31,628 me-type to me-type pathways in the microcircuit. Figure 13e shows the reconstruction of synaptic conductances for a single neuron.

In addition to their diverse kinetic properties, neocortical synapses also display various forms of short-term plasticity (STP), which can be used to classify types of synaptic connections (s-types) (Figure 14a,b). As previously reported, s-types can be separated into facilitating (E1 & I1), depressing (E2 & I2), and pseudo-linear (E3 & I3) types (Figure 14b) [Thomson et al. 1996, Reyes et al. 1999, Gupta et al. 2000, Wang et al. 2002, Beierlein et al. 2003, Wang et al. 2006, for review see Thomson & Lamy, 2007]. It is known that s-types are determined by the me-types of the pre- and post-synaptic neurons (Figure 14c) [Thomson et al. 1993, Thomson et al. 1996, Somogyi et al. 1998, Gupta et al. 2000, Thomson, 2000, Beierlein & Connors, 2002, Beierlein et al. 2003, Feldmeyer et al. 2002, Ali et al. 2004, Bannister & Thomson, 2007, Silberberg & Markram, 2007, Frick et al. 2007]. However, the s-types for all 31,628 unique me-type to me-type pathways in the microcircuit are unlikely to be established experimentally.

We therefore began by mapping what is currently known about the s-types associated with specific me-type to me-type pathways (Figure S8; solid boxes). Although we found no single rule capable of explaining the map, we did identify multiple constraining principles: 1) pyramidal to pyramidal connections are always depressing (E2) [Mason et al. 1991, Thomson et al. 1993, Markram et al. 1997, Thomson & Bannister, 1998, Reyes & Sakmann, 1998, Feldmeyer et al. 1999, Maffei et al. 2004, Mercer et al. 2005, Feldmeyer et al. 2006, Frick et al. 2007, Bannister & Thomson, 2007], 2) pyramidal to interneuron connections are also depressing (E2) [Thomson, 1997, Reyes et al. 1999, Angulo et al. 1999, Wang et al. 2002, Holmgren et al. 2003, Blatow et al. 2003], except for connections onto Martinotti,

## Appendix C. Reconstruction of the Neocortical Microcircuit

---

bitufted and other interneurons displaying spike frequency accommodation, which are facilitating (E1) [Markram et al. 1998, Reyes et al. 1999, Rozov et al. 2004, Ali et al. 2007, Kapfer et al. 2007, Silberberg & Markram, 2007], 3) facilitation from inhibitory neurons is around 2 times stronger than from excitatory neurons [Gupta et al. 2000, Silberberg et al. 2007], 4) synaptic dynamics are preserved across layers for all me-type specific pathways, and 5) the most common s-type (type 2; E2 or I2) was applied to any remaining pathways [Thomson et al. 1996, Reyes & Sakmann 1998, Somogyi et al. 1998, Galarreta & Hestrin, 1998, Reyes et al. 1999, Gupta et al. 2000, Thomson et al. 2002, Holmgren et al. 2003]. The experimental data on which these principles are based are illustrated in Figure S8 (solid boxes).

The identified principles for assigning synaptic dynamics were applied to all uncharacterized pathways (Figure S8; dotted boxes). We applied synaptic dynamics where experimental data was directly available and the above principles where experimental data was unavailable, producing an extrapolated map of synaptic dynamics (Figure 15). The actual dynamic synaptic parameters (Utilization of synaptic efficacy, Use; Time constant for recovery from depression, D; Time constant for recovery from facilitation, F) describing each s-type were drawn from distributions with the c.v. of experimentally measured parameters to prescribe unique synaptic dynamics for individual synapses. However, the map does not capture the intrinsic diversity across individual pathways within an assigned s-type.

The now fully reconstructed microcircuit makes it possible to generate initial predictions of the anatomical and physiological properties of all intrinsic inputs and outputs for each individual neuron in the circuit - the synaptomes (Figure 16).

The NMC portal provides facilities to generate, access and download the synaptomes of any of the 31'000 neurons in the microcircuit, as well as the average synaptome of neurons belonging to any of the 55 m-types, 11 e-types, 207 me-types or 6 s-types in the microcircuit.

The reconstructed synaptomes for individual neurons make a series of testable predictions: 1) The m-, e-, and s-types of neurons providing inputs to a particular cell are strikingly different from those receiving outputs from the cell, i.e. synaptomes are highly asymmetrical); 2) No two neurons connect to the same set of target neurons or even to the same set of m-types (i.e. there are no redundant connections); 3) Each individual neuron targets about  $35 \pm 6\%$  of all possible m-types in all layers and receives input from about  $46 \pm 8\%$  of all possible m-types ( $N = 7$  microcircuits). The reconstruction reproduced the detailed physiology of some synaptic pathways that have already been well characterized experimentally [Figure S9; Thomson & Deuchars, 1997, Feldmeyer et al. 1999, Feldmeyer et al. 2003, Silberberg & Markram, 2007, Ramaswamy et al. 2012, The Reconstructed Neocortical Microcircuit as an *in silico* Resource, in preparation; NMC portal]. Figure S9 illustrates the spectrum of physiological predictions by *in silico* paired recordings and multi-segment dendritic patch recordings.

### C.8 Network dynamics - spontaneous activity

Software was developed to enable supercomputer-based simulation, analysis, and visualization of the reconstructed microcircuit. The NEURON simulator was developed through multiple versions to meet the computational requirements [Hines and Carnevale, 1997]. The software ecosystem made it possible to analyze anatomical and physiological aspects of the reconstruction, to replicate experimental manipulations and recording protocols *in silico* (single-cell, paired recordings, multi-unit activity, knock-outs, etc.), to perform *in silico* experiments not currently possible in biology, to visualize different aspects of the reconstruction, and to mimic biological imaging protocols (Figure S10).

Since the data used to reconstruct the microcircuit were obtained from brain slices *in vitro*, we de-

veloped a workflow to connect microcircuits, recreating a corresponding virtual brain slice whose spontaneous emergent activity could be tested against experimental measurements (Figure 17a).

To reconstruct in vitro-like and in vivo-like experimental conditions, we examined experimental data on the  $Ca^{2+}$  dependence of different s-types and developed a method to modify synaptic parameters according to the reported dependencies [Tsodyks & Markram, 1996, Gupta et al. 2000, Silver et al. 2003, Rozov et al. 2004]. The method involved mapping the postsynaptic potentials of all reported pathways under at least two different extracellular calcium concentrations (Figure S11a). Since it is known that postsynaptic amplitudes can increase or decrease corresponding to changes in release probability (Thomson et al. 1993), we modified the analogous parameter in the synaptic model (utilization of synaptic efficacy, Use) to reflect the effect of extracellular calcium  $[Ca^{+2}]_o$  concentrations. Simulation of the different experimental conditions are consistent with previous reports that a) synapses between excitatory neurons, between excitatory neurons and dendrite targeting interneurons, and between dendrite targeting interneurons and excitatory neurons have a steep calcium dependency; and b) synapses between excitatory and proximal targeting interneurons and between proximal targeting interneurons and excitatory neurons have a shallow calcium dependency (Figure S11a) [Tsodyks & Markram, 1996, Gupta et al. 2000, Silver et al. 2003, Rozov et al. 2004]. Due to a lack of experimental data, synapses between inhibitory neurons are assumed to have level of dependency on  $[Ca^{+2}]_o$  between the two extremes (Figure S11a). Figure S11b illustrates the effects of high (in vitro-like) and low (in vivo-like)  $[Ca^{+2}]_o$  on different s-types. We also estimated how increases in levels of extracellular potassium would affect depolarization in excitatory and inhibitory neurons.

We simulated spontaneous activity in the virtual neocortical slice under depolarized in vitro-like and under in vivo-like calcium conditions [Sanchez-Vives & McCormick, 2000, Bar-Yehuda & Korngreen, 2007]. The virtual slice reproduces the slow oscillations (0.5-1Hz) originating in layers 4 and 5 (Figure 17b1) that are commonly observed in vitro (Figure 17c,d1) [Beierlein et al. 2002, Compte et al. 2008]. When we lowered extracellular  $Ca^{2+}$  levels in the virtual slice to the levels reported in vivo [Borst, 2010], the neurons desynchronized (Figure 17b2). In vitro experiments under similar conditions confirmed the predicted desynchronization (Figure 17d2). Simulation of the virtual slice with different levels of depolarization and extracellular calcium concentrations revealed a spectrum of network states ranging from highly synchronous to asynchronous (Figure 18). Calcium-induced reduction in release probability did not decouple the neurons in the network, which continued to display rich correlation profiles. These in silico experiments predict a continuous spectrum ranging from one extreme state where virtually all neurons are synchronous, to another where they are virtually all asynchronous (the Synchronous-Asynchronous (SA) spectrum). The decrease in the E-I ratio by a factor of  $\approx 3$  when calcium levels are decreased from 2mM to 1.3mM (Figure S11) suggests that the synchronous state is due to runaway excitation and that the shift to the asynchronous state is due to increasingly effective inhibitory control.

Further analysis revealed that synaptically clustered populations of neurons (synaptically coupled assemblies), such as those formed by the common neighbour rule (Figure S12a, b1, b2), remain in synchrony for lower calcium levels further to the right of the spectrum than neurons that do not belong to assemblies (Figure S12c). Assemblies in different layers also lose synchrony at different points on the spectrum (Figure S12d). The point along the spectrum therefore determines the synchrony of neurons in a manner that depends on their connectivity to assemblies and their layer.

To understand the mechanisms determining the position of the microcircuit along the SA spectrum we knocked out inhibitory neurons in different layers. We found that knocking out all non-basket

cells (dendritic targeting cells) (Figure 19a) had virtually no effect, but that knocking out basket cells (soma targeting cells) (Figure 19b) shifted the microcircuit towards a highly synchronous state. The greatest shift was observed when we knocked out basket cells in layers 4 or 5. These results suggest that the position of the microcircuit on the spectrum is strongly determined by changes in the fast inhibitory feedback provided by basket cells in layers 4 and 5. This is consistent with the finding that the asynchronous state is where inhibition is in control of the runaway excitation seen in the synchronous state.

### C.9 Network dynamics - evoked activity

To examine the spatio-temporal pattern of evoked activity, larger circuits consisting of a microcircuit surrounded on all sides by 6 microcircuits (a mesocircuit) was constructed. An algorithm was developed to reconstruct input from the ventroposterior medial thalamic nucleus (VPM) to the central microcircuit in such a way as to satisfy experimental constraints [Benshalom & White, 1986, Herkenham, 1986, Koralek et al. 1988, Gil & Amitai, 1996, Gil et al. 1999, Beierlein et al. 2003, Petreanu et al. 2009, Meyer et al. 2010b, Constantinople & Bruno, 2013]. Consistent with experimental estimates of the numbers of afferent VPM fibres innervating this volume [Meyer et al., 2010a], we instantiated one fibre centered in each minicolumn with a horizontal spread described by a 2D Gaussian distribution (Figure 20a). Using reported layer-by-layer bouton density profiles [Meyer et al., 2010a] (Figure 20a), and experimental measurements of the mean number of synapses/thalamocortical connection in layer 4 [Gil et al. 1999, Amitai, 2001, Bruno & Sakmann, 2006] (Figure 20b), the multi-synapse rule was applied to estimate that each thalamocortical fibre innervates around 800 neurons with an average of 9 synapses/connection (Figure 20b).

As an initial validation we verified the number of synapses formed on L4 PCs (Figure 20c; dark bars) against experimental data [Gil et al. 1999, Amitai, 2001, Bruno & Sakmann, 2006] (Figure 20c; vertical red line). The reconstruction predicts the anatomical locations and average number of synapses formed by thalamocortical (VPM) connections onto every m-type in the microcircuit (see NMC portal). For example, it predicts that thalamocortical (VPM) connections form an average of around 12 synapses onto L5 pyramidal neurons (Figure 20c; light bars), more than for L4 PCs.

Synaptic conductances were assigned as previously described (similar to E2 s-type). Synaptic responses recorded in silico in L4 and L5 PCs under in vivo like conditions matched those reported in the literature [Bruno & Sakmann, 2006, Constantinople & Bruno, 2013]. (Figure 21a,b). Although more synapses formed on L5 pyramidal neurons than on L4 pyramidal neurons, the mean amplitude of PSPs were similar, which can be explained by the greater average path distance of synapses forming on L5 pyramidal cells with respect to those on L4 pyramidal neurons (Figures 21c). To evoke activity in the center of the mesocircuit, we stimulated a progressively increasing number of fibres innervating the center of the circuit with a single synchronous spike. The point on the SA spectrum determined the profile of the stimulus response curve, ranging from a steep sigmoidal with an all-or-none activation of the microcircuit (in vitro-like) as seen in vitro [Beierlein and Connors, 2002] to a shallow sigmoidal reflecting a graded stimulus-response relationship (in vivo-like) (Figure 21d).

Under in vitro-like conditions exhibiting all-or-none activation, we found that synchronous stimulation of 5 or more fibres evoked a run-away response of the microcircuit and a characteristic spreading of activity throughout the mesocircuit. Stimulation of fewer fibres evoked only sparse spiking which could not drive subsequent neurons to fire (but see Beierlein and Connors [2002]). On the other hand, under in-vivo-like conditions the network response magnitudes varied with the number of fibres stimulated

and remained localized, sometimes restricted to a single minicolumn (Figure 22). The point along the SA spectrum therefore determines the spread of activity beyond the microcircuit. This suggests that the emergence of high fidelity functional maps is only possible on the right hand side of the spectrum.

## C.10 Discussion

We present a first draft of the reconstructed synaptic and cellular map of a neocortical microcircuit and a set of simulations that provide a functional benchmark for studying the functions of the microcircuit, layers, neurons, and synapses. Since mapping the microcircuit using only experimental methods is impractical, we developed a biological reconstruction process that uses partial data, fundamental principles and multiple constraints between data parameters to predict a first draft map and provide a principal set of rules to guide and validate the reconstruction, as well as an alternate process when the reconstruction is not performed according to these rules or fails validation.

We do not claim that the map is a definitive one of the rat somatosensory cortex at this age. It is, however, a first step. The map provides a first view of the complexity of the microcircuit, clearly shows that it is impractical to experimentally map even such a small part of the brain and provides a way around this obstacle. The map also points out specific experiments that would most facilitate refinement of the map.

Related to the neurome, community involvement is required to refining the definitions of agreed criteria for the identification of cell and synapse types, the characterization of cell types not included in the current reconstruction, such as the horizontal pyramidal cells, sub-plate cells in L6 and other rare types not captured. Reconstructing the map revealed the central importance of marker proteins expressed in single neurons as well as their global staining patterns for the prediction of the cellular composition, where each protein marker acts as a constraint to the possible frequencies of expression of specific types of neuron. Expression of many proteins is highly dependent on the expression of other proteins, and hence it should not be necessary to map every single protein, but those with the highest interdependencies. The reconstruction underlines the vital importance of the biophysics of genetically expressed ion channels for biologically accurate reconstructions of neurons, which surprisingly have not been obtained despite decades of research (Catterall, 1995; Armstrong & Hille, 1998; Trimmer & Rhodes, 2004; Lai & Jan, 2006;). This illustrates how the reconstruction process can guide further experimentation. Indeed, attempts have begun to fill this major gap in ion channel biophysics (Ranjan et al. 2011; see also Channelpedia – <http://channelpedia.epfl.ch>). General principles governing how ion channels (and any protein) are distributed in a neuron, are important to arrange the ion channels accurately, also surprisingly lacking given the major efforts in cellular and systems biology. Single cell transcriptomics and the principles governing protein translation are fundamental to selecting the subset of ion channels used by specific types of neurons (for reviews see Wang & Bodovitz, 2010; Catterall, 2010).

Related to the connectome, the 5 fundamental parameters and the 4 fundamental principles can guide further experiments to refine the predictions. In general, the reconstructed map demonstrates that the most important parameter is the bouton density of specific neurons. This is because this parameter has the most interdependencies – an axon innervates many other types of neurons. The synapses/connection is also a critical parameter to allow the reconstruction, but since only confidence in the slope has to be increased, not every one of the 31'678 unique pathways need to be mapped experimentally. Axonal reconstructions are critical and much work has to be done generally by the community

## Appendix C. Reconstruction of the Neocortical Microcircuit

---

to render increasingly more accurate morphologies of neurons. Perhaps most important is for connectomics studies to focus on identifying exceptions to statistical connectivity rather than attempting to map each statistically located synapse. Cell densities are also important, but since experimental error can be vast, these values need to be constrained by other parameters. In fact, reconstructing the map illustrates how the process can be used to curate published data. Indeed, we found that connection probabilities reported in the literature also contains potentially enormous experimental errors. Connection probabilities only matched when we strictly mimicked experimental distances between pairs of recorded neurons (not shown).

Related to the synaptome, considerable work is required to generally assign synaptic properties accurately to synapses. The receptor composition and their biophysics at different synapses are fundamental to a general understanding of synaptic transmission. The molecular parameters that determine synaptic dynamics is also a major gap in our current knowledge. The study of the effect of chloride concentration dynamics is required to more accurately capture neuronal and synaptic dynamics more accurately (Khirug et al. 2005; Doyon et al. 2011; for review see Raimondo et al. 2012). Other data such as the precise number and distribution of synapses on different types of neurons and the synaptic density could also further refine the map.

Related to the microcircuit behaviour, the reconstruction reveals a high sensitivity of network dynamics to extracellular calcium concentrations via its impact on synaptic dynamics. Significant changes have been reported in sleep (for review see Tononi & Cirelli, 2003). Since the effect of calcium concentration is exerted via changing synaptic dynamics, neuromodulators are likely to play a critical role in sliding the network along the SA spectrum and hence changing the network properties. The simulations point out the importance of controlled experiments with varied conditions and avoid drawing conclusions about network activity under only one condition.

As the map is refined, predictions will require progressively fewer experiments to gain increasing confidence in predictions from simulation experiments not possible experimentally. The reconstruction process not only offers a formal process for assessing the validity at each step but each level of the reconstruction includes a level of caution (see also below). The reconstruction process also demonstrates that a global collaborative process is essential because of the diversity of the dataset and principles involved (see also below).

We do not claim that the map is representative of all neocortical regions, at different ages and certainly not in different mammalian species (Meyer et al. 2013). The reconstruction process does, however, lay down a novel foundation to enable instantiation of such different microcircuit configurations (e.g. using specific cell densities, m-types, e-types, cellular compositions) and potential variations in principles (e.g. different connectivity principles). Furthermore, its value lies largely in it being a benchmark reconstruction against which other reconstruction can be compared. Deviations are not fatal they expose bifurcating principles operating for example in different ages, regions, and species. For example, at this age of the primary somatosensory cortex, the ascending axons of deeper layer cells are not completely mature. Replacing the morphologies of juvenile neurons with those of adult neurons will increase the upward connectivity and synapse densities (via an increase in connection probability since mean number of synapses/connection and bouton densities in the adult do not seem to change) and instantiates stronger upward connections (data not shown), but do not necessarily require revisions of the principles of connectivity. Other regions, such as the barrel cortex at the same age may also mature earlier (Schlaggar & O'Leary, 1991; Katz & Shatz, 1996; for review see Petersen,

2007), while other regions such as the visual cortex may mature later (Miller, 1986; Fagiolini et al. 1994 ) giving rise to different connectivity which would emerge as the neuronal arbours mature.

The reconstruction reflects a statistical instantiation of an average microcircuit at a specific age (a "snap shot") rather than any individual instantiation since experience-dependent plasticity is not integrated in this first draft. However, it does circumscribe the possible variations in the microcircuit. There is for example, a tight balance between the cell density, extent of the arbourization of each neuron, bouton density, synapses/connection and connection probability where changes in any one of these parameters has implications for all the other parameters. The reconstruction yielded the insight that re-wiring the neurons according to experience would not change the manner in which synapses are distributed on neurons (Hill et al. 2012) nor the overall connectome (The Connectome Algorithm, in preparation; The Predicted Connectome of the Neocortical Microcircuit, in preparation) because the multi-synapse connections are switched in and out (Le Be & Markram, 2006). Indeed, the variance in 7 reconstructions where different subsets of neurons are drawn from the pool and placed in different locations is less than 0.5 SD. This invariance in the connectivity arises from the intrinsic diversity of the morphologies (Hill et al. 2012), which also underlies highly robust synaptic physiology (latency, rise times, amplitudes, decay times, etc) within a pathway even against surprisingly extreme changes in the distribution of synaptic parameters (Ramaswamy et al. 2012).

While validation is performed at each level of the reconstruction, it is possible that errors accumulate and propagate up to through the component models to the topmost compound model (in this case, the activity of the microcircuit). For example, one may argue that if there were small errors at each level (e.g. cell density, mapping gene to protein expression and then to morphologies to validate the cellular composition, the experimental sampling bias to determine the cellular composition itself, the axonal reconstructions, repair and cloning, the relationship between reported synapses/connections and appositions/connection, incorrect classification of neuron types, width of the minicolumns, missing target selectivity that has not yet been identified) the compound model could substantially deviate from the biological instance. While error propagation cannot be prevented entirely, substantial deviations from the biological instantiation is restricted by validation against diverse datasets, which provides also a cross-validation of biological reports, hence experimental data is not simply accepted as accurate. The compound models also broadly validate their component models (e.g. validating the cellular composition, the connectivity or the number of GABAergic synapses, also validates lower level aspects (i.e. the process ensures that validation broadens and deepens as higher level models are built). Nevertheless, it is necessary to continuously challenge the reconstruction with different datasets. For example, the reconstruction predicts an average total synaptic conductance in a single neuron of about 960 nS due to an average of around 500 afferent excitatory neurons yielding an average conductance of 1.9 nS per synapse and, based on experimental data on the average synaptic conductance of glutamatergic receptors, an average of nearly 150-200 glutamatergic receptors, are well within the range of experimental estimates (Yoshimura et al. 2000; Hardingham et al. 2010). The reconstruction process also predicts that if errors do propagate undetected that at some stage the compound model will fail all validation tests thus if compound models pass some validation tests then it signals that errors have not accumulated sufficiently to impact that significantly that level of the model (but they will impact higher level models when integrated).

One may also argue that there are many more details that need to be taken into account such as the glia, vasculature, receptors, signaling molecules, neuromodulation, gap junctions, plasticity, homeostasis, etc. Adding these will of course yield deeper insights into many aspects of the microcircuit,



## Appendix C. Reconstruction of the Neocortical Microcircuit

---

but they are not very likely to impact the main biological features reported in this study. Including vasculature for example would change the path of axons and dendrites to avoid the same space occupied, but because of the statistical nature of the connectivity and the diversity of morphologies this is not expected to change the patterning of synapses significantly. It would also only make sense to integrate the glial and vasculature when molecular detail can be integrated, which in turn only makes sense when single-cell transcriptomes and the proteome of neurons, glia and synapses have been characterized at least sufficiently to reconstruct the biochemical and metabolic pathways that mediate the neuro-vasculature-glial interactions. It would also only make sense to integrate receptors once sufficient data is available on the single-cell transcriptome to allow choosing the appropriate set of ion channels and matching set of receptors for any given genetic (based on the gene expression) type of cell. Deeper level sub-typing of neurons (e.g. based on afferent and efferent profiles, protein and gene expression) would make sense when the relevant data is integrated. It would make sense to refine the sub-typing of neurons when data on layer dependent input and output to the rest of the brain has been characterized sufficiently. A more important source of error as the activity of the microcircuit is studied in greater detail is the accuracy with which the reconstruction can capture stochastic features in ion channels & synapses. While the reconstruction does capture stochastic neurotransmitter release, the synapse model does not take into account recent evidence that indicates multi-vesicular release as the mode of transmission for specific pathways (Huang et al. 2010; Loebel et al. 2008). This first draft reconstruction however provides a framework for integrating such deeper and more specific aspects of the biology and refined classifications. The value of this systematic reconstruction therefore also lies not only in the first draft, but also in observing the differences when new biological data are integrated and in the fact that falsification of the model reveals a key gap in our data and our understanding of the principles, which ultimately drive us back to experiments to challenge the accepted understanding.

As in the case of the structural reconstruction the simulations that test the functional reconstruction, also do not fully explain how the microcircuit functions. They do however provide a solid foundation on which its functions can now be studied. For single neurons, for instance, the manner in which they are electrophysiological characterized is very well established. On the other hand, characterizing the properties of the next level up – the microcircuit – has been unclear. The simulations suggest a simple and essential benchmark to characterize and compare networks. The benchmark involves shifting the network along the SA spectrum and analyzing the network properties at different points of the spectrum. We demonstrate that the network properties such as the response rate, the spreading of activity, and the specific active assemblies of neurons depends on the position on the spectrum and therefore comparing across different networks of neurons requires standardization on the spectrum. The SA spectrum is highly robust and has been observed in all iterations of the reconstruction (over 100) indicating that in itself it is not a special property of the exact configuration of the circuit, but rather a general property of networks containing dynamic synapses and is essentially due to a change in the ratio of excitatory and inhibitory activity (thus it is not necessary to induce the shift only by changing the extracellular  $Ca^{2+}$ ). Indeed, the spectrum can be recreated with a point neuron network and even a mean field network (not shown). On the other hand, virtually any aspect of the microcircuit, albeit to varying degrees, would likely influence the precise set of assemblies engaged along the spectrum. This benchmark can now be used to characterize the role of any biological feature in the behavior of the microcircuit; the role of any neuron, synapse, connection, pathway, and layer in regulating the response rate, the spread of activity, functional clustering of neurons, emergence of oscillations between neurons during a stimulus, cascade of information flow, stability of information processing, to name but a few. In fact, performing a massive sensitivity analysis could yield a look up table prioritizing the sensitivity of a spectrum of such phenomena to each biological element, property & principle. It would make

sense to perform such an analysis after the community has been engaged to refine the reconstruction, reach consensus on issues such as the classification of neurons and synapses and develop benchmark target functions collaboratively.

The reconstruction and simulation rest on a complex ecosystem of software and it is not possible to develop error free complex software. In fact, we had several cases where the compound model failed validation, not because of errors in the biological accuracy, but because of errors in its digital implementation. A similar strategy was therefore employed in developing the software as in the digital microcircuit. The software was constructed in many modules where the level of component software could be isolated and governed by the principle of validate early and often. In the same way that we propose biological refinement to be ultimately achieved by the community challenging and using the reconstruction, we also adopted an open source approach where software can be challenged by peers from inside and from outside the consortium. We therefore acknowledge that there could be error(s) in a reconstruction or validation step, but there cannot be errors in all reconstructions and validations.

In conclusion, the insurmountable number of experiments required to densely characterize even a minute part of the brain suggests that attempting to obtain or waiting for a complete experimental characterization of the brain is not practical. Predictive reconstruction using the partial data and applying fundamental principles is an essential companion approach to experimentally mapping the brain. In this approach most of the biological detail comes from predictions and experimental data is increasingly evaluated for their value in generating and validating these predictions (depends on the information they carry to broadly constrain other parameters or the number of interdependencies). We provide only a sample of testable predictions in this paper. The accompanying papers provide a) the conceptual breakthrough required to algorithmically reconstruct the connectome, b) the novel predicted features of the connectome of the reconstructed microcircuit, c) an experimental data paper describing the experimental data used to perform the reconstruction and point to where the raw data can be obtained, and d) an in silico resource paper describing the online portal that has been constructed to make the reconstruction, tools, methods, software available and processes for global collaboration to challenge and refine the reconstruction and in principle to generalize the process to other brain regions, ages, species, genders and diseases and disease models.

## C.11 Figures and Legends

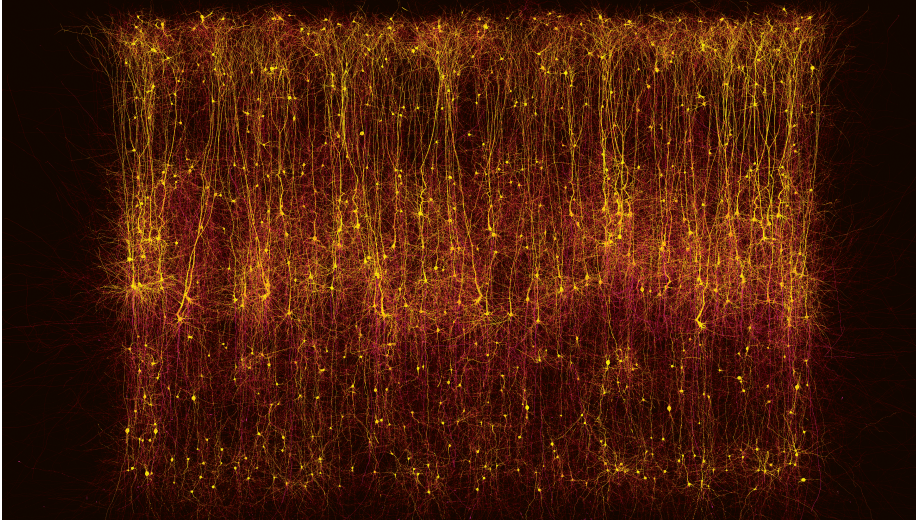


Figure C.1 – **Collage of neocortical neurons.**

A random selection of recorded and reconstructed neocortical neurons in each layer of the somatosensory neocortex. Dendrite, yellow; Axon, red.

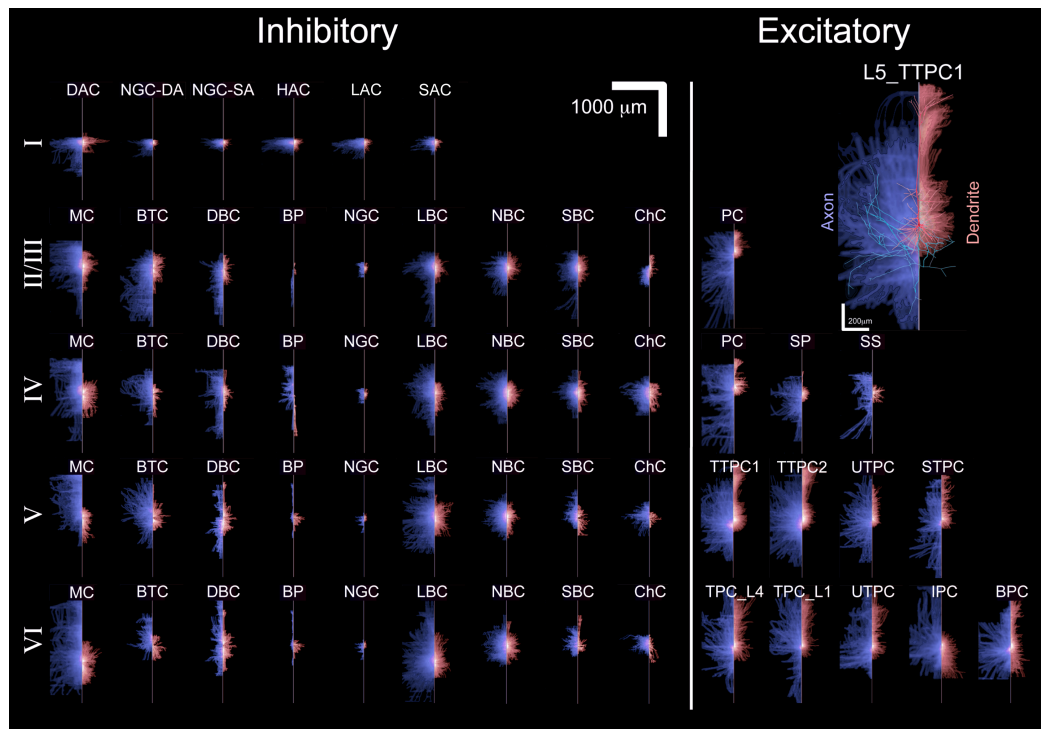


Figure C.2 – **Reconstructing morphological diversity.**

2D projection of fiber density of neocortical m-types obtained by overlaying multiple reconstructions with somata aligned to a single point and summing the fiber length per  $\mu\text{m}^3$  (axon left, blue; dendrite right, red). Left & right panels; density plots for 55 known inhibitory and excitatory m-types arranged horizontally by layer. Layer 6 horizontal pyramidal cells and horizontal sub-plate neurons are not included in this first release of the model. Inset right; fiber density plot of xyz reconstructions of thick-tufted layer 5 pyramidal cell morphologies with an exemplar reconstruction superimposed. NGC-DA, Neurogliaform Cell with dense axonal arborization. NGC-SA, Neurogliaform Cell with slender axonal arborization. HAC, Horizontal Axon Cell. DAC, Descending Axon Cell. DLAC, Dense Local Arborizing Cell. SLAC, Slender Local Arborizing Cell. LBC, Large Basket Cell. NBC, Nest Basket Cell. ChC, Chandelier Cell. SBC, Small Basket Cell. MC, Martinotti Cell. BP, Bipolar Cell. DBC, Double Bouquet Cell. BTC, Bitufted Cell. NGC, Neurogliaform Cell. Excitatory cells in layer 2/3: PC, Pyramidal Cell. In layer 4: SP & SS, Star Pyramidal and Spiny Stellate cells. In layer 5: TTPC1 & TTPC2, Thick-tufted Pyramidal Cells with early bifurcating apical tuft and late bifurcating apical tuft. STPC & UTPC, Slender and Untufted Pyramidal Cells. In layer 6: TPC\_L1 & TPC\_L4, Pyramidal Cells in layer 6 – dendrites terminating in layer 1 and dendrites terminating in layer 4. UTPC, Untufted Pyramidal Cells. BPC, Pyramidal Cell with bipolar dendrites. IPC, Pyramidal Cell with inverted dendrites.

## Appendix C. Reconstruction of the Neocortical Microcircuit

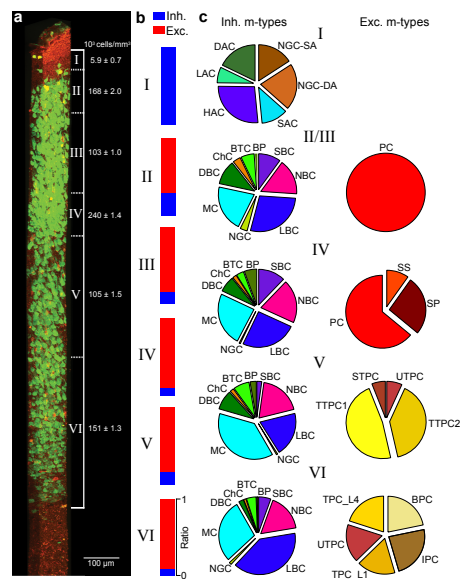


Figure C.3 – **Reconstructing morphological composition.**

(a) Confocal block imaging of dual immunohistochemical labeling of rat P14 somatosensory cortex. NeuN labels neurons (green), GABA labels GABAergic cells including glia (red), dual GABA&NeuN labels only GABAergic neurons (green+red=yellow). (b) Proportions of excitatory (red, NeuN-GABA) and inhibitory (blue, GABA&NeuN) neurons in each layer. (c) Proportions of m-types within the inhibitory (left) and excitatory (right) subpopulations per layer, obtained from morphological classification (n=2000). Frequencies of occurrence of m-types in the unitary microcircuit are determined by combining (b) and (c).

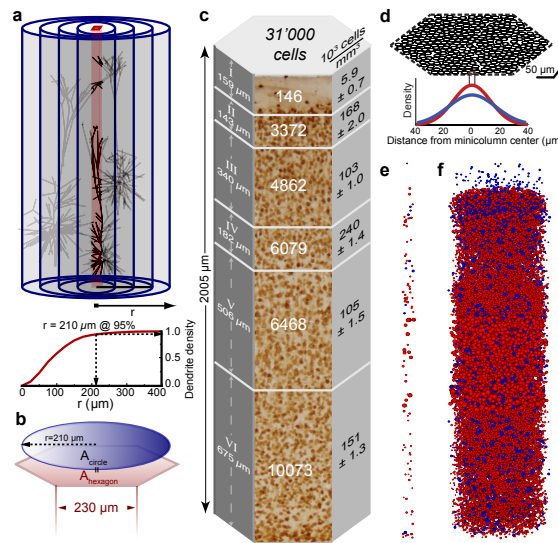


Figure C.4 – **Reconstructing cell densities and positions.**

(a) The horizontal dimension was defined as the smallest circle required for maximal dendritic volume at the center (the larger the circle the more neurons contribute to the volume at the center). The dendritic volume was obtained for the m-type with the largest dendritic morphology (L5\_TTPC1) placed according to derived densities (see below). The cut-off radius was set at 95% of the plateau ( $r = 210 \mu\text{m}$ , graph below). This cut-off radius also holds for microcircuits reconstructed with all m-types (see below). (b) This circle was transformed into a hexagon, preserving the area, to allow tiling while limiting asymmetrical edge effects. (c) The vertical dimension and layer thicknesses were obtained from transitions in neuronal somata size and density in NeuN stained slices ( $n = 6$ ). Layer thicknesses, total number of cells and cell densities per layer are shown.

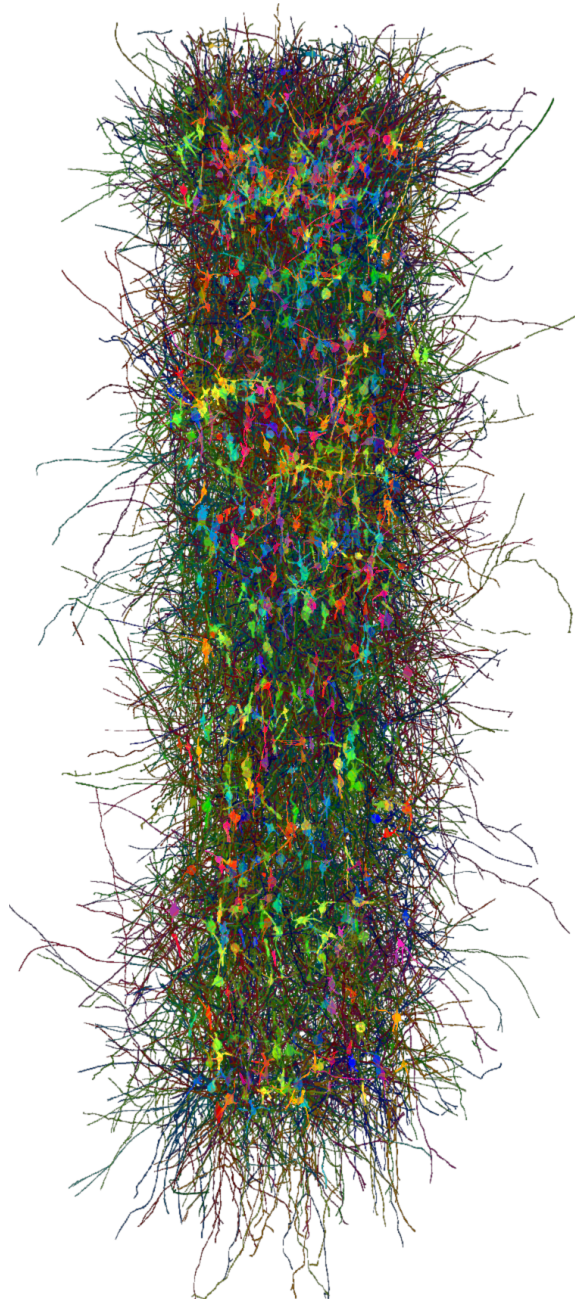


Figure C.5 – **Morphologically reconstructed microcircuit.**

A visualization of all inhibitory morphologies in an instance of the reconstructed microcircuit, colored by m-type.



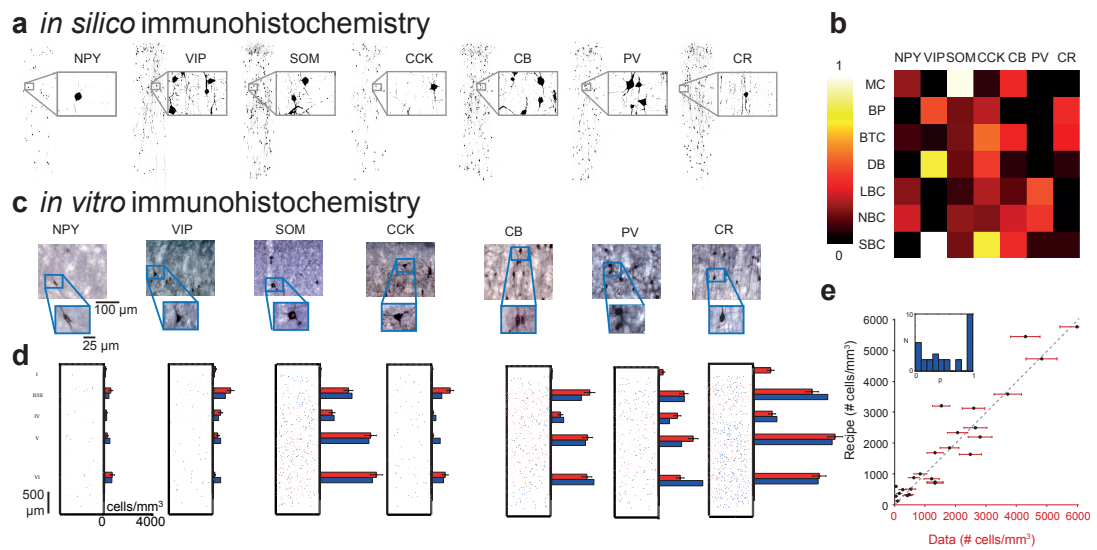


Figure C.6 – Validating morphological composition.

(a) In silico labeling of m-types in the microcircuit for neuropeptides and calcium binding proteins commonly found in inhibitory neurons: Neuropeptide Y (NPY), Vasoactive intestinal polypeptide (VIP), Somatostatin (SOM), Cholecystokinin (CCK), Calbindin (CB), Parvalbumin (PV), and Calretinin (CR). (b) Labeling was performed according to single-cell gene expression determined by RT-PCR on 600 morphologically-identified cell types (m-type to g-type mapping). (c) In vitro labeling using antibodies against the same set of proteins. (d) Labeled cell soma positions and histograms per layer for each protein. To account for unquantified binding affinity and shrinkage, a scaling factor is applied per labeling protein to in silico counts to minimize RMS distance (see methods). Red: in vitro staining, blue: in silico. (e) Plot comparing in vitro vs in silico labelling. Inset: Histogram of P-values to confirm the null hypothesis, t-test.



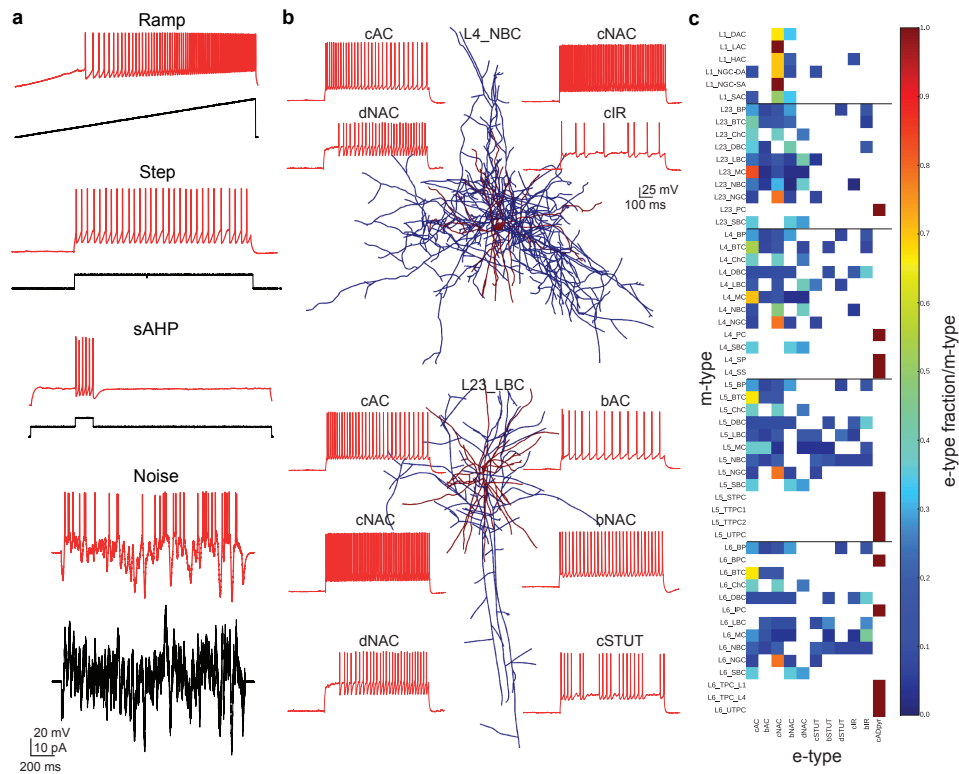


Figure C.7 – Reconstructing morpho-electrical neuron types.

(a) A standardized set of stimulation protocols (e-code) are used to reveal the diversity of electrical types (e-types). A subset of e-code protocols used to characterize and classify e-types is shown. The currents injected into single neurons during whole cell current clamp experiments (bottom) and the voltage responses (top) are shown. (b) Diverse firing patterns observed in two exemplary m-types as revealed by step current injections (top, L4\_NBC; bottom, L23\_LBC). (c) Fractions of e-types (11 e-types) recorded experimentally in each m-type (55 m-types; 207 me-types).

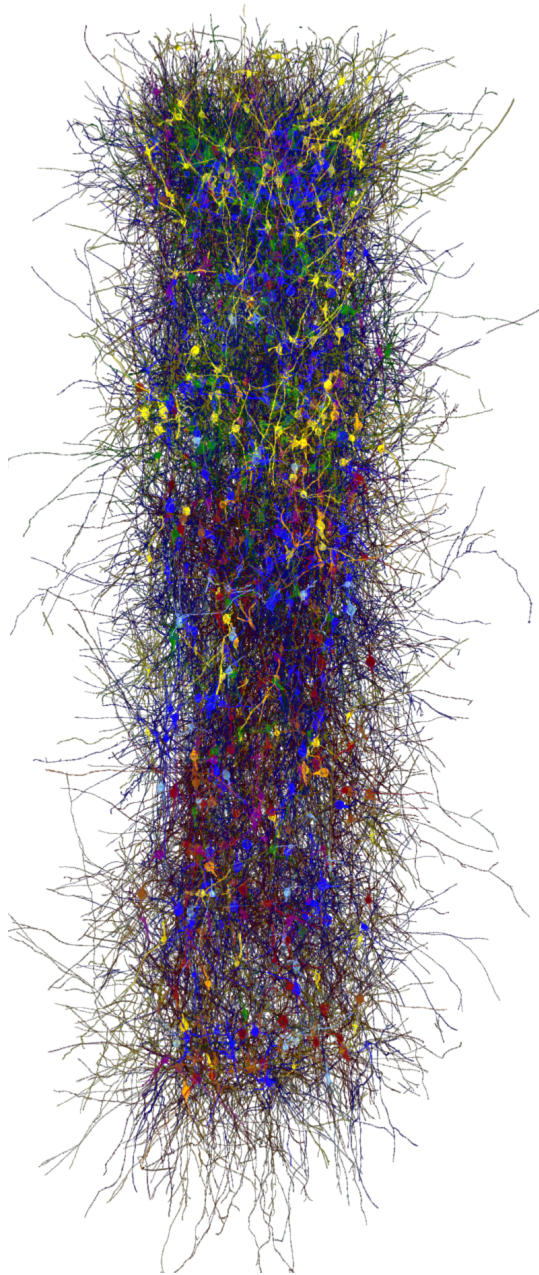


Figure C.8 – **Morpho-electrically reconstructed microcircuit.**

In silico brainbow-like staining of a random selection of inhibitory morphologies in an instance of the microcircuit, colored by e-type.

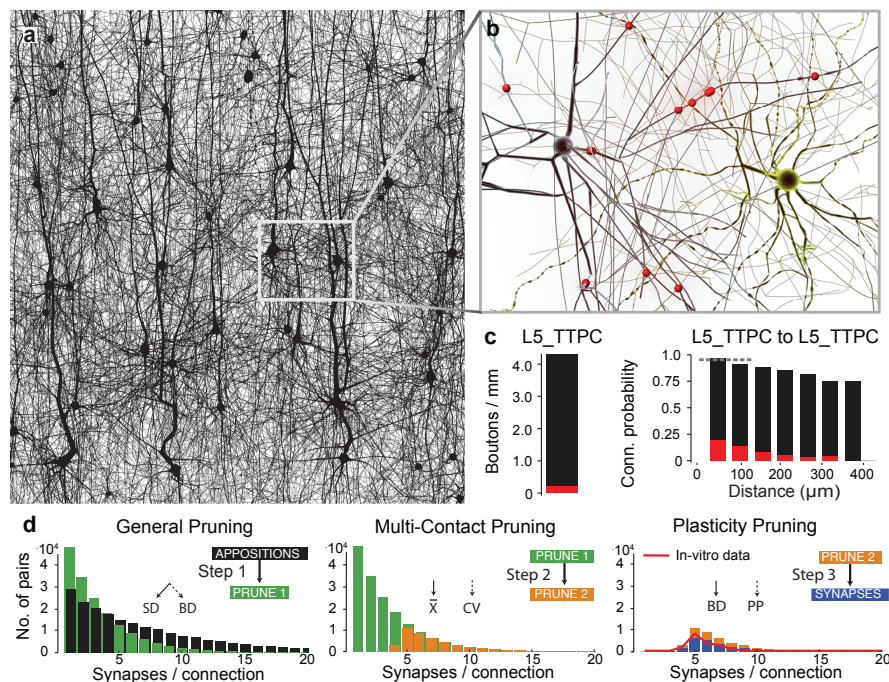


Figure C.9 – Reconstructing the connectome.

The connectome reconstruction algorithm uses anatomical rules to determine morphological appositions and convert a subset into synapses. (a) The unitary microcircuit after all morphologies are placed (5% cell density shown). The resulting high density of fibers leads to a myriad of pairwise morphological appositions. (b) Valid appositions. An algorithm running on a super-computer identifies all appositions ( $< 2.5\mu\text{m}$  for excitatory appositions,  $< 0.5\mu\text{m}$  for inhibitory appositions). Appositions violating biological rules for synapse formation are removed leaving only valid appositions. An example of 11 valid appositions (red circles) found between a layer 2/3 pyramidal cell (left) and a layer 2/3 nest basket cell (right). (c) (left) The bouton density suggested by valid appositions (black bar, assuming one bouton per apposition) far exceeds the density of boutons in biological tissue (red bar). Bouton density on an L5\_TTPC is shown (see Supp. Table X for other m-types). (right) Connection probability as suggested by valid appositions is consistent with the connection probability based on structural appositions found experimentally (dashed gray line, Kalisman et al., 2005), but far exceeds the functional connection probability between L5\_TTPCs (red bars, Perin et al., 2011). (d) three-stage apposition pruning algorithm: Appositions are pruned to constrain the number and distribution of synapses formed for each pairwise connection (illustrated for the L5\_TTPC to L5\_TTPC pathway). General Pruning (left histogram): The algorithm randomly prunes valid appositions (black bars). The appositions can be pruned following two methods: (1) If the distribution of the number of synapses per connection has been obtained experimentally, then the appositions are pruned to match the standard deviation of this distribution (SA, biological parameter, inset, left arrow). (2) For pathways not experimentally characterized, a percentage of appositions is pruned. The percentage is calculated from the additional pruning required following step 2 and 3 (final) to reach a generalized (average across pathways) biological bouton density (BD, derived parameter, inset, right dashed arrow). Multi-Contact Pruning (middle histogram): The second step retains appositions that are part of multi-contact connections, i.e. appositions are admitted with a probability increasing sigmoidally with the number of contacts. (1) If the distribution of the number of synapses per connection has been obtained experimentally, then the half-maximum is chosen to

match the mean of this distribution (biological parameter, inset, left arrow). (2) For pathways not experimentally characterized, the half-maximum is chosen to increase the mean to reach a generalized coefficient of variation of 0.3 (CV, derived parameter, inset, right dashed arrow). Plasticity Pruning (right histogram): The third step prunes a fraction of multi-contact connections to allow for rewiring of the microcircuit (i.e. connections are pruned independently of the number of contacts). (1) The fraction pruned is chosen to match the biological bouton density (BD, biological parameter, inset, left arrow). (2) A generalized value for the fraction pruned is used (PP, derived parameter, right dashed arrow). The final distribution of synapses per connection is consistent with in-vitro measurements of this pathway (red line, Markram et al., 1997,  $p=0.15$ , discrete Kolmogorov-Smirnov test).

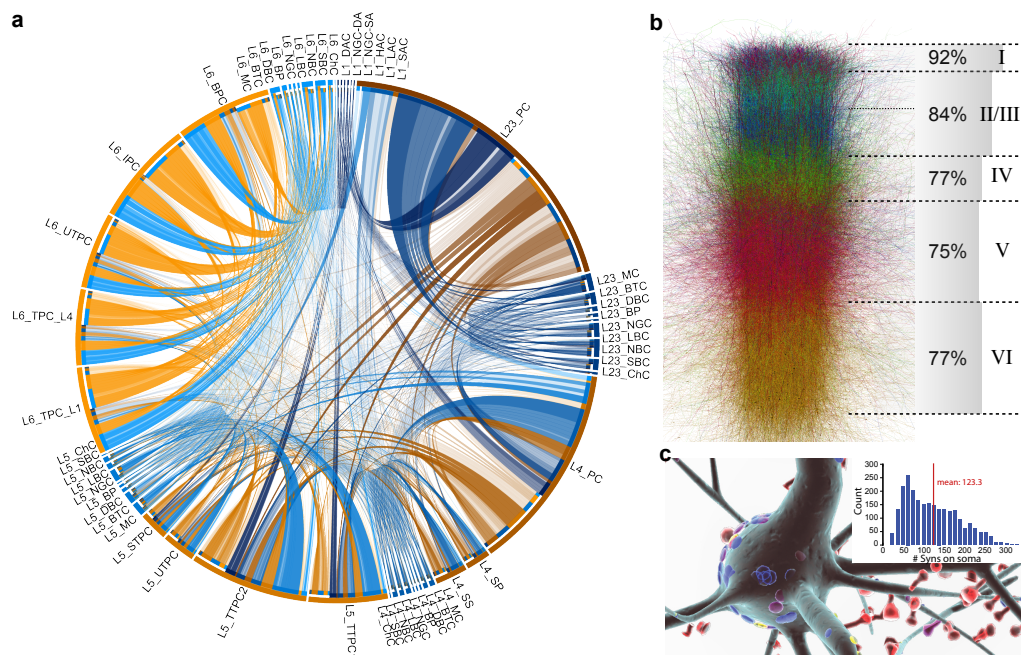


Figure C.10 – **Insights obtained from the predicted map of connectivity.**

(a) The derived connectome of the reconstructed microcircuit. Pyramidal cells and spiny stellates are shown as color-coded triangles based on their layer of origin; Martinotti cells as color-coded hexagons; Basket cells as color-coded cylinders; Bipolar, bitufted, chandelier, neurogliaform and layer 1 interneurons as color-coded rectangles. (b) Estimation of the fraction of afferent input (neighboring microcircuits, fibers from the same brain region, distal cortico-cortical fibers and projection fibers from other brain regions) into the microcircuit needed to reach biological spine densities, with an assumption that one excitatory synapse corresponds to one spine. (c) Rendering of the soma of a L5\_TTPC1 showing inhibitory synapses on the somata (blue disks) and an inset showing the distribution of the predicted number of inhibitory synapses on these pyramidal neurons. Red line indicates mean.



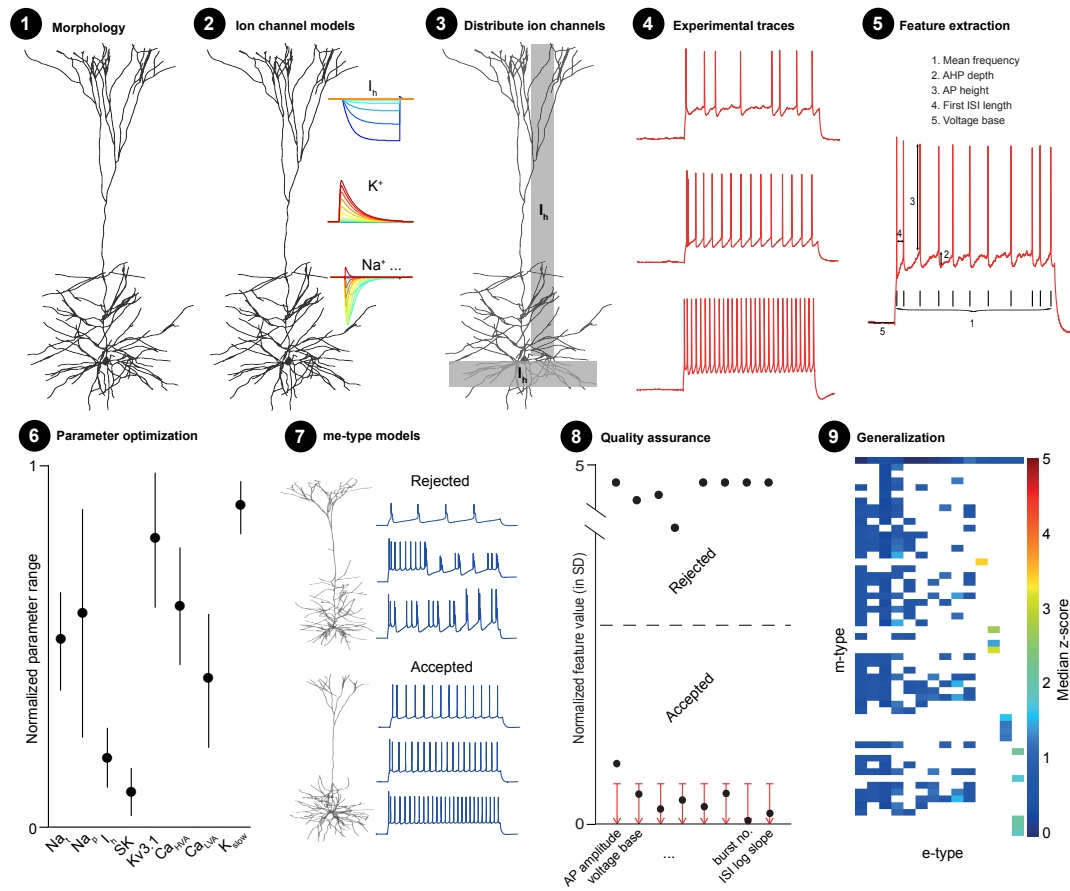
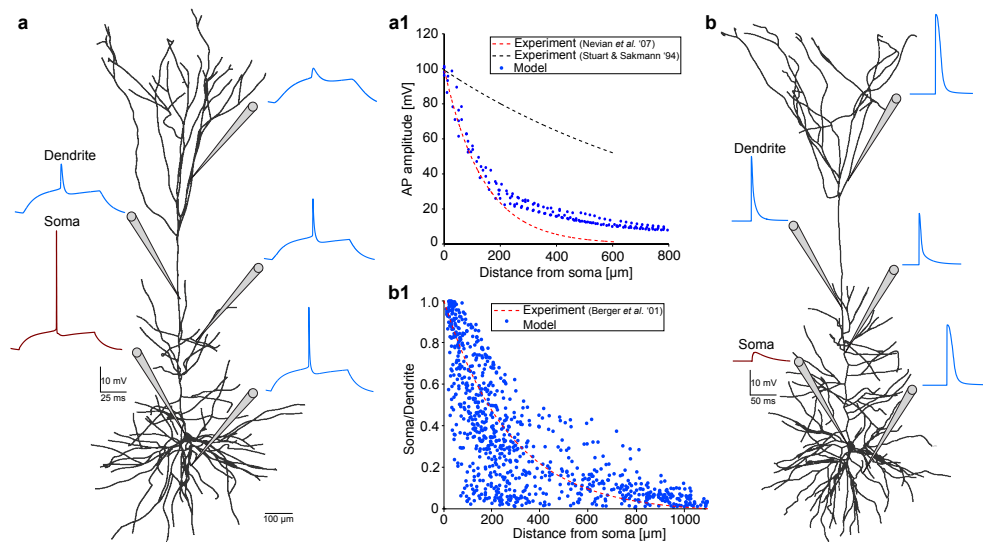


Figure C.11 – **Workflow for reconstructing morpho-electrical behaviors.**

(1) Select exemplar morphology. (2) Selection a set of ion channel models for somata, dendrites and axons. (3) Distribute ion channels along the arbors according to biological data and assumptions. (4) Select experimental traces from a population of recorded cells as targets for reconstruction. (5) Extract voltage and spiking features. (6) Multi-objective optimization of the vector of ion channel conductances to be consistent with the statistics of the extracted biological features. (7) Generalize the vector of conductances to other morphology exemplars of the same m-type and run an in silico e-code on each model neuron. (8) Screen out model not consistent with the statistics of the extracted biological features. (9) Overview of the quality score of accepted models (median z-score).



**Figure C.12 – Validating and predicting passive and active properties.**

(a) Left, simultaneous in silico recordings of EPSPs produced in an apical dendritic section (blue; 500  $\mu\text{m}$  from the soma), and the soma (red) in a thick-tufted layer 5 pyramidal cell. A transient synaptic conductance change was injected at each dendritic section of the morphology and the resulting EPSP was measured simultaneously in the soma. Right, predicted in silico EPSPs to transient synaptic conductance injection at different dendritic locations. (a1) The dendritic to somatic attenuation ratio of in silico EPSPs to transient synaptic conductance change injected at each dendritic section (blue dots) of 10 thick-tufted layer 5 pyramidal cells as compared against a fit of the experimental data (red dashed line; Nevia et al. 2007). (b) Left, simultaneous in silico recordings of back-propagating APs (bAP) in the apical dendrites (blue; located  $\sim 550\mu\text{m}$  from the soma), and the soma (red) in a thick-tufted layer 5 pyramidal cell to a somatic step current injection. Right, predicted in silico bAPs at different dendritic locations to somatic step current injection. (b1) The in silico bAP amplitude at different dendritic locations from the soma (blue dots) to somatic step current injection as compared against a fit of the experimental data (red line; Nevia et al. 2007).

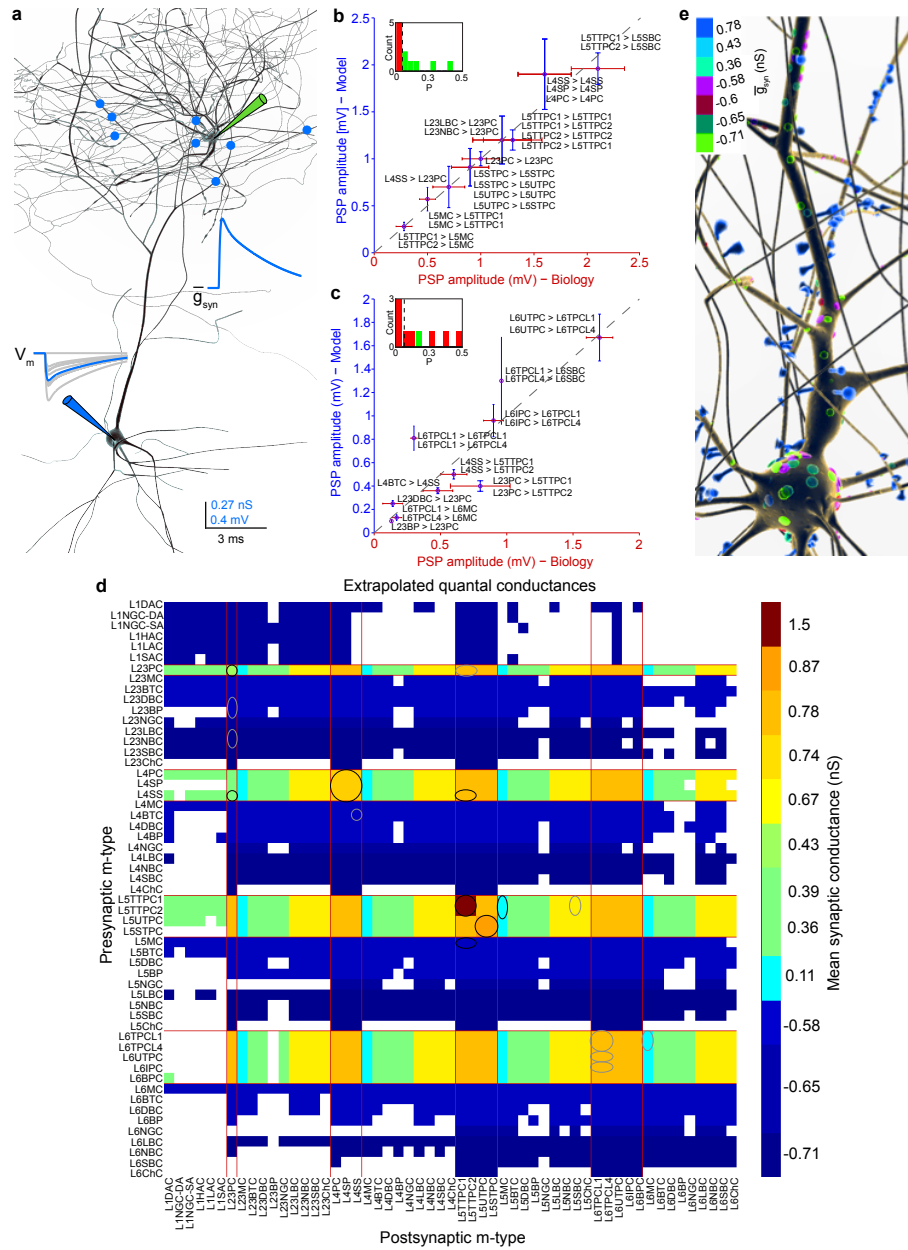


Figure C.13 – Reconstructing quantal synaptic conductances.

(a) In silico patch-clamp recording in a randomly chosen pair of neurons connected through multi-synaptic contacts (blue filled circles) displaying trial-to-trial variability due to stochastic transmitter release. A single AP was evoked by somatic current injection in the presynaptic L6\_IPC (green pipette), which elicited a postsynaptic potential in the target L6\_TPC (grey, individual trials; blue, average of 30 trials). The mean synaptic conductance was adjusted iteratively for all pairs in a pathway to reproduce the biological distribution of EPSP amplitudes (see methods). (b) The in silico PSP amplitudes reconstructed using the iterative conductance fitting approach, compared to biological data for the best characterized pathways. (N = 21). Inset: distribution of p-values of discrete KS-tests comparing model and biological distributions of PSP amplitude for the indicated pathways. Where the actual data



## Appendix C. Reconstruction of the Neocortical Microcircuit

---

samples of the EPSPs were available, we compared them against samples from the model (green bars). Where they were unavailable, we compared against a lognormal distribution published (mean and SA). (c) The derived quantal conductances were extrapolated to examine the physiology of less well experimentally characterized pathways without explicitly fitting to experimental data, but rather to generalized data (N=17). Inset as above. (d) The extrapolated map of quantal conductances: Circles indicate pathways used in b (black) and c (grey) above. Red lines delineate excitatory morphology types. Negative values denote inhibitory conductances. (e) In the absence of experimental data on postsynaptic potentials, mean synaptic conductances are predicted by generalizing from similar pathways allowing extrapolation of mean synaptic conductances for all synapses on a neuron. Yellow and below indicates inhibitory synaptic conductances.

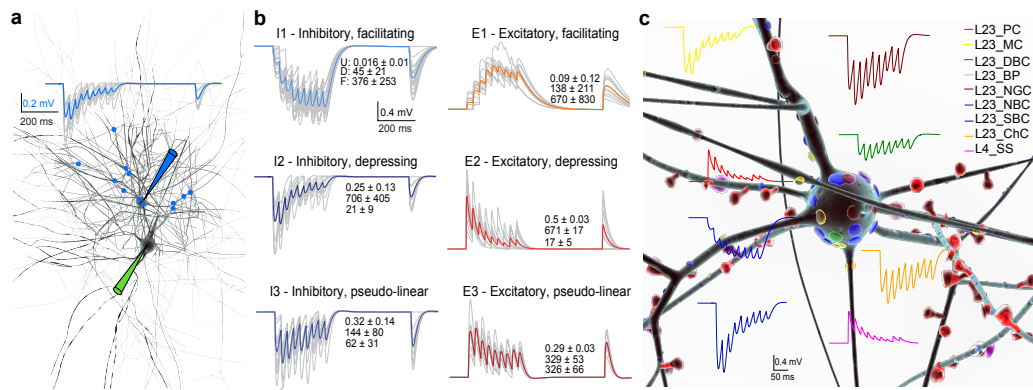


Figure C.14 – Reconstructing synaptic dynamics.

(a) Left, Experimental connection protocols were recreated in silico to record the frequency dependence of synaptic transmission between pairs of neurons. A presynaptic L23\_SBC was stimulated with a 30 Hz pulse train to evoke 8 APs (green pipette) giving rise to an inhibitory facilitating response in the postsynaptic L23\_PC (blue traces). The connection was mediated by 13 synapses (blue filled circles). The individual postsynaptic responses are shown as grey traces and the mean response averaged over 30 trials in shown in blue. (b) The parameters describing 6 s-types in the Tsodyks-Markram phenomenological synapse model. (c) Predicted diversity of s-types in a single L23\_PC.

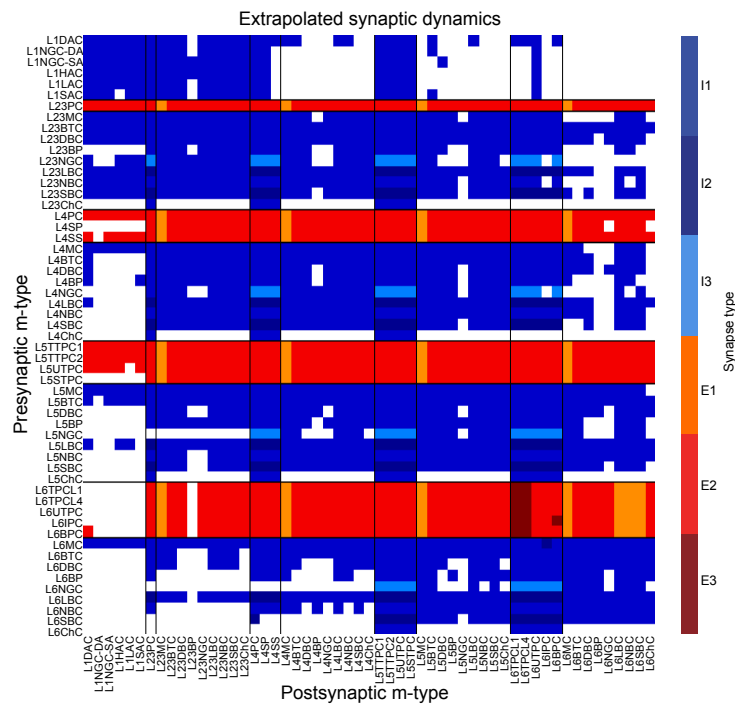


Figure C.15 – Extrapolated map of synaptic dynamics.

The established mapping rules were used to extrapolate s-types for pathways that have not been experimentally characterized to yield a complete map for all 2258 pathways in the reconstructed microcircuit.

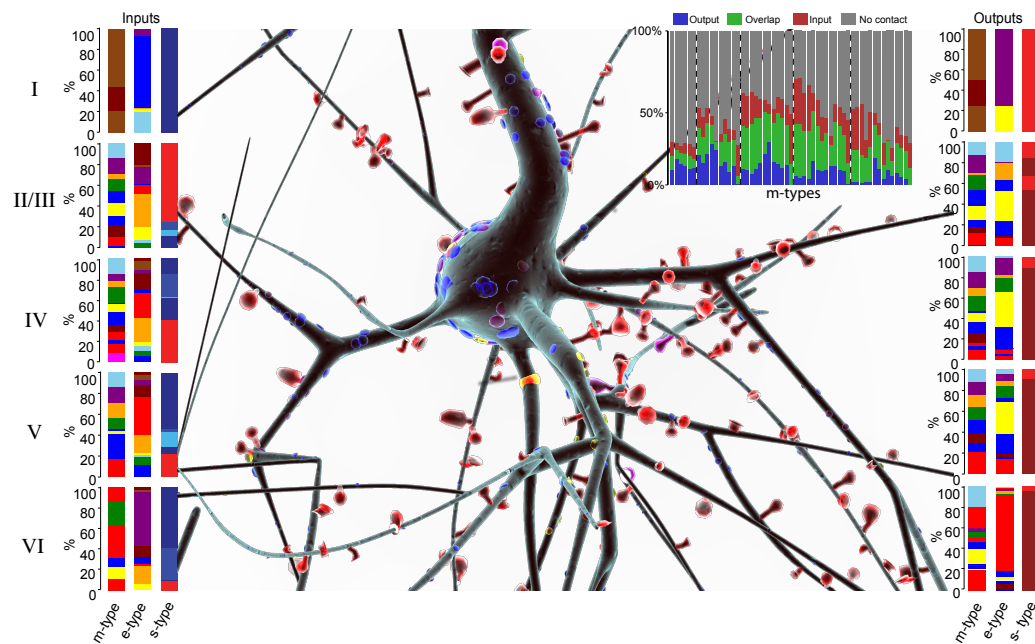


Figure C.16 – **Predicting the synaptome.**

The complete synaptic input (left) from and output (right) to all m-, e- and s-types for a single L5\_TTPC neuron – the synaptome. The inset shows the fraction of targeted and incoming m-types (overlap; green), targeted only (output; blue) and incoming only (input; red) for each of the 55 m-types.

## Appendix C. Reconstruction of the Neocortical Microcircuit

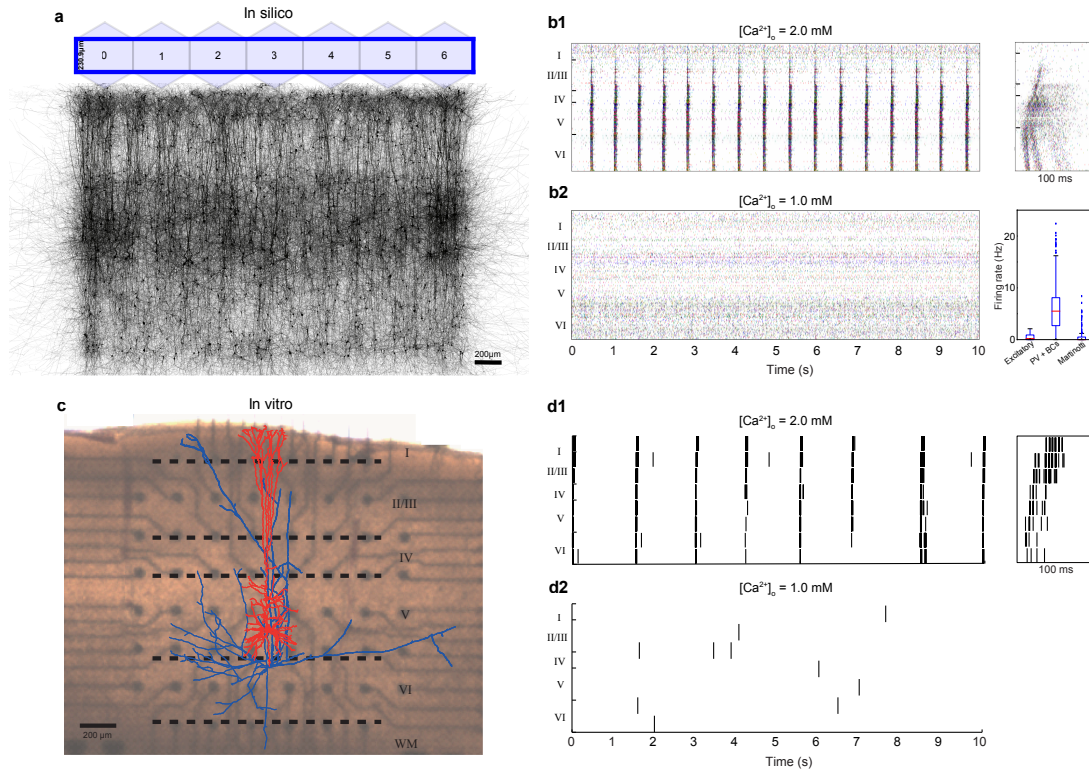


Figure C.17 – **Validating and predicting spontaneous activity.**

(a) Seven unitary microcircuits are connected to form a tissue volume comparable to in vitro cortical slices ( $230.9\mu\text{m} \times 2800\mu\text{m}$ ). A visualization of 5% of all m-types in the reconstructed brain slice. (b1, b2) Multi-unit activity in the *in silico* slice depolarized to a level equivalent to that produced by  $[K^+]_o \approx 5.0\text{mM}$  and  $[Ca^{2+}]_o = 2.0\text{mM}$  (in vivo-like; above raster plot) and by  $[K^+]_o \approx 5.0\text{mM}$  and  $[Ca^{2+}]_o = 1.0\text{mM}$  (in vitro-like; below raster). Upper right: Box plot of mean firing rates for excitatory cells, all LBCs and NBCs (i.e. PV+BCs), and MCs recorded in vivo (red; ref) and in-vivo-like in silico (blue). Lower right: A zoom in of the spiking activity during a network burst initiated on the border of L5-L6. (c) Cortical slices were mounted on a 3D multi-electrode array (MEA) to assess network activity (reconstruction of a layer 5 pyramidal overlaid; dendrites in red, axons in blue). (d1, d2) Experimentally observed asynchronous multi-unit activity under in vitro  $[Ca^{2+}]_o$  (upper raster) and spontaneous low-frequency bursting under standard in vivo  $[Ca^{2+}]_o$  (lower raster) and during depolarization induced by  $[K^+]_o = 5.0\text{mM}$ . Bottom right: A zoom in of the spiking activity during a network burst initiated on the border of L5-L6.

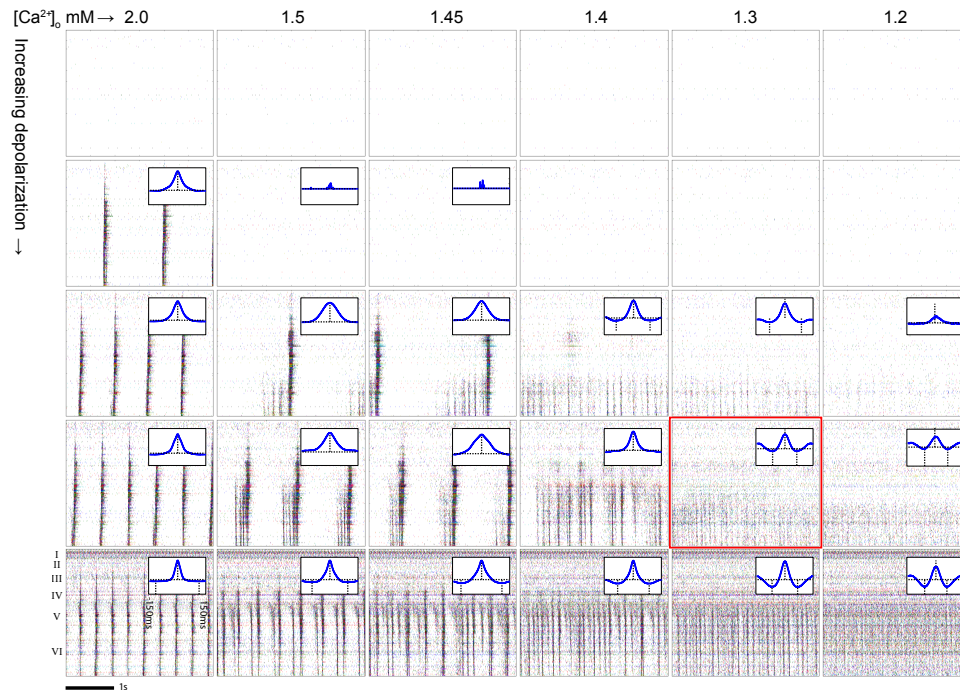


Figure C.18 – **Predicting evoked emergent network states.**

Scanning a wide range of  $[Ca^{2+}]_o$  (horizontal axis) and depolarization levels (vertical axis, see methods) reveals a diversity of emergent network states.  $[Ca^{2+}]_o$  at typical in vitro levels results in synchronous network bursting at a frequency dependent on the level of depolarization. Decreasing  $[Ca^{2+}]_o$  towards in vivo levels results in a transition to asynchronous firing around 1.3mM that is relatively less dependent on the level of network depolarization. In the asynchronous regime, a low amplitude  $>10$ Hz oscillation remains. Spike-spike correlations (insets) reveal that networks are functionally coupled in the asynchronous regime. Raster plots depict spiking activity for a 2.5s interval. The in-vivo-like depolarization- and calcium-level is denoted by the red box outline.

## Appendix C. Reconstruction of the Neocortical Microcircuit

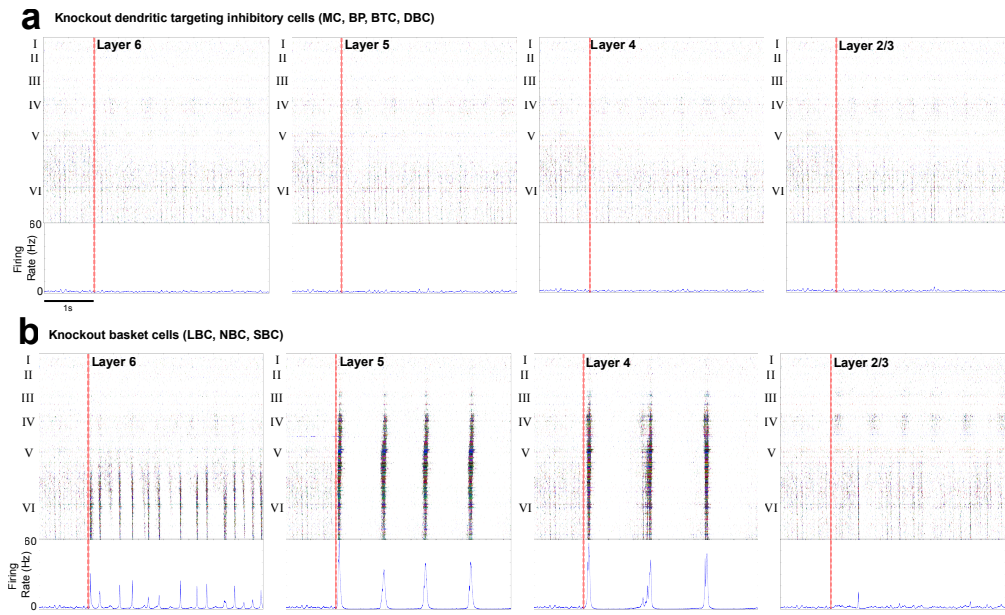


Figure C.19 – Predicting the functions of neurons.

Transient inhibition of class- and layer-specific neurons in silico predicts baskets cells, but not dendritic targeting inhibitory cells are required to maintain the asynchronous state under in-vivo-like conditions. (a) Raster plots (above) and PSTHs (below) for in silico experiments under in vivo-like conditions (as indicated by the red box in Figure 18) silencing the synaptic activity of dendritic targeting cells (MC, BP, BTC, DBC) in layers 6-2/3 (left to right). Vertical red line indicates time of synaptic knockout. (b) Same as in (a), but silencing basket cell populations (LBC, NBC, SBC).

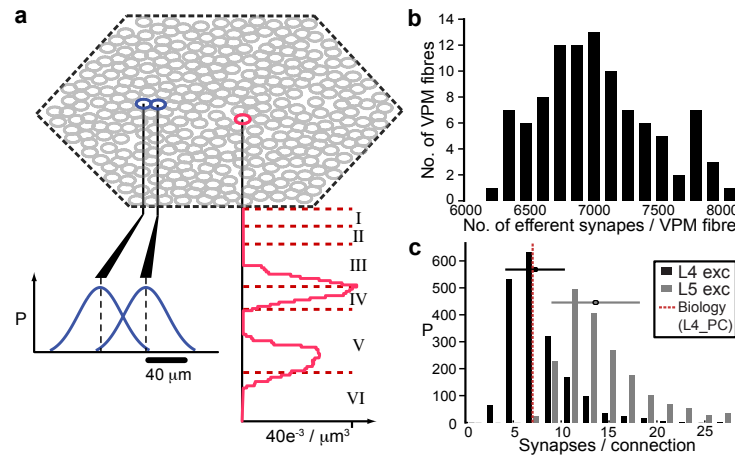


Figure C.20 – **Reconstructing thalamocortical input.**

(a) Thalamo-cortical input is constrained by biological data on the profile of synaptic density across the layers and assuming one thalamocortical fiber per minicolumn (ref). (b) Distribution of number of synapses made by the population of thalamocortical fibers. (c) Synapse density is initially increased by a factor of 3 before pruning according to the multi-synapse rule previously established. This increases the mean number of synapses per connection to excitatory cells in L4 (black bars) and L5 (grey bars).



## Appendix C. Reconstruction of the Neocortical Microcircuit

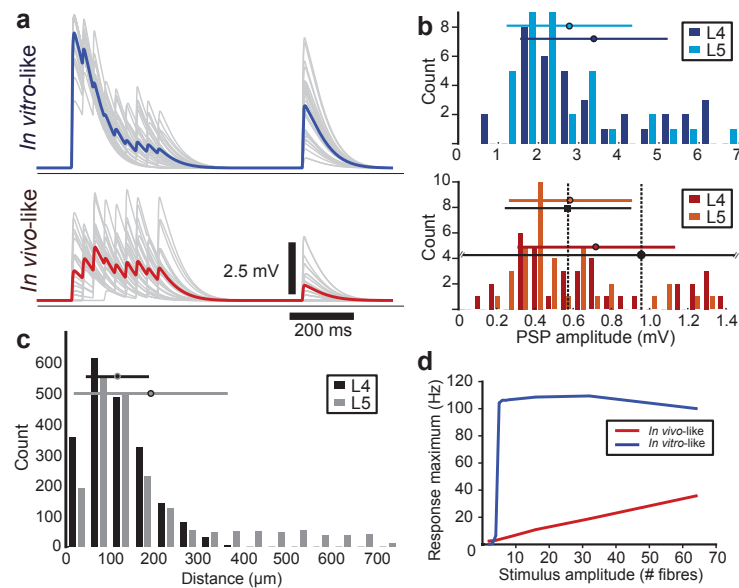


Figure C.21 – Validating and predicting thalamocortical input.

(a) The dynamics of synaptic transmission of thalamocortical connections to L4 excitatory cells under in-vitro-like (above, blue – average trace of 30 trials in grey) and in-vivo-like conditions (below, red – average trace). In-vitro-like conditions give rise to an excitatory depressing response, whereas the same connection under in-vivo-like conditions gives rise to a pseudo-linear response. (b) EPSP amplitude distribution for in-vitro-like (above) and in-vivo-like (below) conditions for randomly sampled TC-L4 and TC-L5 excitatory cells. Colored intervals show mean and SA for respectively colored histograms. Biological data from in-vivo preparations are shown (L4 - black circle, L5 - black square, mean & SA; refs). (c) Distribution of morphological path-length to the soma for TC synapses onto L4 (black) and L5 (grey) excitatory cells. Intervals show mean and SA. (d) Amplitude of population firing rate (at maximum) evoked by stimulating a bundle of central TC fibers each with a single synchronous spike for in-vitro-like (blue) and in-vivo-like (red) conditions. Increasing the stimulus amplitude by adding additional TC fibers to the stimulated bundle evokes an all-or-nothing network response under in-vitro-like conditions for 9 stimulated fibers. Under in-vivo-like conditions, the network response amplitude depends on stimulus amplitude in a sigmoidal manner.

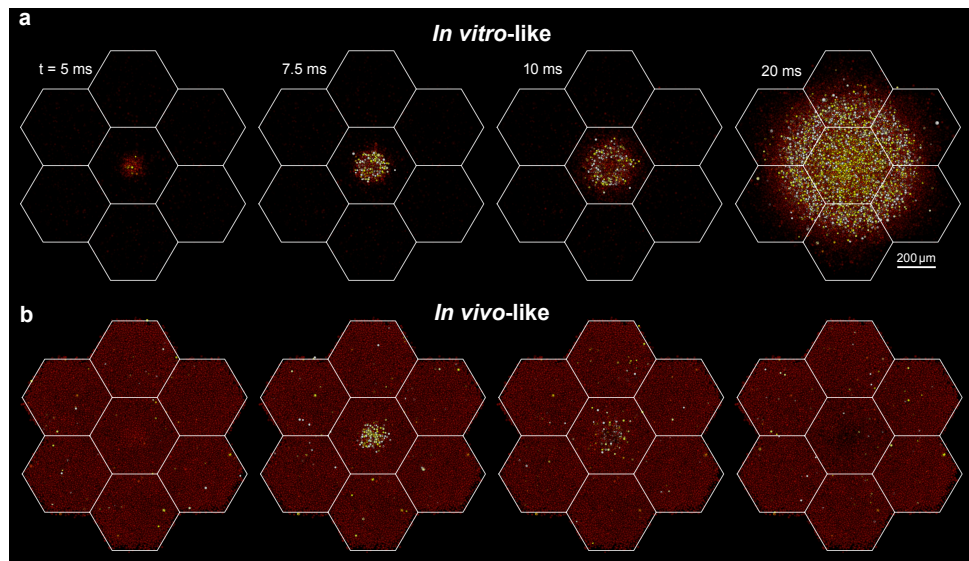


Figure C.22 – **Predicting network requirements for functional maps.**

Network state dependent differences in lateral propagation of evoked responses revealed in microcircuit mosaics. (a) A seven microcircuit mosaic under in vivo-like conditions stimulated with single synchronous spikes to each of 16 TC fibers at the center of the central microcircuit, depicted from above (above) and from the side for a central  $200 \mu\text{m}$  thick cutaway, just before ( $t=0\text{ms}$ ) and  $10\text{ms}$ ,  $20\text{ms}$  and  $40\text{ms}$  after time of stimulation. Neuron cell bodies only are rendered with a heat color map indicating level of depolarization. (b) Same as in a, but under in vitro-like conditions. The depolarization color map has been displaced by  $\sim 15\text{mV}$  to account for increased baseline depolarization in the in vivo-like state.

## A Supplementary Figures

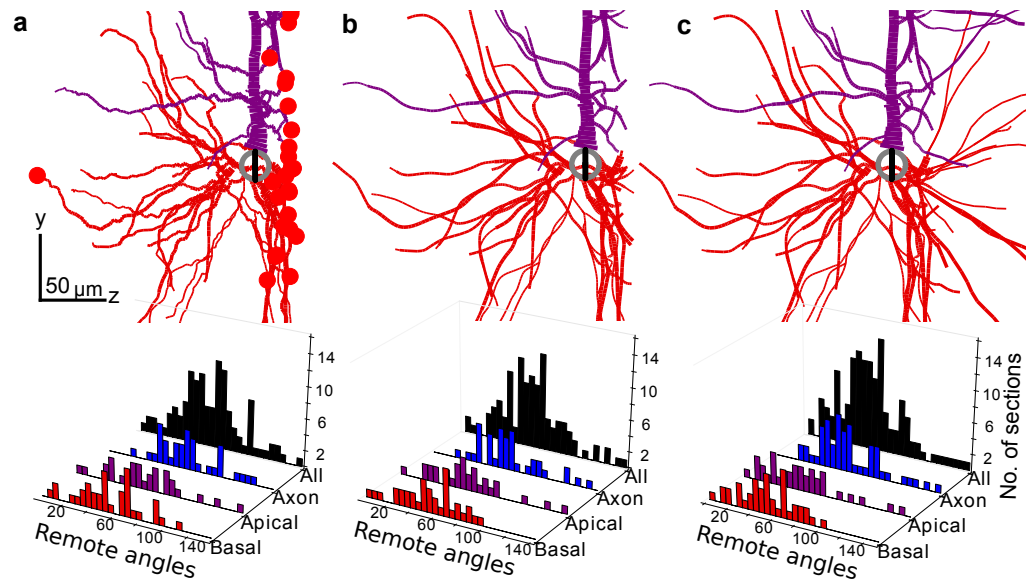


Figure S1 – **Reconstructing morphologies: Repairing.**

(a) Top: reconstructed neuron from a brain slice showing the cut branches. Red dots indicate cut ends where detected. Bottom: Bar plot of branching frequencies and angles. (b) Same for morphologies where tortuosity caused by shrinkage was corrected (unravalled). (c) Same for repaired morphologies.

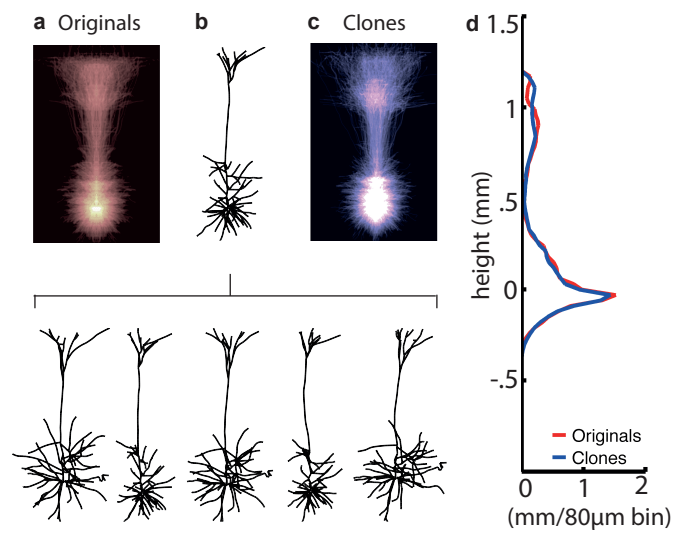


Figure S2 – **Reconstructing morphologies: Cloning.**

(a) Fibre density image of all repaired and unravelled reconstructions L5\_TTPCs overlaid at the soma. (b) The upper reconstructed neuron was cloned by introducing variability in branch lengths and angles; 5 sample clones are shown below. (c) As in (a) for 200 randomly selected clones. (d) Fiber density plot comparing the mean fibre length of original versus cloned L5\_TTPCs in 80µm bins along the y-axis.

## Appendix C. Reconstruction of the Neocortical Microcircuit

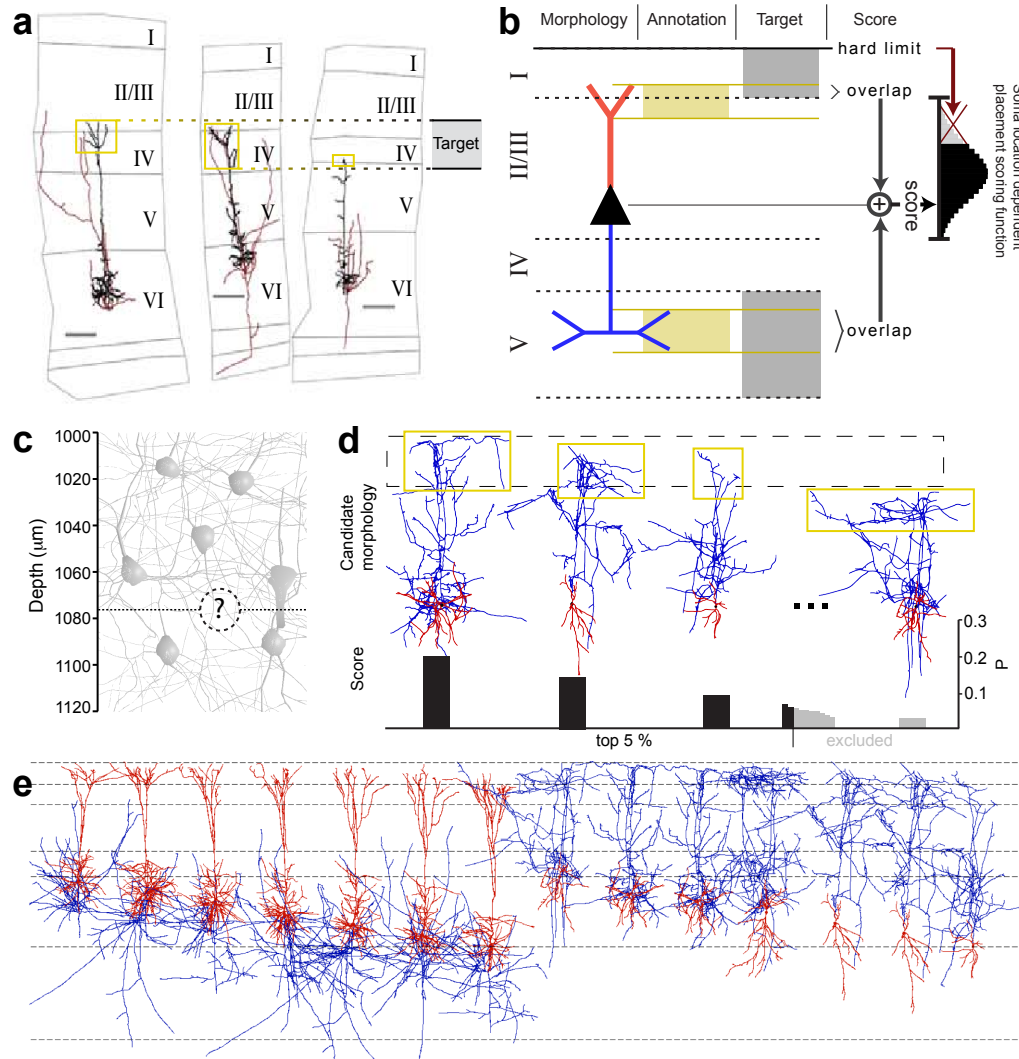


Figure S3 – Reconstructing inter-laminar architecture.

To assign morphologies to soma positions, the most appropriate reconstruction for a predefined position was selected. (a) Annotating morphologies. Constraining rules for placing morphologies of each m-type were derived from experimentally observed dendritic and axonal targeting within and across layers. Arbour regions (e.g. tufts), were manually annotated and their preferred laminar location determined from experimental observations. Arbour region annotation (yellow boxes) and laminar location (dashed lines) are shown for three representative L6 pyramidal cells. Analogous annotation was performed for m-types with observed laminar preferences. (b) The following workflow describes the morphology-placement scoring algorithm: Morphology - placement of L23 PCs. Annotation - annotation of the extent of axonal and dendritic clusters. Target - determination of absolute target depth intervals. Score - calculation of the overlap between annotated and target areas for a given soma position. Violating hard constraints, e.g. when dendrites extending above the pia, results in a zero score. (c) Determination of soma and m-type positions. (d) Selection of morphology. Scores are calculated for all morphologies for all m-type positions. For each position, the top 5% of candidates are selected with a probability proportional to the score. Morphologies (L5\_MC) are depicted according to

descending scores from left to right for a given position. (e) A collage of L5\_TTPC1 (left) and L5\_MC (right) morphologies giving an overview of the resulting placement relative to layer boundaries. Note that the longer the arbour, the deeper the cell is placed, ensuring the arbour terminates in L1.

## Appendix C. Reconstruction of the Neocortical Microcircuit

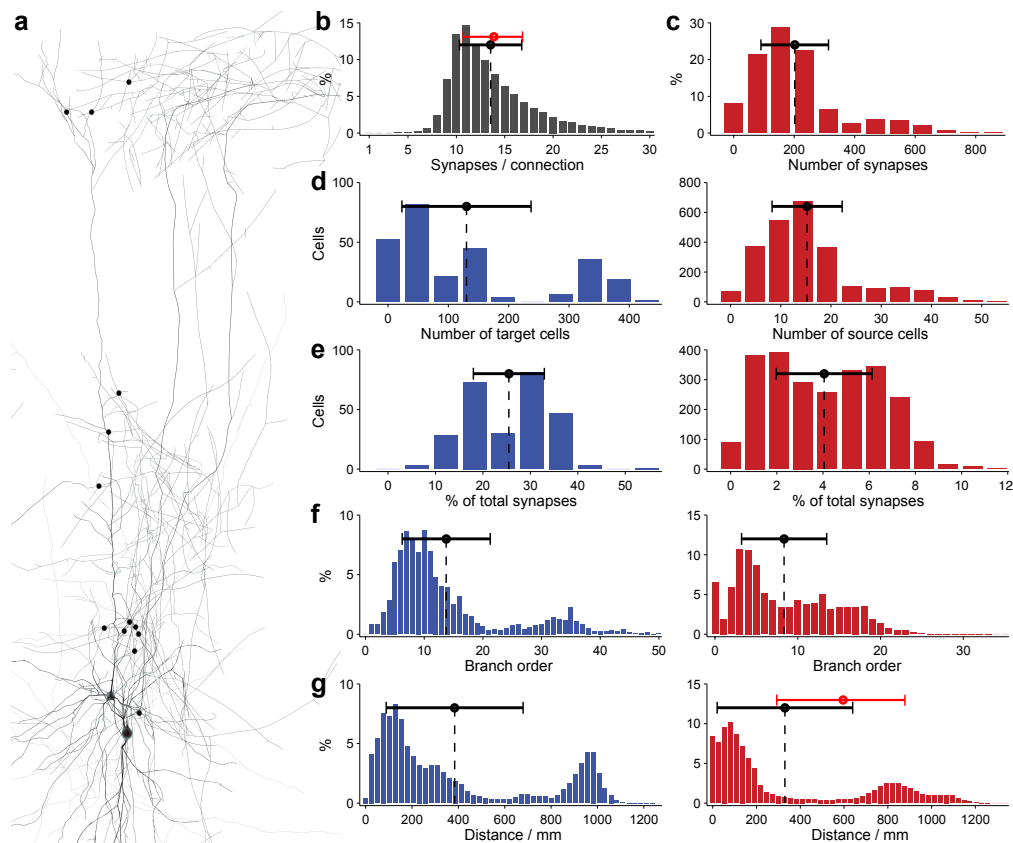


Figure S4 – **Predicting anatomical properties of a synaptic pathway.**

Predicted properties of the L5\_MC to L5\_TTPC2 pathway: a) In silico L5\_MC-L5\_TTPC synaptic connection. Synaptic contacts are shown as black circles (black dashed line, predicted mean; black bar, predicted SD; red bar, experimental data). (b) Number of synapses per connection for this particular pathway. (c) Distribution of the total number of synapses from all L5\_MCs presynaptic to L5\_TTPCs. (d, left) Neuronal divergence; number of L5\_TTPC2 neurons targeted by single L5\_MCs. (d, right) Right: Neuronal convergence, number L5\_MCs targeting single L5\_TTPC2 neurons. (e, left) Synaptic divergence; fraction of all synapses formed by L5\_MCs that target L5\_TTPC2. (e, right). Synaptic convergence; fraction of all synapses formed onto L5\_TTPC2 that originate from L5\_MCs. (f) Axonal (left) and dendritic (right) innervation patterns in terms of branch order of synaptic contacts. (g) Same as f, in terms of geometrical distance of synaptic contacts.

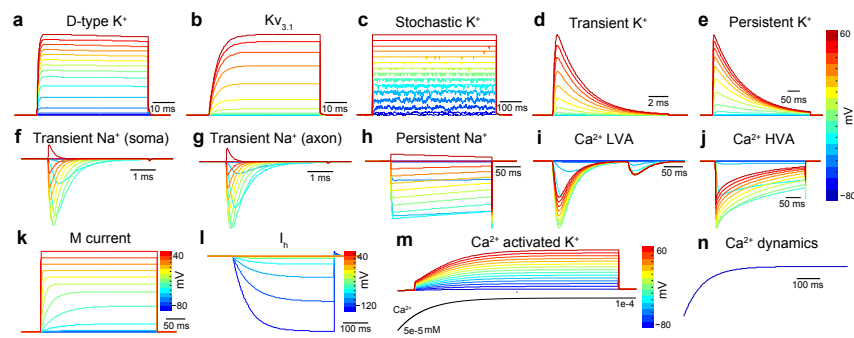


Figure S5 – Modelling ionic mechanisms.

(a to n) Currents generated by voltage step protocols used to test HH model parameters for 13 ion channel classes and one intracellular  $Ca^{2+}$  dynamics model.



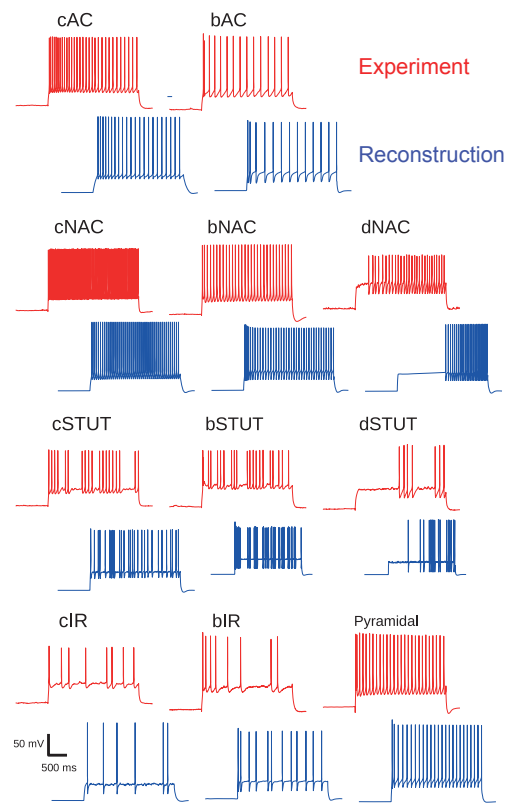


Figure S6 – **Reconstructed e-types.**

The output of the workflow reproduces the full experimental diversity of e-types represented in any m-type. The reconstruction yields conductance-based models (blue) that faithfully reproduce the repertoire of biologically observed e-types in m-types (red).

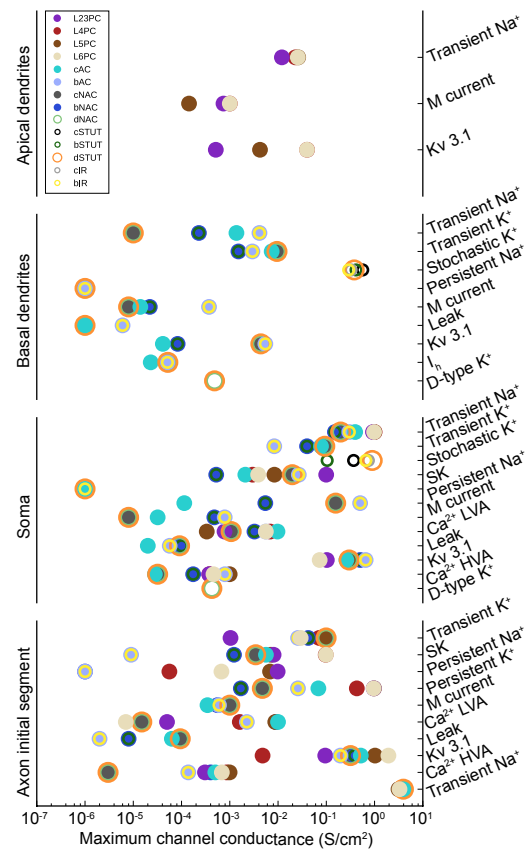


Figure S7 – Ion channel densities reproducing e-types.

The output of the workflow yields a prediction of ion channel densities (x-axis) in all possible locations (y-axis) on neurons belonging to different e-types (shown in different colours).

## Appendix C. Reconstruction of the Neocortical Microcircuit

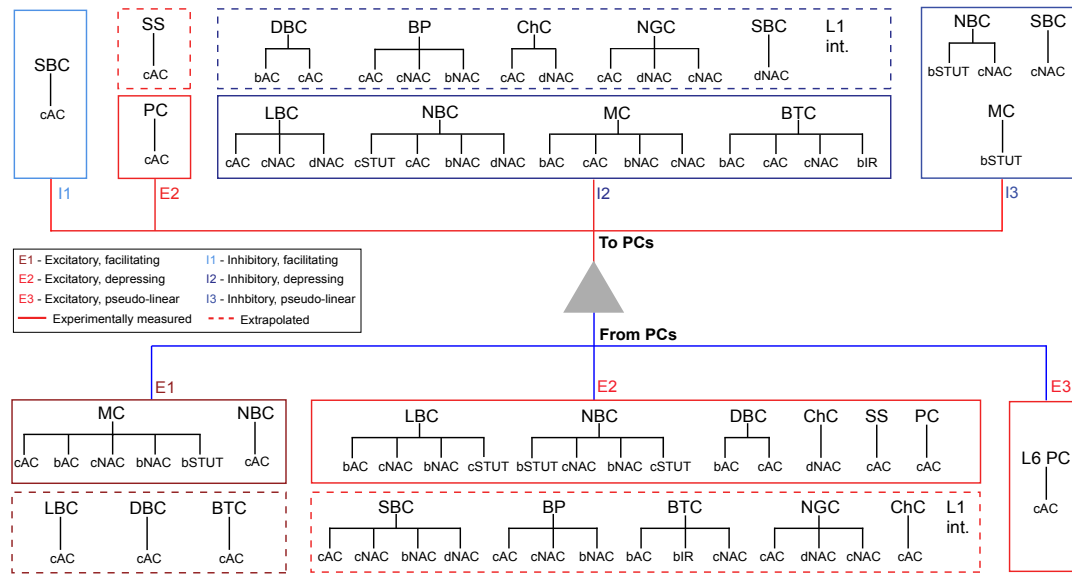
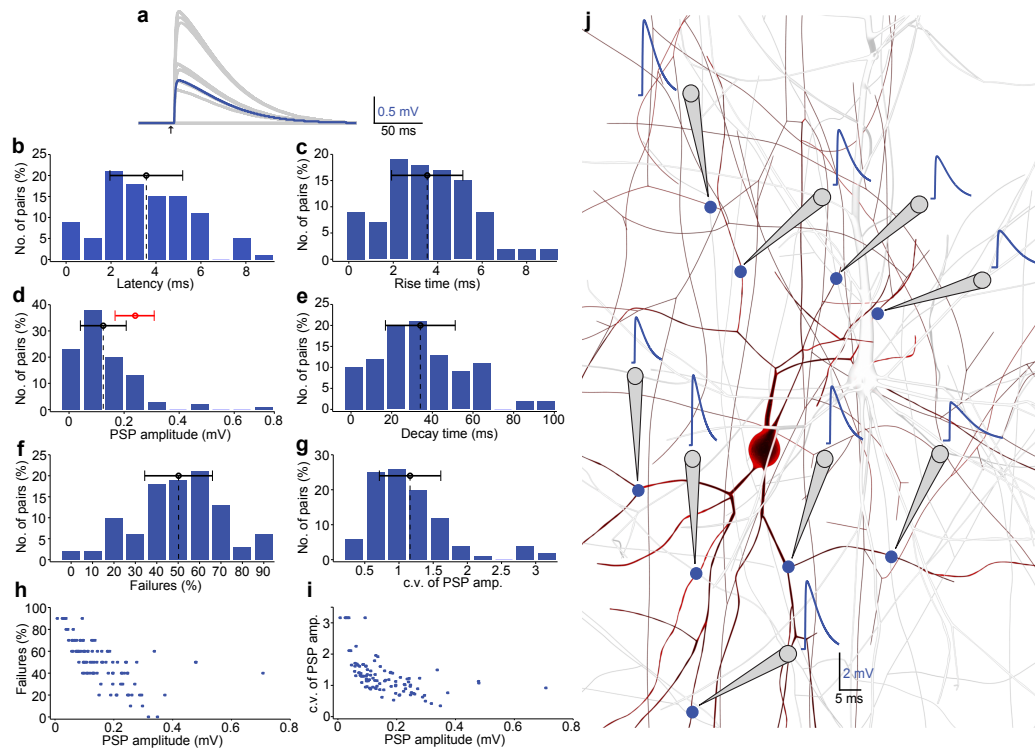


Figure S8 – Reconstructing dynamic synaptic properties for all connections.

Mapping rules for the types of dynamic synapse (s-types) mediating the connection between specific pre and postsynaptic me-types were extracted from the literature. The rules were extrapolated to pre-post me-type combinations that have not yet been studied experimentally. Solid boxes indicate me-type combinations that biological observations have shown to be associated with; dotted boxes indicate mappings based on extrapolated rules. Above, s-types to PCs; below, s-types from PCs.



**Figure S9 – Predicting physiological properties of the L5\_TTPC to L5\_MC synaptic pathway.**

(a) Average time course and amplitude of unitary EPSPs: Unitary presynaptic APs evoked in silico in the presynaptic L5\_TTPC resulted in postsynaptic responses measured in a L5\_MC. The arrow in black indicates the onset of the presynaptic AP. Postsynaptic traces in grey indicate individual responses; the blue trace shows the average response measured in 30 trials. (b) Prediction of synaptic physiology: Histogram of the predicted EPSP onset latency for the L5\_TTPC to L5\_MC pathway ( $n = 100$  pairs, sampled at intersomatic distances  $\leq 100\mu m$ ). The dashed line in black indicates the mean of the distribution; the error bar shows the SD. (c) Histogram of 20-80% EPSP rise time. (d) Histogram of EPSP amplitudes. The red bar shows the mean of the experimental data (e) Histogram of the EPSP decay time constant. (f) Histogram of transmission failures. (g) Histogram of the coefficient of variation (c.v.) or EPSP amplitudes (c.v. is defined as SD/mean of EPSP amplitude). (h) Predicted inverse relationship between the rate of transmission failures and EPSP amplitude. The model predicted a decrease in failure rates with increasing EPSP amplitudes, consistent with a binomial model of release. (i) Same as in (h), but for c.v. of EPSP amplitudes. (j) The model enables direct in silico dendritic patch recordings of single synaptic contacts. The presynaptic L5\_TTPC is shown in light grey and the postsynaptic L5\_MC is shown in red. The connection was mediated by nine synaptic contacts (blue dots). The recording "pipette" at the dendritic site of the synaptic contact is shown in dark grey; corresponding EPSPs are shown in blue.

Appendix C. Reconstruction of the Neocortical Microcircuit

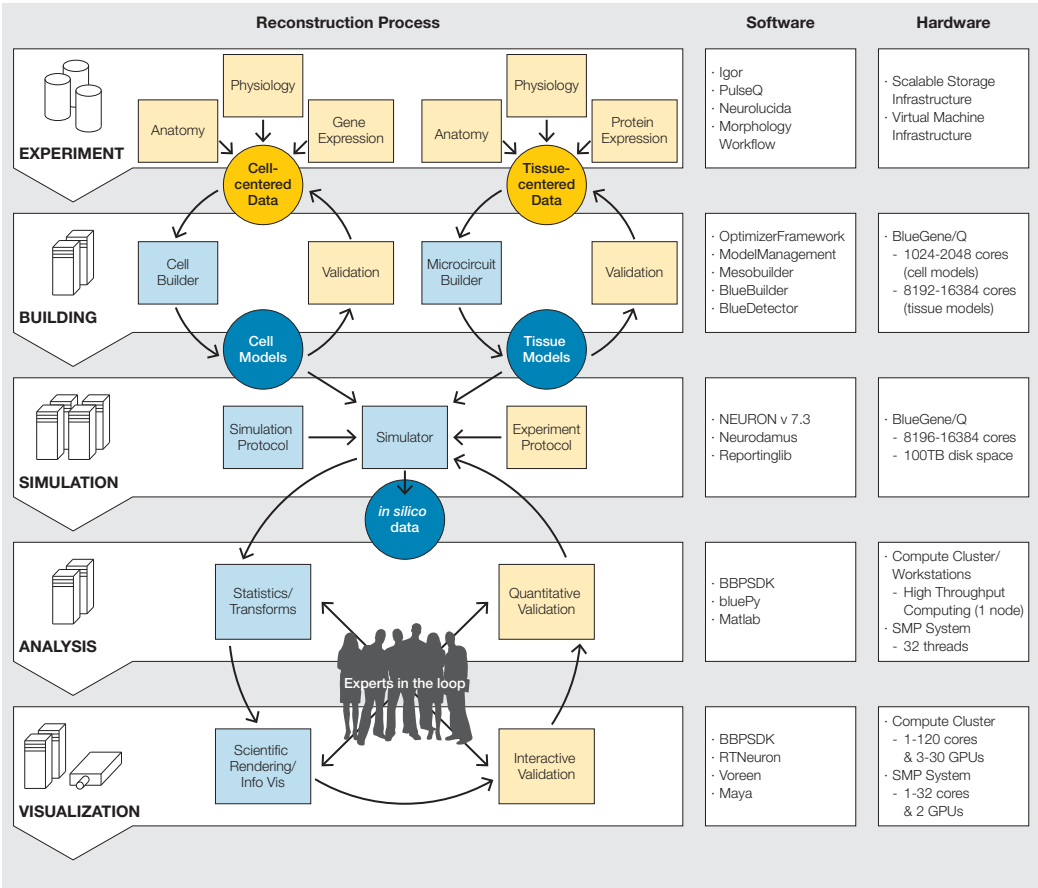


Figure S10 – Infrastructural and computing requirements.

An overview of the infrastructural and computing requirements for a data-driven reconstruction of the neocortical microcircuit.

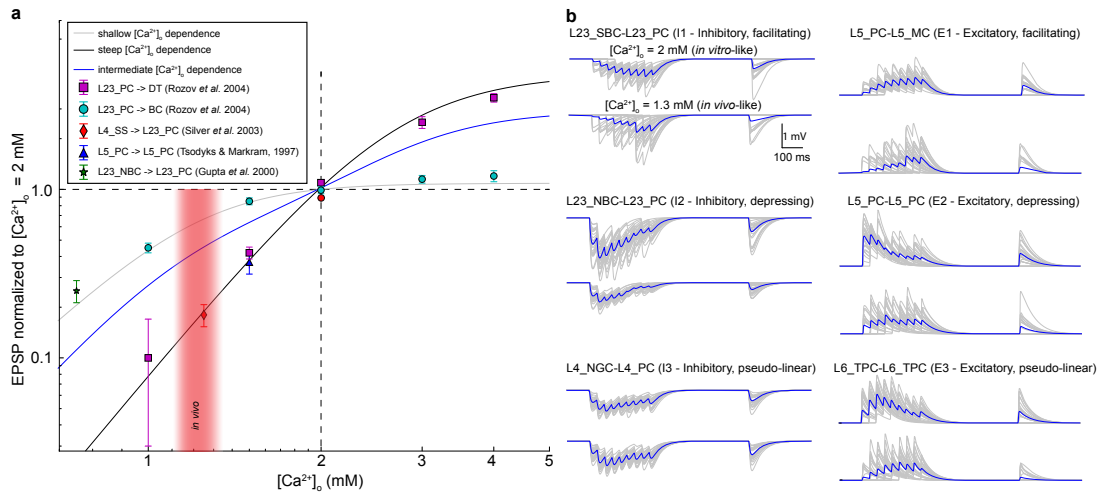


Figure S11 –  $Ca^{2+}$ -sensitivity of synaptic dynamics.

(a) Experimental data on the dependence between EPSP amplitudes and  $[Ca^{2+}]_o$  are consistent with either a steep (black line) or shallow (grey line) dependence (Hill isotherms;  $K_{1/2} = 2.79$  for steep,  $K_{1/2} = 1.09$  for shallow). Based on these sparse data we assumed steep  $Ca^{2+}$  dependency for PC-PC and PC-dendritic targeting type cells and the reverse (DBC, BTC, MC, BP) and a shallow dependency for PC-Soma-Axon targeting and the reverse (LBCs, NBCs, SBCs, ChC). Pathways that had not been studied experimentally were assumed to have an intermediate level of dependency (blue line; average of both). In vivo calcium levels in the range 1.1-1.3 mM are depicted in red (Borst, 2010). (b) Synaptic responses in the presence of an extracellular  $Ca^{2+}$  concentration of 2.0 mM (in vitro-like; upper traces) and 1.3 mM (in vivo-like; lower traces) for synaptic connections with steep (left traces) and shallow (right traces) dependencies.

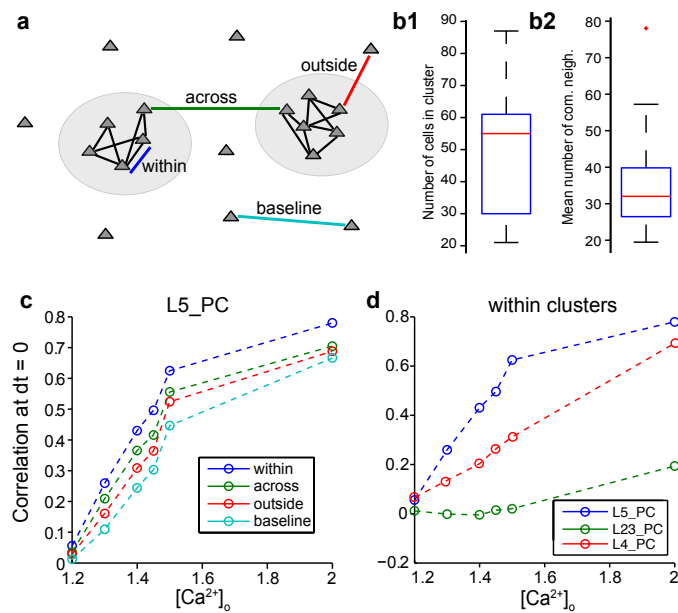


Figure S12 – **Synchrony of synaptically clustered assemblies of neurons.**

(a) We extracted several clusters from a population of excitatory cells, based on the mean number of common neighbours between neurons. We calculated mean spike time correlation (synchrony) of cell pairs at  $dt = 0$  (1) within the same cluster (within), (2) across clusters (across), (3) with and without connectivity to clusters (outside), (4) without connectivity to clusters (baseline). (b) Distribution of the number of neurons in a cluster (b1) and the mean number of common neighbours of cell pairs belonging to the same cluster (b2). Globally, the mean number of common neighbours for pairs of neurons in populations of excitatory cells was  $8 \pm 6$ . (c) Correlation of L5\_PC clusters at  $dt = 0$  for different  $Ca^{2+}$  concentrations (see Fig. 18, Blue: within, green: across, red: outside, teal: baseline). (d) Correlation within clusters of different pyramidal cell types at different  $Ca^{2+}$  concentrations. (Blue: L5\_PC, green: L23\_PC, red: L4\_PC).

# Bibliography

- M. Abeles and M. Goldstein. Multispikes train analysis. *Proc. IEEE*, 65, 1977.
- P. Achermann and A.A. Borbely. Low-frequency ( $< 1$  Hz) oscillations in the human sleep electroencephalogram. *Neuroscience*, 81:213–222, 1997.
- P. R. Adams, D. A. Brown, and A. Constanti. M-currents and other potassium currents in bullfrog sympathetic neurones. *The Journal of Physiology*, 330:537–572, 1982.
- Edgar Douglas Adrian. The basis of sensation. 1928.
- A. M. H. J. Aertsen, G. L. Gerstein, M. K. Habib, and G. Palm. Dynamics of neuronal firing correlation: Modulation of “Effective connectivity”. *J Neurophysiol*, 61(5):900–917, 1989.
- David Amaral. The functional organization of perception and movement. In *Principles of Neural Science*, pages 356–369. McGraw-Hill, New York, NY, USA, 5th edition, 2013. ISBN 9870071390118.
- C. A. Anastassiou, S. M. Montgomery, M. Barahona, G. Buzsáki, and C. Koch. The effect of spatially inhomogeneous extracellular electric fields on neurons. *J. Neurosci.*, 30:1925–1936, 2010.
- C. A. Anastassiou, R. Perin, H. Markram, and C. Koch. Ephaptic coupling of cortical neurons. *Nat Neurosci*, 14(2):217–223, 2011.
- C. A. Anastassiou, R. Perin, G. Buzsáki, H. Markram, and C. Koch. in preparation.
- Costas A Anastassiou, Gyorgy Buzsaki, and Christof Koch. Biophysics of extracellular spikes. *Principles of Neural Coding*, page 15, 2013.
- John C Anderson, Tom Binzegger, Rodney J Douglas, and Kevan A C Martin. Chance or design? some specific considerations concerning synaptic boutons in cat visual cortex. *Journal of neurocytology*, 31(3-5):211–229, June 2002. ISSN 0300-4864. PMID: 12815241.
- M. C. Angulo, J. Rossier, and E. Audinat. Postsynaptic glutamate receptors and integrative properties of fast-spiking interneurons in the rat neocortex. *J Neurophysiol*, page 1295–1302, 1999.
- Jon I. Arellano. Ultrastructure of dendritic spines: correlation between synaptic and spine morphologies. *Frontiers in Neuroscience*, 1(1):131–143, November 2007. ISSN 16624548. doi: 10.3389/neuro.01.1.1.010.2007.
- Michael Armstrong-James, Christopher A Callahan, and Michael A Friedman. Thalamo-cortical processing of vibrissa information in the rat. i. intracortical origins of surround but not centre-receptive fields of layer IV neurones in the rat S1 barrel field cortex. *Journal of comparative neurology*, 303(2): 193–210, 1991.



## Bibliography

---

- Giorgio A Ascoli, Lidia Alonso-Nanclares, Stewart A Anderson, German Barrionuevo, Ruth Benavides-Piccione, Andreas Burkhalter, György Buzsáki, Bruno Cauli, Javier DeFelipe, Alfonso Fairén, et al. Petilla terminology: nomenclature of features of GABAergic interneurons of the cerebral cortex. *Nature Reviews Neuroscience*, 9(7):557–568, 2008.
- R. B. Avery and D. Johnston. Multiple channel types contribute to the low-voltage-activated calcium current in hippocampal CA3 pyramidal neurons. *J Neurosci*, 16:5567–5582, 1996.
- D. S. Bassett and E. Bullmore. Small-world brain networks. *The Neuroscientist*, 12(6):512–523, December 2006. ISSN 1073-8584. doi: 10.1177/1073858406293182. URL <http://nro.sagepub.com/cgi/doi/10.1177/1073858406293182>.
- C Beaulieu, Z Kisvarday, P Somogyi, M Cynader, and A Cowey. Quantitative distribution of GABA-immunopositive and-immunonegative neurons and synapses in the monkey striate cortex (area 17). *Cerebral Cortex*, 2(4):295–309, 1992.
- Clermont Beaulieu and Marc Colonnier. The number of neurons in the different laminae of the binocular and monocular regions of area 17 in the cat. *Journal of Comparative Neurology*, 217(3):337–344, 1983.
- Michael Beierlein and Barry W Connors. Short-term dynamics of thalamocortical and intracortical synapses onto layer 6 neurons in neocortex. *Journal of neurophysiology*, 88(4):1924–1932, October 2002. ISSN 0022-3077. PMID: 12364518.
- M. A. Belluscio, K. Mizuseki, R. Schmidt, R. Kempter, and G. Buzsáki. Cross-frequency phase- phase coupling between theta and gamma oscillations in the hippocampus. *J Neurosci*, 32(423–435), 2012.
- H Berger. Über das elektroenkephalogramm des menschen. *Archiv für Psychiatrie und Nervenkrankheiten*, 87:452–469, 1933.
- E L Bienenstock, L N Cooper, and P W Munro. Theory for the development of neuron selectivity: orientation specificity and binocular interaction in visual cortex. *The Journal of neuroscience: the official journal of the Society for Neuroscience*, 2(1):32–48, January 1982. ISSN 0270-6474. PMID: 7054394.
- Tom Binzegger, Rodney J Douglas, and Kevan AC Martin. A quantitative map of the circuit of cat primary visual cortex. *The Journal of Neuroscience*, 24(39):8441–8453, 2004.
- J. Bock, M. Gruss, S. Becker, and K. Braun. Experience-induced changes of dendritic spine densities in the prefrontal and sensory cortex: Correlation with developmental time windows. *Cerebral Cortex*, 15(6):802–808, September 2004. ISSN 1047-3211, 1460-2199. doi: 10.1093/cercor/bhh181. URL <http://www.cercor.oxfordjournals.org/cgi/doi/10.1093/cercor/bhh181>.
- Barry W Boehm. A spiral model of software development and enhancement. *Computer*, 21(5):61–72, 1988.
- Valentino Braitenberg and A. Schüz. *Cortex: Statistics and geometry of neuronal connectivity*. Springer Verlag, Berlin and New York, 2nd thoroughly rev. edition edition, 1998. ISBN 3540638164.
- C. Brody. Correlations without synchrony. *Neural Computation*, 11(7):1537–1551, 1999.

- Solange P. Brown and Shaul Hestrin. Intracortical circuits of pyramidal neurons reflect their long-range axonal targets. *Nature*, 457(7233):1133–1136, January 2009. ISSN 0028-0836, 1476-4687. doi: 10.1038/nature07658. URL <http://www.nature.com/doifinder/10.1038/nature07658>.
- Daniel P Buxhoeveden, Andrew E Switala, Emil Roy, and Manuel F Casanova. Quantitative analysis of cell columns in the cerebral cortex. *Journal of neuroscience methods*, 97(1):7–17, 2000.
- G. Buzsaki. Theta oscillations in the hippocampus. *Neuron*, 33:325–340, 2002.
- G. Buzsaki. Large-scale recording of neuronal ensembles. *Nature Neurosci.*, 7:446–451, 2004.
- G. Buzsáki, C. A. Anastassiou, and C. Koch. Origin of extracellular fields and currents – EEG, ECoG, LFP and spikes. *Nature Reviews Neuroscience*, 13:407–420, 2012.
- C. Bédard and A. Destexhe. Macroscopic models of local field potentials and the apparent 1/f noise in brain activity. *Biophys J*, 96:2589–2603, 2009.
- C. Bédard, H. Kroger, and A. Destexhe. Modeling extracellular field potentials and the frequency-filtering properties of extracellular space. *Biophys J*, 86:1829–1842, 2004.
- C. Bédard, H. Kröger, and A. Destexhe. Does the 1/f frequency scaling of brain signals reflect self-organized critical states? *Phys Rev Lett*, 97:118102, 2006.
- C. Bédard, S. Rodrigues, N. Roy, D. Contreras, and A. Destexhe. Evidence for frequency-dependent extracellular impedance from the transfer function between extracellular and intracellular potentials: intracellular-LFP transfer function. *J Computat Neurosci*, 29:389–403, 2010.
- J. A. Cardin, E. M. Carlén, K. Meletis, U. Knoblich, F. Zhang, K. Deisseroth, L. H. Tsai, and C. I. Moore. Activation of fast-spiking interneurons induces gamma oscillations and shapes sensory transmission. *Nature*, 459:663–667, 2009.
- Richard Caton. Electrical currents of the brain. *The Journal of Nervous and Mental Disease*, 2(4):610, 1875.
- Bruno Cauli, James T Porter, Keisuke Tsuzuki, Bertrand Lambolez, Jean Rossier, Brigitte Quenet, and Etienne Audinat. Classification of fusiform neocortical interneurons based on unsupervised clustering. *Proceedings of the National Academy of Sciences*, 97(11):6144–6149, 2000.
- Nicolas L Chiaia, Robert W Rhoades, Carol A Bennett-Clarke, Stephen E Fish, and Herbert P Killackey. Thalamic processing of vibrissal information in the rat. i. afferent input to the medial ventral posterior and posterior nuclei. *Journal of Comparative Neurology*, 314(2):201–216, 1991a.
- Nicolas L Chiaia, Robert W Rhoades, Stephen E Fish, and Herbert P Killackey. Thalamic processing of vibrissal information in the rat: II. morphological and functional properties of medial ventral posterior nucleus and posterior nucleus neurons. *Journal of Comparative Neurology*, 314(2):217–236, 1991b.
- D B Chklovskii, B W Mel, and K Svoboda. Cortical rewiring and information storage. *Nature*, 431(7010):782–788, October 2004. ISSN 1476-4687. doi: 10.1038/nature03012. PMID: 15483599.
- J.J. Chrobak, A. Lorincz, and G. Buzsaki. Physiological patterns in the hippocampus-entorhinal cortex system. *Hippocampus*, 10:457–465, 2000.

## Bibliography

---

- L. B. Cohen, B. M. Salzberg, H. V. Davila, W. N. Ross, D. Landowne, A. S. Waggoner, and C. H. Wang. Changes in axon fluorescence during activity: Molecular probes of membrane potential. *The Journal of Membrane Biology*, 19(1):1–36, December 1974. ISSN 0022-2631, 1432-1424. doi: 10.1007/BF01869968. URL <http://link.springer.com/10.1007/BF01869968>.
- C. M. Colbert and E. Pan. Ion channel properties underlying axonal action potential initiation in pyramidal neurons. *Nature Neurosci.*, 5:533–538, 2002.
- Barry W Connors and Michael J Gutnick. Intrinsic firing patterns of diverse neocortical neurons. *Trends in neurosciences*, 13(3):99–104, 1990.
- D. Contreras, I. Timofeev, and M. Steriade. Mechanisms of ion lasting hyperpolarizations underlying slow sleep oscillations in cat corticothalamic networks. *J. Physiol.*, 494:251–264, 1996.
- Eric Courchesne and Karen Pierce. Why the frontal cortex in autism might be talking only to itself: local over-connectivity but long-distance disconnection. *Current Opinion in Neurobiology*, 15(2):225–230, April 2005. ISSN 09594388. doi: 10.1016/j.conb.2005.03.001. URL <http://linkinghub.elsevier.com/retrieve/pii/S0959438805000334>.
- BG Cragg. The density of synapses and neurones in the motor and visual areas of the cerebral cortex. *Journal of Anatomy*, 101(Pt 4):639, 1967.
- A Datwani. NMDA receptor-dependent pattern transfer from afferents to postsynaptic cells and dendritic differentiation in the barrel cortex. *Molecular and Cellular Neuroscience*, 21(3):477–492, November 2002. ISSN 10447431. doi: 10.1006/mcne.2002.1195. URL <http://linkinghub.elsevier.com/retrieve/pii/S1044743102911954>.
- J DeFelipe. Reflections on the structure of the cortical minicolumn. *Neocortical modularity and the cell minicolumn*, page 57–92, 2005.
- Javier DeFelipe. Neocortical neuronal diversity: chemical heterogeneity revealed by colocalization studies of classic neurotransmitters, neuropeptides, calcium-binding proteins, and cell surface molecules. *Cerebral Cortex*, 3(4):273–289, 1993.
- Javier DeFelipe, Lidia Alonso-Nanclares, and Jon I Arellano. Microstructure of the neocortex: comparative aspects. *Journal of neurocytology*, 31(3-5):299–316, June 2002. ISSN 0300-4864. PMID: 12815249.
- Javier DeFelipe, Pedro L. López-Cruz, Ruth Benavides-Piccione, Concha Bielza, Pedro Larrañaga, Stewart Anderson, Andreas Burkhalter, Bruno Cauli, Alfonso Fairén, Dirk Feldmeyer, Gord Fishell, David Fitzpatrick, Tamás F Freund, Guillermo González-Burgos, Shaul Hestrin, Sean Hill, Patrick R. Hof, Josh Huang, Edward G. Jones, Yasuo Kawaguchi, Zoltán Kisvárdy, Yoshiyuki Kubota, David A. Lewis, Oscar Marín, Henry Markram, Chris J. McBain, Hanno S. Meyer, Hannah Monyer, Sacha B. Nelson, Kathleen Rockland, Jean Rossier, John L. R. Rubenstein, Bernardo Rudy, Massimo Scanziani, Gordon M. Shepherd, Chet C. Sherwood, Jochen F. Staiger, Gábor Tamás, Alex Thomson, Yun Wang, Rafael Yuste, and Giorgio A. Ascoli. New insights into the classification and nomenclature of cortical GABAergic interneurons. *Nature Reviews Neuroscience*, 14(3):202–216, February 2013. ISSN 1471-003X, 1471-0048. doi: 10.1038/nrn3444. URL <http://www.nature.com/doifinder/10.1038/nrn3444>.
- A. Destexhe, D. Contreras, and M. Steriade. Spatiotemporal analysis of local field potentials and unit discharges in cat cerebral cortex during natural wake and sleep states. *J Neurosci*, 19:4595–4608, 1997.

- A. Destexhe, M. Rudolph, and D. Paré. The high-conductance state of neocortical neurons *Nat. Rev. Neurosci.*, 4:739–751, 2003.
- K. Diba, C. Koch, and I. Segev. Spike propagation in dendrites with stochastic ion channels. *J Computat Neurosci*, 20:77–84, 2006.
- C. T. Dickson, G. Biella, and M. de Curtis. Slow periodic events and their transition to gamma oscillations in the entorhinal cortex of the isolated guinea pig brain. *J. Neurophysiol.*, 90:39–46, 2003.
- Rodney J Douglas and Kevan AC Martin. Mapping the matrix: the ways of neocortex. *Neuron*, 56(2): 226–238, 2007.
- Shaul Druckmann, Yoav Banitt, Albert A Gidon, Felix Schürmann, Henry Markram, and Idan Segev. A novel multiple objective optimization framework for constraining conductance-based neuron models by experimental data. *Frontiers in neuroscience*, 1:1, 2007.
- Shaul Druckmann, Sean Hill, Felix Schürmann, Henry Markram, and Idan Segev. A hierarchical structure of cortical interneuron electrical diversity revealed by automated statistical analysis. *Cerebral Cortex*, 23(12):2994–3006, 2013.
- Daniella Dumitriu, Rosa Cossart, Josh Huang, and Rafael Yuste. Correlation between axonal morphologies and synaptic input kinetics of interneurons from mouse visual cortex. *Cerebral cortex*, 17(1): 81–91, 2007.
- T Euler. Dendritic processing. *Current Opinion in Neurobiology*, 11(4):415–422, August 2001. ISSN 09594388. doi: 10.1016/S0959-4388(00)00228-2. URL <http://linkinghub.elsevier.com/retrieve/pii/S0959438800002282>.
- Alfonso Fairen, Javier DeFelipe, and José Regidor. Nonpyramidal neurons: general account. *Cerebral cortex*, 1:201–253, 1984.
- E. E. Faselow and B. W. Connors. The roles of somatostatin-expressing (GIN) and fast-spiking inhibitory interneurons in UP-DOWN states of mouse neocortex. *J Neurophysiol*, 104:596–606, 2010.
- Tarec Fares and Armen Stepanyants. Cooperative synapse formation in the neocortex. *Proceedings of the National Academy of Sciences*, 106(38):16463–16468, September 2009. ISSN 0027-8424, 1091-6490. doi: 10.1073/pnas.0813265106. URL <http://www.pnas.org/content/106/38/16463>.
- D. Feldmeyer, J. Lübke, R A. Silver, and B. Sakmann. Synaptic connections between layer 4 spiny neurone- layer 2/3 pyramidal cell pairs in juvenile rat barrel cortex: physiology and anatomy of interlaminar signalling within a cortical column. *The Journal of Physiology*, 538(3):803–822, February 2002. ISSN 0022-3751. doi: 10.1113/jphysiol.2001.012959. URL <http://www.jphysiol.org/cgi/doi/10.1113/jphysiol.2001.012959>.
- D. Feldmeyer, J. Lübke, and B. Sakmann. Efficacy and connectivity of intracolumnar pairs of layer 2/3 pyramidal cells in the barrel cortex of juvenile rats. *The Journal of Physiology*, 575(2):583–602, September 2006a. ISSN 1469-7793. doi: 10.1113/jphysiol.2006.105106. URL <http://onlinelibrary.wiley.com/doi/10.1113/jphysiol.2006.105106/full>.
- Dirk Feldmeyer, Veronica Egger, Joachim Lübke, and Bert Sakmann. Reliable synaptic connections between pairs of excitatory layer 4 neurones within a single 'barrel' of developing rat somatosensory cortex. *The Journal of Physiology*, 521(1):169–190, November 1999. ISSN 0022-3751, 1469-7793. doi: 10.1111/j.1469-7793.1999.00169.x. URL <http://doi.wiley.com/10.1111/j.1469-7793.1999.00169.x>.

## Bibliography

---

- Dirk Feldmeyer, Joachim Lübke, and Bert Sakmann. Efficacy and connectivity of intracolumnar pairs of layer 2/3 pyramidal cells in the barrel cortex of juvenile rats. *The Journal of Physiology*, 575(2):583–602, September 2006b. ISSN 1469-7793. doi: 10.1113/jphysiol.2006.105106. URL <http://onlinelibrary.wiley.com/doi/10.1113/jphysiol.2006.105106/full>.
- Isabelle Ferezou, Florent Haiss, Luc J. Gentet, Rachel Aronoff, Bruno Weber, and Carl C.H. Petersen. Spatiotemporal dynamics of cortical sensorimotor integration in behaving mice. *Neuron*, 56(5):907–923, December 2007. ISSN 08966273. doi: 10.1016/j.neuron.2007.10.007. URL <http://linkinghub.elsevier.com/retrieve/pii/S0896627307007635>.
- Elodie Fino and Rafael Yuste. Dense inhibitory connectivity in neocortex. *Neuron*, 69(6):1188–1203, March 2011. ISSN 08966273. doi: 10.1016/j.neuron.2011.02.025. URL <http://linkinghub.elsevier.com/retrieve/pii/S0896627311001231>.
- Luc J Gentet, Michael Avermann, Ferenc Matyas, Jochen F Staiger, and Carl CH Petersen. Membrane potential dynamics of GABAergic neurons in the barrel cortex of behaving mice. *Neuron*, 65(3):422–435, 2010.
- Luc J Gentet, Yves Kremer, Hiroki Taniguchi, Z Josh Huang, Jochen F Staiger, and Carl CH Petersen. Unique functional properties of somatostatin-expressing GABAergic neurons in mouse barrel cortex. *Nature neuroscience*, 15(4):607–612, 2012.
- A. P. Georgopoulos, H. Merchant, T. Naselaris, and B. Amirikian. Mapping of the preferred direction in the motor cortex. *Proceedings of the National Academy of Sciences*, 104(26):11068–11072, June 2007. ISSN 0027-8424, 1091-6490. doi: 10.1073/pnas.0611597104. URL <http://www.pnas.org/cgi/doi/10.1073/pnas.0611597104>.
- Apostolos P Georgopoulos, John F Kalaska, Roberto Caminiti, and Joe T Massey. On the relations between the direction of two-dimensional arm movements and cell discharge in primate motor cortex. *The Journal of Neuroscience*, 2(11):1527–1537, 1982.
- Apostolos P Georgopoulos, Andrew B Schwartz, and Ronald E Kettner. Neuronal population coding of movement direction. *Science*, 233(4771):1416–1419, 1986.
- Albert Gidon and Idan Segev. Principles governing the operation of synaptic inhibition in dendrites. *Neuron*, 75(2):330–341, July 2012. ISSN 08966273. doi: 10.1016/j.neuron.2012.05.015. URL <http://linkinghub.elsevier.com/retrieve/pii/S0896627312004813>.
- Ziv Gil, Barry W. Connors, and Yael Amitai. Efficacy of thalamocortical and intracortical synaptic connections: Quanta, innervation, and reliability. *Neuron*, 23(2):385–397, June 1999. ISSN 0896-6273. doi: 10.1016/S0896-6273(00)80788-6. URL <http://www.sciencedirect.com/science/article/pii/S0896627300807886>.
- Gabrielle Girardeau, Karim Benchenane, Sidney I Wiener, György Buzsáki, and Michaël B Zugaro. Selective suppression of hippocampal ripples impairs spatial memory. *Nature neuroscience*, 12(10):1222–1223, 2009.
- C. Gold, D. Henze, C. Koch, and G. Buzsáki. On the origin of the extracellular action potential waveform: A modeling study. *J. Neurophysiol.*, 95:3113–3128, 2006.
- C. Gold, D. Henze, and C. Koch. Using extracellular action potential recordings to constrain compartmental models. *J. Comp. Neurosc.*, 23:39–58, 2007.

- T. Goto, R. Hatanaka, T. Ogawa, A. Sumiyoshi, J. Riera, and R. Kawashima. An evaluation of the conductivity profile in the somatosensory barrel cortex of wistar rats. *J Neurophysiol*, 104:3388–3412, 2010.
- Charles M. Gray, Pedro E. Maldonado, Mathew Wilson, and Bruce McNaughton. Tetrodes markedly improve the reliability and yield of multiple single-unit isolation from multi-unit recordings in cat striate cortex. *Journal of Neuroscience Methods*, 63(1-2):43–54, December 1995. ISSN 01650270. doi: 10.1016/0165-0270(95)00085-2. URL <http://linkinghub.elsevier.com/retrieve/pii/0165027095000852>.
- Michael SA Graziano, Charlotte SR Taylor, and Tirin Moore. Complex movements evoked by microstimulation of precentral cortex. *Neuron*, 34(5):841–851, 2002.
- Warren M Grill and Cameron C McIntyre. Extracellular excitation of central neurons: implications for the mechanisms of deep brain stimulation. *Thalamus & Related Systems*, 1(03):269–277, 2001.
- Amiram Grinvald and Rina Hildesheim. VSDI: a new era in functional imaging of cortical dynamics. *Nature Reviews Neuroscience*, 5(11):874–885, November 2004. ISSN 1471-003X, 1471-0048. doi: 10.1038/nrn1536. URL <http://www.nature.com/doi/10.1038/nrn1536>.
- A. Gupta, Y. Wang, and H. Markram. Organizing principles for a diversity of GABAergic interneurons and synapses in the neocortex. *Science*, 287:273–278, 2000.
- R. K. Gupta, B. M. Salzberg, A. Grinvald, L. B. Cohen, K. Kamino, S. Leshner, M. B. Boyle, A. S. Waggoner, and C. H. Wang. Improvements in optical methods for measuring rapid changes in membrane potential. *The Journal of Membrane Biology*, 58(2):123–137, June 1981. ISSN 0022-2631, 1432-1424. doi: 10.1007/BF01870975. URL <http://link.springer.com/10.1007/BF01870975>.
- B. Haider, A. Duque, A. R. Hasenstaub, and D. A. McCormick. Neocortical network activity in vivo is generated through a dynamic balance of excitation and inhibition. *J Neurosci*, 26(17):4535–4545, 2006.
- M. Hausser. Diversity and dynamics of dendritic signaling. *Science*, 290(5492):739–744, October 2000. ISSN 00368075, 10959203. doi: 10.1126/science.290.5492.739. URL <http://www.sciencemag.org/cgi/doi/10.1126/science.290.5492.739>.
- E. Hay, S. Hill, F. Schürmann, H. Markram, and I. Segev. Models of neocortical layer 5b pyramidal cells capturing a wide range of dendritic and perisomatic active properties. *PLoS Computat Biol*, 7:e1002107, 2011.
- Shaul Hestrin and William E Armstrong. Morphology and physiology of cortical neurons in layer i. *The Journal of neuroscience*, 16(17):5290–5300, 1996.
- S. L. Hill, Y. Wang, I. Riachi, F. Schurmann, and H. Markram. PNAS plus: Statistical connectivity provides a sufficient foundation for specific functional connectivity in neocortical neural microcircuits. *Proceedings of the National Academy of Sciences*, September 2012. ISSN 0027-8424, 1091-6490. doi: 10.1073/pnas.1202128109. URL <http://www.pnas.org/cgi/doi/10.1073/pnas.1202128109>.
- M. L. Hines and N. T. Carnevale. The NEURON simulation environment. *Neural Computation*, 9:1179–1209, 1997.
- M. L. Hines and N. T. Carnevale. Expanding NEURON’s repertoire of mechanisms with NMODL. *Neural Computation*, 12:995–1007, 2000.

## Bibliography

---

- M. L. Hines, H. Markram, and F. Schürmann. Fully implicit parallel simulation of single neurons. *J Comput Neurosci*, 25:439–448, 2008.
- A.L. Hodgkin and A.F. Huxley. A quantitative description of membrane current and its application to conduction and excitation in nerve. *J. Physiol.*, 117:500–544, 1952.
- AL Hodgkin and WAH Rushton. The electrical constants of a crustacean nerve fibre. *Proceedings of the Royal Society of London. Series B-Biological Sciences*, 133(873):444–479, 1946.
- Sonja B Hofer, Thomas D Mrsic-Flogel, Tobias Bonhoeffer, and Mark Hübener. Experience leaves a lasting structural trace in cortical circuits. *Nature*, 457(7227):313–317, January 2009. ISSN 1476-4687. doi: 10.1038/nature07487. PMID: 19005470.
- C. Holmgren, T. Harkany, B. Svennenfors, and Y. Zilberter. Pyramidal cell communication within local networks in layer 2/3 of rat neocortex. *The Journal of Physiology*, 551(1):139–153, August 2003. ISSN 0022-3751. doi: 10.1113/jphysiol.2003.044784. URL <http://www.jphysiol.org/cgi/doi/10.1113/jphysiol.2003.044784>.
- C. Holscher, R. Anwyl, and M.J. Rowan. Stimulation on the positive phase of hippocampal theta rhythm induces long-term potentiation that can be depotentiated by stimulation on the negative phase in area CA1 in vivo. *J. Neurosci.*, 17:6470–6477, 1997.
- G.R. Holt and C. Koch. Electrical interactions via the extracellular potential near cell bodies. *J. Comp. Neurosci.*, 6:169–184, 1999.
- Anthony Holtmaat and Karel Svoboda. Experience-dependent structural synaptic plasticity in the mammalian brain. *Nature Reviews Neuroscience*, 10(9):647–658, September 2009. ISSN 1471-003X, 1471-0048. doi: 10.1038/nrn2699. URL <http://www.nature.com/doi/10.1038/nrn2699>.
- S. Hong, S. Ratte, S. A. Prescott, and E. De Schutter. Single neuron firing properties impact correlation-based population coding. *Journal of Neuroscience*, 32(4):1413–1428, January 2012. ISSN 0270-6474, 1529-2401. doi: 10.1523/JNEUROSCI.3735-11.2012. URL <http://www.jneurosci.org/cgi/doi/10.1523/JNEUROSCI.3735-11.2012>.
- Allyson Howard, Gabor Tamas, and Ivan Soltesz. Lighting the chandelier: new vistas for axo-axonic cells. *Trends in Neurosciences*, 28(6):310–316, June 2005. ISSN 01662236. doi: 10.1016/j.tins.2005.04.004. URL <http://linkinghub.elsevier.com/retrieve/pii/S0166223605001049>.
- David H Hubel and Torsten N Wiesel. Ferrier lecture: Functional architecture of macaque monkey visual cortex. *Proceedings of the Royal Society of London. Series B, Biological Sciences*, page 1–59, 1977.
- J. M. Hyman, B. P. Wyble, V. Goyal, C. A. Rossi, and M. E. Hasselmo. Stimulation in hippocampal region CA1 in behaving rats yields long-term potentiation when delivered to the peak of theta and long-term depression when delivered to the trough. *J. Neurosci.*, 23:11725–11731, 2003.
- M. Häusser and A. Roth. Estimating the time course of the excitatory synaptic conductance in neocortical pyramidal cells using a novel voltage jump method. *J Neurosci*, 17:7606–7625, 1997.
- J.G.R. Jefferys. Nonsynaptic modulation of neuronal activity in the brain: Electric currents and extracellular ions. *Physiol. Rev.*, 75:689–723, 1995.

- J.G.R. Jefferys and H.L. Haas. Synchronised bursting of ca1 pyramidal cells in the absence of synaptic transmission. *Nature*, 300:448–450, 1982.
- Allan R. Jones, Caroline C. Overly, and Susan M. Sunkin. The allen brain atlas: 5 years and beyond. *Nature Reviews Neuroscience*, 10(11):821–828, October 2009. ISSN 1471-003X, 1471-0048. doi: 10.1038/nrn2722. URL <http://www.nature.com/doifinder/10.1038/nrn2722>.
- EG Jones, DP Friedman, and SH Hendry. Thalamic basis of place-and modality-specific columns in monkey somatosensory cortex: a correlative anatomical and physiological study. *Journal of neurophysiology*, 48(2):545–568, 1982.
- N. Kalisman. The neocortical microcircuit as a tabula rasa. *Proceedings of the National Academy of Sciences*, 102(3):880–885, January 2005. ISSN 0027-8424, 1091-6490. doi: 10.1073/pnas.0407088102. URL <http://www.pnas.org/cgi/doi/10.1073/pnas.0407088102>.
- E. R. Kandel, J. H. Schwartz, and T. M. Jessel. *Principles of Neural Science*. McGraw-Hill, New York, NY, USA, 5th edition, 2005.
- Eric R. Kandel, Henry Markram, Paul M. Matthews, Rafael Yuste, and Christof Koch. Neuroscience thinks big (and collaboratively). *Nature Reviews Neuroscience*, 14(9):659–664, August 2013. ISSN 1471-003X, 1471-0048. doi: 10.1038/nrn3578. URL <http://www.nature.com/doifinder/10.1038/nrn3578>.
- Fuyuki Karube, Yoshiyuki Kubota, and Yasuo Kawaguchi. Axon branching and synaptic bouton phenotypes in GABAergic nonpyramidal cell subtypes. *The Journal of Neuroscience*, 24(12):2853–2865, March 2004. ISSN 0270-6474, 1529-2401. doi: 10.1523/JNEUROSCI.4814-03.2004. URL <http://www.jneurosci.org/content/24/12/2853>.
- Y. Kawaguchi. Dendritic branch typing and spine expression patterns in cortical nonpyramidal cells. *Cerebral Cortex*, 16(5):696–711, August 2005. ISSN 1047-3211, 1460-2199. doi: 10.1093/cercor/bhj015. URL <http://www.cercor.oxfordjournals.org/cgi/doi/10.1093/cercor/bhj015>.
- Y. Kawaguchi. Dendritic branch typing and spine expression patterns in cortical nonpyramidal cells. *Cerebral Cortex*, 16(5):696–711, August 2006. ISSN 1047-3211, 1460-2199. doi: 10.1093/cercor/bhj015. URL <http://www.cercor.oxfordjournals.org/cgi/doi/10.1093/cercor/bhj015>.
- Y. Kawaguchi and Y. Kubota. Correlation of physiological subgroupings of nonpyramidal cells with parvalbumin- and calbindin d28k-immunoreactive neurons in layer v of rat frontal cortex. *J Neurophysiol*, 70:387–396, 1993.
- Y Kawaguchi and Y Kubota. GABAergic cell subtypes and their synaptic connections in rat frontal cortex. *Cerebral Cortex*, 7(6):476–486, 1997.
- Y Kawaguchi and Y Kubota. Neurochemical features and synaptic connections of large physiologically-identified GABAergic cells in the rat frontal cortex. *Neuroscience*, 85(3):677–701, 1998.
- Yasuo Kawaguchi and Satoru Kondo. Parvalbumin, somatostatin and cholecystokinin as chemical markers for specific GABAergic interneuron types in the rat frontal cortex. *Journal of neurocytology*, 31(3-5):277–287, 2002.
- G Khazen, S Hill, F Schürmann, and H Markram. iSVM: an incremental machine learning approach for recreating ion channel profiles in neocortical neurons. *Front. Neurosci. Conference Abstract: Neuroinformatics*, 2010.



## Bibliography

---

- ZF Kisvarday, KAC Martin, D Whitteridge, and P Somogyi. Synaptic connections of intracellularly filled clutch cells: a type of small basket cell in the visual cortex of the cat. *Journal of Comparative Neurology*, 241(2):111–137, 1985.
- C. Koch and I. Segev, editors. *Methods in Neural Modeling: From Ions to Networks*. MIT Press, Cambridge, MA, 1998.
- C. Koch and I. Segev. The role of single neurons in information processing. *Nature Neurosci.*, 3:1171–1177, 2000.
- M. H. P. Kole, S. Hallermann, and G. J. Stuart. Single ih channels in pyramidal neuron dendrites: Properties, distribution, and impact on action potential output. *J Neurosci*, 26:1677–1687, 2006.
- A. Korngreen and B. Sakmann. (2000)Voltage-gated k<sup>+</sup> channels in layer 5 neocortical pyramidal neurones from young rats: subtypes and gradients. *The Journal of Physiology*, 525:621–639, 2000.
- J. Kozloski. Stereotyped position of local synaptic targets in neocortex. *Science*, 293(5531):868–872, August 2001. ISSN 00368075, 10959203. doi: 10.1126/science.293.5531.868. URL <http://www.sciencemag.org/cgi/doi/10.1126/science.293.5531.868>.
- James Kozloski, Konstantinos Sfyrakis, Sean Hill, F Schurmann, C Peck, and Henry Markram. Identifying, tabulating, and analyzing contacts between branched neuron morphologies. *IBM Journal of Research and Development*, 52(1.2):43–55, 2008.
- M. Krzywinski, J. Schein, I. Birol, J. Connors, R. Gascoyne, D. Horsman, S. J. Jones, and M. A. Marra. Circos: An information aesthetic for comparative genomics. *Genome Research*, 19(9):1639–1645, June 2009. ISSN 1088-9051. doi: 10.1101/gr.092759.109. URL <http://genome.cshlp.org/cgi/doi/10.1101/gr.092759.109>.
- Yoshiyuki Kubota, Sayuri Hatada, Satoru Kondo, Fuyuki Karube, and Yasuo Kawaguchi. Neocortical inhibitory terminals innervate dendritic spines targeted by thalamocortical afferents. *The Journal of neuroscience: the official journal of the Society for Neuroscience*, 27(5):1139–1150, January 2007. ISSN 1529-2401. doi: 10.1523/JNEUROSCI.3846-06.2007. PMID: 17267569.
- M. Köhler, B. Hirschberg, C. T. Bond, J. M. Kinzie, N. V. Marrion, J. Maylie, and J. P. Adelman. Small-conductance, calcium-activated potassium channels from mammalian brain. *Science*, 273:1709–1714, 1996.
- L. Lampl, I. Reichova, and D. Ferster. Synchronous membrane potential fluctuations in neurons of the cat visual cortex. *Neuron*, 22:361–371, 1999.
- Raphael Lamprecht and Joseph LeDoux. Structural plasticity and memory. *Nature Reviews Neuroscience*, 5(1):45–54, January 2004. ISSN 1471-003X, 1471-0048. doi: 10.1038/nrn1301. URL <http://www.nature.com/doi/10.1038/nrn1301>.
- A U Larkman. Dendritic morphology of pyramidal neurones of the visual cortex of the rat: III. spine distributions. *The Journal of comparative neurology*, 306(2):332–343, April 1991. ISSN 0021-9967. doi: 10.1002/cne.903060209. URL <http://www.ncbi.nlm.nih.gov/pubmed/1711059>. PMID: 1711059.
- J.-V. Le Be, G. Silberberg, Y. Wang, and H. Markram. Morphological, electrophysiological, and synaptic properties of corticocallosal pyramidal cells in the neonatal rat neocortex. *Cerebral Cortex*, 17(9):2204–2213, November 2006. ISSN 1047-3211, 1460-2199. doi: 10.1093/cercor/bhl127. URL <http://www.cercor.oxfordjournals.org/cgi/doi/10.1093/cercor/bhl127>.

- J.-V. Le Bé, G. Silberberg, Y. Wang, and H. Markram. Morphological, electrophysiological, and synaptic properties of corticocallosal pyramidal cells in the neonatal rat neocortex. *Cerebral Cortex*, 17: 2204–2213, 2007.
- Sandrine Lefort, Christian Tamm, J-C Floyd Sarria, and Carl CH Petersen. The excitatory neuronal network of the c2 barrel column in mouse primary somatosensory cortex. *Neuron*, 61(2):301–316, 2009.
- H. Lindén, T. Tetzlaff, T. C. Potjans, K. H. Pettersen, S. Grün, M. Diesmann, and G. T. Einevoll. Modeling the spatial reach of the LFP. *Neuron*, 72:859–872, 2011.
- D. S. Ling and L. S. Benardo. Restrictions on inhibitory circuits contribute to limited recruitment of fast inhibition in rat neocortical pyramidal cells. *J Neurophysiol*, 82:1793–1807, 1999.
- N.K. Logothetis and B.A. Wandell. Interpreting the BOLD signal. *Annu. Rev. Physiol.*, 66:735–769, 2004.
- N.K. Logothetis, C. Kayser, and A. Oeltermann. In vivo measurement of cortical impedance spectrum in monkeys: Implications for signal propagation. *Neuron*, 55:809–823, 2007.
- J. Lübke. Morphometric analysis of the columnar innervation domain of neurons connecting layer 4 and layer 2/3 of juvenile rat barrel cortex. *Cerebral Cortex*, 13(10):1051–1063, October 2003. ISSN 1460-2199. doi: 10.1093/cercor/13.10.1051. URL <http://www.cercor.oupjournals.org/cgi/doi/10.1093/cercor/13.10.1051>.
- A. Luczak, P. Bartho, S. L. Marguet, G. Buzsáki, and K. D. Harris. Sequential structure of neocortical spontaneous activity in vivo. *Proc Natl Acad Sci U S A*, 104:347–352, 2007.
- A. Luczak, P. Bartho, and K. D. Harris. Spontaneous events outline the realm of possible sensory responses in neocortical populations. *Neuron*, 62:413–425, 2009.
- J. Magistretti and A. Alonso. Biophysical properties and slow voltage-dependent inactivation of a sustained sodium current in entorhinal cortex layer-II principal neurons a whole-cell and single-channel study. *The Journal of General Physiology*, 114:491–509, 1999.
- Jaakko Malmivuo and Robert Plonsey. *Bioelectromagnetism: principles and applications of bioelectric and biomagnetic fields*. Oxford University Press, 1995.
- H. Markram. The blue brain project. *Nature Rev. Neurosci.*, 16:S46–S46, 2006.
- H Markram. Reconstruction of the neocortical microcircuit. *In preparation*, 2014.
- H. Markram, J. Lübke, M. Frotscher, A. Roth, and B. Sakmann. Physiology and anatomy of synaptic connections between thick tufted pyramidal neurones in the developing rat neocortex. *The Journal of Physiology*, 500(Pt 2):409–440, April 1997. ISSN 0022-3751, 1469-7793.
- Henry Markram and Rodrigo Perin. Innate neural assemblies for lego memory. *Frontiers in Neural Circuits*, 5, 2011. ISSN 1662-5110. doi: 10.3389/fncir.2011.00006. URL <http://www.frontiersin.org/Journal/10.3389/fncir.2011.00006/full>.
- Henry Markram, Maria Toledo-Rodriguez, Yun Wang, Anirudh Gupta, Gilad Silberberg, and Caizhi Wu. Interneurons of the neocortical inhibitory system. *Nat Rev Neurosci*, 5(10):793–807, October 2004. ISSN 1471-003X. doi: 10.1038/nrn1519. URL <http://dx.doi.org/10.1038/nrn1519>.

## Bibliography

---

- L. Marshall, H. Helgadottir, M. Molle, and J. Born. Boosting slow oscillations during sleep potentiates memory. *Nature*, 444:610–613, 2006.
- Nobuko Mataga, Yoko Mizuguchi, and Takao K. Hensch. Experience-dependent pruning of dendritic spines in visual cortex by tissue plasminogen activator. *Neuron*, 44(6):1031–1041, December 2004. ISSN 08966273. doi: 10.1016/j.neuron.2004.11.028. URL <http://linkinghub.elsevier.com/retrieve/pii/S089662730400755X>.
- Laura M McGarry, Adam M Packer, Elodie Fino, Volodymyr Nikolenko, Tanya Sippy, and Rafael Yuste. Quantitative classification of somatostatin-positive neocortical interneurons identifies three interneuron subtypes. *Frontiers in neural circuits*, 4, 2010.
- Cameron C McIntyre and Warren M Grill. Extracellular stimulation of central neurons: influence of stimulus waveform and frequency on neuronal output. *Journal of Neurophysiology*, 88(4):1592–1604, 2002.
- Thomas S. McTavish, Michele Migliore, Gordon M. Shepherd, and Michael L. Hines. Mitral cell spike synchrony modulated by dendrodendritic synapse location. *Frontiers in Computational Neuroscience*, 6, 2012. ISSN 1662-5188. doi: 10.3389/fncom.2012.00003. URL [http://www.frontiersin.org/Computational\\_Neuroscience/10.3389/fncom.2012.00003/abstract](http://www.frontiersin.org/Computational_Neuroscience/10.3389/fncom.2012.00003/abstract).
- Hanno S Meyer, Verena C Wimmer, Mike Hemberger, Randy M Bruno, De Kock, Christiaan Pj, Andreas Frick, Bert Sakmann, and Moritz Helmstaedter. Cell Type–Specific thalamic innervation in a column of rat vibrissa cortex. *Cerebral Cortex*, 20(10):2287–2303, October 2010a. ISSN 1047-3211, 1460-2199. doi: 10.1093/cercor/bhq069. URL <http://cercor.oxfordjournals.org/content/20/10/2287>.
- Hanno S Meyer, Verena C Wimmer, M Oberlaender, Christiaan PJ de Kock, Bert Sakmann, and Moritz Helmstaedter. Number and laminar distribution of neurons in a thalamocortical projection column of rat vibrissa cortex. *Cerebral Cortex*, 20(10):2277–2286, 2010b.
- Hanno S Meyer, Daniel Schwarz, Verena C Wimmer, Arno C Schmitt, Jason N D Kerr, Bert Sakmann, and Moritz Helmstaedter. Inhibitory interneurons in a cortical column form hot zones of inhibition in layers 2 and 5A. *Proceedings of the National Academy of Sciences of the United States of America*, 108(40):16807–16812, October 2011. ISSN 1091-6490. doi: 10.1073/pnas.1113648108. PMID: 21949377 PMCID: PMC3189020.
- K. J. Miller, L. B. Sorensen, J. G. Ojemann, and M. den Nijs. Power-law scaling in the brain surface electric potential. *PLoS Computat Biol*, 5:e1000609, 2009.
- J. Milstein, F. Mormann, I. Fried, and C. Koch. Neuronal shot noise and brownian 1/f<sup>2</sup> behavior in the local field potential. *PLoS ONE*, 4(2):e4338, 2009.
- Yuriy Mishchenko, Tao Hu, Josef Spacek, John Mendenhall, Kristen M. Harris, and Dmitri B. Chklovskii. Ultrastructural analysis of hippocampal neuropil from the connectomics perspective. *Neuron*, 67(6):1009–1020, September 2010. ISSN 08966273. doi: 10.1016/j.neuron.2010.08.014. URL <http://linkinghub.elsevier.com/retrieve/pii/S0896627310006240>.
- U. Mitzdorf. Current source-density method and application in cat cerebral cortex: investigation of evoked potentials and EEG phenomena. *Physiol. Rev.*, 65:37–100, 1985.
- R Ranney Mize. The microcomputer in cell and neurobiology research. 1985.

- S. M. Montgomery, A. Sirota, and G. Buzsáki. Theta and gamma coordination of hippocampal networks during waking and rapid eye movement sleep. *J Neurosci*, 28:6731–6741, 2008.
- V. Mountcastle. The columnar organization of the neocortex. *Brain*, 120(4):701–722, April 1997. ISSN 14602156. doi: 10.1093/brain/120.4.701. URL <http://www.brain.oupjournals.org/cgi/doi/10.1093/brain/120.4.701>.
- Vernon B Mountcastle. Modality and topographic properties of single neurons of cat's somatic sensory cortex. *J. neurophysiol*, 20(4):408–434, 1957.
- Vernon B Mountcastle. *Perceptual neuroscience: The cerebral cortex*. Harvard University Press, 1998.
- Vernon B Mountcastle. Introduction. *Cerebral Cortex*, 13(1):2–4, 2003.
- Vernon B Mountcastle, William H Talbot, Hideo Sakata, and Juhani Hyvarinen. Cortical neuronal mechanisms in flutter-vibration studied in unanesthetized monkeys: Neuronal periodicity and frequency discrimination. *Journal of Neurophysiology*, 1969.
- M. Mukovski, S. Chauvette, I. Timofeev, and M. Volgushev. Detection of active and silent states in neocortical neurons from the field potential signal during SWS. *Cerebral Cortex*, 17:400–414, 2006.
- Guilherme Neves, Sam F. Cooke, and Tim V. P. Bliss. Synaptic plasticity, memory and the hippocampus: a neural network approach to causality. *Nature Reviews Neuroscience*, 9(1):65–75, January 2008. ISSN 1471-003X, 1471-0048. doi: 10.1038/nrn2303. URL <http://www.nature.com/doi/10.1038/nrn2303>.
- C. Nicholson and J. A. Freeman. Theory of current source-density analysis and determination of conductivity tensor for anuran cerebellum. *J Neurophysiol*, 38:356–368, 1975.
- Rudolf Nieuwenhuys. The neocortex. *Anatomy and embryology*, 190(4):307–337, 1994.
- Esther A. Nimchinsky, Bernardo L. Sabatini, and Karel Svoboda. Structure and function of dendritic spines. *Annual Review of Physiology*, 64(1):313–353, March 2002. ISSN 0066-4278, 1545-1585. doi: 10.1146/annurev.physiol.64.081501.160008. URL <http://www.annualreviews.org/doi/abs/10.1146/annurev.physiol.64.081501.160008>.
- Marcel Oberlaender, Christiaan P.J. de Kock, Randy M. Bruno, Alejandro Ramirez, Hanno S. Meyer, Vincent J. Dercksen, Moritz Helmstaedter, and Bert Sakmann. Cell type-specific three-dimensional structure of thalamocortical circuits in a column of rat vibrissa cortex. *Cerebral cortex*, 22(10):2375–2391, 2012.
- J. O'Keefe and M.L. Recce. Phase relationship between hippocampal place units and the EEG theta rhythm. *Hippocampus*, 3:317–330, 1993.
- Adam M. Packer and Rafael Yuste. Dense, unspecific connectivity of neocortical parvalbumin-positive interneurons: a canonical microcircuit for inhibition? *The Journal of neuroscience: the official journal of the Society for Neuroscience*, 31(37):13260–13271, September 2011. ISSN 1529-2401. doi: 10.1523/JNEUROSCI.3131-11.2011. PMID: 21917809.
- C. Pavlides, Y.J. Greenstein, M. Grudman, and J. Winson. Long-term potentiation in the dentate gyrus is induced preferentially on the positive phase of theta-rhythm. *Brain Res.*, 439:383–387, 1988.

## Bibliography

---

- Wilder Penfield and Edwin Boldrey. Somatic motor and sensory representation in the cerebral cortex of man as studied by electrical stimulation. *Brain: A journal of neurology*, 1937.
- R. Perin, T. K. Berger, and H. Markram. A synaptic organizing principle for cortical neuronal groups. *Proc. Natl. Acad. Sci. U.S.A.*, 108(13):5419–5424, 2011.
- Alan Peters. Number of neurons and synapses in primary visual cortex. In *Cerebral cortex*, page 267–294. Springer, 1987.
- Alan Peters and Martin L. Feldman. The projection of the lateral geniculate nucleus to area 17 of the rat cerebral cortex. i. general description. *Journal of Neurocytology*, 5(1):63–84, February 1976. ISSN 0300-4864, 1573-7381. doi: 10.1007/BF01176183. URL <http://link.springer.com/10.1007/BF01176183>.
- Alan Peters and Engin Yilmaz. Neuronal organization in area 17 of cat visual cortex. *Cerebral Cortex*, 3(1):49–68, 1993.
- C C Petersen and B Sakmann. The excitatory neuronal network of rat layer 4 barrel cortex. *The Journal of neuroscience: the official journal of the Society for Neuroscience*, 20(20):7579–7586, October 2000. ISSN 1529-2401. PMID: 11027217.
- K. H. Pettersen and G. T. Einevoll. Amplitude variability and extracellular low-pass filtering of neuronal spikes. *Biophys J*, 94:784–802, 2008.
- K. H. Pettersen, A. Devor, I. Ulbert, A. M. Dale, and G. T. Einevoll. Current-source density estimation based on inversion of electrostatic forward solution: Effects of finite extent of neuronal activity and conductivity discontinuities. *Journal of Neuroscience Methods*, 154(1-2):116–133, June 2006. ISSN 01650270. doi: 10.1016/j.jneumeth.2005.12.005. URL <http://linkinghub.elsevier.com/retrieve/pii/S0165027005004541>.
- K. H. Pettersen, E. Hagen, and G. T. Einevoll. Estimation of population firing rates and current source densities from laminar electrode recordings. *J Comput Neurosci*, 24:291–313, 2008.
- M Piccolino. Luigi galvani and animal electricity: two centuries after the foundation of electrophysiology. *Trends in Neurosciences*, 20(10):443–448, October 1997. ISSN 01662236. doi: 10.1016/S0166-2236(97)01101-6. URL <http://linkinghub.elsevier.com/retrieve/pii/S0166223697011016>.
- Robert Plonsey. *Bioelectric Phenomena*. McGraw-Hill, New York, NY, 1969.
- THOMAS PS Powell and VERNON B Mountcastle. Some aspects of the functional organization of the cortex of the postcentral gyrus of the monkey: a correlation of findings obtained in a single unit analysis with cytoarchitecture. *Bull Johns Hopkins Hosp*, 105(133-62), 1959.
- Karine Pozo and Yukiko Goda. Unraveling mechanisms of homeostatic synaptic plasticity. *Neuron*, 66(3):337–351, May 2010. ISSN 08966273. doi: 10.1016/j.neuron.2010.04.028. URL <http://linkinghub.elsevier.com/retrieve/pii/S0896627310002990>.
- M. I. T. Press, editor. *Using MPI*. Gropp, W. AND Lusk, E. AND Skjellum, A., 2nd edition: portable parallel programming with the message passing interface edition, 1999.
- W. S. Pritchard. The brain in fractal time: 1/f-like power spectrum scaling of the human electroencephalogram. *Int J Neurosci*, 66:119–129, 1992.

- Dale Purves, George Augustine, David Fitzpatrick, Lawrence Katz, Anthony-Samuel LaMantia, James McNamara, and Mark Williams. An overview of cortical structure. In *Neuroscience*. Sinauer Associates, Sunderland, MA, 2nd edition, 2001.
- Srikanth Ramaswamy. *Emergent Properties of in silico Synaptic Transmission in a Model of the Rat Neocortical Column*. PhD thesis, Ecole Polytechnique Federal de Lausanne, Lausanne, 2011.
- Srikanth Ramaswamy, Sean L. Hill, James G. King, Felix Schürmann, Yun Wang, and Henry Markram. Intrinsic morphological diversity of thick-tufted layer 5 pyramidal neurons ensures robust and invariant properties of in silico synaptic connections: Comparison of in vitro and in silico TTL5 synaptic connections. *The Journal of Physiology*, pages no–no, January 2012. ISSN 00223751. doi: 10.1113/jphysiol.2011.219576. URL <http://www.jphysiol.org/cgi/doi/10.1113/jphysiol.2011.219576>.
- JB Ranck. Extracellular stimulation. *Electrical stimulation research techniques*, page 1–36, 1981.
- S. Ray and J. H. R. Maunsell. Different origins of gamma rhythm and high-gamma activity in macaque visual cortex. *PLoS Biol*, 9(4):e1000610, 2011.
- M W Reimann, E Muller, S Ramaswamy, S L Hill, and H Markram. An algorithm to predict the connectome of neural microcircuits. *In preparation*, a.
- M W Reimann, E Muller, S Ramaswamy, S L Hill, and H Markram. A predicted connectome of the neocortical microcircuitry. *In preparation*, b.
- Birdsey Renshaw, Alexander Forbes, and BR Morison. Activity of isocortex and hippocampus: electrical studies with micro-electrodes. *Journal of Neurophysiology*, 3(1):74–105, 1940.
- J. Rettig, F. Wunder, M. Stocker, R. Lichtinghagen, F. Mastiaux, S. Beckh, W. Kues, and et al. Characterization of a shaw-related potassium channel family in rat brain. *The EMBO Journal*, 11:2473–2486, 1992.
- I. Reuveni, A. Friedman, Y. Amitai, and M. J. Gutnick. Stepwise repolarization from  $ca^{2+}$  plateaus in neocortical pyramidal cells: Evidence for nonhomogeneous distribution of HVA  $ca^{2+}$  channels in dendrites. *J Neurosci*, 13:4609–4621, 1993.
- Alex Reyes, R Lujan, A Rozov, N Burnashev, P Somogyi, and B Sakmann. Target-cell-specific facilitation and depression in neocortical circuits. *Nature neuroscience*, 1(4):279–285, 1998.
- Robert V. Riccio and Murray A. Matthews. Effects of intraocular tetrodotoxin on dendritic spines in the developing rat visual cortex: a golgi analysis. *Developmental Brain Research*, 19(2):173–182, April 1985. ISSN 01653806. doi: 10.1016/0165-3806(85)90189-0. URL <http://linkinghub.elsevier.com/retrieve/pii/0165380685901890>.
- J. J. Riera, T. Ogawa, T. Goto, A. Sumiyoshi, H. Nonaka, A. Evans, H. Miyakawa, and R. Kawashima. Pitfalls in the dipolar model for the neocortical EEG sources. *J Neurophysiol*, 108:956–975, 2012.
- T. Rinaldi, K. Kulangara, K. Antonello, and H. Markram. Elevated NMDA receptor levels and enhanced postsynaptic long-term potentiation induced by prenatal exposure to valproic acid. *Proc Natl Acad Sci U S A*, 104:13501–13506, 2007a.
- T. Rinaldi, G. Silberberg, and H. Markram. Hyperconnectivity of local neocortical microcircuitry induced by prenatal exposure to valproic acid. *Cerebral Cortex*, 18(4):763–770, July 2007b. ISSN 1047-3211, 1460-2199. doi: 10.1093/cercor/bhm117. URL <http://www.cercor.oxfordjournals.org/cgi/doi/10.1093/cercor/bhm117>.

## Bibliography

---

- Per E. Roland. Dynamic depolarization fields in the cerebral cortex. *Trends in Neurosciences*, 25(4): 183–190, April 2002. ISSN 01662236. doi: 10.1016/S0166-2236(00)02125-1. URL <http://linkinghub.elsevier.com/retrieve/pii/S0166223600021251>.
- Sandrine Romand, Yun Wang, Maria Toledo-Rodriguez, and Henry Markram. Morphological development of thick-tufted layer v pyramidal cells in the rat somatosensory cortex. *Frontiers in Neuroanatomy*, 5, 2011. ISSN 1662-5129. doi: 10.3389/fnana.2011.00005. URL <http://www.frontiersin.org/Neuroanatomy/10.3389/fnana.2011.00005/abstract>.
- U. Rutishauser, I. B. Ross, A. N. Mamelak, and E. M. Schuman. Human memory strength is predicted by theta-frequency phase-locking of single neurons. *Nature*, 464:903–907, 2010.
- N Saitou and M Nei. The neighbor-joining method: a new method for reconstructing phylogenetic trees. *Molecular biology and evolution*, 4(4):406–425, July 1987. ISSN 0737-4038. PMID: 3447015.
- Carlo Sala and Menahem Segal. Dendritic spines: the locus of structural and functional plasticity. *Physiological reviews*, 94(1):141–188, January 2014. ISSN 1522-1210. doi: 10.1152/physrev.00012.2013. PMID: 24382885.
- M. V. Sanchez-Vives and D. A. McCormick. Cellular and network mechanisms of rhythmic recurrent activity in neocortex. *Nat. Neurosci.*, 10:1027–1034, 2000.
- L. Sarid, R. Bruno, B. Bruno, I. Segev, and D. Feldmeyer. Modeling a layer 4-to-layer 2/3 module of a single column in rat neocortex: interweaving in vitro and in vivo experimental observation. *Proc Natl Acad Sci U S A*, 104:16353–16358, 2007.
- JW Scannell, GAPC Burns, CC Hilgetag, MA O’Neil, and Malcolm P Young. The connectional organization of the cortico-thalamic system of the cat. *Cerebral Cortex*, 9(3):277–299, 1999.
- E. W. Schomburg, C. A. Anastassiou, G. Buzsáki, and C. Koch. The spiking component of oscillatory extracellular potentials in the rat hippocampus. *Journal of Neuroscience*, 32:11798–11811, 2012.
- Almut Schüz and Günther Palm. Density of neurons and synapses in the cerebral cortex of the mouse. *Journal of Comparative Neurology*, 286(4):442–455, 1989.
- Gordon M G Shepherd, Armen Stepanyants, Ingrid Bureau, Dmitri Chklovskii, and Karel Svoboda. Geometric and functional organization of cortical circuits. *Nature Neuroscience*, 8(6):782–790, May 2005. ISSN 1097-6256. doi: 10.1038/nn1447. URL <http://www.nature.com/doifinder/10.1038/nn1447>.
- Y. Shu, A. Hasenstaub, and D. A. McCormick. Turning on and off recurrent balanced cortical activity. *Nature*, 423:288–293, 2003.
- Y. Shu, Y. Yu, J. Yang, and D. A. McCormick. Selective control of cortical axonal spikes by a slowly inactivating  $k^+$  current. *Proc Natl Acad Sci U S A*, 104:11453–11458, 2007.
- G. Silberberg and H. Markram. Disynaptic inhibition between neocortical pyramidal cells mediated by martinotti cells. *Neuron*, 53:735–746, 2007.
- Gilad Silberberg, Anirudh Gupta, and Henry Markram. Stereotypy in neocortical microcircuits. *Trends in neurosciences*, 25(5):227–230, 2002.

- R. A. Silver. High-probability unquantal transmission at excitatory synapses in barrel cortex. *Science*, 302(5652):1981–1984, December 2003. ISSN 0036-8075, 1095-9203. doi: 10.1126/science.1087160. URL <http://www.sciencemag.org/cgi/doi/10.1126/science.1087160>.
- P. Somogyi. A specific 'axo-axonal' interneuron in the visual cortex of the rat. *Brain Research*, 136: 345–350, 1977.
- P. Somogyi, T.F. Freund, and A. Cowey. The axo-axonic interneuron in the cerebral cortex of the rat, cat and monkey. *Neuroscience*, 7(11):2577–2607, November 1982. ISSN 03064522. doi: 10.1016/0306-4522(82)90086-0. URL <http://linkinghub.elsevier.com/retrieve/pii/0306452282900860>.
- Peter Somogyi, Gábor Tamás, Rafael Lujan, and Eberhard H. Buhl. Salient features of synaptic organisation in the cerebral cortex. *Brain Research Reviews*, 26(2-3):113–135, May 1998. ISSN 01650173. doi: 10.1016/S0165-0173(97)00061-1. URL <http://linkinghub.elsevier.com/retrieve/pii/S0165017397000611>.
- Sen Song, Per Jesper Sjöström, Markus Reigl, Sacha Nelson, and Dmitri B. Chklovskii. Highly nonrandom features of synaptic connectivity in local cortical circuits. *PLoS Biology*, 3(3):e68, 2005. ISSN 1544-9173, 1545-7885. doi: 10.1371/journal.pbio.0030068.
- Olaf Sporns and Jonathan D. Zwi. The small world of the cerebral cortex. *Neuroinformatics*, 2(2):145–162, 2004. ISSN 1539-2791. doi: 10.1385/NI:2:2:145. URL <http://link.springer.com/10.1385/NI:2:2:145>.
- J F Staiger, R Kötter, K Zilles, and H J Luhmann. Laminar characteristics of functional connectivity in rat barrel cortex revealed by stimulation with caged-glutamate. *Neuroscience research*, 37(1):49–58, May 2000. ISSN 0168-0102. PMID: 10802343.
- Jochen F Staiger, Iris Flagmeyer, Dirk Schubert, Karl Zilles, Rolf Kötter, and Heiko J Luhmann. Functional diversity of layer IV spiny neurons in rat somatosensory cortex: quantitative morphology of electrophysiologically characterized and biocytin labeled cells. *Cerebral Cortex*, 14(6):690–701, 2004.
- A Stepanyants and D Chklovskii. Neurogeometry and potential synaptic connectivity. *Trends in Neurosciences*, 28(7):387–394, July 2005a. ISSN 01662236. doi: 10.1016/j.tins.2005.05.006. URL <http://linkinghub.elsevier.com/retrieve/pii/S0166223605001311>.
- A. Stepanyants, L. M. Martinez, A. S. Ferecsko, and Z. F. Kisvarday. The fractions of short- and long-range connections in the visual cortex. *Proceedings of the National Academy of Sciences*, 106(9): 3555–3560, February 2009. ISSN 0027-8424, 1091-6490. doi: 10.1073/pnas.0810390106. URL <http://www.pnas.org/cgi/doi/10.1073/pnas.0810390106>.
- Armen Stepanyants and Dmitri B. Chklovskii. Neurogeometry and potential synaptic connectivity. *Trends in Neurosciences*, 28(7):387–394, July 2005b. ISSN 0166-2236. doi: 10.1016/j.tins.2005.05.006. URL <http://www.sciencedirect.com/science/article/pii/S0166223605001311>.
- Armen Stepanyants, Patrick R. Hof, and Dmitri B. Chklovskii. Geometry and structural plasticity of synaptic connectivity. *Neuron*, 34(2):275–288, April 2002. ISSN 08966273. doi: 10.1016/S0896-6273(02)00652-9. URL <http://linkinghub.elsevier.com/retrieve/pii/S0896627302006529>.
- Armen Stepanyants, Gábor Tamás, and Dmitri B Chklovskii. Class-specific features of neuronal wiring. *Neuron*, 43(2):251–259, July 2004. ISSN 0896-6273. doi: 10.1016/j.neuron.2004.06.013. PMID: 15260960.



## Bibliography

---

- Armen Stepanyants, Judith A Hirsch, Luis M Martinez, Zoltán F Kisvárdy, Alex S Ferecskó, and Dmitri B Chklovskii. Local potential connectivity in cat primary visual cortex. *Cerebral Cortex*, 18(1):13–28, January 2008. ISSN 1047-3211, 1460-2199. doi: 10.1093/cercor/bhm027. URL <http://cercor.oxfordjournals.org/content/18/1/13>.
- M. Steriade, D. Contreras, R. Curro-Dossi, and A. Nunez. The slow oscillation in reticular thalamic and thalamocortical neurons: scenario of sleep rhythm generation in interacting thalamic and neocortical networks. *J. Neurosci.*, 13:3284–3299, 1993a.
- M. Steriade, A. Nunez, and F. Amzica. Intracellular analysis of relations between the slow (< 1 hz) neocortical oscillation and other sleep rhythms of the electroencephalogram. *J. Neurosci.*, 13:3266–3283, 1993b.
- M. Steriade, A. Nunez, and F. Amzica. A novel oscillation of neocortical neurons in vivo: depolarizing and hyperpolarizing components. *J. Neurosci.*, 13:252–265, 1993c.
- E. A. Stern, A. E. Kincaid, and C. J. Wilson. Impact of network activities on neuronal properties on corticothalamic systems. *J. Neurophysiol.*, 77:1697–1715, 1997.
- CF Stevens. *Neurophysiology: A primer*. Wiley, New York, NY, 1966.
- G. Stuart and N. Spruston. Determinants of voltage attenuation in neocortical pyramidal neuron dendrites. *J Neurosci*, 18:3501–3510, 1998.
- G. Stuart, J. Schiller, and B. Sakmann. Action potential initiation and propagation in rat neocortical pyramidal neurons. *J Physiol*, 505:617–632, 1997.
- Karel Svoboda, Winfried Denk, David Kleinfeld, David W Tank, et al. In vivo dendritic calcium dynamics in neocortical pyramidal neurons. *Nature*, 385(6612):161–165, 1997.
- János Szabadics, Gábor Tamás, and Ivan Soltesz. Different transmitter transients underlie presynaptic cell type specificity of GABAA, slow and GABAA, fast. *Proceedings of the National Academy of Sciences*, 104(37):14831–14836, 2007.
- J. Szentágothai. The ‘module-concept’ in cerebral cortex architecture. *Brain Research*, 95(2-3):475–496, September 1975. ISSN 00068993. doi: 10.1016/0006-8993(75)90122-5. URL <http://linkinghub.elsevier.com/retrieve/pii/0006899375901225>.
- A. Thomson. Synaptic interactions in neocortical local circuits: dual intracellular recordings in vitro. *Cerebral Cortex*, 7(6):510–522, September 1997. ISSN 14602199. doi: 10.1093/cercor/7.6.510. URL <http://www.cercor.oupjournals.org/cgi/doi/10.1093/cercor/7.6.510>.
- A M Thomson, D C West, J Hahn, and J Deuchars. Single axon IPSPs elicited in pyramidal cells by three classes of interneurons in slices of rat neocortex. *The Journal of physiology*, 496 ( Pt 1):81–102, October 1996. ISSN 0022-3751. PMID: 8910198.
- I. Timofeev and M. Steriade. Low-frequency rhythms in the thalamus of intact-cortex and decorticated cats. *J. Neurophysiol.*, 76:4152–4168, 1996.
- I. Timofeev, F. Grenier, M. Bazhenov, and M. Steriade. Origin of slow cortical oscillations in deafferented cortical slabs. *Cereb. Cortex*, 10, 2000.

- M. Toledo-Rodriguez, B. Blumenfeld, C. Wu, J. Luo, B. Attali, P. Goodman, and H. Markram. Correlation maps allow neuronal electrical properties to be predicted from single-cell gene expression profiles in rat neocortex. *Cereb Cortex*, 14:1310–1327, 2004.
- Maria Toledo-Rodriguez, Philip Goodman, Milena Illic, Caizhi Wu, and Henry Markram. Neuropeptide and calcium-binding protein gene expression profiles predict neuronal anatomical type in the juvenile rat. *The Journal of physiology*, 567(2):401–413, 2005.
- Misha Tsodyks, Klaus Pawelzik, and Henry Markram. Neural networks with dynamic synapses. *Neural Computation*, 10(4):821–835, May 1998. ISSN 0899-7667, 1530-888X. doi: 10.1162/089976698300017502. URL <http://www.mitpressjournals.org/doi/abs/10.1162/089976698300017502>.
- Arjen van Ooyen, Andrew Carnell, Sander de Ridder, Bernadetta Tarigan, Huibert D. Mansvelder, Fetsje Bijma, Mathisca de Gunst, and Jaap van Pelt. Independently outgrowing neurons and geometry-based synapse formation produce networks with realistic synaptic connectivity. *PLoS ONE*, 9(1):e85858, January 2014. ISSN 1932-6203. doi: 10.1371/journal.pone.0085858. URL <http://dx.plos.org/10.1371/journal.pone.0085858>.
- Y. Wang. Anatomical, physiological, molecular and circuit properties of nest basket cells in the developing somatosensory cortex. *Cerebral Cortex*, 12(4):395–410, April 2002. ISSN 14602199. doi: 10.1093/cercor/12.4.395. URL <http://www.cercor.oupjournals.org/cgi/doi/10.1093/cercor/12.4.395>.
- Y. Wang, M. Toledo-Rodriguez, A. Gupta, C. Wu, G. Silberberg, J. Luo, and H. Markram. Anatomical, physiological and molecular properties of martinotti cells in the somatosensory cortex of the juvenile rat. *The Journal of Physiology*, 561(1):65–90, August 2004. ISSN 0022-3751. doi: 10.1113/jphysiol.2004.073353. URL <http://www.jphysiol.org/cgi/doi/10.1113/jphysiol.2004.073353>.
- J. Waters. Background synaptic activity is sparse in neocortex. *Journal of Neuroscience*, 26(32):8267–8277, August 2006. ISSN 0270-6474, 1529-2401. doi: 10.1523/JNEUROSCI.2152-06.2006. URL <http://www.jneurosci.org/cgi/doi/10.1523/JNEUROSCI.2152-06.2006>.
- Carol Welker and Thomas A. Woolsey. Structure of layer IV in the somatosensory neocortex of the rat: Description and comparison with the mouse. *The Journal of Comparative Neurology*, 158(4):437–453, December 1974. ISSN 0021-9967, 1096-9861. doi: 10.1002/cne.901580405. URL <http://doi.wiley.com/10.1002/cne.901580405>.
- E L White. *Cortical Circuits. Synaptic Organization of the Cerebral Cortex*. Birkhauser, Basel, 1989.
- Linda Wilbrecht, Anthony Holtmaat, Nick Wright, Kevin Fox, and Karel Svoboda. Structural plasticity underlies experience-dependent functional plasticity of cortical circuits. *The Journal of neuroscience: the official journal of the Society for Neuroscience*, 30(14):4927–4932, April 2010. ISSN 1529-2401. doi: 10.1523/JNEUROSCI.6403-09.2010. PMID: 20371813.
- V. C. Wimmer, R. M. Bruno, C. P. J. de Kock, T. Kuner, and B. Sakmann. Dimensions of a projection column and architecture of VPM and POm axons in rat vibrissal cortex. *Cerebral Cortex*, 20(10):2265–2276, May 2010. ISSN 1047-3211, 1460-2199. doi: 10.1093/cercor/bhq068. URL <http://www.cercor.oxfordjournals.org/cgi/doi/10.1093/cercor/bhq068>.
- Thomas A Woolsey and Hendrik Van der Loos. The structural organization of layer IV in the somatosensory region (SI) of mouse cerebral cortex: the description of a cortical field composed of discrete cytoarchitectonic units. *Brain research*, 17(2):205–242, 1970.

## Bibliography

---

- Santiago Ramón y Cajal. *Histologie du système nerveux de l'homme & des vertébrés*. Consejo Superior de Investigaciones Científicas, Instituto Ramon y Cajal, 1909.
- Y. Yoshimura, F. Kimura, and T. Tsumoto. Estimation of single channel conductance underlying synaptic transmission between pyramidal cells in the visual cortex. *Neuroscience*, 88:347–352, 1999.
- WG Young, EA Nimchinsky, PR Hof, JH Morrison, and FE Bloom. NeuroZoom software user guide and reference books. *YBM Inc., San Diego*, page 1038, 1997.
- S. Zanos, T. P. Zanos, V. Z. Marmarelis, G. A. Ojemann, and E. E. Fetz. Relationships between spike-free local field potentials and spike timing in human temporal cortex. *J Physiol*, 107:1808–1821, 2011.

CURRICULUM VITAE  
Michael Wolfgang Reimann, Dipl. Inf. (Bioinformatics)

PhD Student - EFPL, Lausanne, Switzerland  
[michael.reimann@epfl.ch](mailto:michael.reimann@epfl.ch)

**Personal Details:**

Name:	Michael Wolfgang Reimann
Address:	Chemin de la Cocarde 11 1024 Ecublens Switzerland
Date of Birth:	30.12.1981
Nationality:	German
Marital Status:	Single
Children:	None
Languages:	German, English, French, Japanese

**Interests:**

*Travelling*  
*Foreign culture, in particular Japanese*  
*Digital photography*  
*Short Stories (Literature)*  
*Programming*  
*'Hardware hacking'*

**Education**

**'Diplom' (Master) in Bioinformatics** (February 2008)

**Thesis:** Using inertial information alone to estimate linear self-displacement with varying durations of constant velocity

**Specialization:** Neurobiology

**Supervisor:** Prof. Dr. Heinrich H. Bühlhoff

Max Planck Institute for Biological Cybernetics, Tuebingen, Germany

**'Vordiplom' (Bachelor) in Bioinformatics** (October 2004)

**Thesis:** Mislocalization of stimuli shortly before the onset of a saccade

**Supervisor:** Prof. Uwe Ilg

Eberhard Karls University Tuebingen, Germany

**Internship** (06/01/07 – 07/29/08) under supervision of Prof. Dr. Heinrich H. Bühlhoff  
at the Max Planck Institute for Biological Cybernetics, Tuebingen, Germany

**Project participation**

**Assistant-Doctorant** (since March 09)

**Supervisor:** Prof. Henry Markram, EPFL; Prof. Sean Hill, EPFL & Dr. Eilif Müller, EPFL

Analysis and improvement of an *in-silico* reconstruction of a neocortical microcircuit.

**Research assistant** (07/15/08 – 02/01/09)

**Supervisor:** Dr. Christoph von Laßberg, University of Leipzig, Germany

Working on a project on the coordination and interdependence of eye movements, body movements and muscle activation in top gymnasts.

**Research assistant** (09/15/06 – 05/01/07)

**Supervisor:** Boris Kleber, Dipl.-Psych., University of Tuebingen, Germany

Record and analyze EEG data in a project on neurofeedback for professional singers

**Publications & Presentations:**

The Blue Brain Consortium and Markram (2014). Reconstruction of the Neocortical Microcircuit. In preparation for submission to Nature

Reimann, Muller, Ramaswamy and Markram (2014). An algorithm to predict the Connectome of Neural Microcircuits. In preparation for submission to Nature Neuroscience

Reimann, Muller, Ramaswamy and Markram (2014). A Predicted Connectome of the Neocortical Microcircuitry. In preparation for submission to Nature Neuroscience

Reimann, Anastassiou, Perin, Hill, Markram and Koch (2013). A biophysically detailed model of neocortical local field potentials predicts the critical role of active membrane currents. *Neuron*, 79 (2):375-390, July 2013. PMID: 23889937

Reimann, Campos, Butler, Beykirch and Bühlhoff (2008): Using inertial information alone to estimate linear self-displacement with varying durations of constant velocity

von Laßberg, C., Reimann, M., Krug, J. (2009). Vismo – a prototype software solution for integration of vestibular, oculomotor, spinalmotor and 3D-kinematic data in sports. In: Loland, S., Bø, K., Fasting, K., Hallén, J., Ommundsen, Y., Roberts, G., Tsolakidis, E. (Eds.), Proceedings of 14<sup>th</sup> Annual Congress of European College of Sport Science (402), Norwegian School of Sport Sciences, Oslo/Norway.